

THREE-DIMENSIONAL STEADY STATE AND TRANSIENT EDDY CURRENT
MODELING

by

Subhra Paul

A dissertation submitted to the faculty of
The University of North Carolina at Charlotte
in partial fulfillment of the requirements
for the degree of Doctor of Philosophy in
Electrical Engineering

Charlotte

2013

Approved by:

Dr. Jonathan Bird

Dr. Robert Cox

Dr. Sukumar Kamalasan

Dr. Ryan Adams

Dr. Yuri Godin

©2013
Subhra Paul
ALL RIGHTS RESERVED

ABSTRACT

SUBHRA PAUL. Three-dimensional steady state and transient eddy current modeling
(Under the direction of Dr. JONATHAN BIRD)

Maglev transportation using electrodynamic wheels is a promising new technology aimed at providing a low cost, high-speed and environmental friendly mode of transportation. In this technology, Halbach permanent magnet rotors, termed electrodynamic wheels, are simultaneously rotated and translationally moved above a conductive non-magnetic guideway. The time-changing magnetic field created in the airgap between the rotors and guideway induces eddy currents in the guideway which in turn interact with the magnetic rotor field to produce suspension and propulsion or braking forces which are required for maglev transportation. This technology offers an integrated suspension and propulsion system.

In this dissertation the eddy current distribution in the conductive guideway has been modeled in three-dimension. An approach for the computation of the static magnetic fields due to the Halbach rotor has been presented using novel magnetic charge sheet concept. Finite element models have been developed to study the steady state and transient eddy current field distribution. Three analytic models have been developed to compute the electromagnetic forces and torque acting on the rotor as well as joule loss in the guideway. The models include the heave, translational and rotational motion of the magnetic rotor for dynamic simulation. The developed analytic and finite element models are highly generic and thus can be applied to any magnetic source. The developed finite element models have been validated by comparing it with commercial finite element software and previously developed boundary coupled steady state finite element model.

Commercial finite element software and two experimental setups have been used to verify the developed analytic models. Computational efficiency of the presented models has been compared with the previously developed finite element model and commercial software. Good performance of the developed models has been achieved.

DEDICATION

I dedicate this dissertation to my parents, Anita Paul and Triptikar Paul.

ACKNOWLEDGEMENTS

I am especially thankful to my advisor Dr. Jonathan Bird for his immense support and guidance. This dissertation would not have been presented in this form without his help. I would like to extend my appreciation to the committee members Dr. Robert Cox, Dr. Ryan Adams, Dr. Sukumar Kamalasan and Dr. Yuri Godin for taking time to be on my committee and read my dissertation.

I would gratefully like to thank JMAG Corporation for the use of their finite-element analysis software and National Science Foundation for the funding provided. This material is based upon work supported by the National Science Foundation under Grant No. 0925941. I am grateful to the Graduate School for providing me financial assistance through Graduate Assistant Support Plan throughout my research. Also, I express my sincere gratitude to my department and advisor, Dr. Jonathan Bird, for financially assisting me with Teaching Assistantship and Research Assistantship respectively.

I would also like to thank Nirmal Paudel and Walter Bomela for providing me with the experimental setup.

TABLE OF CONTENTS

LIST OF SYMBOLS	xiii
LIST OF ABBREVIATIONS	xvi
CHAPTER 1: INTRODUCTION AND REVIEW	1
1.1. Introduction	1
1.2. Maglev- How It Works	2
1.2.1. Suspension or Levitation System	2
1.2.2. Propulsion System	7
1.3. Advantages and Disadvantages of Maglev	10
1.3.1. Advantages	10
1.3.2. Disadvantages	12
1.4. Idea of EDW	13
1.5. Comparison of EDW with Existing Operating Maglevs	15
1.6. Recent Work on EDW Project	17
1.7. Research Goal	20
1.8. Organization of Dissertation	22
CHAPTER 2: MAGNETIC SOURCE FIELD MODELING USING MAGNETIC CHARGE	24
2.1. Introduction	24
2.2. Cylindrical Magnetic Charge Sheet	27
2.2.1. Derivation of Charge Density	28
2.2.2. External Field Calculation	31
2.2.3. Validation Using Rotor Model	33
2.3. Planar Charge Sheet	38

	viii
2.3.1. Derivation of Charge Density	38
2.3.2. External Field Calculation	39
2.3.3. Validation Using Rotor Model	40
2.4. Summary	41
CHAPTER 3: THREE-DIMENSIONAL EDDY CURRENT MODELING USING FINITE ELEMENT ANALYSIS	42
3.1. Introduction	42
3.2. A Review of Numerical Analysis of Eddy Current Distribution of Moving Parts	43
3.3. Transient Modeling	46
3.3.1. Conductive Region Formulation	46
3.3.2. Nonconductive Region Formulation	51
3.3.3. Boundary Condition	52
3.3.4. Initial Condition, Meshing and Solver Settings	55
3.3.5. Model Validation	58
3.4. Steady State Modeling	66
3.4.1. Governing Equation Formulation	66
3.4.2. Meshing and Solver Settings	67
3.4.3. Model Validation	67
3.5. Summary	74
CHAPTER 4: A BRIEF SURVEY OF ANALYTIC EDDY CURRENT MODELING IN THREE DIMENSION	76
4.1. Introduction	76
4.2. Review of Existing 3-D Analytical Methods	77
4.2.1. Conductive Half-Space	77
4.2.2. Conductive Domain with Finite Dimensions	82

	ix
4.3. Need for New Method	83
4.4. Conclusion	84
CHAPTER 5: 3-D ANALYTIC EDDY CURRENT MODELING FOR A CONDUCTIVE PLATE OF INFINITE DIMENSION	85
5.1. Introduction	85
5.2. Governing Equation Formulation	86
5.2.1. Conductive Region (Ω_{II})	88
5.2.2. Nonconductive Regions (Ω_I and Ω_{III})	92
5.3. Boundary Conditions	93
5.4. Derivation of General Solutions	95
5.4.1. Conductive Region (Ω_{II})	95
5.4.2. Nonconductive Regions (Ω_I and Ω_{III})	97
5.5. Source Field Modeling	98
5.6. Field Solution	102
5.6.1. Solution for the TE Potential	102
5.6.2. Solution for the Magnetic Vector Potential	106
5.6.3. Solution for the Magnetic Flux Density	106
5.7. Calculation of Electromagnetic Force	108
5.7.1. Calculation using Maxwell's Stress Tensor	109
5.7.2. Calculation using Fictitious Magnetic Charge	113
5.8. Power Transfer Calculation	116
5.9. Electromagnetic Torque Calculation	117
5.10. Power Loss Calculation	117
5.11. Electromagnetic Stiffness Constant Calculation	119

	x
5.12. Electromagnetic Damping Constant Calculation	120
5.13. Model Validation	127
5.13.1. Field Validation	128
5.13.2. Force and Power Loss Validation	131
5.14. Stiffness and Damping Coefficients Results	136
5.15. Summary	145
CHAPTER 6: 3-D ANALYTIC EDDY CURRENT MODELING FOR FINITE WIDTH CONDUCTIVE PLATE	147
6.1. Introduction	147
6.2. Governing Equation Formulation	150
6.2.1. Conductive Region (Ω_{II})	150
6.2.2. Nonconductive Regions I and III (Ω_I and Ω_{III})	151
6.2.3. Nonconductive Regions IV and V (Ω_{IV} and Ω_V)	152
6.3. Boundary Conditions	152
6.4. Derivation of General Solutions	155
6.4.1. Conductive Region (Ω_{II})	155
6.4.2. Nonconductive Regions I and III (Ω_I and Ω_{III})	158
6.5. Source Field Formulation	159
6.6. Field Solution	163
6.6.1. Solution for the Magnetic Vector Potential	164
6.6.2. Solution for the Magnetic Flux Density	172
6.7. Calculation of Electromagnetic Force	175
6.7.1. Calculation using Maxwell's Stress Tensor	175
6.7.2. Simplified Stress Tensor Calculation	177

	xi
6.7.3. Calculation using Lorentz method	180
6.8. Power Loss, Total Power Transfer and Torque Calculation	181
6.9. Model Validation	183
6.9.1. Field Validation	183
6.9.2. Force and Power Loss Validation	192
6.10. Limitation of the Proposed Model and Improved 3-Component Vector Potential Model	197
6.10.1. Governing Equations and Boundary Conditions	201
6.10.2. Source Field Modeling	203
6.10.3. Field Solution	203
6.10.4. Model Validation	204
6.11. Summary	207
CHAPTER 7: 3-D ANALYTIC EDDY CURRENT MODELING FOR FINITE PLATE WIDTH INCLUDING EDGE-EFFECT	209
7.1. Introduction	209
7.2. Governing Equation Formulation	211
7.2.1. Conductive Region (Ω_{II})	212
7.2.2. Nonconductive Region (Ω_V)	216
7.2.3. Nonconductive Regions Ω_I and Ω_{III}	218
7.3. Boundary Condition and Field Solution	220
7.3.1. Determination of Unknown Eigenvalues	220
7.3.2. Determination of Unknown Coefficients	223
7.4. Force Calculation	229
7.4.1. Thrust Force Calculation	229
7.4.2. Lift Force Calculation	233

	xii
7.4.3. Lateral Force Calculation	236
7.5. Model Validation	240
7.5.1. Field Validation	240
7.5.2. Force Validation	241
7.6. Summary	245
CHAPTER 8: EXPERIMENTAL RESULTS AND VERIFICATION	247
8.1. Introduction	247
8.2. Comparison with a Pendulum Setup	247
8.2.1. Description of the Experimental Setup	247
8.2.2. Dynamics of the Forced Oscillation	250
8.3. Comparison with Multi-DOF EDW Maglev	253
8.3.1. Torque and Power Transfer Comparison	254
8.3.2. Lift Force Verification	262
8.4. Summary	265
CHAPTER 9: CONCLUSION AND FUTURE WORKS	266
9.1. Introduction	266
9.2. Conclusion	266
9.3. Research Contributions	268
9.4. Future Research Works	269
BIBLIOGRAPHY	271
APPENDIX A : DERIVATION OF CONTINUOUS FOURIER SERIES FROM DISCRETE FOURIER TRANSFORM (DFT)	289

LIST OF SYMBOLS

H	magnetic field intensity
B	magnetic flux density
E	electric field intensity
V	electric scalar potential
A	magnetic vector potential
W	second order magnetic vector potential
J	eddy current density
W_a	transverse electric potential
W_b	transverse magnetic potential
ϕ	magnetic scalar potential
μ_r	relative magnetic permeability
μ_0	permeability of free space [$4\pi \times 10^{-7}$]
ρ_m	magnetic charge density
q_e	electric point charge
ρ_e	electric surface charge density
B_{rem}	remnant magnetic flux density
σ	conductivity
ω_m	mechanical angular frequency
ω_e	electrical angular frequency
v	velocity vector
v_x	translational velocity
v_c	circumferential velocity of rotor

v_y	heave velocity
s_l	slip speed
w_o	rotor width
r_o	rotor outer radius
r_i	rotor inner radius
P	number of pole-pair of rotor
g	airgap
h	thickness of conductive medium
l	length of conductive medium
w	width of conductive medium
ξ	Fourier frequency with respect to x -direction
k, ψ	Fourier frequency with respect to z -direction
Γ	boundary surface
Ω	volume region
F	force vector
F_x	thrust force
F_y	lift force
F_z	lateral force
P_{loss}	power loss
S	density of power flow
$P_{transfer}$	power transfer
$\text{Re}\{ \}$	real part of complex number
$\text{Im}\{ \}$	imaginary part of complex number

G	gravity of earth [9.81ms^{-2}]
T_{em}	electromagnetic torque
\hat{n}	normal vector
\hat{x}	normal vector along the x -axis
\hat{y}	normal vector along the y -axis
\hat{z}	normal vector along the z -axis
\hat{r}	normal vector along radial direction
T^w	transmission function of TE potential
R^w	reflection function of TE potential
δ	Dirac delta function
w_s	width of magnetic charge sheet
l_s	length of magnetic charge sheet
ρ_{mn}	Fourier components of charge density
m	mass of maglev vehicle
c	viscous damping coefficient
K	stiffness coefficient
ζ	sliding friction coefficient
D	duty ratio
K_t	motor torque constant

LIST OF ABBREVIATIONS

Maglev	magnetic levitation
PM	permanent magnet
SC	superconductor
ER	electromagnetic river
LISM	linear induction synchronous motor
EDW	electrodynamic wheel
EMS	electromagnetic suspension
EDS	electrodynamic suspension
LSM	linear synchronous motor
LIM	linear induction motor
FEA	finite element analysis
BEM	boundary element method
SOVP	second order vector potential
MVP	magnetic vector potential
TREE	truncated region eigenfunction expansion
TM	transverse magnetic
TE	transverse electric
DFT	discrete Fourier Transform
BLDC	brushless DC

CHAPTER 1 : INTRODUCTION AND REVIEW

1.1. Introduction

With a projected population growth of 48 million in the US by 2030 [1, 2], there is an increasing need for a quick, economic, energy efficient and environmental friendly urban and intercity transportation system [3]. At this hour of civilization with growing world pollution and diminishing natural resources, such as oil, it would be wise to investigate alternative modes of transportation. The Automobile industry is investing heavily in electric and hybrid cars [4-8]. However, the price of the vehicles may discourage the majority of the population from using them. In addition, studies have revealed that building new roads or expanding existing ones to relieve traffic congestion may turn out to be futile exercise as building new roads simply spurs additional traffic [9-11]. Traffic often is said to behave more like a gas than a liquid - it expands to fill the available space [12]. Hence, expanding highways is unlikely to meet the growing demand of quick urban transportation. With flights not being suitable for daily mode of intercity transportation for cost and saturation of routing, the only remaining alternatives are high-speed trains.

In the 21st century magnetic levitation (maglev) stand out as an outstanding technology for high-speed trains. Before discussing its advantages and drawbacks, it would be helpful to have a brief understanding of maglev technology. Section 1.2 provides a brief literature review of the existing maglev technologies to identify the advantages and disadvantages of such technologies which are summarized in section 1.3.

The Electrodynamic Wheel (EDW) concept is discussed in Section 1.4 and its performance is compared with other existing technologies in section 1.5. The recent work on the EDW technology and the motivation behind this research work is outlined in section 1.6 which is followed by the research goals and dissertation format in section 1.7 and 1.8 respectively.

1.2. Maglev- How It Works

As the name suggests, the train is suspended above and propelling along the guideway using magnetic fields. An excellent literature review of different suspension and propulsion technologies of maglevs is already present in [13-16]. So here repetition will be avoided. Only the basic operating principle of a maglev train will be discussed in this section with a purpose of familiarizing the reader with the technology.

1.2.1. Suspension or Levitation System

The levitation system can be broadly categorized into two types depending on the mechanism used. In the first type, electromagnetic repulsion force between the vehicle and guideway is used to lift the vehicle and this is called Electrodynamic Suspension (EDS) [17-22] system. The second type utilizes electromagnetic attraction force between the vehicle and guideway for levitation and termed as Electromagnetic Suspension (EMS) [15-17, 19, 22-26] system. There are varieties of ways to achieve this force of attraction or repulsion between the stationary guideway and moving vehicle as discussed next.

1.2.1.1. Electrodynamic Suspension System

In the simplest design, permanent magnets (PM) of high coercive material, such as barium-ferrite, are placed along each side of the vehicle and guideway as shown in Figure 1.1. The repulsion force between the set of magnets provide levitation and guidance force

[18, 24, 27]. One of the advantages of using ferrite PM is that there are no induced eddy currents. Thus the problems with drag force due to such currents do not arise and also high lift force can be achieved with this design [15]. However, the main demerit of this approach is its inherent instability which can be noted from Earnshaw's theorem [15, 16, 28]. Active control is required to create stability in this design. In addition, the cost of the permanent magnet guideway is too much for practical, long distance transport systems [19].

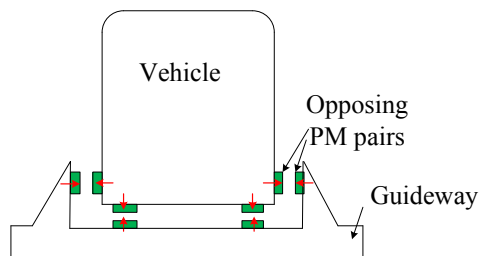


Figure 1.1. Magnetic suspension based on the repulsive force between magnets on a vehicle and guideway [19].

In the second approach, proposed by Danby and Powell in 1966 [29, 30], superconductive (SC) coils are mounted on the vehicle which moves over a simple conductive sheet guideway as shown in Figure 1.2. As the vehicle moves, a time changing magnetic field, due to the SC coils, induces current in the guideway which repels the vehicle according to Lenz's law. The drawback of this approach is the induced currents in the guideway produce power loss in the guideway and large drag force on the vehicle.

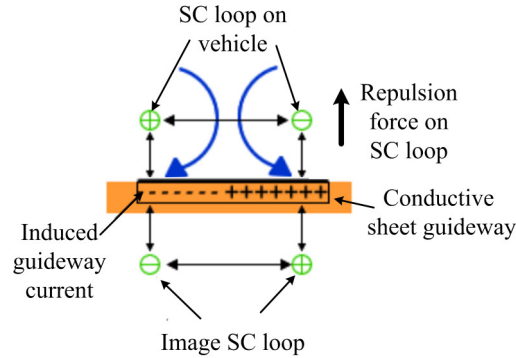


Figure 1.2. Magnetic suspension based on the repulsive force between superconductive coils on vehicle and simple conductive guideway [19].

In order to reduce the power loss and drag force on the vehicle, Danby and Powell proposed to have simple conductor loops on the guideway instead of a conductive sheet [31] as shown in Figure 1.3.

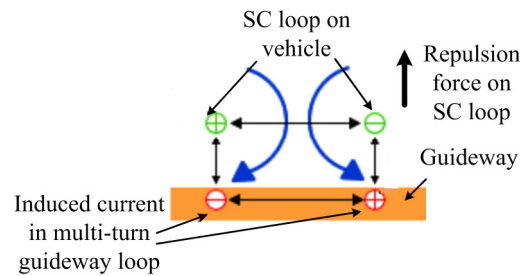


Figure 1.3. Magnetic suspension based on the repulsive force between superconductive coils on vehicle and conductor loops on guideway [19].

To reduce the power loss and drag force further, Danby and Powell proposed a null flux suspension guideway topology [32, 33]. There are many geometric forms of null flux loops. But they have the same feature. The null flux loops are wound on the guideway in such a way that when the vehicle is in an equilibrium position, the net magnetic flux through the loop is zero which makes the induced current zero [32, 34]. As a result, induced current in the null flux loop is much smaller than conductive sheet guideway or simple conductor loops on the guideway. This greatly reduces the power loss and drag force. One such null flux loop is the “Figure of 8 loop” as shown in Figure 1.4. The loops #1 and #2 are connected in opposite direction and coupled to form a complete circuit

[19]. When the SC coil is moved from its equilibrium position, the induced current in the loop pushes the SC coil towards the equilibrium. When mounted on the vertical side of the guideway, it provides vertical restoring force to the SC coil. When it is mounted on the horizontal surface of the guideway, as shown in Figure 1.4 (b), it provides lateral restoring force.

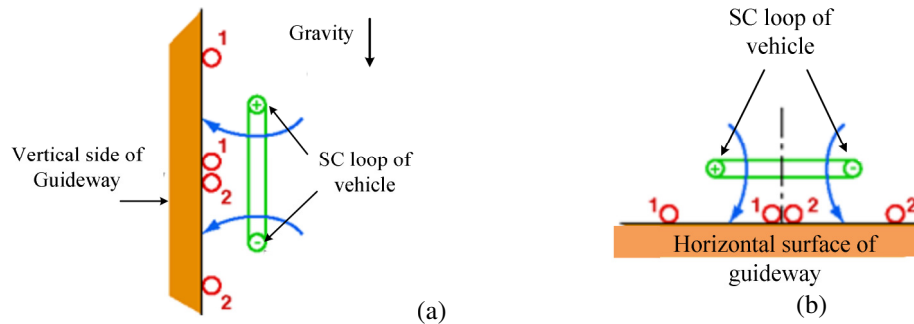


Figure 1.4. Magnetic suspension based on the repulsive force between superconductive coils on vehicle and “Figure of 8 loop” on the vertical side of the guideway [19]. (a) Vertical “Figure of 8 loop” for vertical stability and (b) horizontal “Figure of 8 loop” for lateral stability.

The null flux loop is used for levitation as well as for providing vertical stability for the Japanese high speed maglev JR MLX 01 as shown in Figure 1.5.

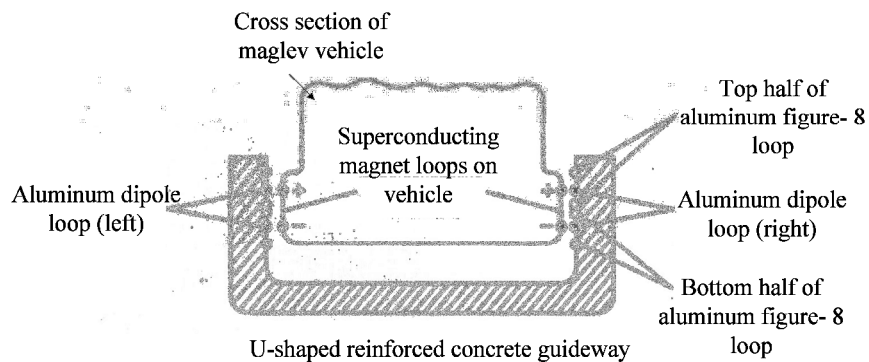


Figure 1.5. Null flux suspension system using “Figure of 8 loop” on guideway used in JR MLX 01[35].

1.2.1.2. Electromagnetic Suspension System

An electromagnetic suspension system (EMS) was first proposed by Graeminger in 1912 [36]. Electromagnetic suspension employs electromagnets on the underside of the vehicle and ferromagnetic material such as iron plates on the guideway as shown in Figure 1.6. The vehicle is suspended due to the attraction force between the

electromagnet and iron plates [15, 17-19]. In Figure 1.6, the arrows show the direction of the attraction force between iron plate and electromagnets. Unlike EDS, EMS suspension is inherently unstable because as the electromagnets move closer to the plate, the force of attraction increases which draws the electromagnets even closer to the plate. To achieve vertical stability gap sensors and a feedback control scheme is used [37-39]. The Transrapid of German [40, 41] and HSST of Japan [38] use an EMS suspension and guidance system. The levitation and guidance system of the Transrapid is shown in Figure 1.7 while Figure 1.8 shows the feedback control mechanism employed in the HSST – 100L for air gap regulation.

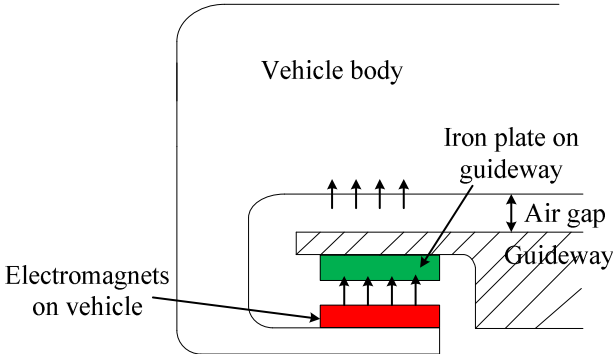


Figure 1.6. Electromagnetic suspension based on attraction between iron plate on guideway and electromagnets on vehicle.

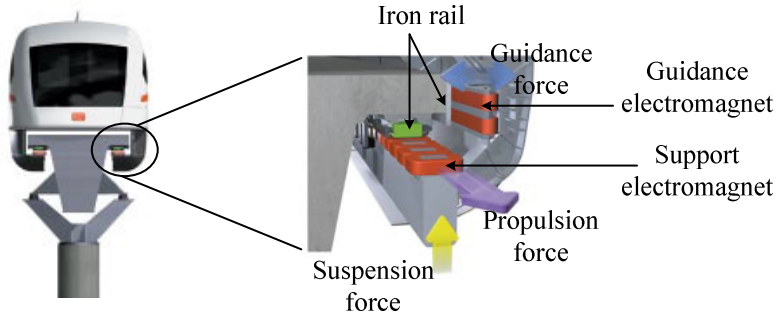


Figure 1.7. EMS suspension and guidance system employed in Transrapid [40].

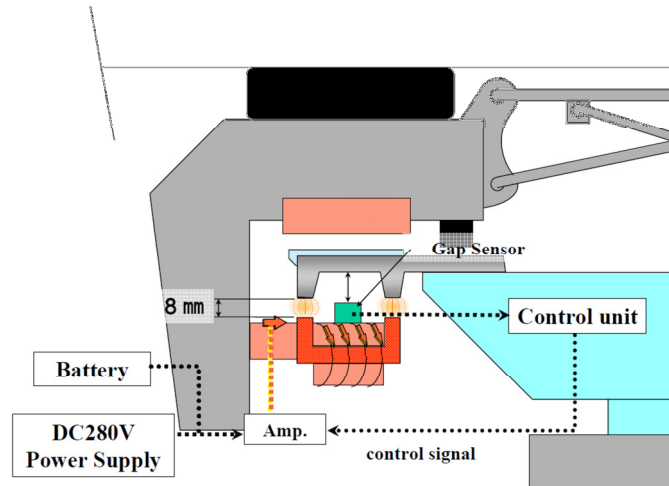


Figure 1.8. Feedback control mechanism of HSST-100L to regulate the air gap [42].

1.2.2. Propulsion System

The propulsion systems used in current maglev vehicles can be divided into two main categories depending on the type of linear motor used: (1) Linear synchronous motor and (2) linear induction motor. The operating principle of each one will be briefly described below.

1.2.2.1. Linear Synchronous Motor propulsion

Linear synchronous motor (LSM) propulsion was proposed by Danby and Powell for maglev applications [43, 44] and since then it has been studied by many researchers [41, 45-49]. Its operating principle is the same as its rotary counterpart. This propulsion system uses sinusoidally distributed poly-phase windings on the guideway that carry alternating poly-phase current which can be supplied from the conventional power grid. When energized, the LSM windings create a travelling magnetic field which moves with the alternating current frequency or synchronous frequency. The travelling field acts on the permanent magnets, electromagnets or superconducting magnets onboard the vehicle to push it forward. The vehicle moves at the same speed as the magnetic wave, that is at synchronous speed [50]. The speed is continuously regulated only by varying the

frequency of the alternating current. By reversing the direction of the travelling wave, non-contact braking is achieved and the braking energy can be fed back to the grid [40].

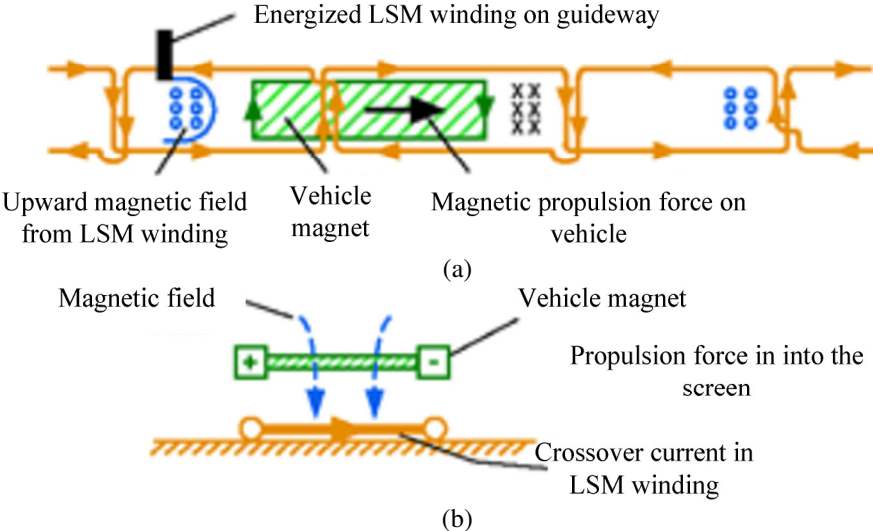


Figure 1.9. (a) Top view and (b) end view of propulsion mechanism using linear synchronous motor [19].

The Transrapid (with an operational speed of 400 – 500 km/h) and JR MLX 01 (the world’s fastest train with maximum speed of 581 km/h) use the LSM propulsion system [40-42]. Figure 1.10 shows the propulsion system used in the Transrapid. Alternating poly-phase current fed into 3-phase motor winding attached to the guideway, shown in Figure 1.10 (a), creates a travelling magnetic field as shown in Figure 1.10 (b).

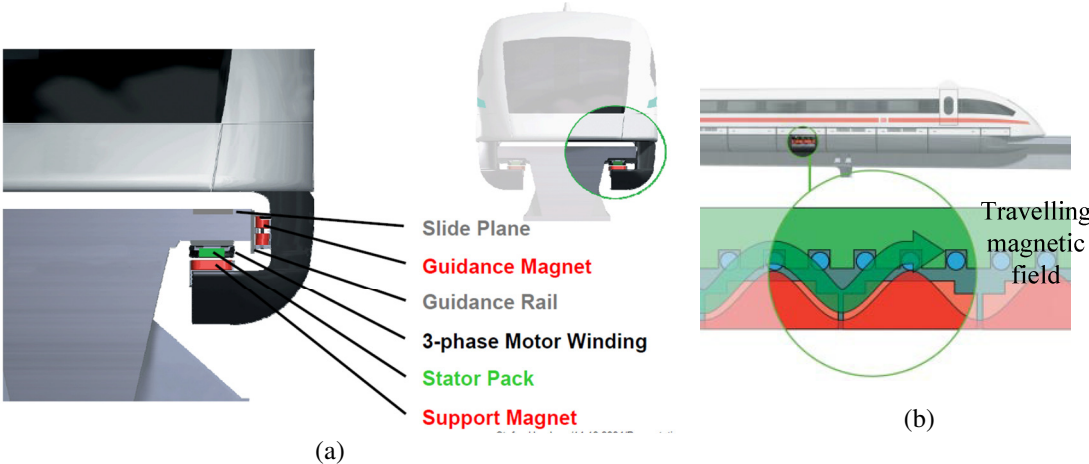


Figure 1.10. Propulsion system of German Transrapid [40].

1.2.2.2. Linear Induction Motor propulsion

A linear induction motor (LIM), as shown in Figure 1.11, has been used for maglev propulsion [38, 42, 51-53]. It works on the same principle as its rotary counterpart. The stator of the LIM has sinusoidally distributed windings which when supplied with alternating poly-phase current creates a travelling magnetic wave. The travelling wave moves with synchronous speed, v_s . The rotor is a thin plate made of conductive material such as aluminum with back iron. The travelling magnetic wave induces eddy currents in the rotor. The induced eddy currents interact with the travelling field to produce thrust force and the rotor moves at a speed, v_x , less than the synchronous speed, v_s [54].

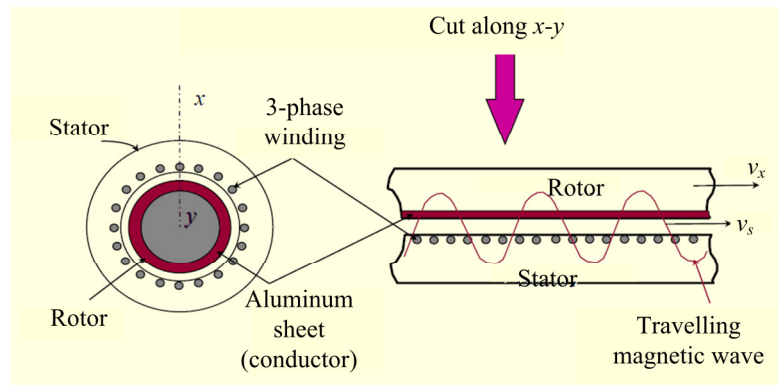


Figure 1.11. Operating principle of linear induction motor.

The LIM is used for propulsion in the HSST [38, 42] (operational speed of 100 kmph) which is shown in Figure 1.12. In the HSST, the poly phase windings are mounted on the moving vehicle and an aluminum plate with back iron is mounted on the stationary guideway.

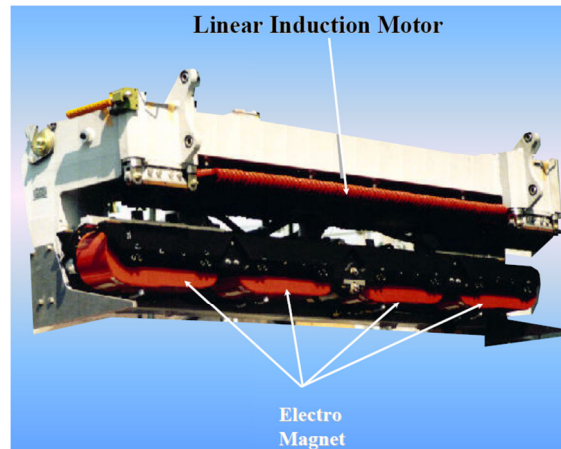


Figure 1.12. A vehicle module of HSST showing Linear induction motor and electromagnets [42]. The LIM is used for propulsion while the electromagnets are used for electromagnetic suspension discussed before.

1.3. Advantages and Disadvantages of Maglev

1.3.1. Advantages

Understanding basic maglev technology helps one identify the following advantages over traditional modes of transportation such as automobiles, conventional trains and flights.

- Maglev is very energy efficient. It does not burn oil but instead consumes electricity which can be produced using sustainable and renewable energy sources like wind and solar. At 300 miles per hour (m/h) in the open atmosphere, it has been calculated that a Maglev train consumes only 0.4 megajoules per passenger mile, compared to 4 megajoules per passenger mile of oil fuel for a 20-miles-per-gallon auto that carries 1.8 people (the national average) at 60 miles per hour [35].
- This technology reduces the air pollution as it emits less CO₂ than other transportation modes [35]. Figure 1.13 shows CO₂ emission comparison among Transrapid, conventional high-speed train German ICE and other modes of transportation.

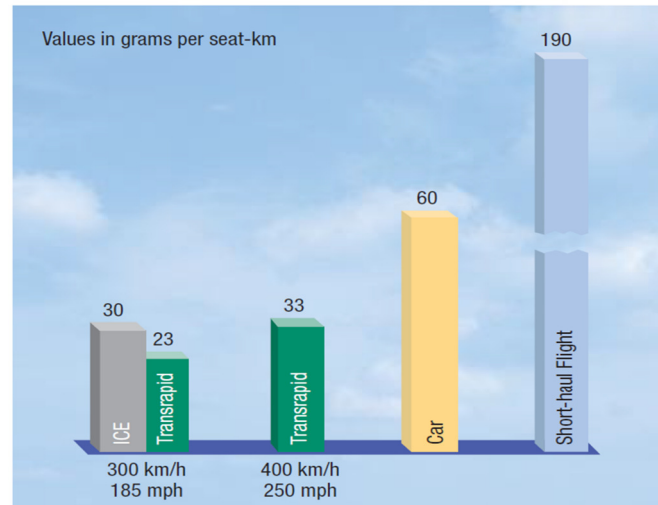


Figure 1.13. CO₂ emissions for different modes of transportation [40].

Also maglev trains emit less noise due to the non-contact levitation and propulsion technology. Less noise makes maglev suitable for transportation in urban areas. At speeds up to 155m/h the Transrapid almost operates soundlessly in urban areas as shown in Figure 1.14.

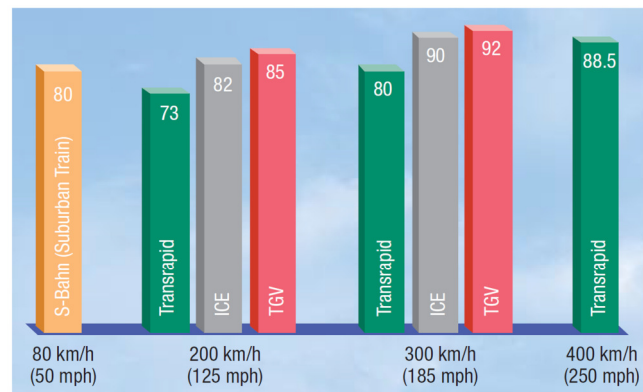


Figure 1.14. Noise level [dB] at a distance of 82 ft [40].

- It almost removes the dependency on oil. The typical oil consumption of maglev is shown in Figure 1.15 along with other modes of transportation.

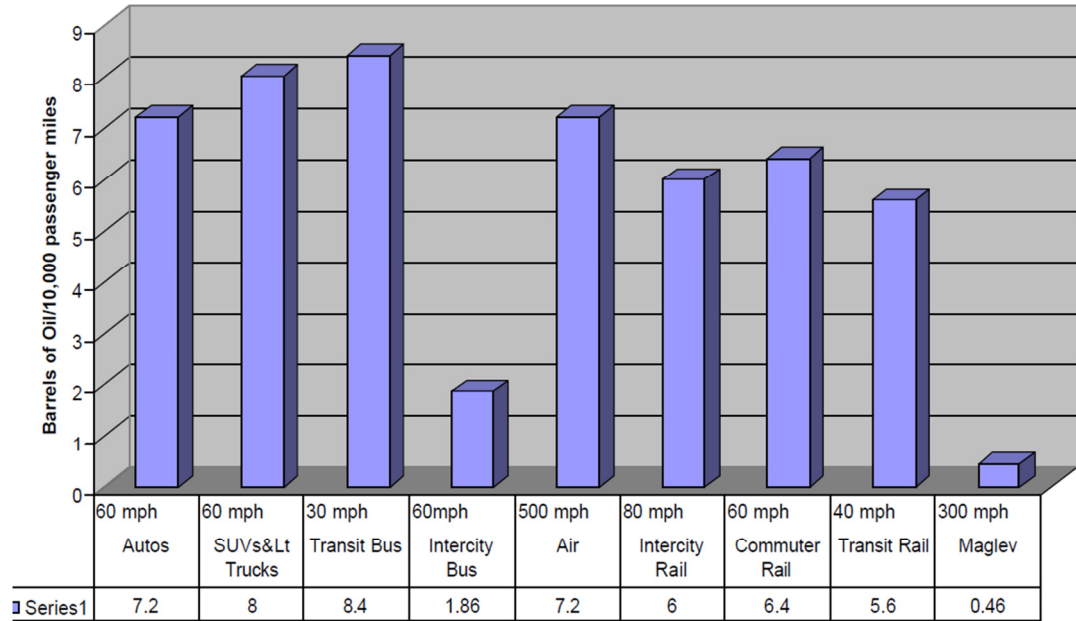


Figure 1.15. Energy efficiency by transport mode in barrels of oil per 10,000 passenger miles [55].

- Maglev guideways and vehicles last longer than trucks and automobiles with minimal maintenance because of its non-contact type operation [35].

1.3.2. Disadvantages

In spite of possessing the said advantages, the implementation of maglev trains throughout the world is very limited. This may be due to the initial investment cost to set up the infrastructure. The JR MLX 01 and Transrapid have an approximate cost of \$60 million per mile [56]. Hence for maglev technology to be implemented throughout the world, its cost must be greatly reduced. As discussed in section 0, two separate systems for propulsion and suspension are invariably employed in current operating maglevs. It is intuitive that integrating the two separate systems into one and using a passive guideway should lead to a significant reduction in the construction cost.

1.4. Idea of EDW

Research has been conducted to find an integrated propulsion and suspension system for maglev and a brief summary of that is provided in Table 1.1.

Table 1.1: Different integrated suspension and propulsion technologies

Technology	Characteristics	Example
Linear induction synchronous motor (LISM)	<ul style="list-style-type: none"> • Uses electromagnetic attraction between LSM field coil on vehicle and iron rail on guideway for levitation [57]. • Linear induction motor for propulsion [58]. • Allows small air gap due to EDS type levitation [22, 59]. 	Magnibus 01 test vehicle of Romania [57, 60]
Self-excited Linear synchronous motor	<ul style="list-style-type: none"> • Levitation is due to attractive force between the wound part of the LSM on the vehicle and ferromagnetic rail on the guideway. • LSM is used for propulsion • Electromagnetic attraction force reduces at high speed and gradually becomes negative. Hence it is not suitable for high-speed application [13]. • Allows small air gap due to EDS type levitation [22, 59]. 	ROMAG test vehicle of US [61]
Electromagnetic river (ER)	<ul style="list-style-type: none"> • Levitation is due the electromagnetic repulsion between the LIM primary winding current on the guideway (active) and secondary aluminum without back iron on vehicle (passive) [62]. • Propulsion is due to LIM [62, 63]. • Suffers from very low power factor [13]. 	Small scale set-up.
Magnet rotation	<ul style="list-style-type: none"> • Levitation is achieved due to electromagnetic repulsion between superconducting magnets [64] or rare earth permanent magnets [65-69] and passive conductive guideway. • Propulsion is due to the interaction between rotating magnets and conductive guideway. Braking force results depending on slip speed. • Eliminates low power factor issue of ER. • Superconductive magnets idea is costly. Rare earth magnets can be used. 	Small scale experimental set-up

After studying the available options for an integrated propulsion and suspension maglev system, Bird [13, 70] investigated an Electrodynamic wheel (EDW) concept in which Halbach rotors would move and rotate above a conductive sheet guideway made of non-magnetic material such as aluminum as shown in Figure 1.16. A Halbach rotor is a permanent magnet rotor made of rare-earth alloy neodymium–iron–boron (NdFeB) and is

named after late physicist Klaus Halbach of Lawrence Berkeley National Laboratory. The magnet segments of a Halbach rotor are radially and azimuthally magnetized so as to focus the entire magnetic field outside the rotor while cancelling it inside as shown in Figure 1.17. As a result, it can produce strong magnetic field in the air gap and thus is a suitable choice for maglev applications. By adjusting the number of magnet segments, the magnetic field can be made sinusoidal in the air gap.

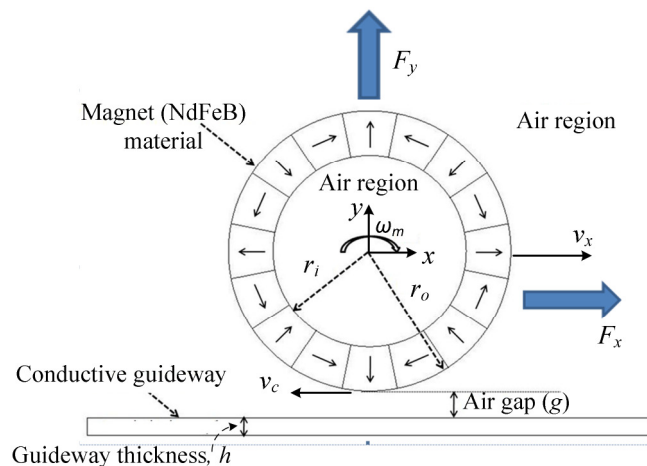


Figure 1.16. Translationally moving and rotating EDW above a passive conductive guideway [13].

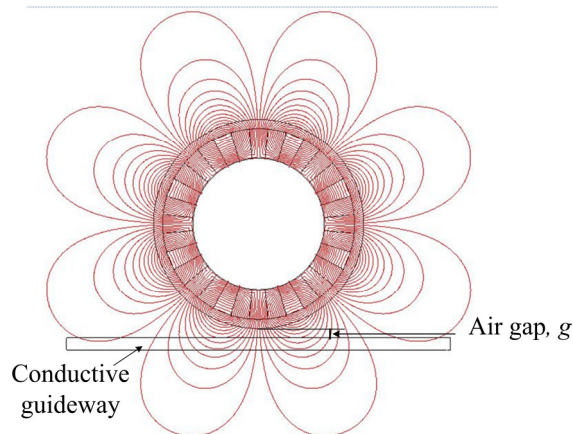


Figure 1.17. Magnetic flux density $|B|$ pattern of a static 32 segment EDW created using JMAG [71]

Electrodynamic suspension mechanism is used here to levitate the vehicle. As the rotor rotates, induced eddy current in the conductive sheet guideway interacts with the source field to repel the rotor according to Lenz's law and thus the vehicle is suspended.

As discussed before, this suspension can be inherently stable. In [13] Bird termed the Halbach rotor as electrodynamic wheel (EDW) because of the levitation mechanism used.

This technology works much like a linear induction motor to generate propulsion force. When the EDW rotates and moves along the guideway, the time changing sinusoidal magnetic field induces eddy current in the guideway which then interacts with the rotor field to produce propulsion or drag depending on slip speed. The difference between the circumferential velocity and translational velocity of the rotor is called slip speed (s_l). Hence

$$s_l = \omega_m r_o - v_x \quad (1.1)$$

where ω_m , v_x and r_o are the mechanical angular speed [rads^{-1}], translational speed [ms^{-1}] and outer radius of the rotor [m]. If the slip speed is positive, propulsion force results and pushes the vehicle ahead. But if it is negative, drag force is generated and slows the vehicle down. This is illustrated in Figure 1.18.

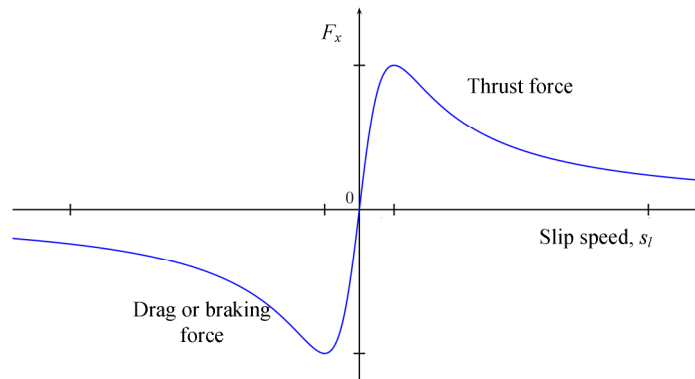


Figure 1.18. Thrust or drag force vs. slip speed.

1.5. Comparison of EDW with Existing Operating Maglevs

EDW technology allows propulsion and suspension of the vehicle by using only an aluminum sheet guideway and Halbach magnetic rotor or EDW. A brief comparative

analysis between EDW and existing operating maglev technologies is provided in Table 1.2 and Table 1.3.

Table 1.2: Comparison between EDW and existing operating maglev technologies

Name of Maglev	Characteristics
Transrapid	<ul style="list-style-type: none"> • Uses electromagnets attached to the vehicle for suspension which is inherently unstable. Active control required for vertical stability. • Allows small air gap (~3/8th - 1/2 inch) [22, 56, 59] which makes guideway maintenance difficult and expensive. • Uses LSM for propulsion. This makes guideway construction costly and complex. • Guideway structure is elevated. • Guideway cost ~\$60 million/ mile [56].
JR MLX 01	<ul style="list-style-type: none"> • Uses superconducting magnets for suspension. It needs extra cooling system on board. So expensive [22]. • Can operate at large air gap as it operates on EDS [22, 56, 59, 72] (~6 - 10 inch). Guideway maintenance easy. • Levitation is inherently stable. • Uses LSM for propulsion which makes guideway construction costly. • Guideway structure is elevated. • Guideway cost ~\$60 million/ mile [56].
HSST	<ul style="list-style-type: none"> • Uses electromagnets attached to vehicle for levitation which is inherently unstable. Needs active control for vertical stability. • Allows small air gap [22, 56]. So guideway maintenance costly. • Uses LIM for propulsion with 3-phase motor windings on the vehicle and aluminum plate with back iron on guideway. Vehicle design complex. • Guideway structure is elevated.
Proposed EDW	<ul style="list-style-type: none"> • Uses Halbach rotor for suspension as well as propulsion. • Levitation is stable but highly underdamped. • Allows large air gap [22, 72]. Hence guideway maintenance easy and inexpensive. • Guideway is made of aluminum which is cheap. • Guideway structure is flat, not elevated. Hence construction cost less than elevated structure.

Table 1.3: Different integrated suspension and propulsion technologies [13]

Name of Maglev	Source of loss
Transrapid	<ul style="list-style-type: none"> • Drag force losses. • I^2R losses in EMS coils on vehicle. • I^2R losses in EMS iron on guideway. • I^2R losses in LSM coils on guideway. • I^2R losses in LSM iron on guideway.
JR MLX 01	<ul style="list-style-type: none"> • Drag force losses. • I^2R losses in LSM coils on guideway. • I^2R losses in LSM iron on guideway. • I^2R losses in EDS coils on guideway. • Magnetic cooling losses.
HSST	<ul style="list-style-type: none"> • Drag force losses. • I^2R losses in EMS coils. • I^2R losses in EMS guideway. • I^2R losses in LIM 3-phase winding on vehicle. • I^2R losses in LIM aluminum plate on guideway. • Hysteresis losses in iron on guideway. • Power factor correction losses.
Proposed EDW	<ul style="list-style-type: none"> • Large I^2R losses in guideway. • I^2R losses in wheel motor. • Mechanical losses in wheel.

1.6. Recent Work on EDW Project

Initially Bird proposed a split sheet guideway topology [13, 73-75] as it would provide lateral restoring force and thus lateral stability. However, studies revealed that, for the same rotor parameters, this guideway topology reduces the lift force by a large extent and thrust by lesser extent [13, 74]. As a result, the lift-to-weight ratio is also reduced compared to single sheet guideway as shown in Figure 1.19. Better performance can be achieved with split sheet guideway by increasing the rotor width which would increase the manufacturing cost of the EDWs. Also split sheet topology increases power loss in the guideway compared to single sheet topology [13, 74]. Hence the idea of split sheet topology was abandoned.

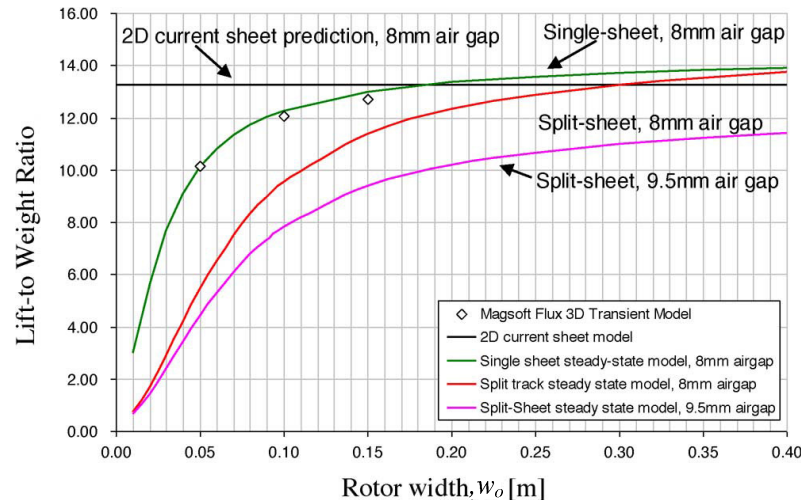


Figure 1.19. Lift-to-weight ratio vs. rotor width for split sheet and single sheet guideway topology [13, 75]. EDW dimension is kept same for both guideway topologies.

Bobba has worked on 3-D finite element modeling of a Halbach rotor moving above a single sheet conductive guideway using JMAG [71]. He developed an analytic model of the magnetic field created by a Halbach rotor using a Fourier Bessel function approach [76]. Bobba also studied the performance characteristics such as lift-to-weight ratio, thrust efficiency, magnetic rolling resistance for wheels in series using a 2-D steady state finite element model in Comsol developed by Bird [77, 78].

More recently Paudel developed a 2-D analytic steady state and transient model of the rotational and translational movement of a Halbach rotor above single sheet guideway [14, 79-82]. He analytically calculated the thrust and lift force acting on the rotor as well as power loss in the guideway analytically. For experimental verification, Paudel set up a pendulum model by hanging an EDW near a guideway wheel as shown in Figure 1.20 [81, 82]. Due to the action of the lift force and gravity, the EDW would oscillate and eventually come to a steady state condition as shown in Figure 1.21 which shows a comparison between the experimental and 2-D analytic model [79]. The difference between the two models is clearly noted. It is due to the fact that the 2-D model fails to

take into account the finite width of the guideway and rotor. Hence there is a clear need for modeling the Halbach rotor motion in 3-D analytically to achieve a better performance. In addition, in [14] very small electromagnetic damping was reported for a maglev vehicle with four EDWs. Hence, the damping and stiffness coefficients need to be determined in 3-D analytically for better understanding of the contributing factors in order to improve the dynamic performance of such EDW technology.

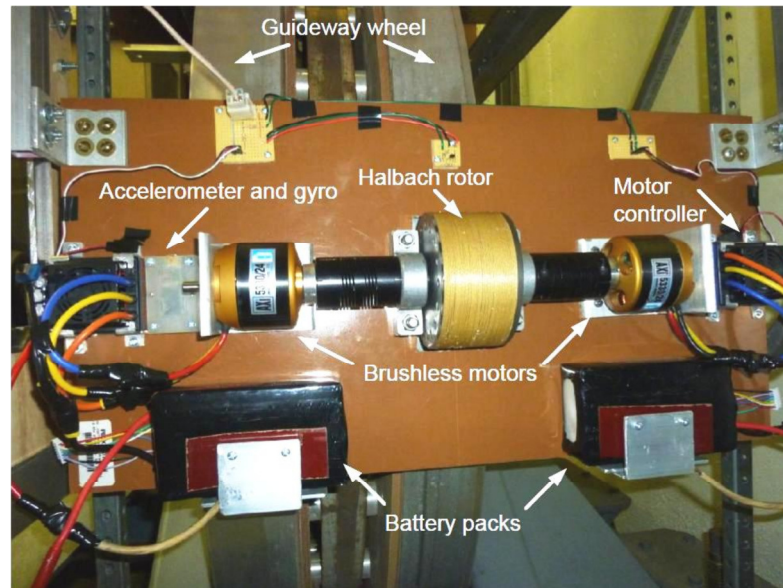


Figure 1.20. Experimental set-up showing EDW, brushless DC motors, batteries pack [14]

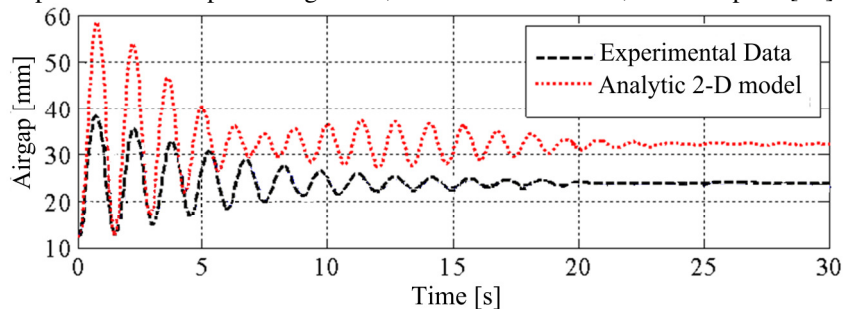


Figure 1.21. Air gap profile obtained using 2-D analytic model and experimental setup [14]

The recent work performed on the EDW technology as discussed in this section is summarized in Table 1.4.

Table 1.4: Summary of the recent work performed on the EDW technology

Authors	Work completed
Bird [13]	<ul style="list-style-type: none"> ➤ Proposed the concept of EDW. ➤ 2-D and 3-D steady state model in FEA with source modeled using current sheet. ➤ 2-D transient model in FEA with source modeled using current sheet. ➤ Proposed split-sheet and single-sheet guideway topology.
Bobba [71]	<ul style="list-style-type: none"> ➤ 3-D analytic permanent magnet rotor field computation using Bessel function. ➤ 3-D transient FEA model using JMAG.
Paudel [14]	<ul style="list-style-type: none"> ➤ 2-D analytic steady state model with heave velocity for eddy current force and power loss calculation. Source field was modeled using current sheet. ➤ 2-D analytic transient model for the calculation of force and power loss. Source field was modeled using current sheet. ➤ 2-D stiffness and damping analysis. ➤ Investigation of dynamic behavior of 2-DOF EDW maglev vehicle with 2-D steady state and transient force equations.

1.7. Research Goal

The above discussion regarding recent work on EDW technology has identified the need for a new 3-D analytic model to take into account the finite width of the EDW and guideway. Also the analytic model should be able to compute the electromagnetic fields, forces, power loss and torque not only when the rotor is at the center but also when it is laterally offset above the guideway. The analytic model will provide greater insight and allow control techniques to be examined.

Eddy current induction is used in a variety of applications such as eddy current testing [83-85], eddy current dampers [86-88] and brakes [89-91] in addition to the maglev technology. Thus, another goal of the dissertation is to make the developed models applicable for all the specified applications. With this aim, the finite element and analytic derivations are performed in such a way that they are valid for any type of magnetic source such as current coils, electromagnets or permanent magnets. Only for model validation purposes, a Halbach rotor has been used. The words “plate” instead of

“guideway” and “magnetic source” instead of “magnetic rotor” have been used to make the derivation generic.

In order to achieve the stated goals, the following tasks need to be performed:

- A computationally efficient method of computing the 3-D magnetic fields due to a magnetic source is required. The source modeling technique can then be used throughout the dissertation for source field computation. The existing analytic method of field calculation of a Halbach rotor using current sheet approach [75] is computationally expensive. Finite element models need to be developed in commercial FEA software for validation purposes.
- For analytic model validation, computationally efficient 3-D transient and steady state models using finite element analysis are required to model the interaction between a moving magnetic source and conductive plate. The models should be able to include the heave as well as translational and rotational motion of the source unlike most of the commercial finite element softwares.
- Although finite element models can simulate the eddy current distribution due to the motion of a magnetic source above a conductor, an analytic model is always advantageous due to its computational efficiency. New 3-D analytic model is required for this purpose.
- Electromagnetic damping and stiffness coefficients need to be calculated from the analytic model.

Table 1.5 outlines the required tasks and the relevant chapters of this dissertation.

Table 1.5: Summary of the required tasks on the EDW technology

Model type	Task(s)	Chapter(s)
Analytic	<ul style="list-style-type: none"> • Magnetic source field modeling using magnetic charge sheet • This source modeling technique will be used throughout the research for source field modeling • Model will be developed in Matlab 	2
FEA	<ul style="list-style-type: none"> • Segmented PM rotor modeling using Comsol and JMAG. • These FEA rotor models will be used to validate the magnetic charge sheet based magnetic source field computation technique 	2
FEA	<ul style="list-style-type: none"> • 3-D transient and steady state models of eddy current distribution in a conductive plate. • Models will be developed in Comsol. • The FEA models will be used to provide insight into eddy current distribution in a conductive plate and develop 3-D analytic models. 	3
FEA	<ul style="list-style-type: none"> • Development of transient model of a Halbach rotor rotating above a conductive plate using Magsoft FEA software. • The source will have only rotational motion • The model will be used to validate the 3-D FEA transient and steady state models of Comsol. 	3
Analytic	<ul style="list-style-type: none"> • 3-D eddy current models for eddy current field computation 	5,6,7
Analytic	<ul style="list-style-type: none"> • 3-D eddy current models for eddy current force, torque and joule loss computation 	5,6,7
Analytic	<ul style="list-style-type: none"> • 3-D Electromagnetic stiffness and damping coefficient calculation 	5
-	<ul style="list-style-type: none"> • Experimental verification of the developed analytic models 	8

1.8. Organization of Dissertation

This dissertation is organized in the following format.

Chapter 1 outlines the need for new high-speed transportation system for urban area and why maglev high-speed trains should be considered. The chapter also introduces the reader to the EDW technology and the recent work performed on this technology till date. Chapter 1 also identifies the research goal of this dissertation.

Chapter 2 discusses the magnetic source modeling in air using a fictitious magnetic charge sheet approach.

Chapter 3 presents a finite element modeling technique for a magnetic source moving over a conductive plate in both transient and steady state conditions.

Chapter 4 reviews the existing 3-D analytic models to study the interaction between a moving magnetic source and a nearby conductive medium. The need for new analytic model is identified.

Chapter 5 presents a computationally fast 3-D analytic model using a second order vector potential method for infinite plate width problems. The model assumes finite thickness of the plate and it models vertical, lateral and translational motion of the source.

Chapter 6 presents a 3-D analytic model for finite width conductive plate using magnetic vector potential. The model assumes that the plate has a finite thickness. Both vertical and translational motion of the source is considered.

Chapter 7 presents a 3-D analytic model for finite width conductive plate including edge-effect using the second order vector potential and truncated region eigenfunction expansion. The model assumes that the plate has a finite thickness. Only rotational motion of the source is considered.

Chapter 8 qualitatively verifies the developed analytic models with experimental results.

Chapter 9 presents summarizes the research work presented in this dissertation and outlines the future direction of research to be performed.

CHAPTER 2 : MAGNETIC SOURCE FIELD MODELING USING MAGNETIC CHARGE

2.1. Introduction

In a number of applications the magnets operate in regions surrounded by air such as microactuators [92], diamagnetic levitation devices [93], non-contact type magnetic torque transmitters [94-97], magnetic latching [98, 99], 3-D force sensors [100] and torque and position sensors [101, 102]. Fully numerical based calculation methods such as the finite element analysis (FEA) method or boundary element method are often used to calculate the magnetic fields created by 3-D magnetic devices. However, such methods are often not fast enough for real-time analysis and control purposes. Analytical approaches are of primary importance for the design of many devices [103]. In many of these applications due to the absence of any other material that can perturb or contribute to the magnetic field, the problem region typically consists of the magnet itself [104].

Analytic 3-D field solutions for a number of magnet shapes have been derived. Bancel [105] derived the field equations for a parallelepipedic permanent magnet (PM). Later Furlani [104] provided a semianalytic field solution for radially polarized magnets based on amperian model which needs two numerical integrations. Rakotoarison [106] proposed another semianalytic solution to find the magnetic field created by radially magnetized segments based on Coulombian approach which reduced the number of numerical integrations by one. The proposed approach modeled each magnet segment

using surface and volume magnetic charge. More recently Ravaud presented a fully analytic model for ring permanent magnets by considering only surface charge using elliptic integrals of the first kind [103]. Bird derived an analytic model for a Halbach rotor by modeling the radial and azimuthal magnet segments using current sheet which required two numerical integrations [13, 75]. The analytic approaches are computationally expensive for a complicated magnet source such as a magnetic rotor with many segments since computing the net field involves summing up the field contribution from each magnet segment. Also the methods proposed are not general purpose.

Recently the charge simulations method [107] was utilized to model the external magnetic field due to a set of magnets. Kwon et al. [108] used a spherical distribution of charges enclosing the magnets to calculate the far-field due to a permanent magnet rotor. More recently Selvaggi et al. used an analytic based charge simulation approach using toroidal harmonics employing a cylindrical charge distribution to provide a more accurate near-field and far-field solution [109]. The idea of the charge simulation approach is to replace the original magnets by a hypothetical surface of equivalent discrete fictitious magnetic charges called the 'charge surface' [109, 110] as shown in Figure 2.1(b). The 'charge surface' reproduces the magnetic field as the original set of magnets in any region external to the 'charge surface'. In [108-111] the first step of finding the charge distribution on the 'charge surface' is to find the magnetic scalar potential at another hypothetical surface, called the 'potential surface' and is shown in Figure 2.1(b), external and concentric to the charge surface using finite element modeling or integral equation

method. Using these potentials the charge distribution on the ‘charge surface’ is computed using Coulomb’s law [108, 112].

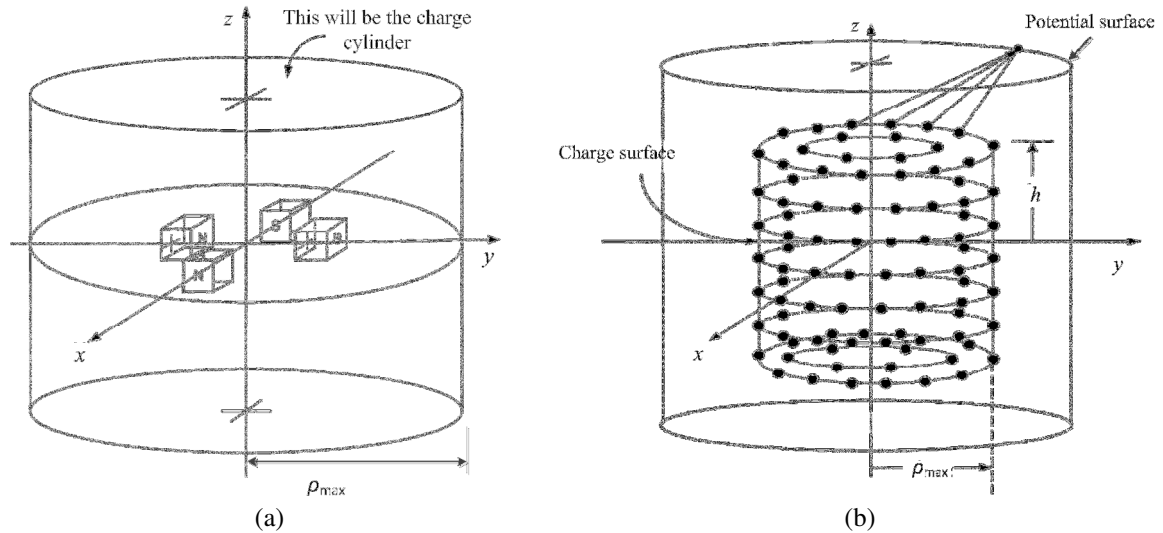


Figure 2.1 (a) The original set of magnets are enclosed by a hypothetical cylindrical ‘charge surface’. All the potential and field values external to the charge cylinder can now be calculated using the charges on the cylinder; (b) the ‘charge surface’ is enclosed by a cylindrical ‘potential surface’ which is used to compute the charges on the ‘charge surface’ [109].

The use of the charge simulation approach to first find the potential surface and then charge surface is quite complex [110, 111].

The purpose of this chapter is to demonstrate that a continuous magnetic charge distribution, rather than discrete charges, can also be used to accurately model the external field due to an arbitrary magnetic source. The proposed will thus replace the original complicated source field equations with faster and simpler equivalent magnetic charge sheet equations. As the concept of the magnetic charge does not exist in reality, this is only a fictitious model.

In this chapter the source field at an external point will be calculated by using, first a cylindrical and then a planer charge sheet. The next section introduces the cylindrical charge sheet concept and determines the charge density from the normal component of the flux density. It validates the results by comparing with an FEA Halbach rotor model

and surface mounted PM rotor. In section 2.3, the planar charge sheet concept is introduced, fields are calculated and finally results are compared with the FEA. The calculation time of both approaches is compared using a Halbach and surface mounted PM rotor. A brief summary of this chapter is provided in section 2.4

2.2. Cylindrical Magnetic Charge Sheet

The idea of the charge sheet is first explained using a very simple 2-D diagram of a bar magnet as shown in Figure 2.2. In Figure 2.2(b) the original bar magnet of Figure 2.2(a) has been replaced with a circular magnetic charge sheet completely enclosing the magnet. The charge density on the sheet is such that it produces the same field in the external air region as the original magnet. The charge density on the circular sheet will be derived in this chapter.

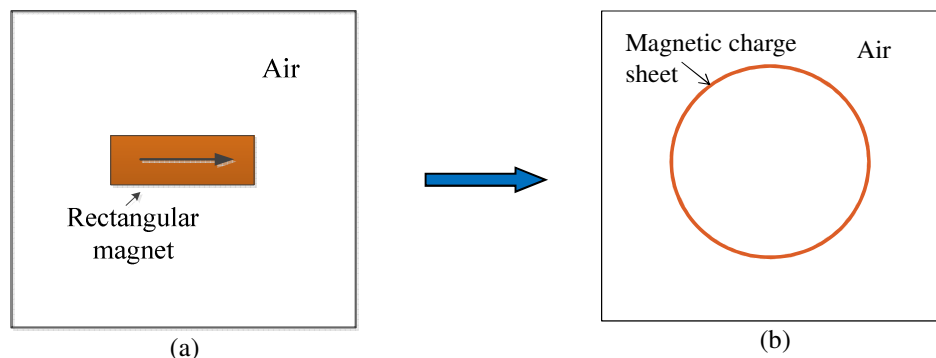


Figure 2.2 (a) A rectangular bar magnet is air; (b) the magnet is replaced with an equivalent circular magnetic charge sheet.

Extending the idea to the 3-D, if one has a PM rotor as in Figure 2.3(a) and need to know the source field in an external air region, then the PM rotor can be replaced with a charge sheet as shown in Figure 2.3(b), cylindrical in shape, completely enclosing the magnet so that it will produce exactly the same field in the external air region as the original PM rotor.

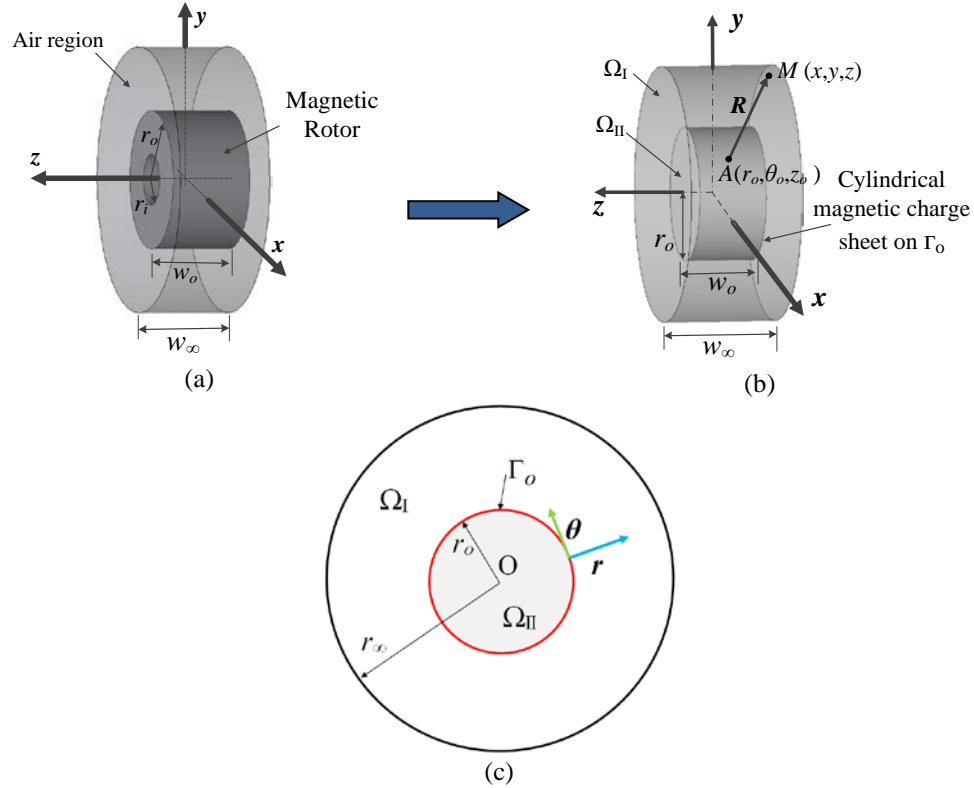


Figure 2.3 (a) Schematic of a 3-D permanent magnet rotor; (b) 3-D view of magnetic charge sheet model with a charge sheet placed on Γ_o ; (c) cross-sectional view of the charge cylinder model.

Referring to Figure 2.3(b) and Figure 2.3(c), the region enclosed by the sheet is Ω_{II} and consists of air. The charge sheet is located at $r = r_o$ and has a width w_o . The outer cylinder with width w_∞ is a magnet-free air region and designated as Ω_I . Also it is assumed that only the magnetic field outside the sheet i.e. in Ω_I is of interest.

2.2.1. Derivation of Charge Density

In the presence of a magnetic charge the governing magnetostatic equations for this problem are [112, 113]

$$\nabla \cdot \mathbf{B} = \rho_m \quad (2.1)$$

$$\nabla \times \mathbf{H} = 0 \quad (2.2)$$

$$\mathbf{B} = \mu_0 \mathbf{H} \quad (2.3)$$

where ρ_m is the fictitious magnetic charge volume density [Wbm^{-3}]. As \mathbf{H} is curl-free field, this can be written in terms of gradient of another scalar potential because the curl of gradient of a scalar is zero [112, 114]

$$\mathbf{H} = -\nabla\phi \quad (2.4)$$

The scalar potential ϕ is called the magnetic scalar potential. Substituting (2.4) into (2.3) relates the magnetic flux density, \mathbf{B} , with the magnetic scalar potential, ϕ , as [112, 114]

$$\mathbf{B} = -\mu_0\nabla\phi \quad (2.5)$$

Substituting (2.5) into (2.1) gives the governing equation that completely describes the field [112, 114]

$$\nabla^2\phi(r, \theta, z) = -\frac{1}{\mu_0}\rho_m \quad (2.6)$$

By integrating both sides of (2.1) the integral form of Gauss's Law is [115]

$$\oint_S \mathbf{B} \cdot d\mathbf{s} = \int_V \rho_m dV \quad (2.7)$$

where the closed surface S encloses a volume V with charge density ρ_m .

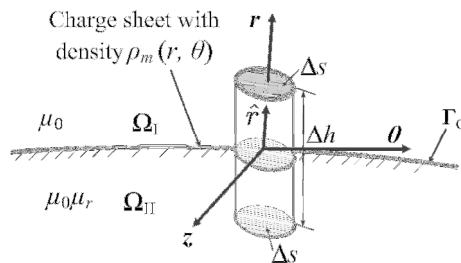


Figure 2.4 Small cylinder placed between the magnetic charge sheet with surface Δs and height Δh .

Consider placing a small cylindrical box on the charge sheet as shown in Figure 2.4. The field on the surface of the box can be determined by using (2.7). In the limit of $\Delta h \rightarrow 0$, one finds from (2.7)

$$\oint_S \mathbf{B} \cdot d\mathbf{s} = (\mathbf{B}^I \cdot \hat{r} - \mathbf{B}^{II} \cdot \hat{r})\Delta S \quad (2.8)$$

or

$$\oint_S \mathbf{B} \cdot d\mathbf{s} = \hat{r} \cdot (\mathbf{B}^I - \mathbf{B}^{II})\Delta S \quad (2.9)$$

where \hat{r} is the outward normal vector on Γ_o

And from the right hand side of (2.7) in the limit of $\Delta h \rightarrow 0$,

$$\oint_S \mathbf{B} \cdot d\mathbf{s} = \rho_m \Delta S \quad (2.10)$$

where ρ_m becomes the surface charge density. From (2.9) and (2.10) it is concluded that

$$B_r^I - B_r^{II} = \rho_m, \text{ on } \Gamma_o \quad (2.11)$$

The tangential field components on the boundary are related by

$$\hat{r} \times \left(\frac{1}{\mu_0} \mathbf{B}^I - \frac{1}{\mu_0 \mu_r} \mathbf{B}^{II} \right) = 0, \text{ on } \Gamma_o \quad (2.12)$$

All of the flux density in regions Ω_I and Ω_{II} is due to the charge ρ_m placed on Γ_o and the

\mathbf{B}^I and \mathbf{B}^{II} fields will emanate from the charge sheet, thus

$$B_r^{II}(r_o, \theta_o, z_o) = -B_r^I(r_o, \theta_o, z_o), \text{ on } \Gamma_o \quad (2.13)$$

Substituting (2.13) into (2.11) gives

$$\rho_m = 2B_r^I, \text{ on } \Gamma_o \quad (2.14)$$

or in general,

$$\rho_m(\theta_o, z_o) = 2B_n^s(r_o, \theta_o, z_o), \text{ on } \Gamma_o \quad (2.15)$$

where the superscript 's' indicates flux density due to the original magnet source and subscript 'n' indicates normal component. Hence it is derived that the charge density is

twice the normal component of flux density created by the original magnet source on Γ_o . This normal component can be obtained using analytic or FEA methods as discussed later.

Equation (2.15) can be used to find a charge distribution that will accurately describe the original source field external to the sheet.

2.2.2. External Field Calculation

The magnetostatic field external to the cylindrical charge sheet can be determined using either an integral or differential approach. The calculation time for both methods will be assessed. The differential approach using Bessel functions has been addressed by Bobba in the past [71]. Here only the integral or Coulombian approach will be presented.

The integral solution to (2.6) for the charge cylinder is [106, 112]

$$\phi(x, y, z) = \frac{1}{4\pi\mu_0} \int_0^{2\pi} \int_{-w_o/2}^{w_o/2} \frac{\rho_m(\theta_o, z_o)r_o}{R} dz_o d\theta_o \quad (2.16)$$

where

$$R = \sqrt{(x - r_o \cos \theta_o)^2 + (y - r_o \sin \theta_o)^2 + (z - z_o)^2} \quad (2.17)$$

is the scalar distance between any point of interest $M(x, y, z)$ external to the sheet and $A(r_o, \theta_o, z_o)$ on the sheet as shown in Figure 2.3(b). Utilizing (2.15) the flux density external to the rotor is

$$\mathbf{B}(x, y, z) = \frac{1}{4\pi} \int_0^{2\pi} \int_{-w_o/2}^{w_o/2} \frac{\rho_m(\theta_o, z_o)}{R^3} r_o \mathbf{R} dz_o d\theta_o \quad (2.18)$$

where

$$\mathbf{R} = (x - r_o \cos \theta_o) \hat{x} + (y - r_o \sin \theta_o) \hat{y} + (z - z_o) \hat{z} \quad (2.19)$$

If it is further assumed that the radial flux density of the source does not alter along the axial length of the rotor, which is true for many PM rotors, the charge density remains constant throughout the z -axis and hence can be represented using step functions as

$$\rho_m(\theta_o, z_o) = 2B_n^s(r_o, \theta_o)[u(z_o + w_o / 2) - u(z_o - w_o / 2)] \quad (2.20)$$

where $u(z_o + w_o/2)$ and $u(z_o - w_o/2)$ are step functions that ensure that the charge is uniform across the charge sheet width. In this case the integration along z_o can be performed analytically. Substituting (2.20) into (2.18) and integrating it with respect to z_o , the magnetic flux density components are determined to be

$$B_x(x, y, z) = \frac{B_n^s(r_o, \theta_o)r_o}{2\pi} \int_0^{2\pi} \frac{(x - r_o \cos \theta_o)}{r^2} \left[\frac{2z + w_o}{\sqrt{4r^2 + (2z + w_o)^2}} - \frac{2z - w_o}{\sqrt{4r^2 + (2z - w_o)^2}} \right] d\theta_o \quad (2.21)$$

$$B_y(x, y, z) = \frac{B_n^s(r_o, \theta_o)r_o}{2\pi} \int_0^{2\pi} \frac{(y - r_o \sin \theta_o)}{r^2} \left[\frac{2z + w_o}{\sqrt{4r^2 + (2z + w_o)^2}} - \frac{2z - w_o}{\sqrt{4r^2 + (2z - w_o)^2}} \right] d\theta_o \quad (2.22)$$

$$B_z(x, y, z) = \frac{B_n^s(r_o, \theta_o)r_o}{\pi} \int_0^{2\pi} \left[\frac{1}{\sqrt{4r^2 + (2z - w_o)^2}} - \frac{1}{\sqrt{4r^2 + (2z + w_o)^2}} \right] d\theta_o \quad (2.23)$$

where

$$r^2 = x^2 + y^2 + r_o^2 - 2r_o(x \cos \theta_o + y \sin \theta_o) \quad (2.24)$$

is the magnitude of the projection of \mathbf{R} on the x - y plane. The integration with respect to θ_o in (2.21)-(2.23) is performed numerically.

2.2.3. Validation Using Rotor Model

The presented source field modeling approach was validated by creating an equivalent cylindrical charge sheet for a Halbach and a surface mounted PM rotor.

2.2.3.1. Halbach PM rotor in air

Halbach rotors, as shown in Figure 2.5, focus the magnetic flux only outside of the rotor while cancelling it inside. It produces almost a perfectly sinusoidal field in the external air region. The sinusoidal nature of the air gap field depends on the number of segments of the rotor. With an increase in segment number the unwanted harmonics can be removed and only the significant Fourier component remains at a frequency equal to the number of the pole pairs of the rotor.

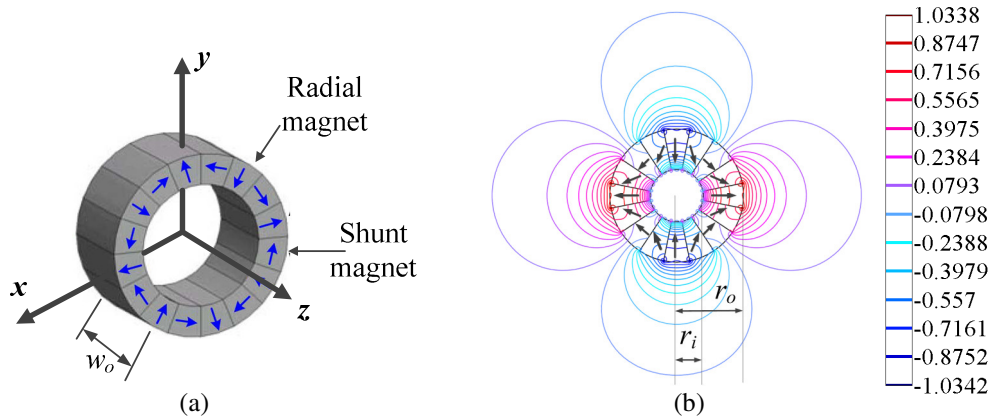


Figure 2.5 (a) Segmented 4 pole pair Halbach rotor with radial and shunt magnets; (b) A 2 pole-pair Halbach rotor B_r contour plot with magnetization direction shown

In [116] Xia *et al.* showed that in 2-D the external field of a Halbach rotor can be accurately modeled by

$$\mathbf{B}^s(r, \theta) = B^{hr}(r) \cos(P\theta) \hat{r} + B^{hr}(r) \sin(P\theta) \hat{\theta} \quad (2.25)$$

where superscript 'hr' indicates Halbach rotor field and

$$B^{hr}(r) = \frac{2B_{rem}P(1 + \mu_r)(r_i^{P+1} - r_o^{P+1})r_o^{2P}}{(1 + P)[(1 - \mu_r)^2 r_i^{2P} - (1 + \mu_r)^2 r_o^{2P}]} \frac{1}{r^{P+1}} \quad (2.26)$$

and μ_r , P , r_o , r_i and B_{rem} are the relative permeability, pole-pairs, outer radius, inner radius and remnant flux density of the rotor respectively.

From (2.25) the radial component flux density is rewritten as

$$B_r^s(r, \theta) = \frac{2B_{rem}P(1 + \mu_r)(r_i^{P+1} - r_o^{P+1})r_o^{2P} \cos(P\theta)}{(1 + P)[(1 - \mu_r)^2 r_i^{2P} - (1 + \mu_r)^2 r_o^{2P}]} \frac{1}{r^{P+1}} \quad (2.27)$$

On the rotor surface, at $(r, \theta, z) = (r_o, \theta_o, 0)$, $B_z=0$ and therefore in this special location the 2-D and 3-D fields are the same. Also for Halbach magnetized rotor the magnetization does not change along the axial direction of the rotor. Hence the charge distribution remains constant throughout the width of the rotor, w_o . These observations enable the charge density function on the charge sheet to be determined using only 2-D field information from (2.20) where

$$B_n^s(r_o, \theta_o) = B_r^s(r_o, \theta_o) \quad (2.28)$$

Hence substituting (2.27) into (2.21)-(2.23) the flux density components at any external point in space can be calculated. Utilizing the parameters given in Table 2.1 the Coulombian and Bessel solution accuracy was compared with the FEA model in Figure 2.6.

Table 2.1: 3-D Halbach Rotor Parameters

	Description	Value	Unit
Halbach rotor	Outer radius, r_o	26	mm
	Inner radius, r_i	9.62	mm
	Remnant flux density, B_{rem}	1.42	T
	Width, w_o	52	mm
	Pole-pairs, P	2	-
	Magnet permeability, μ_r	1.108	-

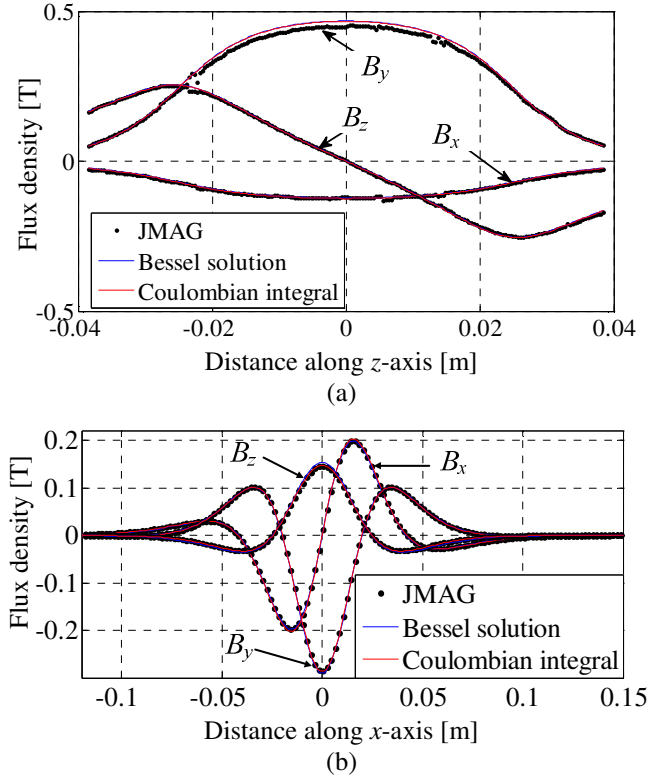


Figure 2.6 (a) Comparison of the B_x , B_y and B_z flux density between JMAG FEA and 3-D magnetic charge model along the z -axis at $(x, y) = (10, -9.5)$ mm; (b) Comparison of the flux density components along the x -axis at $(y, z) = (-9.5, 20)$ mm.

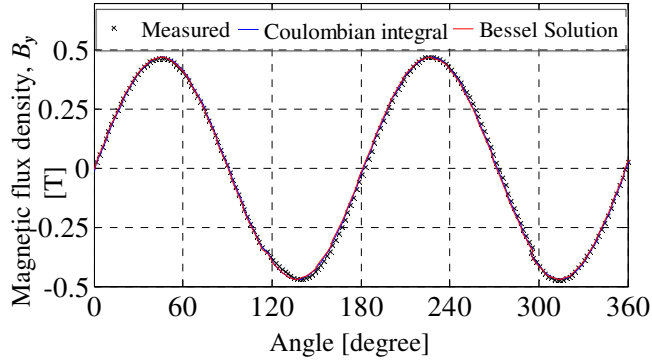
The parameters of the 16 segment experimental Halbach rotor, as shown in Figure 2.7, are listed in Table 2.2 and a field comparison with the integral and Bessel function solution method is shown in Figure 2.8. A very good agreement between the experimental and analytic models was obtained.

Table 2.2: Experimental Halbach Rotor Parameters

	Description	Value	Unit
Halbach rotor	Outer radius, r_o	26	mm
	Inner radius, r_i	10	mm
	Remnant flux density, B_{rem}	1.42	T
	Width, w_o	52	mm
	Pole-pairs, P	2	-
	Magnet permeability, μ_r	1.108	-



Figure 2.7 Experimental 2 pole-pair Halbach rotor with 16 segments

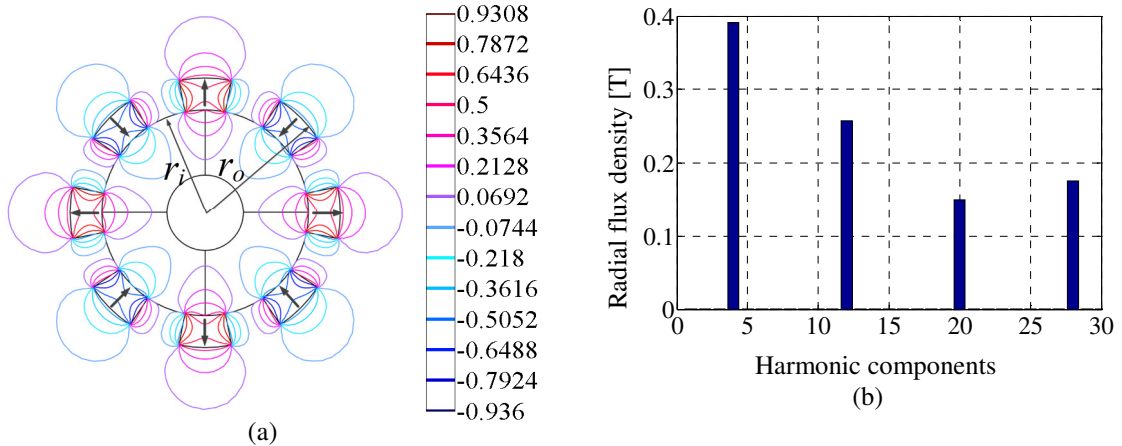


(a)

Figure 2.8 (a) Comparison of the B_y rotor flux density between experimental set-up and analytic models. Measurement was taken at $z=0\text{mm}$ and 6.4mm away from the surface of the rotor

2.2.3.2. Surface Mounted PM Rotor in Air

The radial flux density, B_r , for a surface mounted PM rotor is shown in Figure 2.9(a) as well as the corresponding harmonic components of B_r on the rotor surface ($r=r_o$).



(a)

(b)

Figure 2.9 (a) 2-D B_r contour plot of the surface mounted PM rotor. (b) Corresponding B_r harmonic components at $r=r_o$.

Unlike the Halbach rotor the radial field of surface PM rotor is harmonically rich. As the magnetization is not a function of the z -axis the charge sheet will be uniform across

the length of the rotor width. Therefore from 2-D FEA the source radial flux density on the rotor surface can be determined to be

$$B_r^s(r_o, \theta_o) = \frac{1}{r_o} \sum_{n=0}^N F_z^n \cos(n\theta_o) \quad (2.29)$$

where F_z^n is the magnitude of n^{th} harmonic. As the magnetization of the rotor does not change along its axial direction, the charge density function for the surface PM rotor can be obtained by substituting (2.29) into (2.20). Hence substituting (2.29) into the Coulombian solution, (2.21)-(2.23), enables the field due to the surface PM rotor to be accurately reproduced. The accuracy is validated by the comparison shown in Figure 2.9. Table 2.3 gives the parameters used in this comparison. Very close agreement of results was obtained.

Table 2.3: Surface Mount PM Rotor Parameters

	Description	Value	Unit
	Outer radius, r_o	34	mm
	Inner radius, r_i	26	mm
Surface mount PM rotor	Remnant flux density, B_{rem}	1.42	T
	Width, w_o	52	mm
	Pole-pairs, P	4	
	Magnet permeability, μ_r	1.055	

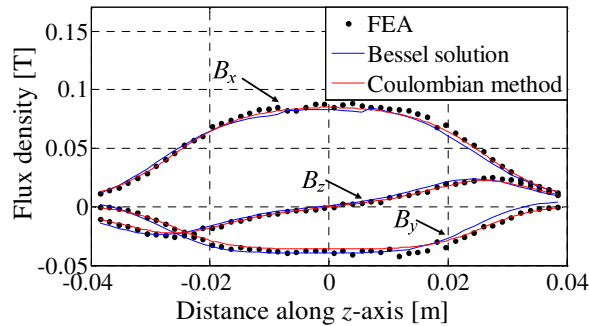


Figure 2.10 Comparison of the B_x , B_y and B_z flux density between COMSOL FEA and cylindrical charge sheet model along the z -axis at $(x, y) = (10, -9.5)$ mm.

2.3. Planar Charge Sheet

Assume an application where the magnetic source is located near a conductive plate and the source field interaction with the plate is of primary concern e.g. in eddy current testing [117, 118] or magnetic levitated vehicle applications [75]. Figure 2.11(a) shows the side view of a current carrying coil above a conductive quarter space. Figure 2.11(b) replaces the coil with an equivalent rectangular charge sheet with surface density $\rho_m(x,z)$ located in between the original coil and the conductor. The charge sheet is equivalent to the original coil in the sense that it will project the same amount of magnetic field onto the conductor as the original coil would do.

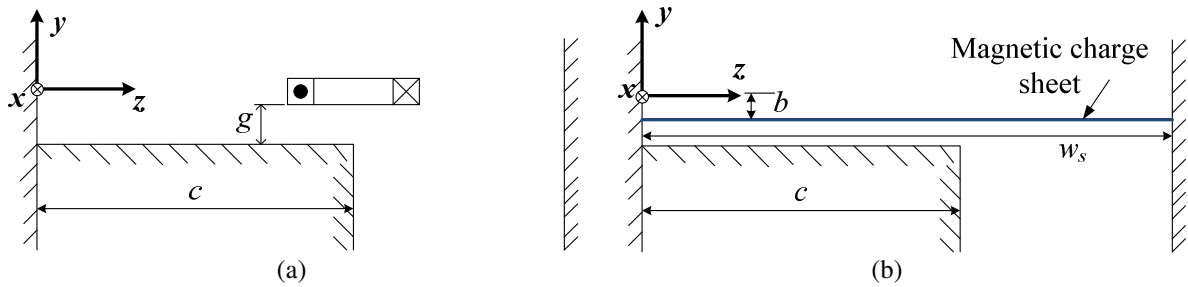


Figure 2.11 (a) Side view of a cylindrical coil above a right angled conductive quarter space of width c ; (b) the coil is replaced with an equivalent rectangular charge sheet of width w_s

2.3.1. Derivation of Charge Density

From (2.14) it can be readily seen that the charge density is twice the normal component of the source flux density incident on the charge sheet. Hence

$$\rho_m(x, z) = 2 B_y^s(x, y, z) \Big|_{y=-b} \tag{2.30}$$

A perspective view of the sheet with problem regions is shown in Figure 2.12.

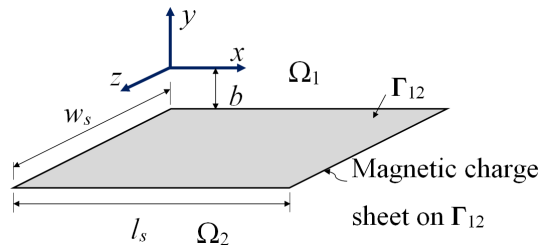


Figure 2.12 Rectangular planer charge sheet centered at $y=-b$

2.3.2. External Field Calculation

Assume the charge sheet is sufficiently wide in the x and z -directions that the source field is zero on the boundary edges i.e.

$$\rho_m(x, 0) = \rho_m(x, w_s) = 0 \quad (2.31)$$

$$\rho_m(0, z) = \rho_m(l_s, z) = 0 \quad (2.32)$$

where w_s, l_s are the width and length of the sheet respectively.

In this case the surface charge density can be expressed as

$$\rho_m(x, z) = \sum_{n=1}^N \sum_{m=1}^M \rho_{mn} \sin(\xi_m x) \sin(\psi_n z), \text{ on } \Gamma_{12} \quad (2.33)$$

where using (2.30) the Fourier coefficients are

$$\rho_{mn} = \frac{8}{l_s w_s} \int_{z=0}^{w_s} \int_{x=0}^{l_s} B_y^s(x, -b, z) \sin(\xi_m x) \sin(\psi_n z) dx dz \quad (2.34)$$

with

$$\psi_n = \frac{n\pi}{w_s} \quad (2.35)$$

$$\xi_m = \frac{m\pi}{l_s} \quad (2.36)$$

The fields above and below the charge sheet in Ω_1, Ω_2 are governed by

$$\nabla^2 \phi = 0 \quad (2.37)$$

Using the separation of variable method and noting that the field must decay with distance from the charge sheet; one obtains

$$\phi_1(x, y, z) = \sum_{n=1}^N \sum_{m=1}^M C_{mn} \sin(\psi_n z) \sin(\xi_m x) e^{-\chi_{nm}(y+b)}, \text{ in } \Omega_1 \quad (2.38)$$

$$\phi_2(x, y, z) = \sum_{n=1}^N \sum_{m=1}^M D_{mn} \sin(\psi_n z) \sin(\xi_m x) e^{\chi_{mn}(y+b)}, \text{ in } \Omega_2 \quad (2.39)$$

where

$$\chi_{mn} = \sqrt{\psi_n^2 + \xi_m^2} \quad (2.40)$$

and C_{nm} , D_{nm} are unknowns. Utilizing (2.5) and substituting (2.38) and (2.39) into the boundary conditions (2.11) and (2.12) the unknowns are determined to be

$$D_{mn} = C_{mn} = -\frac{\rho_{mn}}{2\mu_0\chi_{mn}} \quad (2.41)$$

As one is interested in the field below the charge sheet in Ω_2 , substituting (2.41) into (2.39) and using (2.5) yields

$$B_{2,x} = \sum_{n=1}^N \sum_{m=1}^M \frac{\xi_m \rho_{mn}}{2\chi_{mn}} \cos(\xi_m x) \sin(\psi_n z) e^{\chi_{mn}(y+b)} \quad (2.42)$$

$$B_{2,y} = \sum_{n=1}^N \sum_{m=1}^M \frac{\rho_{mn}}{2} \sin(\xi_m x) \sin(\psi_n z) e^{\chi_{mn}(y+b)} \quad (2.43)$$

$$B_{2,z} = \sum_{n=1}^N \sum_{m=1}^M \frac{\psi_n \rho_{mn}}{2\chi_{mn}} \sin(\xi_m x) \cos(\psi_n z) e^{\chi_{mn}(y+b)} \quad (2.44)$$

2.3.3. Validation Using Rotor Model

To illustrate the validity of this concept the external field due to the 2 pole-pair Halbach rotor as shown in Figure 2.5(b) and defined in Table 2.1 is modeled in Cartesian coordinates using the planar charge sheet. The surface charge density is obtained using (2.30) after calculating the B_y field due to the Halbach rotor at $y = -b$ from the rotor center using (2.22).

Figure 2.13 shows comparisons between the FEA and the planar charge sheet model. A good match was obtained. Finally the calculation time for different methods has been compared in Table 2.4.

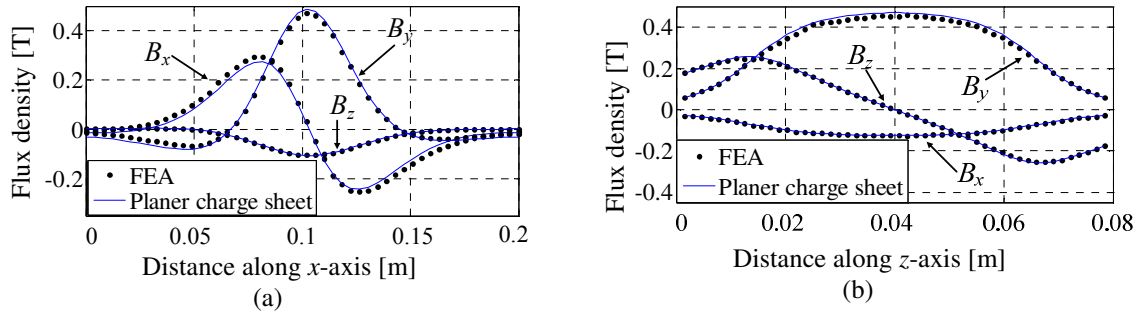


Figure 2.13 Field comparison between the FEA and rectangular shape charge sheet model. The planar charge sheet was placed at 5mm below the Halbach PM rotor. (a) along the x-axis at $(y, z) = (-9.5\text{mm}, 10\text{mm})$, (b) along the z-axis at $(x, y) = (10, -9.5)\text{mm}$.

Table 2.4: Calculation Time Comparison

Calculation Approach	Halbach PM Rotor	Surface PM Rotor
Finite element method	481s	348.12 s
Coulombian (integral) method	3×10^{-4} s	7.8×10^{-3} s
Bessel (differential) method	0.3244s	7.43 s
Planar charge sheet method	1.391×10^{-3} s	33.32×10^{-3} s

2.4. Summary

A generalized 3-D magnetic charge sheet method has been presented that enables the external field due to a magnetic source to be accurately reproduced using an equivalent magnetic charge sheet. Both cylindrical and planar magnetic charge sheets were used to demonstrate the applicability of the method. If the magnetic source has a complicated structure then by representing the magnetic source with an equivalent magnetic charge sheet the calculation time needed to determine the external field can be greatly reduced. This approach could also be used to calculate far-fields. The generality of this 3-D model has been validated by comparing it against commercially available JMAG, Comsol FEA software and an experimental Halbach rotor.

CHAPTER 3 : THREE-DIMENSIONAL EDDY CURRENT MODELING USING FINITE ELEMENT ANALYSIS

3.1. Introduction

In this chapter three-dimensional transient and steady state finite element models are developed for a magnetic source simultaneously moving and or rotating above a stationary conductive plate. The model has been developed using the magnetic vector potential in the conductive region and magnetic scalar potential in the non-conductive regions. The source field is analytically modeled using magnetic charge sheet and coupled into the boundary conditions of the interface between the conductive and non-conductive regions. The developed model is valid for any kind of magnetic source and it is verified by using a Halbach rotor as the source. Forces acting on the moving source are indirectly computed by applying Maxwell's stress tensor on the conductive plate. Forces and power loss in the plate are compared against commercial finite element analysis software and an already existing steady state Comsol model [75]. In section 3.2 a brief review of the existing eddy current modeling techniques involving moving parts is presented. In section 3.3 the transient modeling technique has been outlined. The steady state finite element model is presented in section 3.4 and a summary of this chapter is given in section 3.5.

3.2. A Review of Numerical Analysis of Eddy Current Distribution of Moving Parts

Research in numerical computation of eddy current problems involving dynamics of moving parts began more than three decades ago. It was mainly motivated by the need for developing an analysis tool to model the dynamic behavior of various electrical devices [119, 120]. Finite element analysis (FEA) methods or boundary integral method [121, 122] have been used to obtain the space distribution of electromagnetic fields in electrical machines with static parts or in static condition. Unlike static machine parts, for machines with linear or rotational motion it is important to know its key characteristics such as torque or inductance variation at different positions of the rotor. Hence many positions of the rotor have to be modeled and solved in FEA. Initially developed 3-D transient FEA models required the re-meshing of the entire model for each rotor position which involves extensive pre-processing and was very time consuming [123].

In order to circumvent this issue a significant amount of research has been carried out in the area of moving grid method also called sliding mesh technique [85, 124-129]. This typically involves using independent finite element meshes for the moving and stationary parts that are free to rotate or translate with respect to each other. Thus it eliminates the need for re-meshing at each rotor position. Several techniques have been proposed to couple the independent meshes. Special air gap elements were proposed by Razek [125] while Ratnajeevan applied Delaunay criterion [126] for mesh optimization to make the mesh adaptive to prevent destruction of mesh while the rotor mesh rotates and stator mesh stays stationary. The problem of overlapping meshes has been discussed by Tsukerman [129] and moving band techniques by Demenko [127].

A more general method to link independent meshes is using Lagrange multipliers. The method was applied to 2-D [128] and also to 3-D eddy current problems [130]. But the implementation of this method leads to an ill-conditioned finite element stiffness matrix making standard iterative solvers either slow or unable to converge to a solution [131].

A more computationally efficient approach, if possible, would be to avoid sliding mesh techniques altogether. Also, in the dynamic simulation of a device with linear motion such as in magnetic levitated vehicle [74, 75, 77, 78] as shown in Figure 3.1, modeling the translational motion by physically moving the rotor part becomes impractical for high translational speed as it will require large stator plate length to reach steady state [74].

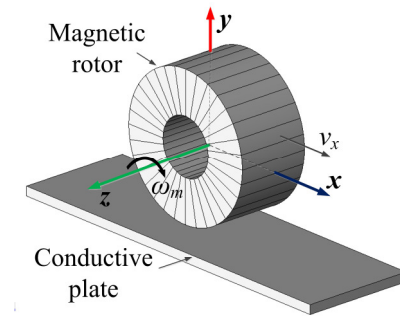


Figure 3.1 A segmented Halbach rotor with rotational and translational motion above conductive plate.

Previously a 3-D steady state model of magnetic rotor both translationally moving and rotating above a conductive plate was presented by Bird [74] in which the rotor field was modeled using a novel fictitious magnetic charge boundary condition while the conductive and nonconductive regions were modeled using a convective $\mathbf{A}-\phi$ steady state finite element model. Although this approach could model both rotation and translational motion of the rotor, the modeling of the steady state rotation using a complex magnetic charge boundary necessitates a large nonconductive region to be

modeled particularly when the rotor diameter is large. Therefore, in order to reduce computational burden, another steady state model was presented in which the rotor field was modeled analytically using a novel complex current sheet approach where each shunt and radial magnet segment of the magnetic rotor was modeled using an equivalent current sheet and the analytical source field was coupled to the conductive plate by including it in the plate boundary conditions [75]. This model had the definite advantage of reducing the problem region down to only the conductive plate and nonconductive air region (without magnetic rotor) and also it enabled the rotor position to be changed with ease without moving the boundary mesh. However as this approach was modeling each radial and shunt magnet of the rotor by a current sheet, the steady state model was computationally expensive.

In the proposed finite element model outlined in this chapter, the magnetic rotor has been modeled analytically using magnetic charge sheet (discussed in Chapter 2). The applicability of source modeling technique using charge sheet to any kind of magnetic source makes the proposed finite element model suitable for any source in motion as well. For further reduction of computation time the conductive and nonconductive regions have been modeled using a convective $\mathbf{A}-\phi$ method. The translational motion of the rotor is modeled by including equal and opposite velocity term in the plate governing equation. Forces acting on the moving source and power loss in the conductive plate will be evaluated and compared against standard FEA software.

The assumptions of the proposed FEA models are listed below:

- The conductive plate is linear, homogenous and simply connected
- The plate is continuous with constant conductivity and non-magnetic.

- The magnetic source has translational, heave and lateral motion along with rotational motion.
- The translational motion of the source is uniform.
- The frequency is sufficiently low in order for the quasi-static approximation to be valid. Precisely, the wavelength in the free-space is assumed to be large compared to the dimension of the plate and magnetic source, which is always true for maglev applications

3.3. Transient Modeling

If the magnetic source's motion is analytically modeled then the finite element problem regions will simplify down to conductive, Ω_c , and nonconductive regions, Ω_{nc} , as shown in Figure 3.2. The conductive and nonconductive region normal vectors on the conductive region boundary Γ_c have been defined as \hat{n}_c and \hat{n}_{nc} respectively.

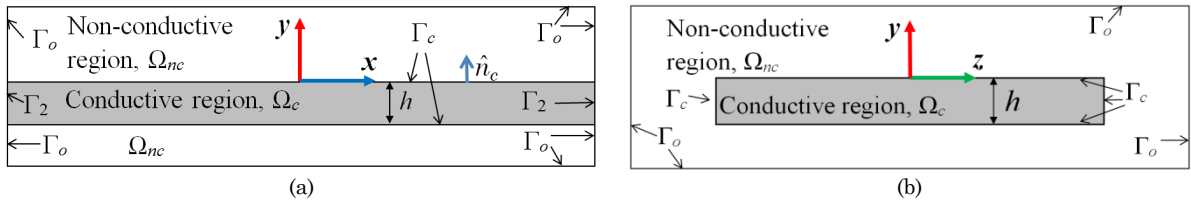


Figure 3.2. (a) The x - y and (b) z - y view of the problem region consisting of only conductive and non-conductive regions. The effect of the magnetic source is taken into account by the boundary conditions on the boundary Γ_c .

3.3.1. Conductive Region Formulation

Electromagnetic problems can be categorized into two types: low frequency and high frequency problems. Eddy current modeling falls into the first type. The applicable quasi-static Maxwell's equations are (neglecting displacement current in Ampere's law due to low frequency) [112]

$$\nabla \times \mathbf{E} = -\frac{d\mathbf{B}}{dt} \quad (3.1)$$

$$\nabla \times \mathbf{H} = \mathbf{J} \quad (3.2)$$

$$\nabla \cdot \mathbf{B} = 0 \quad (3.3)$$

The conductive region material is assumed to be linear, homogeneous, simply connected and nonmagnetic such as aluminum. In the presence of a moving conductive medium, the following constitutive relations relate the field vectors [115]

$$\mathbf{J} = \sigma \mathbf{E} \quad (3.4)$$

$$\mathbf{B} = \mu_0 \mathbf{H} \quad (2.3)$$

where σ and μ_0 represent the conductivity [Sm^{-1}] of the plate and permeability [Hm^{-1}] of free space. Substituting (3.4) and (2.3) into (3.1) gives

$$\nabla \times \frac{\mathbf{B}}{\mu_0} - \sigma \mathbf{E} = \mathbf{0} \quad (3.5)$$

As the divergence of a curl is zero [132], the magnetic flux density can be expressed in terms of the magnetic vector potential as [112]

$$\mathbf{B} = \nabla \times \mathbf{A} \quad (3.6)$$

Using (3.6), the x , y and z -components of the magnetic flux density can be obtained as

$$B_x = \frac{\partial A_z}{\partial y} - \frac{\partial A_y}{\partial z} \quad (3.7)$$

$$B_y = \frac{\partial A_x}{\partial z} - \frac{\partial A_z}{\partial x} \quad (3.8)$$

$$B_z = \frac{\partial A_y}{\partial x} - \frac{\partial A_x}{\partial y} \quad (3.9)$$

Substituting (3.6) into (3.1) gives

$$\nabla \times \mathbf{E} = - \frac{d}{dt} (\nabla \times \mathbf{A}) \quad (3.10)$$

Solving (3.10), the electric field intensity \mathbf{E} is found to be

$$\mathbf{E} = - \frac{d\mathbf{A}}{dt} \quad (3.11)$$

If the source is moving, it is noted that

$$\frac{d\mathbf{A}(x, y, z, t)}{dt} = \frac{\partial \mathbf{A}}{\partial t} + \frac{\partial \mathbf{A}}{\partial x} \frac{\partial x}{\partial t} + \frac{\partial \mathbf{A}}{\partial y} \frac{\partial y}{\partial t} + \frac{\partial \mathbf{A}}{\partial z} \frac{\partial z}{\partial t} \quad (3.12)$$

Here it is assumed that the source can have translational, v_x , and heave motion, v_y . Thus (3.12) becomes

$$\frac{d\mathbf{A}(x, y, z, t)}{dt} = \frac{\partial \mathbf{A}}{\partial t} + v_x \frac{\partial \mathbf{A}}{\partial x} + v_y \frac{\partial \mathbf{A}}{\partial y} \quad (3.13)$$

Equation (3.13) can also be written as

$$\frac{d\mathbf{A}(x, y, z, t)}{dt} = \frac{\partial \mathbf{A}}{\partial t} + (\mathbf{v} \cdot \nabla) \mathbf{A} \quad (3.14)$$

where \mathbf{v} is the velocity vector. Substituting (3.14) into (3.11) yields the electric field intensity

$$\mathbf{E} = - \frac{\partial \mathbf{A}}{\partial t} - (\mathbf{v} \cdot \nabla) \mathbf{A} \quad (3.15)$$

Substituting (3.15) into (3.4) the current density can be obtained in terms of the magnetic vector potential

$$\mathbf{J} = -\sigma \left(\frac{\partial \mathbf{A}}{\partial t} + v_x \frac{\partial \mathbf{A}}{\partial x} + v_y \frac{\partial \mathbf{A}}{\partial y} \right) \quad (3.16)$$

Separating the scalar components, one finds

$$J_x = -\sigma \left(\frac{\partial A_x}{\partial t} + v_x \frac{\partial A_x}{\partial x} + v_y \frac{\partial A_x}{\partial y} \right) \quad (3.17)$$

$$J_y = -\sigma \left(\frac{\partial A_y}{\partial t} + v_x \frac{\partial A_y}{\partial x} + v_y \frac{\partial A_y}{\partial y} \right) \quad (3.18)$$

$$J_z = -\sigma \left(\frac{\partial A_z}{\partial t} + v_x \frac{\partial A_z}{\partial x} + v_y \frac{\partial A_z}{\partial y} \right) \quad (3.19)$$

Substituting (3.15) and (3.6) into (3.5), one obtains

$$\nabla \times \frac{1}{\mu_0} (\nabla \times \mathbf{A}) = \sigma \left(-\frac{\partial \mathbf{A}}{\partial t} - (\mathbf{v} \cdot \nabla) \mathbf{A} \right) \quad (3.20)$$

Using the identity [114]

$$\nabla \times \nabla \times \mathbf{A} = \nabla(\nabla \cdot \mathbf{A}) - \nabla^2 \mathbf{A} \quad (3.21)$$

and the Coulomb gauge [114, 115]

$$\nabla \cdot \mathbf{A} = 0 \quad (3.22)$$

(3.20) reduces to

$$\nabla^2 \mathbf{A} = \mu_0 \sigma \left(\frac{\partial \mathbf{A}}{\partial t} + (\mathbf{v} \cdot \nabla) \mathbf{A} \right) \quad (3.23)$$

Or,

$$\nabla^2 \mathbf{A} = \mu_0 \sigma \left(\frac{\partial \mathbf{A}}{\partial t} + v_x \frac{\partial \mathbf{A}}{\partial x} + v_y \frac{\partial \mathbf{A}}{\partial y} \right) \quad (3.24)$$

Equation (3.24) is the governing equation for the conductive plate in terms of the magnetic vector potential.

In order to find a solution of (3.24) numerically, the Galerkin weighted residual method has been used [133]. The residual or error from (3.24) for the assumed magnetic vector

potential solutions A_x , A_y and A_z is

$$R_i = \nabla^2 A_i - \mu_0 \sigma \left(\frac{\partial A_i}{\partial t} + v_x \frac{\partial A_i}{\partial x} + v_y \frac{\partial A_i}{\partial y} \right), \quad i = x, y, z \quad (3.25)$$

In order to find the numerical solution for A_x , A_y and A_z , the integral of the residual multiplied with a weighting function over the entire domain is set to zero i.e.,

$$\int_{\Omega_c} N_i R_i d\Omega_c = 0, \quad i = x, y, z \quad (3.26)$$

where, for example, N_x is the x -component of the shape function. Substituting (3.25) into (3.26) gives

$$\int_{\Omega_c} N_i \left[\nabla^2 A_i - \mu_0 \sigma \left(\frac{\partial A_i}{\partial t} + v_x \frac{\partial A_i}{\partial x} + v_y \frac{\partial A_i}{\partial y} \right) \right] d\Omega_c = 0, \quad i = x, y, z \quad (3.27)$$

Using the Green's first identity [134]

$$\int_{\Omega_c} N_i \nabla^2 A_i d\Omega_c = - \int_{\Omega_c} (\nabla N_i \cdot \nabla A_i) d\Omega_c + \int_{\Gamma_c} N_i (\nabla A_i \cdot \hat{n}_c) d\Gamma_c \quad (3.28)$$

Substituting (3.28) into (3.27), the governing equation for the conductive region is obtained in the following weak form [135]

$$\begin{aligned} - \int_{\Omega_c} \nabla N_i \cdot \nabla A_i d\Omega_c - \mu_0 \sigma \int_{\Omega_c} N_i \left(\frac{\partial A_i}{\partial t} + v_x \frac{\partial A_i}{\partial x} + v_y \frac{\partial A_i}{\partial y} \right) d\Omega_c \\ + \int_{\Gamma_c} N_i (\nabla A_i \cdot \hat{n}_c) d\Gamma_c = 0, \quad i = x, y, z \end{aligned} \quad (3.29)$$

The first two terms of (3.29) are the subdomain equations for the plate region Ω_c while the last term is the boundary condition on conductive plate boundary Γ_c .

3.3.2. Nonconductive Region Formulation

The total magnetic flux density in the nonconductive region Ω_{nc} is composed of a field due to the magnetic source (\mathbf{B}^s) and reflected field (\mathbf{B}^r) in the air region due to the induced eddy currents in the conductive plate

$$\mathbf{B}_{nc} = \mathbf{B}^s + \mathbf{B}^r, \text{ in } \Omega_{nc} \quad (3.30)$$

Due to the absence of free current in Ω_{nc} the reflected flux density can be expressed in terms of the magnetic scalar potential, ϕ , as

$$\mathbf{B}^r = -\mu_0 \nabla \phi, \text{ in } \Omega_{nc} \quad (2.5)$$

Substituting (2.5) into (3.30), the total flux density in Ω_{nc} is given by

$$\mathbf{B}_{nc} = \mathbf{B}^s - \mu_0 \nabla \phi, \text{ in } \Omega_{nc} \quad (3.31)$$

After taking divergence on both sides of (3.31) and using (3.3), the governing equation for the air region is obtained as

$$\mu_0 \nabla^2 \phi = 0, \text{ in } \Omega_{nc} \quad (3.32)$$

Therefore if the effect of the source magnetic field is accounted for by the boundary conditions on the air-conductor interfaces Γ_c , it is not necessary to explicitly model source's field within the nonconductive region [136, 137]. Using the Galerkin weighted residual method [133] and Green's first identity [134], the weak form of (3.32) will be

$$\mu_0 \int_{\Omega_{nc}} \nabla \phi \cdot \nabla w_f d\Omega_{nc} - \mu_0 \int_{\Gamma_c} w_f \nabla \phi \cdot \hat{n}_{nc} d\Gamma_c = 0 \quad (3.33)$$

where w_f is the weighting function. Here the first term is the subdomain equation for nonconductive region Ω_{nc} and the second one is the boundary condition on the interface

between the nonconductive and conductive region i.e. Γ_c .

3.3.3. Boundary Condition

The continuity of the normal component of the magnetic flux density and tangential component of the magnetic field intensity is satisfied on Γ_c i.e.,

$$\hat{n}_c \cdot (\mathbf{B}_c - \mathbf{B}_{nc}) = 0, \text{ on } \Gamma_c \quad (3.34)$$

$$\hat{n}_c \times (\mathbf{H}_c - \mathbf{H}_{nc}) = 0, \text{ on } \Gamma_c \quad (3.35)$$

Utilizing (3.6) and (3.31) and noting that the conductive medium is non-magnetic, (3.34) and (3.35) can be rewritten as [136, 138]

$$\hat{n}_c \cdot (\mathbf{B}^s - \mu_0 \nabla \phi) = \hat{n}_c \cdot (\nabla \times \mathbf{A}), \text{ on } \Gamma_c \quad (3.36)$$

$$\hat{n}_c \times (\mathbf{B}^s - \mu_0 \nabla \phi) = \hat{n}_c \times \nabla \times \mathbf{A}, \text{ on } \Gamma_c \quad (3.37)$$

Also in order to ensure uniqueness of the solution

$$\hat{n}_c \cdot \mathbf{A} = 0, \text{ on } \Gamma_c \quad (3.38)$$

must be enforced [137, 139, 140]. This also sets the normal component of the induced eddy current on Γ_c to zero i.e.

$$\hat{n}_c \cdot \mathbf{J} = 0 \quad (3.39)$$

In order to couple conductive and nonconductive regions, the scalar boundary condition in (3.33) needs to be expressed in terms of the magnetic vector potential terms.

Using (3.36) the boundary term in (3.33) can be written as [137]

$$\mu_0 \int_{\Gamma_c} w_f \nabla \phi \cdot \hat{n}_c d\Gamma_c = \int_{\Gamma_c} w_f (\mathbf{B}^s - \nabla \times \mathbf{A}) \cdot \hat{n}_c d\Gamma_c, \text{ on } \Gamma_c \quad (3.40)$$

Expanding (3.36) one finds

$$\mu_0 \frac{\partial \phi}{\partial x} = B_x^s - \frac{\partial A_z}{\partial y} + \frac{\partial A_y}{\partial z} \quad (3.41)$$

$$\mu_0 \frac{\partial \phi}{\partial y} = B_y^s - \frac{\partial A_x}{\partial z} + \frac{\partial A_z}{\partial x} \quad (3.42)$$

$$\mu_0 \frac{\partial \phi}{\partial z} = B_z^s - \frac{\partial A_y}{\partial x} + \frac{\partial A_x}{\partial y} \quad (3.43)$$

Substituting (3.41)-(3.43) into (3.40) gives the following boundary condition coupling the scalar potential, ϕ , with the source field and magnetic vector potential for region Ω_{nc}

$$\int_{\Gamma_c} w_f \left[\left(B_x^s - \frac{\partial A_z}{\partial y} + \frac{\partial A_y}{\partial z} \right) \hat{n}_{cx} + \left(B_y^s - \frac{\partial A_x}{\partial z} + \frac{\partial A_z}{\partial x} \right) \hat{n}_{cy} + \left(B_z^s - \frac{\partial A_y}{\partial x} + \frac{\partial A_x}{\partial y} \right) \hat{n}_{cz} \right] d\Gamma_c = 0, \text{ on } \Gamma_c \quad (3.44)$$

where, for example, \hat{n}_{cx} is the x -component normal vector to the conductive plate region.

Similarly the vector potential boundary conditions in (3.29) must be replaced with the scalar potential terms. For instance, for $i=x$ the boundary condition in (3.29) together with (3.38) gives

$$\int_{\Gamma_c} N_x \left[\left(\frac{\partial A_x}{\partial x} + A_x \right) \hat{n}_{cx} + \frac{\partial A_x}{\partial y} \hat{n}_{cy} + \frac{\partial A_x}{\partial z} \hat{n}_{cz} \right] d\Gamma_c = 0, \text{ on } \Gamma_c \quad (3.45)$$

Using (3.41)-(3.43) enables (3.45) to be expressed in terms of the magnetic scalar potential, ϕ , and source field as

$$\int_{\Gamma_c} N_x \left[\left(A_x - \frac{\partial A_y}{\partial y} - \frac{\partial A_z}{\partial z} \right) \hat{n}_{cx} + \left(\mu_0 \frac{\partial \phi}{\partial z} + \frac{\partial A_y}{\partial x} - B_z^s \right) \hat{n}_{cy} + \left(\frac{\partial A_z}{\partial x} - \mu_0 \frac{\partial \phi}{\partial y} + B_y^s \right) \hat{n}_{cz} \right] d\Gamma_c = 0, \text{ on } \Gamma_c \quad (3.46)$$

Similar relations are obtained for the y and z -components of the vector potential

$$\int_{\Gamma_c} N_y \left[\left(\frac{\partial A_x}{\partial y} - \mu_0 \frac{\partial \phi}{\partial z} - B_z^s \right) \hat{n}_{cx} + \left(A_y - \frac{\partial A_x}{\partial x} - \frac{\partial A_y}{\partial y} \right) \hat{n}_{cy} + \left(\frac{\partial A_z}{\partial y} + \mu_0 \frac{\partial \phi}{\partial x} - B_x^s \right) \hat{n}_{cz} \right] d\Gamma_c = 0, \text{ on } \Gamma_c \quad (3.47)$$

$$\int_{\Gamma_c} N_z \left[\left(\frac{\partial A_x}{\partial z} + \mu_0 \frac{\partial \phi}{\partial y} - B_y^s \right) \hat{n}_{cx} + \left(\frac{\partial A_y}{\partial z} - \mu_0 \frac{\partial \phi}{\partial x} + B_x^s \right) \hat{n}_{cy} + \left(A_z - \frac{\partial A_y}{\partial y} - \frac{\partial A_z}{\partial z} \right) \hat{n}_{cz} \right] d\Gamma_c = 0, \text{ on } \Gamma_c \quad (3.48)$$

The Dirichlet boundary condition has been applied on all of the remaining non-conductive boundaries

$$\phi = 0, \text{ on } \Gamma_o \quad (3.49)$$

The inclusion of the translational source field effect into the plate requires that the conductive plate must be very long. The model with a finite plate length can result in the field not being zero at the ends of the plate. This can result in non-physical field reflections, leading to the solver failing to converge. To avoid this, the Neumann boundary condition has been applied in the direction of the field translation, on boundary Γ_2

$$\frac{\partial A_i}{\partial x} = 0, \quad i = x, y, z, \text{ on } \Gamma_2 \quad (3.50)$$

Using the subdomain equations given by (3.29) and (3.33) within the conductive and nonconductive regions as well as the boundary conditions (3.44), (3.46)-(3.50) enables the convective finite element \mathbf{A} - ϕ model to be defined.

The source field appears only in the boundary conditions (3.46)-(3.48) which can be easily evaluated using the magnetic charge sheet technique discussed in chapter 2 making

the proposed method applicable for any kind of magnetic source with linear and/or rotational motion.

It must be noted that depending on the source location and relative size of the source and plate, the source field is added on the side and bottom surfaces of the plate. If the source is located at the center above the plate and the plate width is much larger than the source, the source field only needs to be added only on the top Γ_c . Otherwise one has to include it on all the interface boundaries.

If the source is located at the center of the plate, induced eddy currents in the plate flow parallel to the top surface of the plate that is the currents flow in the x - z plane. Hence the y -component of the current, J_y , is negligible [141]. Due to the small thickness of the plate, this current component is very small even when the source is laterally shifted from the center of the plate along z -axis. As the induced current density J_y is related to the magnetic vector potential A_y by (3.16), the y -component vector potential is also very small compared to the x and z -components. This will be illustrated later in Figure 3.16 and Figure 3.17.

3.3.4. Initial Condition, Meshing and Solver Settings

The initial condition for the unknown parameters in the conductive and nonconductive medium are set as zero i.e.

$$\phi(x, y, z, t)|_{t=0} = 0, \quad i = x, y, z \quad (3.51)$$

$$A_i(x, y, z, t)|_{t=0} = 0, \quad i = x, y, z \quad (3.52)$$

In finite element analysis the accuracy of the solution depends highly on the size of the meshes. It is desired to have fine mesh in the conductive medium whereas the mesh in the non-conductive region can be comparatively larger. The different mesh size used in

different parts of the finite element model is outlined in Table 3.1 below. The mesh plot of the model is shown in Figure 3.3.

Table 3.1: Mesh size for different regions of the finite element model

Region	Maximum mesh size [mm]
Conductive plate	2
Non-conductive air region	20

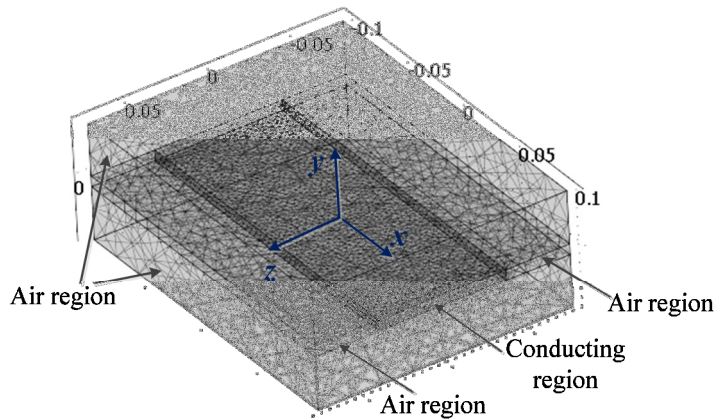


Figure 3.3. Perspective view of mesh plot of different subdomains in the transient finite element model.

Choosing the correct solver is another important factor while solving numerical problems. There are two main types of solvers in numerical computing: direct and indirect. The finite element analysis breaks down the entire problem region into meshes of selected sizes and shapes with unknown parameters assigned to each vertex of the geometrical shape of the mesh. For example, a triangular mesh (used in the current model) is shown in Figure 3.4 with three vertices a, b and c each associated with a set of unknown parameters ϕ^i , A_x^i , A_y^i and A_z^i for $i = 1, 2, 3$. These unknowns are known as degrees of freedoms (DOFs).

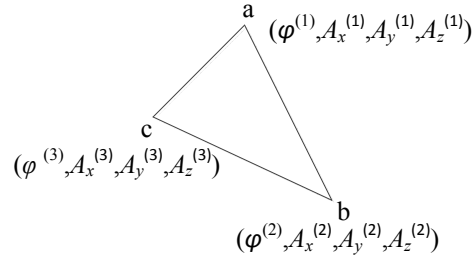


Figure 3.4. Triangular finite element mesh

The finite element analysis program reformulates the original problem into the following linear equation

$$A\bar{x} = b, \quad \bar{x} = [\phi^i \ A_x^i \ A_y^i \ A_z^i \dots]^T \quad (3.53)$$

where the coefficient matrix A and the right hand side vector b are known quantities from the governing equations (3.29)-(3.33) and boundary conditions (3.40), (3.46)-(3.50) and initial condition setting and \bar{x} is the unknown vector to solve. Superscript 'T' stands for transpose.

In the direct methods, (3.53) is solved using direct factorization of the A matrix such as the Cholesky, Lower-Upper triangular (LU) decomposition or Singular Value Decomposition (SVD) techniques whereas in the indirect methods, (3.53) is solved using iterative methods like Generalized Minimal Residual (GMRES), Conjugate gradients or Geometric Multigrid [142]. Also, if matrix A is ill-conditioned or close to being ill-conditioned, the iterative solver does not converge or converges very slowly. For better performance it is recommended to smooth the matrix using preconditioner before trying to factorize it [135].

If the dimension of matrix A is $m \times n$, a direct solver usually needs $O(m^3)$ floating point operations (FLOPs) whereas an iterative one takes only $O(m^2)$. Hence the memory requirement for the latter is much less [142]. The direct solvers are very efficient for

problems involving upto 100,000 DOFs depending on the available memory, but for larger DOFs iterative solvers are recommended [135]. For the present transient simulation with the mesh size outlined in Table 3.1 the generated DOFs is approximately 330,000 and A is positive definite. So the chosen solver is time-dependent GMRES with Symmetric Successive Over-Relaxation (SSOR) preconditioner.

3.3.5. Model Validation

For validation purpose, a segmented Halbach rotor has been used as the source. The accuracy of this boundary coupled finite element 3-D transient model is highly dependent on the accuracy of the Halbach rotor field model. The 3-D transient model was validated by comparing it with JMAG and Magsoft flux 3-D transient models when there is no translational motion and also with a previously developed 3-D finite element steady state model [75] in which both translational and rotational motion are present. No translational motion was used by JMAG and Magsoft flux because the current version cannot simultaneously model 3-D translational and rotational motion.

Despite (3.29) containing both convective and diffusive terms, no spurious oscillatory behavior has been observed in this formulation and therefore upwinding technique discussed in [13] was not used.

3.3.5.1. Comparison with Commercial Transient 3-D Finite Element Model (Zero Translational Velocity)

Using the parameters given in Table 3.2, the transient boundary coupled $\mathbf{A}-\phi$ model was compared with a JMAG 3-D transient model as shown in Figure 3.5. The Field comparison of a Halbach rotor along the surface of the conductive plate created by JMAG FEA and the analytic 3-D model, discussed in chapter 2, is shown in Figure 3.6. A close agreement was obtained.

Table 3.2 : Simulation parameters for zero translational velocity

	Description	Value	Unit
Rotor	Outer radius, r_o	26	mm
	Inner radius, r_i	10	mm
	Width, w_o	52	mm
	Remnant magnetic flux density, B_{rem}	1.42	T
	Relative permeability, μ_r	1.108	-
	Pole pairs, P	2	-
Conductive plate	Conductivity, σ	2.459×10^7	Sm^{-1}
	Width, w	77	mm
	Length, l	200	mm
	Thickness, h	6.3	mm
	Air-gap between rotor and plate, g	5	mm

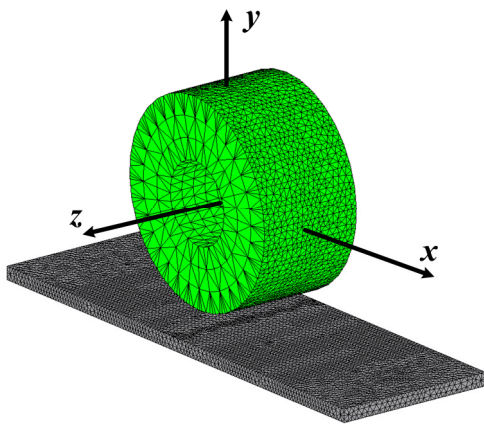


Figure 3.5. Example of the mesh used by the transient JMAG 3-D model in which Halbach rotor is rotated over a conductive plate

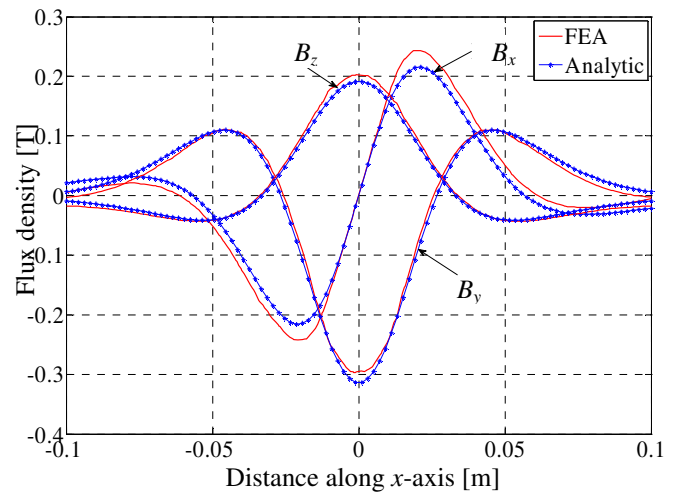


Figure 3.6. B_x , B_y and B_z magnetic flux density comparison between a JMAG FEA model and the magnetic charge analytic model along the plate surface at $(y, z) = (-10, 30)$ mm from center of the Halbach rotor.

In the developed transient model the forces were evaluated using the Lorentz method [112, 143]. The thrust, lift and lateral forces are calculated, respectively, by

$$F_x = \int_{\Omega_c} (J_y B_{c,z} - J_z B_{c,y}) d\Omega_c, \quad (3.54)$$

$$F_y = \int_{\Omega_c} (J_z B_{c,x} - J_x B_{c,z}) d\Omega_c \quad (3.55)$$

$$F_z = \int_{\Omega_c} (J_x B_{c,y} - J_y B_{c,x}) d\Omega_c \quad (3.56)$$

The power loss in the plate is calculated using

$$P_{Loss} = \frac{1}{\sigma} \int_{\Omega_c} (J_x^2 + J_y^2 + J_z^2) d\Omega_c, \quad (3.57)$$

where, for example, $B_{c,x}$ and J_x are the x -component of the magnetic flux density and eddy current density in the conductive medium. In (3.54)-(3.57) the integration is performed over the entire conductive plate domain Ω_c .

The presented finite element model was formulated using Comsol. Comparison of the thrust, lift and lateral forces calculated using the presented Comsol model as well as JMAG and Magsoft flux 3-D transient models is shown in Figure 3.7 when the rotor or source is laterally offset along the z -axis by 10 and 25 mm and rotating at a speed of 4000 RPM. Figure 3.8 shows power loss comparison for the mentioned lateral offset values and rotational speed of 4000 and 8000 RPM. Excellent match of results among different models especially between JMAG and the developed model has been achieved.

As can be seen from Figure 3.7 and Figure 3.8, Magsoft flux FEA and the presented Comsol model produce high overshoot in the lift force and power loss results as soon as the simulation starts. This is due to the fact that at the start of the simulation, the field in the conductive plate is initially set to zero (refer to (3.52)) and therefore the conductive plate suddenly experiences a flux change due to the source field. As a result, this produces a ‘non-physical’ lift force. It happened only in simulation. On the other hand, JMAG assumes that the initial field in the conductive region is defined as the source field. As a result, JMAG does not produce any sudden peak in the lift force.

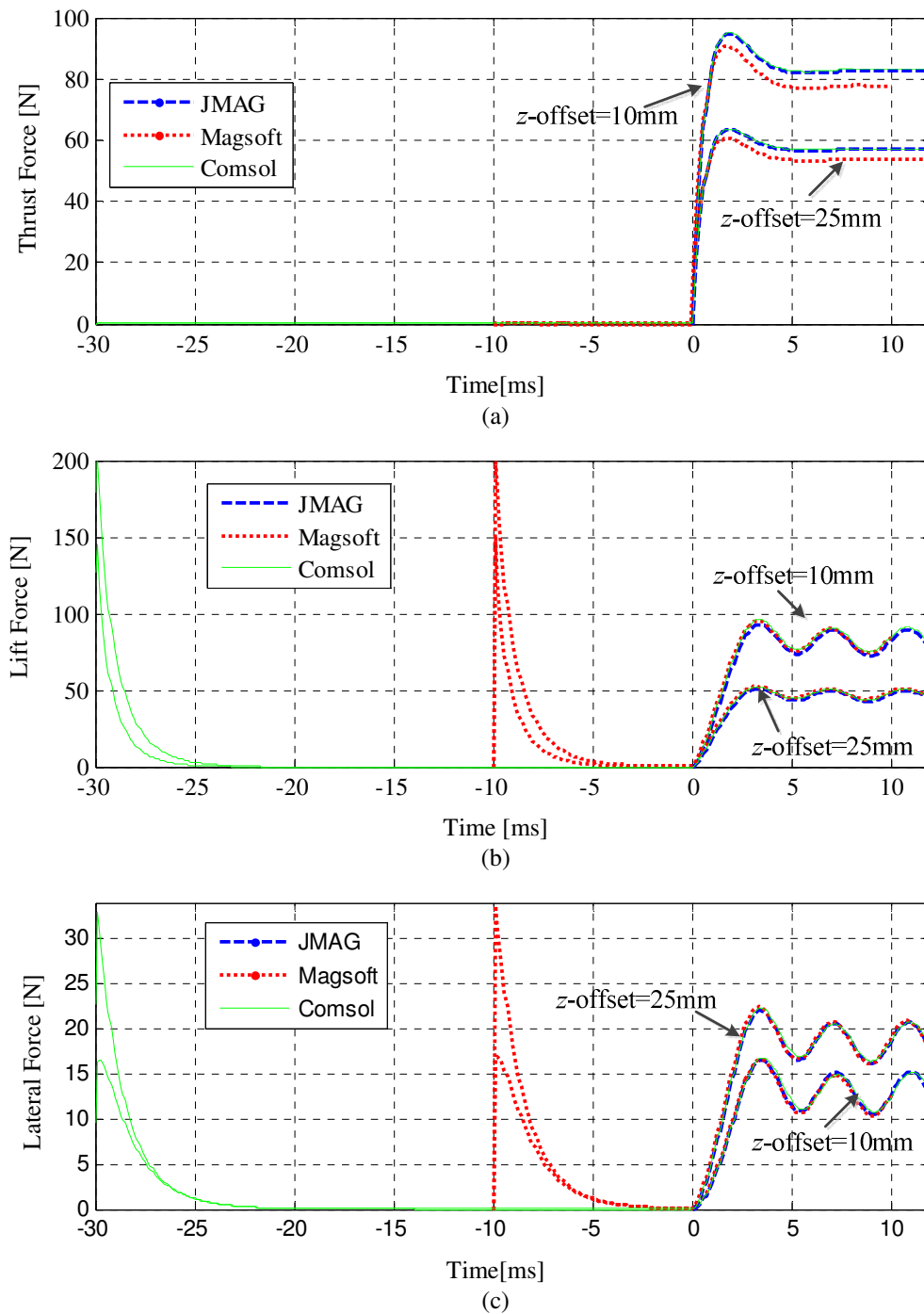


Figure 3.7. (a) Thrust, (b) Lift and (c) lateral force comparison for 4000 RPM and zero translational velocity among Comsol finite element model, JMAG and Magsoft flux 3-D finite element models for different lateral offsets of the rotor

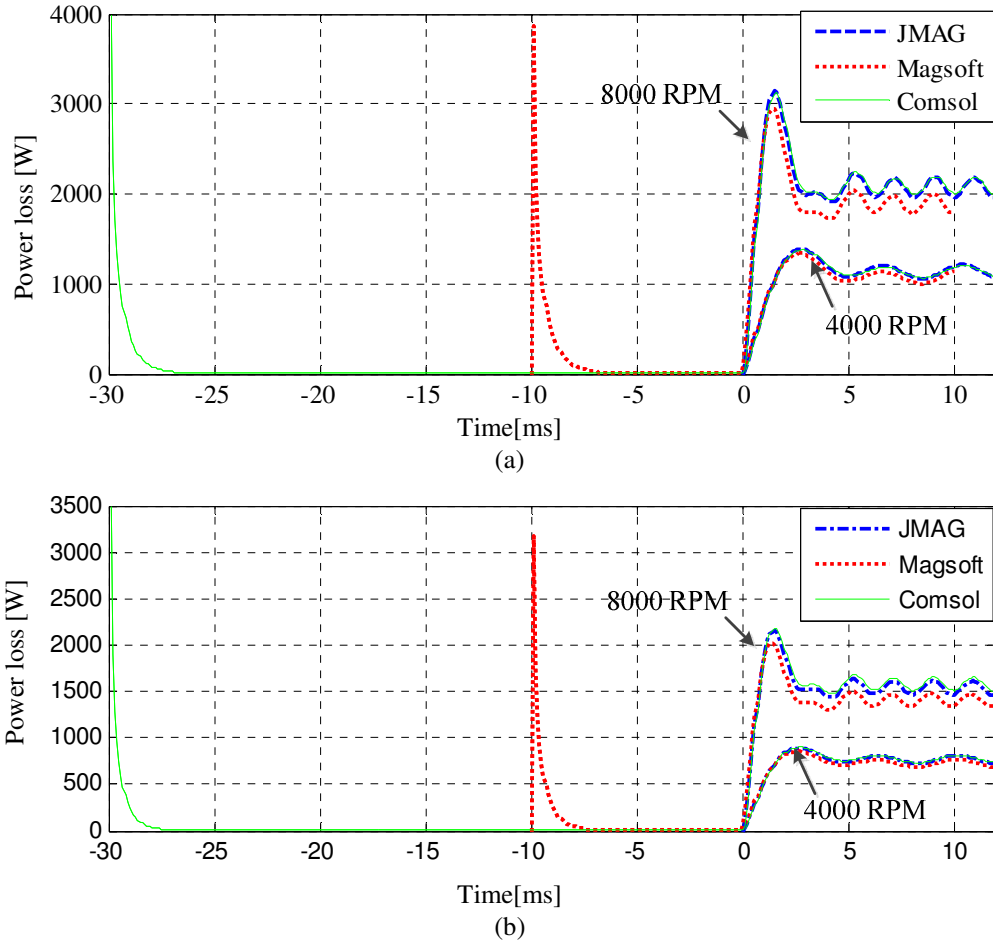


Figure 3.8. Power loss comparison among Comsol finite element model and commercial JMAG and Magsoft flux 3-D finite element models for (a) lateral offset of 10mm and (b) lateral offset of 25mm. Translational velocity of the rotor is zero.

It is generally preferred to start the rotational and translational motion of the rotor only after the field in the air and conductive region have become equal to each other or in other words, the lift force and power loss has decayed to zero from the initial spike. From Figure 3.7 and Figure 3.8, it is noticed that this decay takes approximately 30ms for Comsol and 10ms for Magsoft flux FEA. Hence rotation of the rotor was initiated in Comsol and Magsoft accordingly. As in JMAG FEA this initial spike was not present, the simulation results do not have this time lag.

Force comparison among different finite element models also showed that the proposed model using Comsol is computationally more efficient than other two

counterparts. The average computation time for the transient simulation for 4000 and 8000 RPM of the rotor for different FEA models is outlined in Table 3.3. A Dell workstation with an Intel Xeon-E5520 dual core processor with 22GB RAM was used. The Comsol and Magsoft computation time results are shown for the period after the decay of the initial peak. All the computation times are for 12ms of transient simulation as shown in Figure 3.7 and Figure 3.8.

Table 3.3 : Computation time for different finite element transient models

Model type	Computation time
Magnetic charge based transient model using Comsol v3.5a	54 min
JMAG transient	5 hr 40 min
Magsoft flux transient	5 hr 21 min

The accuracy of the developed Comsol based FEA transient model has been calculated with respect to the JMAG and Magsoft transient models for thrust, lift, lateral force and joule loss at lateral offset of 25mm and shown in Table 3.4

Table 3.4 : Accuracy of the developed Comsol based transient FEA model

Force	Error with JMAG transient [%]	Error with Magsoft transient [%]
Thrust	1.22	6.54
Lift	4.1	2.72
Lateral	1	3
Power loss	0.9	6.5

3.3.5.2. Comparison with 3-D Finite Element Steady State Model (Non-zero Translational Velocity)

The JMAG and Magsoft finite element software cannot simulate translation and rotation simultaneously, so they are not used to simulate non-zero translational velocity transients. Hence, a previously developed 3-D boundary coupled $\mathbf{A}-\phi$ steady state model using a novel current sheet approach [75] is used to compare the lift and thrust with the developed transient model. A comparison is made over a range of slip values for 15ms^{-1}

translational velocity and when the rotor is at center of the plate. The slip speed is defined by (1.1) and rewritten here for convenience

$$s_l = \omega_m r_o - v_x \quad (1.1)$$

where ω_m is mechanical angular speed [rads^{-1}] and r_o is outer radius [m] of the rotor.

The force and power loss comparison between the two models highly depends on the accuracy of the static rotor field modeling. The magnetic flux density created by the Halbach rotor has been compared on the surface of the plate between the two models, as shown in Figure 3.9 and Figure 3.10, using the parameters listed in Table 3.5.

Table 3.5 : Simulation parameters for non-zero translational velocity

	Description	Value	Unit
Rotor	Outer radius, r_o	50	mm
	Inner radius, r_i	34.2	mm
	Width, w_o	50	mm
	Remnant magnetic flux density, B_{rem}	1.42	T
	Relative permeability, μ_r	1.055	-
	Pole pairs, P	4	-
Conductive plate	Conductivity, σ	2.459×10^7	Sm^{-1}
	Width, w	77	mm
	Length, l	200	mm
	Thickness, h	6.3	mm
	Air-gap between rotor and plate, g	9.5	mm

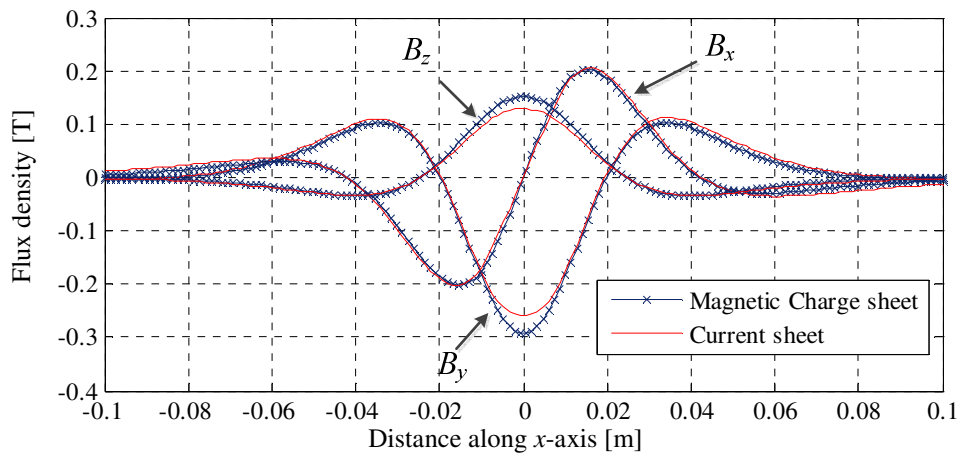


Figure 3.9. Source magnetic flux density comparison between current sheet approach and magnetic charge method for $(y, z) = (-9.5, 20)$ mm from the center of the rotor

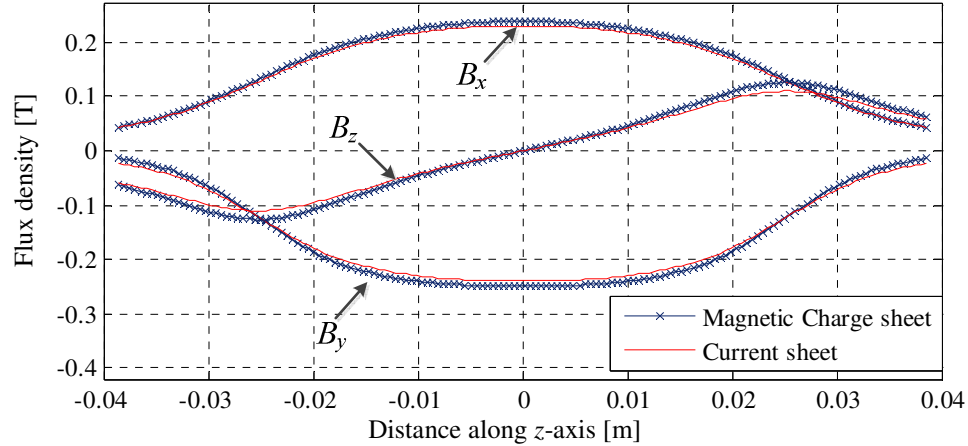


Figure 3.10. Source magnetic flux density comparison between current sheet approach and magnetic charge method for $(x, y) = (10, -9.5)$ mm from the center of the rotor

Using the parameters given in Table 3.5, the force comparison between the $\mathbf{A}\text{-}\phi$ steady state model using current sheet [75] and developed transient model is shown in Figure 3.12. In the comparison, only the steady state values from the transient simulation have been compared with the steady state model results which is illustrated in Figure 3.11.

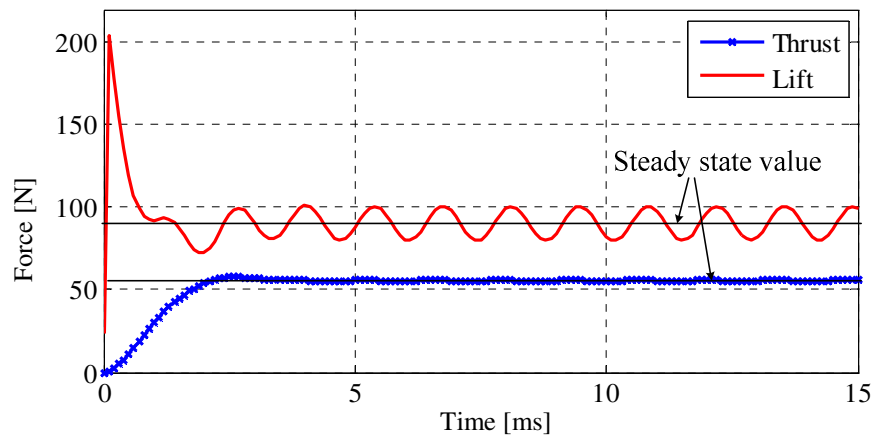


Figure 3.11. Thrust and lift force plot vs. time obtained using the developed 3-D finite element transient model for 15ms^{-1} translational velocity and 14ms^{-1} slip speed.

It is seen that for negative slip speeds the x -directional force is the drag force (which creates braking on the rotor) and for positive slip speeds it becomes a thrust force (moves the source forward). Figure 3.13 shows the power loss comparison between the two models. An excellent match of results is obtained.

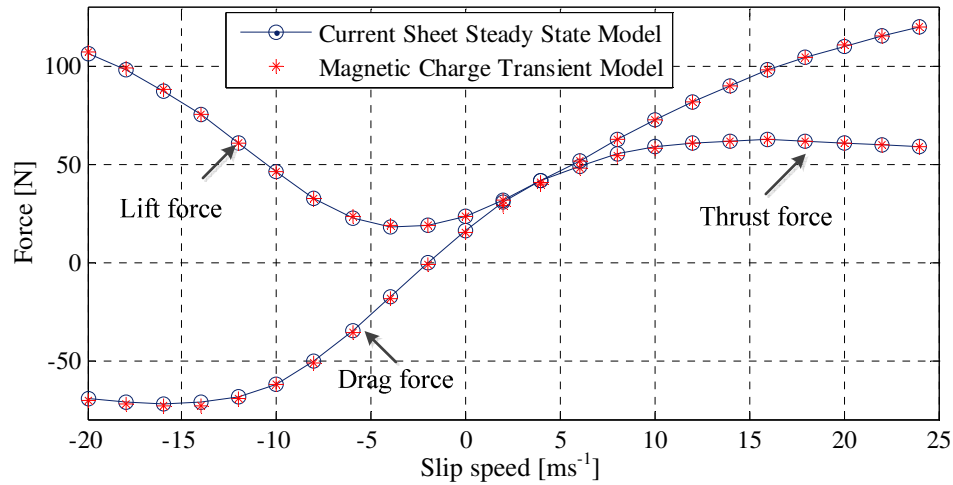


Figure 3.12. Thrust and lift force comparison between 3-D boundary coupled $\mathbf{A}\text{-}\varphi$ transient model based on magnetic charge sheet and steady state model based on current sheet for 15ms^{-1} translational velocity. The magnetic rotor is located at the center of the conductive plate.

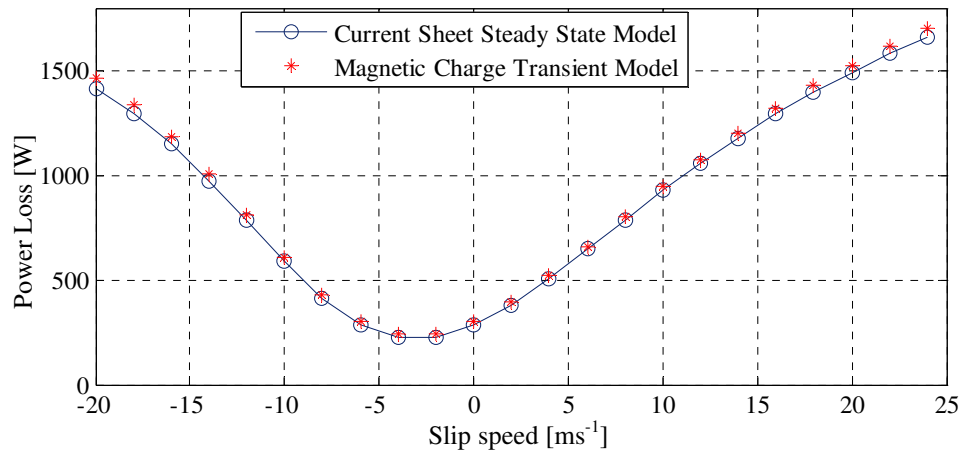


Figure 3.13. Power loss comparison between three-dimensional boundary coupled $\mathbf{A}\text{-}\varphi$ transient model based on magnetic charge sheet and steady state model based on current sheet for 15ms^{-1} translational velocity. The magnetic rotor is located at the center of the conductive plate. Both the models are written in Matlab and Comsol v3.5a

3.4. Steady State Modeling

3.4.1. Governing Equation Formulation

The steady state model satisfies the same governing equations for the subdomains and boundaries as the transient counterpart with the only exception being the absence of time-dependent terms from the subdomain equation.

If the rotor's angular electrical frequency is ω_e [rads⁻¹], at steady state the vector potential in the conductive plate can be written as

$$\mathbf{A}(x, y, z, t) = \mathbf{A}(x, y, z) e^{j\omega_e t} \quad (3.58)$$

Substituting (3.58) into (3.29), the governing equation for subdomain Ω_c in steady state condition becomes

$$-\int_{\Omega_c} \nabla N_n \cdot \nabla A_n d\Omega_c - \mu_0 \sigma \int_{\Omega_c} N_n \left(v_x \frac{\partial A_n}{\partial x} + j\omega_e A_n \right) d\Omega_c = 0, \quad n = x, y, z \quad (3.59)$$

and the boundary conditions are given by (3.46)-(3.48). The subdomain equations and boundary conditions are given by (3.33). Additionally (3.49) is satisfied on Γ_o . Also for translational motion simulation the conductive region vector potential must satisfy (3.50) on Γ_2 .

3.4.2. Meshing and Solver Settings

The mesh size is kept the same as the transient simulation and given by Table 3.1. For the solver, stationary GMRES was chosen along with SSOR preconditioner.

3.4.3. Model Validation

The z -component magnetic vector potential field in the conductive plate and x -component induced eddy current obtained from the developed steady state FEA model are shown in Figure 3.14 and Figure 3.15 respectively.

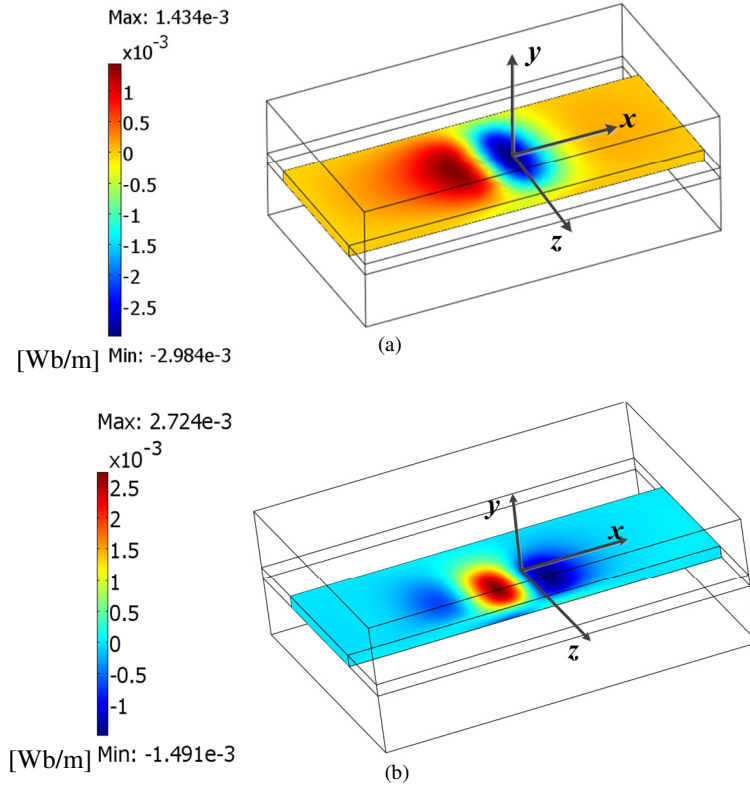


Figure 3.14. The A_z magnetic vector potential field due to the induced eddy current in the conductive plate region is shown for 20ms^{-1} translational velocity and 20ms^{-1} slip speed. The magnetic rotor is (a) located at the center of the conductive plate and (b) shifted from the center of the conductive plate by 20mm. The model is written in Matlab and Comsol v3.5a.

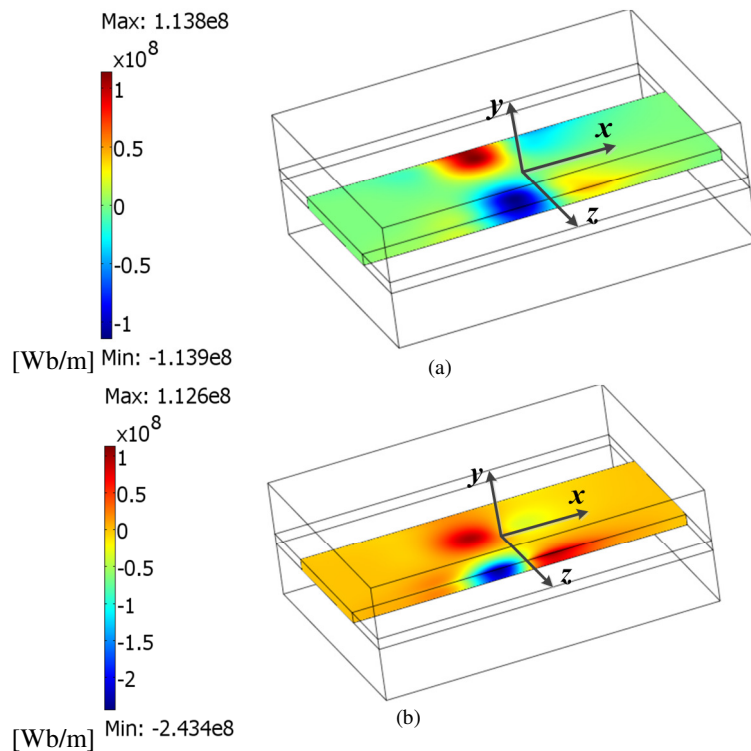


Figure 3.15. The J_x induced eddy current in the conductive plate region is shown for 20ms^{-1} translational velocity and 20ms^{-1} slip speed. The magnetic rotor is (a) located at the center of the conductive plate and (b) shifted from the center of the conductive plate by 20mm.

Figure 3.16 and Figure 3.17 illustrate the A_y field in the plate. It is evident that it is very small and only significant near the edges of the plate.

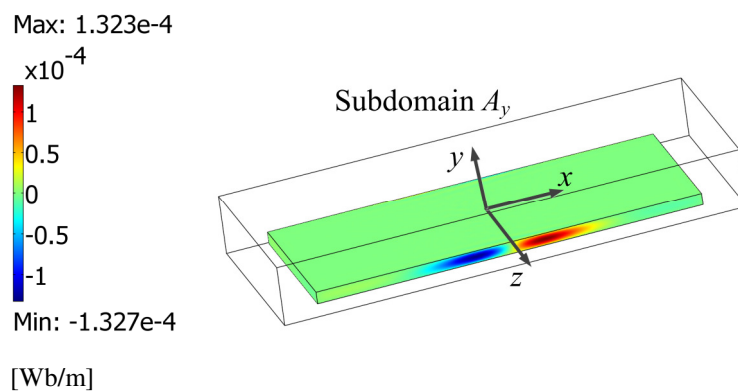


Figure 3.16. The FEA calculated A_y magnetic vector potential field in the conductive plate is shown when the rotor is at the center of the plate.

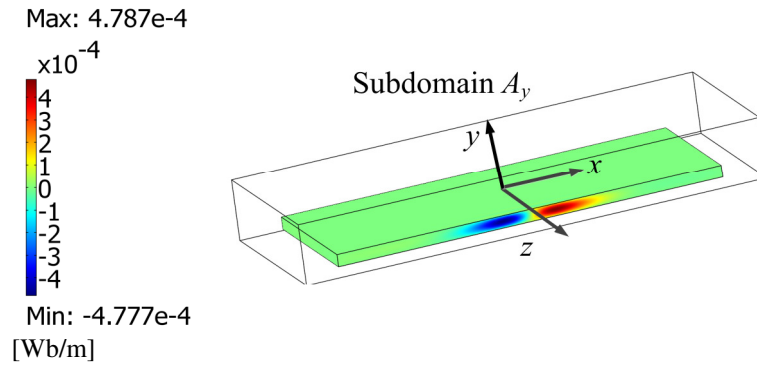


Figure 3.17. The FEA calculated A_y magnetic vector potential field in the conductive plate is shown when the rotor is shifted from the center by 20mm along the z -axis.

Like the transient model, the developed steady state FEA model is formulated using Comsol. For validation purposes, a segmented Halbach rotor has been used as the source. The steady state model was validated by comparing it with the JMAG and Magsoft flux 3-D transient model when there is no translational motion and also with a previously developed steady state model [75] in the presence of translational motion of the source.

3.4.3.1. Comparison with Commercial Transient 3-D Finite Element Model (Zero Translational Velocity)

Using the parameters given in Table 3.2, the presented steady state model was compared with the final steady state results from the JMAG and Magsoft flux transient FEA models. The force comparison is shown in Figure 3.18. Figure 3.19 shows the power loss comparison for a rotor lateral offset of 10 and 25mm.

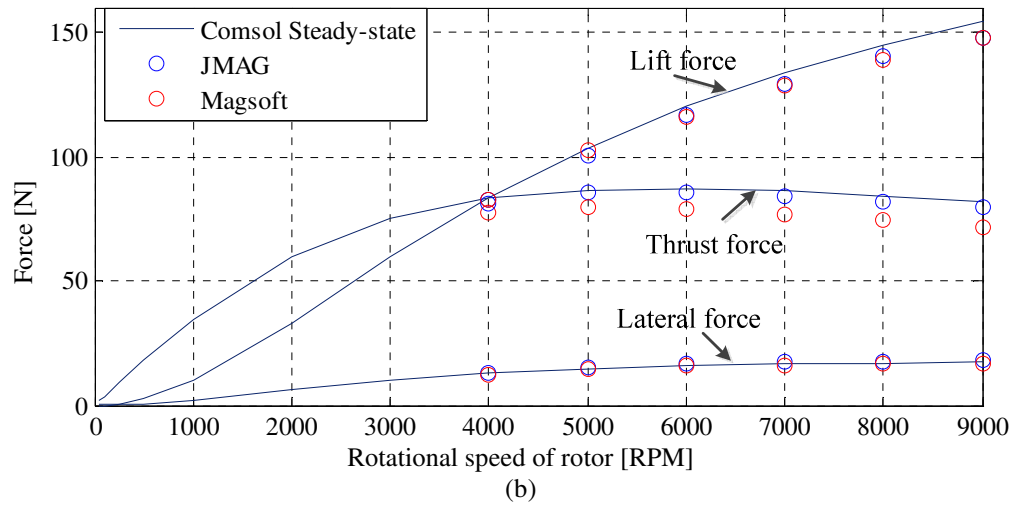
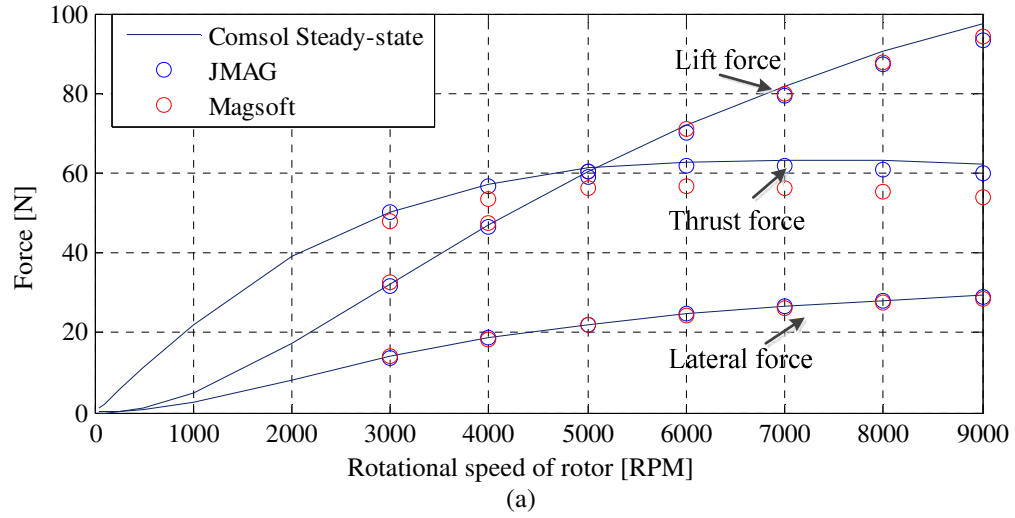


Figure 3.18. Thrust, Lift and lateral force comparison for zero translational velocity among Comsol finite element model and commercial JMAG and Magsoft flux 3-D finite element models when (a) the lateral offset of the rotor is 25mm and (b) the lateral offset is 10mm.

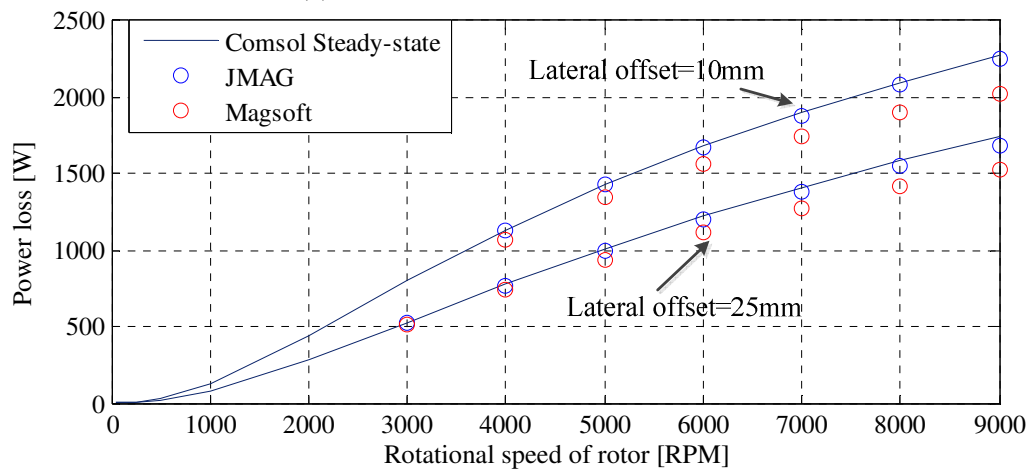


Figure 3.19. Power loss comparison for zero translational velocity among Comsol finite element model and commercial JMAG and Magsoft flux 3-D finite element models for different lateral offset values

The accuracy of the developed Comsol based FEA steady state model has been calculated with respect to the JMAG and Magsoft transient models for thrust, lift, lateral force and joule loss at lateral offset value of 10mm and shown in Table 3.6.

Table 3.6 : Accuracy of the developed Comsol based steady state FEA model

Force	Error with JMAG transient [%]	Error with Magsoft transient [%]
Thrust	2.36	9.65
Lift	5.4	4.87
Lateral	0.1	1
Power loss	3.48	1.84

3.4.3.2. Comparison with 3-D Finite Element Steady State Model (Non-Zero Translational Velocity)

The force and power loss comparisons between the developed magnetic charge based steady state model and previously developed current sheet based steady state model [75] are shown in Figure 3.20 and Figure 3.21 respectively for 25mm lateral offset of the rotor and 15ms^{-1} translational velocity. The parameters used are listed in Table 3.5.

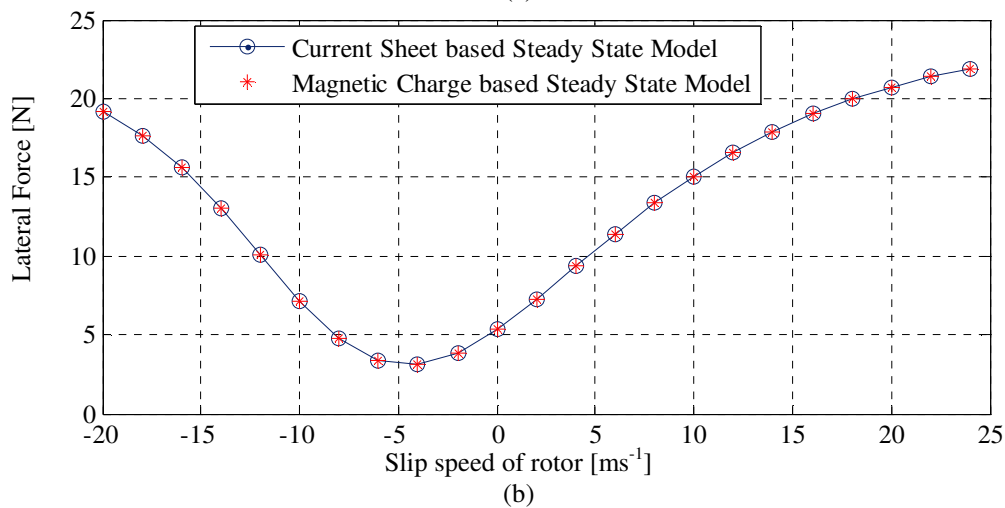
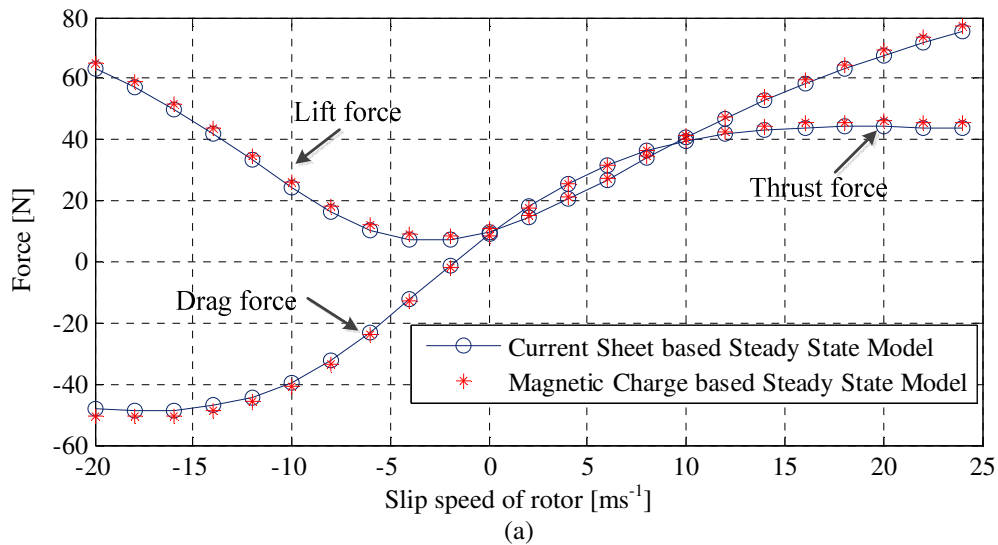


Figure 3.20. (a) Thrust/drag and lift force, (b) lateral force comparison for 15ms^{-1} translational velocity and 25mm lateral offset between magnetic charge and current sheet models.

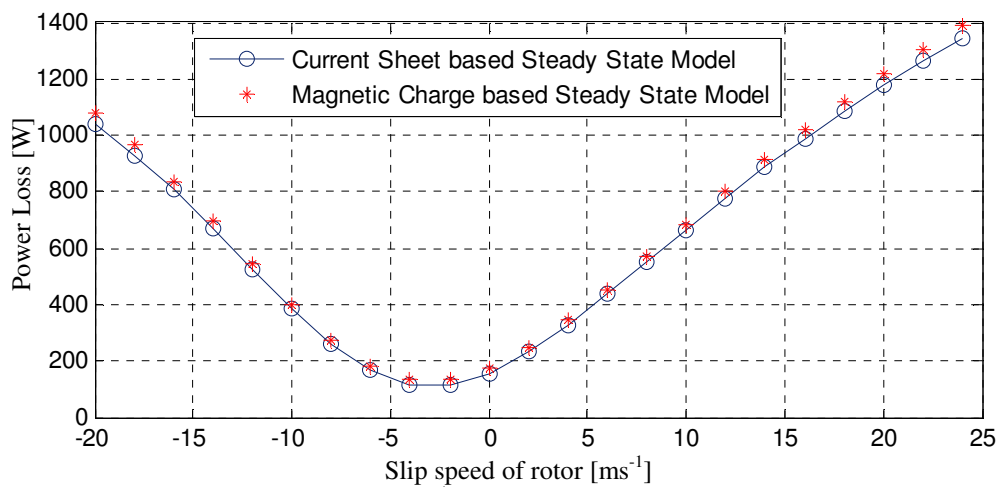


Figure 3.21. power loss comparison for 15ms^{-1} translational velocity and 25mm lateral offset

Table 3.7 shows a comparison of the computation time taken by the current sheet and magnetic charge based steady state models to simulate one slip speed of Figure 3.20 and Figure 3.21. It is seen that charge sheet based approach is almost 4 times faster. This is due to the fact that source modeling technique using charge sheet is much faster than the current sheet approach.

Table 3.7 : Computation time comparison between Magnetic charge and Current sheet based steady state finite element models

Model type	Calculation time
Magnetic charge based steady state model	1 min 40 s
Current sheet based steady state model [75]	8 min

3.5. Summary

This chapter has presented 3-D transient and steady state finite element models to simulate the forces acting on a magnetic source when it is rotating and/or translationally moving above a conductive plate. A brief summary of the developed FEA transient and steady state models is presented in Table 3.8. The presented model was validated by comparing it with standard finite element software (JMAG and Magsoft Flux) and already existing Comsol steady state model for zero and non-zero translational velocity respectively. Overall very good performance of the presented finite element models has been achieved.

Table 3.8 : Summary of the presented FEA transient and steady state models

Model assumptions	Model characteristics
<ul style="list-style-type: none"> • Conductive plate is linear, simply connected and homogenous • Conductive plate has constant conductivity and is non-magnetic • The source has uniform motion • Frequency is low 	<ul style="list-style-type: none"> • Does not physically model the magnetic source; instead applies the source field in boundary conditions which leads to reduced simulation time • Can be applicable for any magnetic source • Computes the source field using magnetic charge sheet which helps reduce the simulation time • Models translational as well as rotational motion of the source • Model has been developed in Comsol v3.5a.

CHAPTER 4 : A BRIEF SURVEY OF ANALYTIC EDDY CURRENT MODELING IN THREE DIMENSION

4.1. Introduction

When a magnetic source moves in the vicinity of a conductive material, time varying magnetic fields induce eddy currents in the conductor which in turn interacts with the source magnetic field to create velocity dependent drag or thrust force and/or lift force. In magnetic levitated vehicles (maglev) the thrust and lift force are utilized while the drag force is an impairing factor [13, 74, 75]. But the later can be utilized in applications like eddy current damping [86-88, 144] and braking [89-91, 145-147]. Also eddy current interaction with conductive material is utilized in eddy current testing (ECT) to detect flaws or cracks in the conductive material [83, 84, 117, 118, 148-152]. In ECT a probe coil is moved over the conductor. In the presence of any crack in the conductor, the impedance of the eddy current path changes due to discontinuity in the conductivity. This change is measured by the probe coil.

Finite element analysis (FEA) methods have been a hugely successful tool for analyzing eddy current distributions in conductive medium. An enormous amount of research has been conducted in this field in the past. The beauty of FEA is its ability to accurately model field distribution in simply connected [136, 153-158] or multiply connected conductor [140, 159-164] of complicated geometry with constant or varying conductivity. However analytic modeling techniques are more appealing because of their

computational efficiency compared to FEA. There is a considerable amount of publications on the 3-D analytic modeling of eddy currents in linear conductive medium. Hence it is considered appropriate to devote a chapter to study the existing analytical modeling techniques in order to fully appreciate the need for further research contributions in this field.

In the next section a brief survey will be presented and in section 4.3 the need for new methods will be discussed.

4.2. Review of Existing 3-D Analytical Methods

Depending on the geometry of the conductive medium the existing analytical methods can be categorized into two main groups: models for conductive half-space and conductive domain with finite dimensions.

4.2.1. Conductive Half-Space

The induced eddy current distribution in a conductive half-space due to a current carrying coil has been studied extensively [165-176]. The magnetic scalar potential cannot be used inside the conductor due to the presence of current and therefore the magnetic vector potential (MVP) has been mainly used to formulate the fields which is defined as

$$\mathbf{B} = \nabla \times \mathbf{A} \quad (3.6)$$

The governing equations are

$$\nabla^2 \mathbf{A} = 0, \text{ in nonconductive region} \quad (3.60)$$

$$\nabla^2 \mathbf{A} = \mu\sigma \frac{\partial \mathbf{A}}{\partial t}, \text{ in conductive region} \quad (3.61)$$

where μ , σ are the permeability and conductivity of the conductive medium.

Hammond [177] calculated the eddy current field in a conductive medium due to the presence of a circular current loop, as shown in Figure 4.1, using magnetic vector potential in the conductive and nonconductive current free regions.

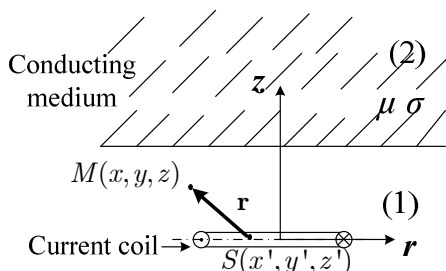


Figure 4.1. Circular current coil parallel to conductive half-space [177]

Dodd and Deeds in their classic work extended the ideas of Hammond by calculating the induced eddy current field in a two-conductor rod [166] and layers of conductive media [178] due to a circular coil of rectangular cross section. Like the work by Hammond, due to the axisymmetric nature of the coil, the cylindrical coordinate system was used and hence the obtained field solution was in terms of Bessel functions.

Hannakam [165] calculated the force on two parallel wires carrying current in opposite directions near a very thin conductor. Later Reitz [167] extended the work done by Hannakam by calculating the forces on magnetic monopole, dipole and rectangular current coil when they move near a conductor using the magnetic vector potential in cartesian coordinate system. Hannakam [165] and Reitz [167] assumed the conductive plate thickness to be smaller than the skin depth for the dominant frequencies in the excitation field. With this assumption, the eddy current variation along the thickness of the plate was neglected. Beissner and Sablik generalized the work by Dodd and Deeds [166] to model the eddy current in a conductive half-space due to a nonsymmetric coil [168]. The eddy current distribution in a conductive plate of finite thickness was modeled due to moving rectangular current filament [169], circular current loop [179] and also

elliptic current excitation [171] while Rao [170] used a perturbation technique to study the field induced due to a moving current filament above a conductor with finite thickness using a power series approach.

In the models discussed above, the total magnetic vector potential in the nonconductive region, for example in region 1 of Figure 4.1, is composed of the potential due to induced eddy current in the conductor and due to the current coil. But deriving the latter can be complicated and time consuming procedure depending on the coil geometry as one needs to apply the Ampere's current law on the coil to derive the magnetic vector potential [112, 168, 170, 177, 178] as given by

$$A_i(x, y, z) = \frac{\mu}{4\pi} \int J_i(x', y', z') \frac{1}{r} dv \quad (3.62)$$

where A_i and J_i are respectively the i -th component of the magnetic vector potential and source current in the coil respectively and

$$r = \sqrt{(x - x')^2 + (y - y')^2 + (z - z')^2} \quad (3.63)$$

is the distance between the current element (S) and point of observation (M) as shown in Figure 4.1. In (3.62) integration is performed over the entire distribution of source current.

However, the derivation of the magnetic vector potential of the source field can be avoided for simple geometrical shape of the exciter. Panas [169, 171] applied the source current field only in the interface boundary conditions for rectangular and elliptic current excitation.

In addition to the magnetic vector potential, the second order vector potential (SOVP) has also been successfully used to solve problems in the cylindrical [180], spherical [181]

and cartesian [182] coordinate systems. Since \mathbf{A} field is solenoidal (due to Coulomb gauge given by (3.22)), the SOVP, which is denoted as \mathbf{W} , can be defined as [182, 183]

$$\mathbf{A} = \nabla \times \mathbf{W} \quad (3.64)$$

where \mathbf{W} can be decomposed into two scalar potentials, one transverse to the electric field and called as transverse electric (TE) potential and another transverse to the magnetic field and called as transverse magnetic (TM) potential as follows [141, 173, 182-184]

$$\mathbf{W} = \hat{n}W_a + \hat{n} \times \nabla W_b \quad (3.65)$$

where \hat{n} is the unit vector along any of the three directions of 3-D space, W_a is the TE potential and W_b is the TM potential. Hence, in the SOVP approach only two components need to be solved instead of three components in the magnetic vector potential approach. That reduces computational complexity and computation time. The choice of \hat{n} depends on the application. For example, in the study of eddy current fields in a planar conductive half-space [182], as shown in Figure 4.2, \hat{n} is chosen to be a unit vector along the z -direction. This choice was due to the fact that in a conductive half-space eddy current flows parallel to the plane at $z=0$ irrespective of the position and shape of the inducing coil [141, 171, 182, 185]. Hence this selection of \hat{n} eliminates the need for TM potential, W_b . The entire problem can then be formulated only in terms of a single scalar potential, W_a [182].

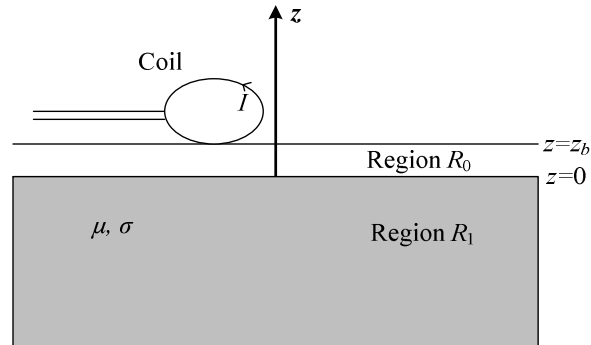


Figure 4.2. Circular current coil of arbitrary shape above a conductive half-space [182]

The magnetic flux density, \mathbf{B} , has also been used to model the eddy current induced in a conductive medium due to different excitation types [150, 186, 187]. Sadhegai and Salemi [185, 188] generalized the field modeling technique using the magnetic field intensity as they stated that the source field is required to be known only at the air-conductor interface in the absence of the latter to find eddy current distribution inside the conductive medium. For example, in Figure 4.3 the source field is required to be known only at the $z=0$ plane in the absence of the plate. The source field is then included in the boundary conditions satisfying the continuity of the normal component of the magnetic flux density and tangential component of the magnetic field intensity. Sadhegai and Salemi considered straight current wire, solenoid exciter, elliptic loop exciter to validate their model [185, 188].

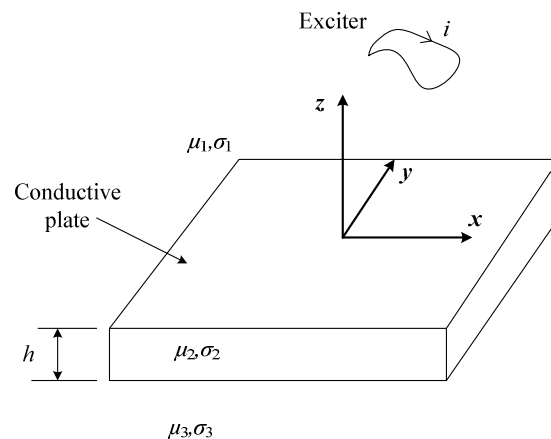


Figure 4.3. Circular current coil of arbitrary shape above a conductive medium of finite thickness [185]

4.2.2. Conductive Domain with Finite Dimensions

The conductive half-space modeling techniques can be applicable when the conductor plate is large enough for the field to decay at its boundaries. Otherwise finite domain length has to be considered as the presence of domain boundary restricts eddy current path and modifies the field inside the conductive region. Field analysis in a finite width conductive medium is of immense interest for magnetic levitation [13, 74, 75, 189, 190]. Also in eddy current testing, the cracks can often occur near the edges of a conductive plate, therefore consideration of the edge effect of such a plate is essential for eddy current testing [118, 149]. In all these applications the models outlined in the last section will fail to model the eddy current distribution due to the assumption of infinite domain length.

Urankar [191] presented a semi-analytic integral solution for the force acting on a conductive medium of arbitrary shape and finite width using the magnetic vector potential. However, in order to compute the force the integral equations need to be evaluated over the conductive domain as well as the exciter domain. This does not seem to be a computationally efficient approach.

The eddy current distribution due to the edge effect of a finite width conductive plate or conductive plate with a hole has been considered using second order vector potential [117, 118, 149, 151, 192] and magnetic vector potential [148]. In these publications, the modal solutions to eddy current problems in conductive regions of the finite dimension was achieved by truncating the originally infinite problem domain using appropriate boundary condition on the truncation boundaries. This method is known as the truncated region eigenfunction expansion (TREE) [141]. The main challenge in this approach is the

numerical computation of the complex valued eigenvalues for the conductive region [192]. Although the recent publications using TREE approach considered the finite width of the plate with hole/ crack for impedance variation calculation, it has not considered finite thickness plate for force calculation [117, 148, 192].

Recently Pluk *et al.* [144] used a mirroring technique [193, 194] to consider the finite length and width of the conductive plate and provided a semi-analytic solution for the induced current density. Also the authors calculated the damping force using numerical integration.

4.3. Need for New Method

In this dissertation a computationally efficient analytic method is sought that is capable of calculating the induced field in a conductive plate of finite thickness and width due to the presence of an arbitrary magnetic source. The computation time should be as small as possible in order to offer the potential for real time computing. Hence the present challenge is to, first, find a general source field modeling technique which does not depend on the geometry of the source; second, take into account the finite thickness and width of the conductive plate and third, make the method computationally fast.

Out of the discussed methods in this chapter, the one presented by Sadhegi and Salemi [185, 188] helps one generalize the source field, but this method does not take into account the finite width of the plate. Also the proposed method used the magnetic field intensity which requires one to solve for nine unknowns in the conductive region. On the other hand, Panas and Kriezis [169] provided a decoupled set of equations for the magnetic vector potential leading to an easier computation but did not consider the finite

domain length. A new method thus calls for the combination of the previous two. This idea will be investigated in chapter 6.

Also the research completed by Theodoulidis and Kriezis [182] will be generalized for any magnetic source using SOVP in the conductive and nonconductive regions in chapter 5.

In chapter 7 the TREE formulation using the second order vector potential will be applied to a conductive plate of finite thickness to include its edge effect. Computation time for different modeling approaches will be discussed.

4.4. Conclusion

A brief survey of the analytic modeling techniques was presented in this chapter. As the determination of the quasi-static electromagnetic field of a magnetic source, especially current coil, in the presence of an electrical conductor is well researched topic in the literature, the brief survey would avoid any duplication of the previous work and also would guide to the right direction in finding new method. Next few chapters will discuss on the new proposed methods.

CHAPTER 5 : 3-D ANALYTIC EDDY CURRENT MODELING FOR A CONDUCTIVE PLATE OF INFINITE DIMENSION

5.1. Introduction

As mentioned in chapter 4, this chapter will discuss eddy current modeling in a large conductive plate due to any magnetic source moving above the plate at any arbitrary position. The second order vector potential (SOVP) will be used to formulate the conductive and nonconductive regions. This, in some sense, will provide a generalization of the work presented by Theodoulidis and Kriezis [182] who computed induced field distributions due to a current coil of arbitrary shape. In dynamic simulation the magnetic source may have vertical oscillatory motion under the influence of lift force and its own weight. Therefore in order to study dynamic behavior of such a magnetic source moving above a conductive plate, one should incorporate the vertical and lateral motion along with the principle velocity of the source. Not many authors have included vertical and lateral motion in studying dynamics. There are few exceptions like Rodgers considered the heave motion in 2-D analytic and finite element model to study dynamic performance of a linear induction machine in steady state condition [195]. Paudel *et al.* modeled the heave velocity in steady state model to study magnetic stiffness and damping characteristics of a magnetic levitated vehicle [81, 82]. In [150] Itaya *et al.* the authors studied the effect of forward and lateral motion of the magnetic source on the induced eddy current density in a conductive plate.

In this chapter, forces acting on the magnetic source will be computed using two different approaches: Maxwell's stress tensor and magnetic charge. It will be shown that both methods produce the same result, as expected. Also the torque acting on the source and power loss in the conductive plate will be computed. The results will be compared against a previously developed finite element steady state model using magnetic charge, discussed in chapter 3, and also current sheet based steady state finite element model [75].

The rest of the chapter is arranged as follows: section 5.2 describes the governing equations for all the problem regions outlined above. Section 5.3 describes the boundary conditions which will be followed by the derivation of general solutions in section 5.4. Section 5.5 will talk about the source field modeling; solutions for the electromagnetic fields will be provided in section 5.6; electromagnetic forces will be computed using Maxwell's stress tensor and magnetic charge approach in section 5.7 which will be followed by total power transfer, electromagnetic torque and power loss calculations in sections 5.8, 5.9 and 5.10 respectively; electromagnetic stiffness and damping constants will be calculated in section 5.11 and 5.12 respectively; model validation will be performed in section 5.13; stiffness and damping characteristics will be discussed in 5.14 and a brief summary of this chapter will be provided in section 5.15.

5.2. Governing Equation Formulation

Consider an application of maglev transportation [13, 74, 75] where a magnetic rotor is moved above a conductive plate, as shown in Figure 5.1. The linear motion of the center of mass of the rotor due to its rotational motion is v_c .

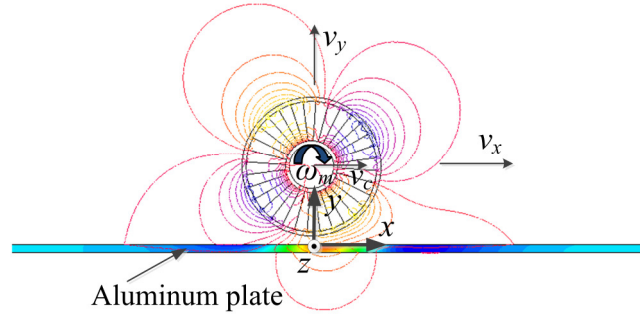


Figure 5.1. The x - y view of a 2 pole pair Halbach rotor moving and rotating over a conductive aluminum plate. The figure shows isoline plot of the radial component magnetic flux density in air region and isosurface plot of the current density in the conductive plate. The model was created in Magsoft flux 3-D..

The schematic of the problem region is shown in Figure 5.2 with the source located at height g above the conductive plate surface with l , w and h being the length, width and thickness of the conductive plate. Also the source velocities in x , y and z -directions as well as mechanical angular velocity ω_m are shown in the figure. It must be noted here that although the schematic of Figure 5.2 displays a magnetic rotor as the source, the proposed analytic model is applicable to any kind of magnetic source.

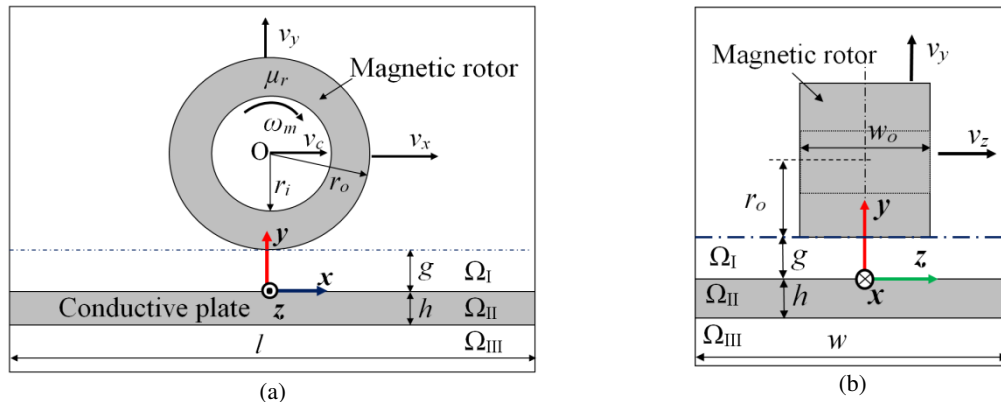


Figure 5.2. The (a) x - y and (b) z - y view of the problem region with magnetic source located at height g above the conductive plate surface.

The assumptions of this analytic model are listed below:

- The plate has infinitely large width, w , and length, l .
- The plate has finite thickness, h .
- The plate is continuous with constant conductivity and non-magnetic.
- The plate is linear and homogenous.

- The magnetic source has translational, heave and lateral motion along with rotational motion.
- The frequency is sufficiently low in order for the quasi-static approximation to be valid. Precisely, the wavelength in the free-space is assumed to be large compared to the dimension of the plate and magnetic source, which is always true for maglev applications.

The conductive medium is located at $y=0$ of the Cartesian coordinate system which creates three regions as shown in Figure 5.2:

- Region I (Ω_I) is the air or nonconductive region between the magnetic source and conductive plate located at $0 \leq y \leq g$
- Region II (Ω_{II}) is the conductive region located at $-h \leq y \leq 0$
- Region III (Ω_{III}) is the air or nonconductive region below the conductive plate located at $y \leq -h$.

5.2.1. Conductive Region (Ω_{II})

In the presence of the eddy current in the conductive region, the magnetic vector potential is an obvious choice for modeling the region. However this analytic approach requires one to solve for three unknowns in the conductive region. Instead a formulation using the second order vector potential (SOVP) reduces the number of unknowns by one. Therefore, SOVP has been utilized in the proposed analytic model which is denoted as \mathbf{W} and defined as [141, 182, 183]

$$\mathbf{A} = \nabla \times \mathbf{W} \quad (3.64)$$

where \mathbf{A} is the magnetic vector potential. As discussed in chapter 4, \mathbf{W} can be split into TE and TM potentials with y preferred direction as follows [117, 141, 182-184, 196]

$$\mathbf{W} = \hat{y}W_a + \hat{y} \times \nabla W_b \quad (5.1)$$

Here \hat{y} is the unit vector along the y -direction while W_a and W_b are the TE and TM potential respectively. In this chapter a steady state solution for the scalar TE and TM potentials is assumed as given by [74, 79]

$$W_i(x, y, z, t) = W_i^{\text{II}}(x, y, z)e^{-j\omega_e t}, \quad i = a, b \quad (5.2)$$

where ω_e is the electrical angular frequency of the source in rads^{-1} . ω_e can be due to excitation current frequency or the angular speed of the rotor. A clockwise rotation of the rotor, ω_m , induces a linear motion, v_c , at its center of mass in the positive x -direction as shown in Figure 5.1 and Figure 5.2. However, as in this dissertation the rotor is assumed fixed in space and plate in movable state, the positive clockwise rotational motion of the rotor can be simulated by inducing a linear motion in the plate in the negative x -direction. As a result, the exponential term of the TE potential given by (5.2) is taken as negative. In (5.2) superscript 'II' indicates region II. The governing equation of the conductive region in terms of the magnetic vector potential has already been derived in chapter 3 and rewritten below for convenience

$$\nabla^2 \mathbf{A} = \mu_0 \sigma \left(\frac{\partial \mathbf{A}}{\partial t} - v_x \frac{\partial \mathbf{A}}{\partial x} - v_y \frac{\partial \mathbf{A}}{\partial y} - v_z \frac{\partial \mathbf{A}}{\partial z} \right) \quad (3.24)$$

where σ is the conductivity (Sm^{-1}) of the plate and v_x, v_y, v_z are velocity of the rotor in the x, y and z directions respectively (ms^{-1}). Substituting (3.64) into (3.24) gives

$$\nabla^2 (\nabla \times \mathbf{W}) = \mu_0 \sigma \left(\frac{\partial}{\partial t} - v_x \frac{\partial}{\partial x} - v_y \frac{\partial}{\partial y} - v_z \frac{\partial}{\partial z} \right) (\nabla \times \mathbf{W}) \quad (5.3)$$

Substituting (5.1) into (5.3) gives

$$\begin{aligned} \nabla^2 (\nabla \times (\hat{y}W_a + \hat{y} \times \nabla W_b)) = \\ \mu_0\sigma \left(\frac{\partial}{\partial t} - v_x \frac{\partial}{\partial x} - v_y \frac{\partial}{\partial y} - v_z \frac{\partial}{\partial z} \right) (\nabla \times (\hat{y}W_a + \hat{y} \times \nabla W_b)) \end{aligned} \quad (5.4)$$

Rearranging terms yields

$$\begin{aligned} \nabla \times \left[\hat{y} \left(\nabla^2 W_a - \mu_0\sigma \left(\frac{\partial}{\partial t} - v_x \frac{\partial}{\partial x} - v_y \frac{\partial}{\partial y} - v_z \frac{\partial}{\partial z} \right) W_a \right) + \right. \\ \left. \hat{y} \times \nabla \left(\nabla^2 W_b - \mu_0\sigma \left(\frac{\partial}{\partial t} - v_x \frac{\partial}{\partial x} - v_y \frac{\partial}{\partial y} - v_z \frac{\partial}{\partial z} \right) W_b \right) \right] = 0 \end{aligned} \quad (5.5)$$

Equation (5.5) is satisfied if the TE and TM scalar potentials satisfy the following 3-D scalar Helmholtz equation

$$\frac{\partial^2 W_i^\Pi}{\partial x^2} + \frac{\partial^2 W_i^\Pi}{\partial y^2} + \frac{\partial^2 W_i^\Pi}{\partial z^2} = \mu_0\sigma \left(\frac{\partial W_i^\Pi}{\partial t} - v_x \frac{\partial W_i^\Pi}{\partial x} - v_y \frac{\partial W_i^\Pi}{\partial y} - v_z \frac{\partial W_i^\Pi}{\partial z} \right), \quad (5.6)$$

$i = a, b$

Substituting (5.2) into (5.6) yields the governing equation for Ω_Π in steady state

$$\frac{\partial^2 W_i^\Pi}{\partial x^2} + \frac{\partial^2 W_i^\Pi}{\partial y^2} + \frac{\partial^2 W_i^\Pi}{\partial z^2} = -\mu_0\sigma \left(j\omega_e W_i^\Pi + v_x \frac{\partial W_i^\Pi}{\partial x} + v_y \frac{\partial W_i^\Pi}{\partial y} + v_z \frac{\partial W_i^\Pi}{\partial z} \right), \quad (5.7)$$

$i = a, b$

There is a freedom in choosing the unit vector of (5.1). Here it is chosen along the y -direction, but could have been selected along the x or z -direction [141]. But the choice is not only a matter of preference but also a matter of convenience as shall be shown shortly.

Utilizing (3.64) and (5.1) the components of the magnetic vector potential are related to W_a and W_b as follows

$$A_x^\Pi = -\frac{\partial W_a^\Pi}{\partial z} - \frac{\partial^2 W_b^\Pi}{\partial x \partial y} \quad (5.8)$$

$$A_y^{\text{II}} = \frac{\partial^2 W_b^{\text{II}}}{\partial x^2} + \frac{\partial^2 W_b^{\text{II}}}{\partial z^2} \quad (5.9)$$

$$A_z^{\text{II}} = \frac{\partial W_a^{\text{II}}}{\partial x} - \frac{\partial^2 W_b^{\text{II}}}{\partial z \partial y} \quad (5.10)$$

From (5.9) it is noticed that the A_y component is a function of W_b only. This is because the unit vector of (5.1) has been chosen along the y direction. As eddy current flows parallel to top conductive surface at $y=0$ for a large conductive plate [141, 182, 185, 188], the A_y component is zero. As a result, W_b has to be zero. The conductive medium can thus be represented only in terms of W_a . This is illustrated in Figure 5.3.

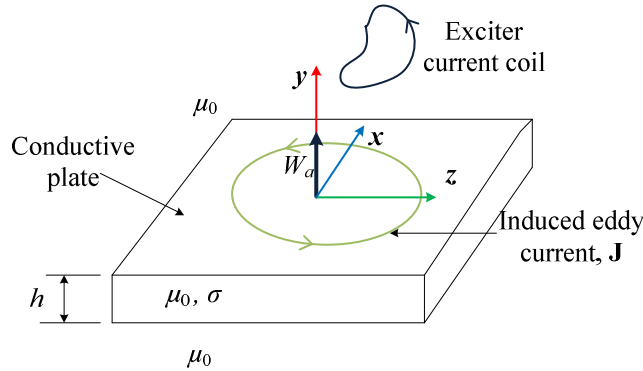


Figure 5.3. Diagram of the induced eddy current and TE potential (W_a) in a conductive plate of infinitely large width and length, but finite thickness.

Noting the relationship between the magnetic flux density and magnetic vector potential [115]

$$\mathbf{B} = \nabla \times \mathbf{A} \quad (3.6)$$

yields

$$\mathbf{B} = \nabla \times \nabla \times \mathbf{W} \quad (5.11)$$

Substituting (5.1) into (5.11) and ignoring W_b , the relationship between the flux density and W_a potential within the conductive region is obtained as follows

$$B_x^{\text{II}} = \frac{\partial^2 W_a^{\text{II}}}{\partial x \partial y} \quad (5.12)$$

$$B_y^{\text{II}} = -\frac{\partial^2 W_a^{\text{II}}}{\partial x^2} - \frac{\partial^2 W_a^{\text{II}}}{\partial z^2} \quad (5.13)$$

Substituting (5.6) into (5.13) B_y^{II} can also be written as

$$B_y^{\text{II}} = \frac{\partial^2 W_a^{\text{II}}}{\partial y^2} + \mu_0 \sigma \left(j\omega_e W_a^{\text{II}} + v_x \frac{\partial W_a^{\text{II}}}{\partial x} + v_y \frac{\partial W_a^{\text{II}}}{\partial y} + v_z \frac{\partial W_a^{\text{II}}}{\partial z} \right) \quad (5.14)$$

and

$$B_z^{\text{II}} = \frac{\partial^2 W_a^{\text{II}}}{\partial z \partial y} \quad (5.15)$$

5.2.2. Nonconductive Regions (Ω_{I} and Ω_{III})

In the nonconductive or air regions, the conductivity term is zero and thus the magnetic flux density equations defined by (5.12), (5.14) and (5.15) are related to W_a by

$$\mathbf{B}^i = \frac{\partial^2 W_a^i}{\partial x \partial y} \hat{x} + \frac{\partial^2 W_a^i}{\partial y^2} \hat{y} + \frac{\partial^2 W_a^i}{\partial z \partial y} \hat{z}, \quad i = \text{I, III} \quad (5.16)$$

which can also be written as

$$\mathbf{B}^i = \nabla \left(\frac{\partial W_a^i}{\partial y} \right), \quad i = \text{I, III} \quad (5.17)$$

The relationship between the magnetic flux density, \mathbf{B} , and magnetic scalar potential, ϕ , is given by [115]

$$\mathbf{B} = -\mu_0 \nabla \phi \quad (2.5)$$

Comparing (5.17) with (2.5) the following can be written relating the magnetic scalar potential, ϕ , with the TE potential, W_a , for air regions I and III

$$\phi^i = -\frac{1}{\mu_0} \frac{\partial W_a^i}{\partial y}, \quad i = \text{I, III} \quad (5.18)$$

In region I, the total TE potential is composed of the source field, $W_a^{I,s}$ and reflected field, $W_a^{I,r}$, due to the induced eddy currents in the region II as given by

$$W_a^I = W_a^{I,s} + W_a^{I,r} \quad (5.19)$$

where $W_a^{I,s}$ and $W_a^{I,r}$ are the potential due to the source and reflected field respectively.

In region III, the total TE potential is the transmitted field due to the induced eddy currents in the conductive region. The source, reflected and transmitted TE potentials within regions I, II and III are illustrated in Figure 5.4.

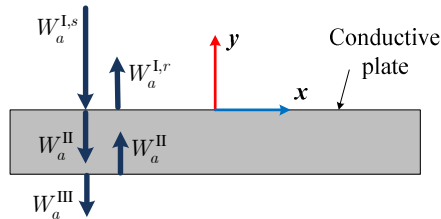


Figure 5.4. Diagram illustrating the source, reflected and transmitted TE potentials.

As the conductivity is zero in the nonconductive regions, from (5.7) the TE potentials are seen to satisfy the following Laplace's equations in regions I and III [117, 118, 141]

$$\nabla^2 W_a^{I,s} = 0 \quad (5.20)$$

$$\nabla^2 W_a^{I,r} = 0 \quad (5.21)$$

$$\nabla^2 W_a^{III} = 0 \quad (5.22)$$

5.3. Boundary Conditions

The continuity of the tangential components of the magnetic field intensity and normal component of the magnetic flux density must be satisfied across the interface $y=0$ and $y=-h$. As the relative permeability of the conductive medium is unity, the boundary conditions are

$$B_x^{I,s} + B_x^{I,r} = B_x^{II}, \text{ at } y = 0 \quad (5.23)$$

$$B_y^{I,s} + B_y^{I,r} = B_y^{II}, \text{ at } y = 0 \quad (5.24)$$

$$B_z^{I,s} + B_z^{I,r} = B_z^{II}, \text{ at } y = 0 \quad (5.25)$$

$$B_x^{II} = B_x^{III,t}, \text{ at } y = -h \quad (5.26)$$

$$B_y^{II} = B_y^{III,t}, \text{ at } y = -h \quad (5.27)$$

$$B_z^{II} = B_z^{III,t}, \text{ at } y = -h \quad (5.28)$$

However, it is found that (5.23) - (5.28) hold true if the continuity of the TE potential and its normal derivative is satisfied across the interface or saying mathematically [181]

$$W_a^{I,s} + W_a^{I,r} = W_a^{II}, \text{ at } y = 0 \quad (5.29)$$

$$\frac{\partial W_a^{I,s}}{\partial y} + \frac{\partial W_a^{I,r}}{\partial y} = \frac{\partial W_a^{II}}{\partial y}, \text{ at } y = 0 \quad (5.30)$$

$$W_a^{II} = W_a^{III}, \text{ at } y = -h \quad (5.31)$$

$$\frac{\partial W_a^{II}}{\partial y} = \frac{\partial W_a^{III}}{\partial y}, \text{ at } y = -h \quad (5.32)$$

Thus instead of solving six boundary conditions (5.23) - (5.28), only four (5.29) - (5.32) are required at the air-conductor interfaces in the SOVP model.

In addition, at the domain outer boundaries, as shown in Figure 5.2, at $x = \pm l / 2$ and $z = \pm w / 2$ the Dirichlet boundary condition is satisfied i.e. all the scalar TE potentials are set to zero at these boundaries.

5.4. Derivation of General Solutions

5.4.1. Conductive Region (Ω_{II})

Using the separation of variables method [132], the TE potential in Ω_{II} can be written as

$$W_a^{II}(x, y, z) = X(x)Y(y)Z(z) \quad (5.33)$$

Substituting (5.33) into (5.6) and dividing both sides by $X(x)Y(y)Z(z)$ (assuming they are non-zero functions of spatial variables) yields

$$\frac{X''}{X} + \frac{Y''}{Y} + \frac{Z''}{Z} = -\mu_0\sigma \left(j\omega_e + v_x \frac{X'}{X} + v_y \frac{Y'}{Y} + v_z \frac{Z'}{Z} \right) \quad (5.34)$$

where the superscript prime indicates differentiation.

Let,
$$X(x) = e^{j\xi_m x} \quad (5.35)$$

and
$$Z(z) = e^{jk_n z} \quad (5.36)$$

where the spatial frequencies are defined as

$$\xi_m = \frac{2\pi m}{l}, \quad -\infty \leq m \leq \infty \quad (5.37)$$

$$k_n = \frac{2\pi n}{w}, \quad -\infty \leq n \leq \infty \quad (5.38)$$

Here it is assumed that l and w are large enough to decay the TE potential to zero at $x = \pm l / 2$ and $z = \pm w / 2$. Hence, complex Fourier series has been used to represent the x and z dependency in (5.35) and (5.36) instead of sine series. Substituting (5.35) and (5.36) into (5.34) gives for all m, n

$$-\xi_m^2 + \frac{Y''}{Y} - k_n^2 = -\mu_0\sigma \left(j\omega_e + jv_x\xi_m + jv_zk_n + v_y \frac{Y'}{Y} \right) \quad (5.39)$$

$$\text{or,} \quad \frac{Y''}{Y} + \mu_0\sigma v_y \frac{Y'}{Y} - \left(\xi_m^2 + k_n^2 - j\mu_0\sigma(\omega_e + v_x\xi_m + v_zk_n) \right) = 0 \quad (5.40)$$

$$\text{or,} \quad \frac{Y''}{Y} + \mu_0\sigma v_y \frac{Y'}{Y} - \gamma_{mn}^2 = 0 \quad (5.41)$$

where

$$\gamma_{mn}^2 = \xi_m^2 + k_n^2 - j\mu_0\sigma(\omega_e + v_x\xi_m + v_zk_n) \quad (5.42)$$

The roots of (5.41) are

$$\alpha_{mn} = 0.5(-\mu_0\sigma v_y + \sqrt{(\mu_0\sigma v_y)^2 + 4\gamma_{mn}^2}) \quad (5.43)$$

$$\beta_{mn} = 0.5(-\mu_0\sigma v_y - \sqrt{(\mu_0\sigma v_y)^2 + 4\gamma_{mn}^2}) \quad (5.44)$$

Hence the general solution for $Y(y)$ is

$$Y(y) = C_{mn}^{\text{II}} e^{\alpha_{mn}y} + D_{mn}^{\text{II}} e^{\beta_{mn}y} \quad (5.45)$$

Substituting (5.35), (5.36) and (5.45) into (5.33) the general solution for the W_a potential within the conductive region is obtained as

$$W_a^{\text{II}}(x, y, z) = \sum_{m=-M}^M \sum_{n=-N}^N e^{j\xi_m x} e^{jk_n z} \left(C_{mn}^{\text{II}} e^{\alpha_{mn}y} + D_{mn}^{\text{II}} e^{\beta_{mn}y} \right), \quad -h \leq y \leq 0 \quad (5.46)$$

The Fourier series is assumed to have M and N harmonics in the x and z directions respectively. The error introduced by this series truncation can be minimized by increasing the number of harmonics. C_{mn}^{II} and D_{mn}^{II} are unknowns and will be determined

by applying boundary conditions. It must be noted that only the real part of (5.46) must be considered when evaluating the physical field.

5.4.2. Nonconductive Regions (Ω_I and Ω_{III})

Applying the separation of variables method [132] to (5.21), the following general solution can be derived for the TE potential within air region I

$$W_a^{I,r}(x, y, z) = \sum_{m=-M}^M \sum_{n=-N}^N e^{j\xi_m x} e^{jk_n z} C_{mn}^I e^{-\kappa_{mn} y}, \quad 0 \leq y \leq g \quad (5.47)$$

where

$$\kappa_{mn} = \sqrt{\xi_m^2 + k_n^2} \quad (5.48)$$

Only the negative exponential of y is used since the reflected field decays with distance away from the conductive plate. Only the real part of (5.47) is meaningful when calculating the physical field. The source field formulation will be discussed in section 5.5.

Similarly from (5.22) the following general solution can be obtained for the TE potential of region III

$$W_a^{III}(x, y, z) = \sum_{m=-M}^M \sum_{n=-N}^N e^{j\xi_m x} e^{jk_n z} C_{mn}^{III} e^{\kappa_{mn}(y+h)}, \quad y \leq -h \quad (5.49)$$

In (5.49) the positive exponential of y ensures that the field decays with distance away from the conductive plate. It must be noted that only the real part of (5.49) has any physical significance.

5.5. Source Field Modeling

In the proposed model, the TE potential within region I due to the magnetic source, $W_a^{1,s}$, is calculated from the knowledge of the source magnetic flux density using planar magnetic charge sheet [76] as outlined below.

It is assumed that a planar charge sheet is placed at height $y=g$ above the plate surface parallel to it as shown in Figure 5.5. Using (2.30) which is rewritten below for convenience

$$\rho_m(x, z) = 2 B_y^s(x, y, z) \Big|_{y=g} \quad (2.30)$$

and (2.43) the y -component magnetic flux density of the source in region I can be obtained as follows

$$B_y^{1,s}(x, y, z) = \sum_{m=-M}^M \sum_{n=-N}^N e^{j\xi_m x} e^{jk_n z} e^{\kappa_{mn}(y-g)} S_{mn}^y, \quad 0 \leq y \leq g \quad (5.50)$$

The exponential term of y makes sure that the source field increases with distance towards the original magnetic source.

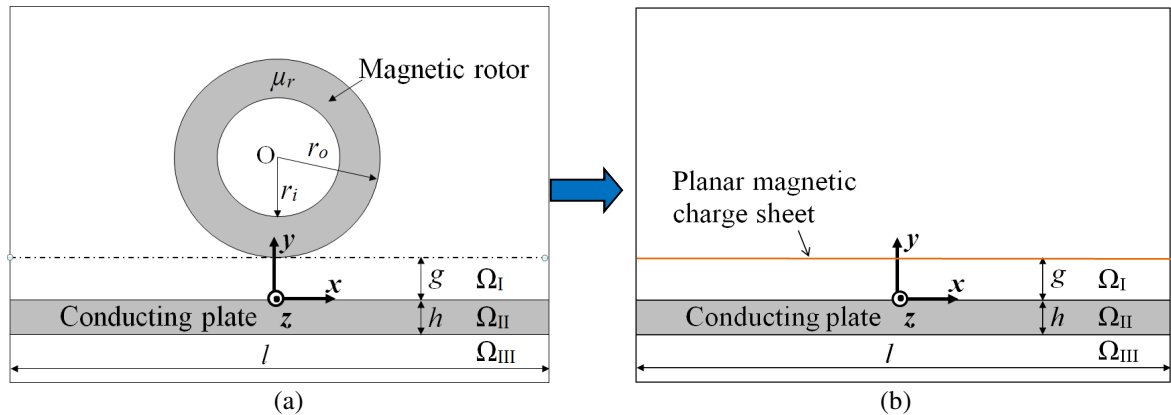


Figure 5.5. (a) x - y view of the magnetic source. The source is located at $(x_c, y_c, z_c) = (0, r_o + g, 0)$; (b) the source is replaced by an equivalent planar magnetic charge sheet located at $y = g$ above the conductive plate surface.

In order to determine the Fourier series coefficients, S_{mn}^y , the source y-component flux density is first computed on the charge sheet surface at discrete sampling points along the x and z axes using (2.22). Shifting the coordinate of the center of the source from $(0,0,0)$ to $(0,y_c,0)$, the source B_y field is calculated using

$$B_y^s = \frac{B_r^s(r_o, \theta_o)r_o}{2\pi} \int_0^{2\pi} \frac{(g - y_c - r_o \sin \theta_o)}{r^2} \left[\frac{2z + w_o}{\sqrt{4r^2 + (2z + w_o)^2}} - \frac{2z - w_o}{\sqrt{4r^2 + (2z - w_o)^2}} \right] d\theta_o \quad (5.51)$$

where,
$$r^2 = x^2 + (g - y_c)^2 + r_o^2 - 2r_o(x \cos \theta_o + (g - y_c) \sin \theta_o) \quad (5.52)$$

Noting that

$$y_c = r_o + g \quad (5.53)$$

substituting (5.53) into (5.52) gives

$$r^2 = x^2 + 2r_o^2 - 2r_o(x \cos \theta_o - r_o \sin \theta_o) \quad (5.54)$$

Two dimensional discrete Fourier transform (2-D DFT) is applied on the source B_y field computed using (5.51). The resulting discrete Fourier sequence is converted into a continuous exponential Fourier series as discussed in Appendix A to obtain the coefficients S_{mn}^y . The original B_y source field and reconstructed field using (A.22) on the charge sheet surface are shown in Figure 5.6 and Figure 5.7.

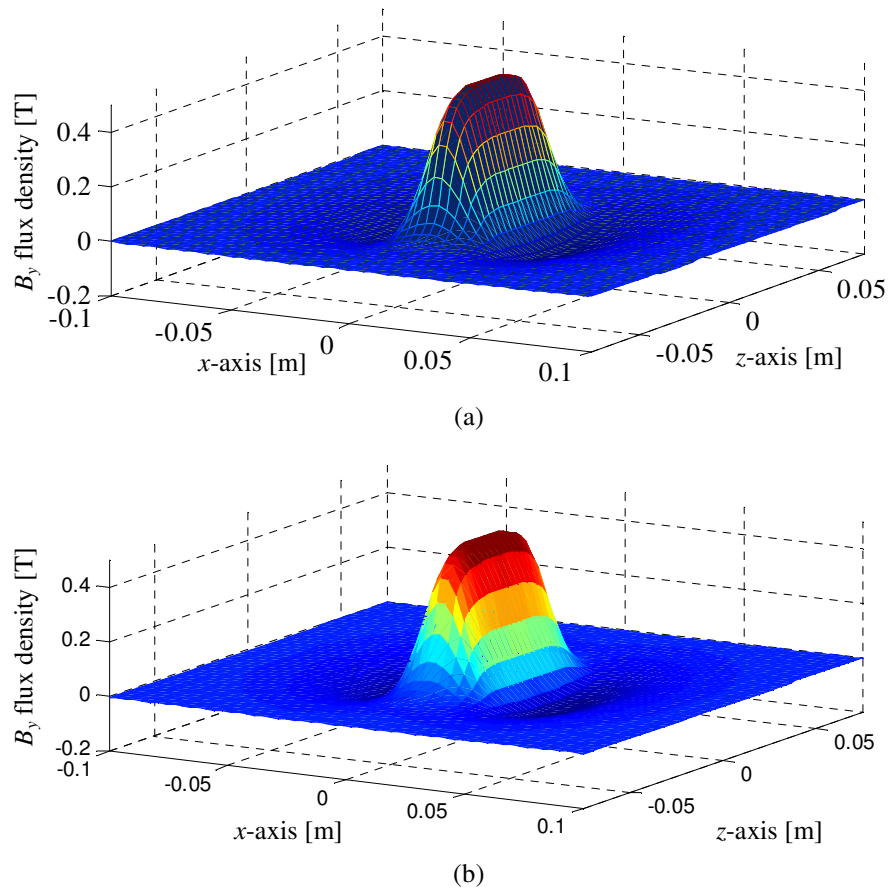


Figure 5.6. (a) Original B_y source field and (b) reconstructed B_y field using (A.19) on the charge sheet kept at 5mm above the conductive plate.

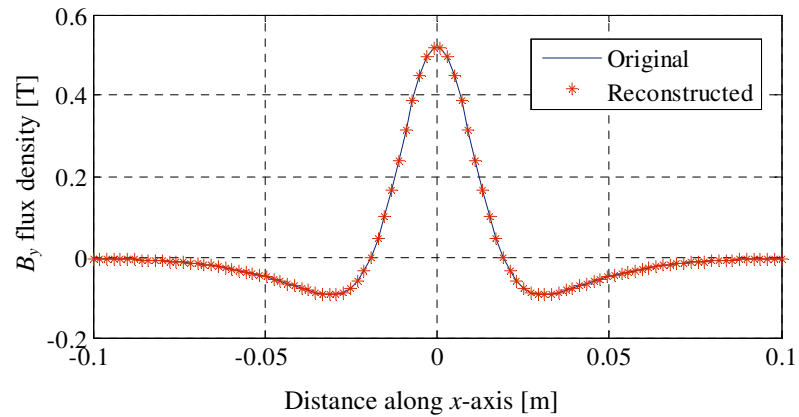


Figure 5.7. Comparison of the original and reconstructed B_y source field along x -axis at $z = 0$.

Equation (5.16) relates the TE potential with the y -component magnetic flux density due to the source as

$$\frac{\partial^2 W_a^{1,s}}{\partial y^2} = B_y^{1,s} \quad (5.55)$$

or,

$$W_a^{1,s} = \int_{-\infty}^y \int_{-\infty}^y B_y^{1,s} dy dy \quad (5.56)$$

Thus integrating (5.50) twice with respect to y gives the source TE potential in region I

$$W_a^{1,s} = \sum_{m=-M}^M \sum_{n=-N}^N e^{j\xi_m x} e^{jk_n z} S_{mn}^w e^{\kappa_{mn}(y-g)}, \quad 0 \leq y < g \quad (5.57)$$

where

$$S_{mn}^w = \frac{1}{\kappa_{mn}} S_{mn}^y, \quad 0 \leq y < g \quad (5.58)$$

Using (5.16) and (5.57) the x and z components of the source flux density in region I are determined to be

$$B_x^{1,s} = \sum_{m=-M}^M \sum_{n=-N}^N e^{j\xi_m x} e^{jk_n z} j\xi_m \kappa_{mn} S_{mn}^w e^{\kappa_{mn}(y-g)}, \quad 0 \leq y < g \quad (5.59)$$

$$B_z^{1,s} = \sum_{m=-M}^M \sum_{n=-N}^N e^{j\xi_m x} e^{jk_n z} jk_n \kappa_{mn} S_{mn}^w e^{\kappa_{mn}(y-g)}, \quad 0 \leq y < g \quad (5.60)$$

Substituting (5.58) into (5.59)-(5.60), $B_x^{1,s}$ and $B_z^{1,s}$ can be rewritten as

$$B_x^{1,s} = \sum_{m=-M}^M \sum_{n=-N}^N e^{j\xi_m x} e^{jk_n z} S_{mn}^y e^{\kappa_{mn}(y-g)} \frac{j\xi_m}{\kappa_{mn}}, \quad 0 \leq y < g \quad (5.61)$$

$$B_z^{1,s} = \sum_{m=-M}^M \sum_{n=-N}^N e^{j\xi_m x} e^{jk_n z} S_{mn}^y e^{\kappa_{mn}(y-g)} \frac{jk_n}{\kappa_{mn}}, \quad 0 \leq y < g \quad (5.62)$$

Equations (5.61), (5.62) express the x and z flux density components due to the source in terms of the y -component and will be useful for force and power loss calculation.

5.6. Field Solution

5.6.1. Solution for the TE Potential

Substituting (5.47), (5.46) and (5.57) into (5.29) and cancelling out common terms gives for each m, n

$$S_{mn}^w e^{-\kappa_{mn}g} + C_{mn}^I = C_{mn}^{II} + D_{mn}^{II}, \text{ at } y = 0 \quad (5.63)$$

Substituting (5.47), (5.46) and (5.57) into (5.30) yields

$$\kappa_{mn} \left(S_{mn}^w e^{-\kappa_{mn}g} - C_{mn}^I \right) = \alpha_{mn} C_{mn}^{II} + \beta_{mn} D_{mn}^{II}, \text{ at } y = 0 \quad (5.64)$$

Similarly substituting TE potentials for regions II and III from (5.46) and (5.49) into (5.31) at $y = -h$ gives

$$C_{mn}^{III} = C_{mn}^{II} e^{-\alpha_{mn}h} + D_{mn}^{II} e^{-\beta_{mn}h}, \text{ at } y = -h \quad (5.65)$$

Finally substituting (5.46) and (5.49) into (5.32) gives

$$\kappa_{mn} C_{mn}^{III} = \alpha_{mn} C_{mn}^{II} e^{-\alpha_{mn}h} + \beta_{mn} D_{mn}^{II} e^{-\beta_{mn}h}, \text{ at } y = -h \quad (5.66)$$

Eliminating C_{mn}^I from (5.63) and (5.64) one has

$$(\alpha_{mn} + \kappa_{mn}) C_{mn}^{II} + (\beta_{mn} + \kappa_{mn}) D_{mn}^{II} = 2\kappa_{mn} S_{mn}^w e^{-\kappa_{mn}g} \quad (5.67)$$

and eliminating C_{mn}^{III} from (5.65) and (5.66) gives

$$(\alpha_{mn} - \kappa_{mn}) e^{-\alpha_{mn}h} C_{mn}^{II} + (\beta_{mn} - \kappa_{mn}) e^{-\beta_{mn}h} D_{mn}^{II} = 0 \quad (5.68)$$

Equations (5.67) and (5.68) can be in the following matrix form

$$\begin{bmatrix} (\alpha_{mn} + \kappa_{mn}) & (\beta_{mn} + \kappa_{mn}) \\ (\alpha_{mn} - \kappa_{mn}) e^{-\alpha_{mn}h} & (\beta_{mn} - \kappa_{mn}) e^{-\beta_{mn}h} \end{bmatrix} \begin{bmatrix} C_{mn}^{II} \\ D_{mn}^{II} \end{bmatrix} = \begin{bmatrix} 2\kappa_{mn} S_{mn}^w e^{-\kappa_{mn}g} \\ 0 \end{bmatrix} \quad (5.69)$$

From (5.69) unknowns C_{mn}^{II} and D_{mn}^{II} can be obtained using Cramer's rule [132]. The solutions are

$$C_{mn}^{\text{II}} = 2\kappa_{mn} S_{mn}^w e^{-\kappa_{mn}g} (\beta_{mn} - \kappa_{mn}) e^{-\beta_{mn}h} / Q_{mn} \quad (5.70)$$

$$D_{mn}^{\text{II}} = -2\kappa_{mn} S_{mn}^w e^{-\kappa_{mn}g} (\alpha_{mn} - \kappa_{mn}) e^{-\alpha_{mn}h} / Q_{mn} \quad (5.71)$$

where

$$Q_{mn} = (\alpha_{mn} + \kappa_{mn})(\beta_{mn} - \kappa_{mn}) e^{-\beta_{mn}h} - (\beta_{mn} + \kappa_{mn})(\alpha_{mn} - \kappa_{mn}) e^{-\alpha_{mn}h} \quad (5.72)$$

is the determinant of the coefficient matrix in (5.69). Substituting (5.70) and (5.71) back into (5.46) gives the TE potential for conductive plate region in terms of the source TE field as

$$W_a^{\text{II}} = \sum_{m=-M}^M \sum_{n=-N}^N e^{j\xi_m x} e^{jk_n z} S_{mn}^w e^{-\kappa_{mn}g} T_{mn}^w(y), \quad -h \leq y \leq 0 \quad (5.73)$$

where

$$T_{mn}^w(y) = 2\kappa_{mn} \left[\frac{(\beta_{mn} - \kappa_{mn}) e^{(\alpha_{mn}y - \beta_{mn}h)} - (\alpha_{mn} - \kappa_{mn}) e^{(\beta_{mn}y - \alpha_{mn}h)}}{Q_{mn}} \right] \quad (5.74)$$

can be regarded as the transmission function relating the TE potential of the source to the transmitted potential in the conductive plate. It is worth noting that as the transmission function is source independent, this solution is valid for any magnetic source located at any location above the conductive region.

Using (5.63) the reflected TE potential coefficients are

$$C_{mn}^{\text{I}} = C_{mn}^{\text{II}} + D_{mn}^{\text{II}} - S_{mn}^w e^{-\kappa_{mn}g}, \quad \text{at } y = 0 \quad (5.75)$$

Substituting (5.70) and (5.71) into (5.75) yields

$$C_{mn}^I = 2\kappa_{mn} S_{mn}^w e^{-\kappa_{mn}g} \left[\frac{(\beta_{mn} - \kappa_{mn})e^{-\beta_{mn}h} - (\alpha_{mn} - \kappa_{mn})e^{-\alpha_{mn}h}}{Q_{mn}} \right] - S_{mn}^w e^{-\kappa_{mn}g} \quad (5.76)$$

Using the transmission function definition given by (5.74), (5.76) can be written as

$$C_{mn}^I = S_{mn}^w e^{-\kappa_{mn}g} T_{mn}^w(0) - S_{mn}^w e^{-\kappa_{mn}g} \quad (5.77)$$

or,
$$C_{mn}^I = S_{mn}^w e^{-\kappa_{mn}g} (T_{mn}^w(0) - 1) \quad (5.78)$$

where $T_{mn}^w(0)$ is the transmission function $T_{mn}^w(y)$ evaluated at $y=0$. Substituting (5.78)

into (5.47) the reflected TE potential for region I can be obtained

$$W_a^{I,r} = \sum_{m=-M}^M \sum_{n=-N}^N e^{j\xi_m x} e^{jk_n z} e^{-\kappa_{mn}y} S_{mn}^w e^{-\kappa_{mn}g} (T_{mn}^w(0) - 1), \quad 0 \leq y \leq g \quad (5.79)$$

or,
$$W_a^{I,r} = \sum_{m=-M}^M \sum_{n=-N}^N e^{j\xi_m x} e^{jk_n z} S_{mn}^w e^{-\kappa_{mn}g} R_{mn}^w(y), \quad 0 \leq y \leq g \quad (5.80)$$

where
$$R_{mn}^w(y) = e^{-\kappa_{mn}y} [T_{mn}^w(0) - 1] \quad (5.81)$$

can be thought of as reflection function that relates the incident TE potential of the source to the reflected potential in region I. At $y=0$, one finds

$$R_{mn}^w(0) = T_{mn}^w(0) - 1 \quad (5.82)$$

This is the same relationship that applies to high-frequency plane waves.

Substituting (5.72) and (5.74) into (5.82) yields

$$R_{mn}^w(0) = 2\kappa_{mn} \frac{(\beta_{mn} - \kappa_{mn})e^{-\beta_{mn}h} - (\alpha_{mn} - \kappa_{mn})e^{-\alpha_{mn}h}}{(\alpha_{mn} + \kappa_{mn})(\beta_{mn} - \kappa_{mn})e^{-\beta_{mn}h} - (\beta_{mn} + \kappa_{mn})(\alpha_{mn} - \kappa_{mn})e^{-\alpha_{mn}h}} - 1 \quad (5.83)$$

$$R_{mn}^w(0) = \frac{(\beta_{mn} - \kappa_{mn})(\alpha_{mn} - \kappa_{mn})(e^{-\alpha_{mn}h} - e^{-\beta_{mn}h})}{(\alpha_{mn} + \kappa_{mn})(\beta_{mn} - \kappa_{mn})e^{-\beta_{mn}h} - (\beta_{mn} + \kappa_{mn})(\alpha_{mn} - \kappa_{mn})e^{-\alpha_{mn}h}} \quad (5.84)$$

Now defining,

$$\varsigma_{mn} = 0.5\sqrt{(\mu_0\sigma v_y)^2 + 4\gamma_{mn}^2} \quad (5.85)$$

(5.84) can be written as

$$R_{mn}^w(0) = \frac{(\alpha_{mn} - \kappa_{mn})(\beta_{mn} - \kappa_{mn})(e^{-\varsigma_{mn}h} - e^{\varsigma_{mn}h})}{(\alpha_{mn} + \kappa_{mn})(\beta_{mn} - \kappa_{mn})e^{\varsigma_{mn}h} - (\alpha_{mn} - \kappa_{mn})(\beta_{mn} + \kappa_{mn})e^{-\varsigma_{mn}h}} \quad (5.86)$$

Using (5.43), (5.44) the following relations are derived

$$\begin{aligned} (\alpha_{mn} - \kappa_{mn})(\beta_{mn} - \kappa_{mn}) &= \kappa_{mn}^2 - \kappa_{mn}(\alpha_{mn} + \beta_{mn}) + \alpha_{mn}\beta_{mn} \\ &= \kappa_{mn}^2 - \gamma_{mn}^2 + \kappa_{mn}\mu_0\sigma v_y \end{aligned} \quad (5.87)$$

Substituting (5.42) and (5.48) into (5.87) gives

$$(\alpha_{mn} - \kappa_{mn})(\beta_{mn} - \kappa_{mn}) = \mu_0\sigma(v_y\kappa_{mn} + j(\omega_e + v_x\xi_m + v_zk_n)) \quad (5.88)$$

Then,

$$\begin{aligned} (\alpha_{mn} + \kappa_{mn})(\beta_{mn} - \kappa_{mn}) &= \alpha_{mn}\beta_{mn} - \kappa_{mn}(\alpha_{mn} - \beta_{mn}) - \kappa_{mn}^2 \\ &= -\gamma_{mn}^2 - \kappa_{mn}^2 - \kappa_{mn}\sqrt{(\mu_0\sigma v_y)^2 + 4\gamma_{mn}^2} \end{aligned} \quad (5.89)$$

Substituting (5.42) and (5.48) into (5.89) gives

$$(\alpha_{mn} + \kappa_{mn})(\beta_{mn} - \kappa_{mn}) = -2\kappa_{mn}^2 + j\mu_0\sigma(\omega_e + v_x\xi_m + v_zk_n) - 2\kappa_{mn}\varsigma_{mn} \quad (5.90)$$

And then,

$$\begin{aligned} (\alpha_{mn} - \kappa_{mn})(\beta_{mn} + \kappa_{mn}) &= \alpha_{mn}\beta_{mn} + \kappa_{mn}(\alpha_{mn} - \beta_{mn}) - \kappa_{mn}^2 \\ &= -\gamma_{mn}^2 - \kappa_{mn}^2 + \kappa_{mn}\sqrt{(\mu_0\sigma v_y)^2 + 4\gamma_{mn}^2} \end{aligned} \quad (5.91)$$

Substituting (5.42) and (5.48) into (5.91) gives

$$(\alpha_{mn} - \kappa_{mn})(\beta_{mn} + \kappa_{mn}) = -2\kappa_{mn}^2 + j\mu_0\sigma(\omega_e + v_x\xi_m + v_zk_n) + 2\kappa_{mn}\varsigma_{mn} \quad (5.92)$$

Substituting (5.88), (5.90) and (5.92) into (5.86) gives

$$R_{mn}^w(0) = \frac{-\mu_0\sigma(v_y\kappa_{mn} + j(\omega_e + v_x\xi_m + v_zk_n))(e^{\varsigma_{mn}h} - e^{-\varsigma_{mn}h})}{-\left[2\kappa_{mn}^2 - j\mu_0\sigma(\omega_e + v_x\xi_m + v_zk_n)\right](e^{\varsigma_{mn}h} - e^{-\varsigma_{mn}h}) - 2\kappa_{mn}\varsigma_{mn}(e^{\varsigma_{mn}h} + e^{-\varsigma_{mn}h})} \quad (5.93)$$

$$R_{mn}^w(0) = \frac{\mu_0\sigma(v_y\kappa_{mn} + j(\omega_e + v_x\xi_m + v_zk_n))\sinh(\varsigma_{mn}h)}{\left[2\kappa_{mn}^2 - j\mu_0\sigma(\omega_e + v_x\xi_m + v_zk_n)\right]\sinh(\varsigma_{mn}h) + 2\kappa_{mn}\varsigma_{mn}\cosh(\varsigma_{mn}h)} \quad (5.94)$$

Equation (5.94) can be written as (assuming $\sinh(\varsigma_{mn}h) \neq 0$)

$$R_{mn}^w(0) = \frac{\mu_0\sigma(\kappa_{mn}v_y + j(\omega_e + \xi_mv_x + k_nv_z))}{2\kappa_{mn}^2 - j\mu_0\sigma(\omega_e + \xi_mv_x + k_nv_z) + 2\kappa_{mn}\varsigma_{mn}\coth(\varsigma_{mn}h)} \quad (5.95)$$

5.6.2. Solution for the Magnetic Vector Potential

Substituting (5.73) into (5.8) and (5.10) the x and z -components of the magnetic vector potential in the conductive plate are obtained as (noting that the TM potential is zero)

$$A_x^{\text{II}}(x, y, z) = -j \sum_{m=-M}^M \sum_{n=-N}^N k_n e^{j\xi_m x} e^{jk_n z} S_{mn}^w e^{-\kappa_{mn}y} T_{mn}^w(y), \quad -h \leq y \leq 0 \quad (5.96)$$

$$A_z^{\text{II}}(x, y, z) = j \sum_{m=-M}^M \sum_{n=-N}^N \xi_m e^{j\xi_m x} e^{jk_n z} S_{mn}^w e^{-\kappa_{mn}y} T_{mn}^w(y), \quad -h \leq y \leq 0 \quad (5.97)$$

5.6.3. Solution for the Magnetic Flux Density

5.6.3.1. Solution for the transmitted flux density

Using (5.12), (5.13), (5.15), (5.58) and (5.73), the transmitted magnetic flux density components in the conductive plate region can be expressed in terms of the incident y -component source flux density as follows

$$B_x^{\text{II}}(x, y, z) = \sum_{m=-M}^M \sum_{n=-N}^N e^{j\xi_m x} e^{jk_n z} S_{mn}^y e^{-\kappa_{mn} y} \frac{j\xi_m}{\kappa_{mn}^2} \frac{dT_{mn}^w(y)}{dy}, \quad -h \leq y \leq 0 \quad (5.98)$$

$$B_y^{\text{II}}(x, y, z) = \sum_{m=-M}^M \sum_{n=-N}^N e^{j\xi_m x} e^{jk_n z} S_{mn}^y e^{-\kappa_{mn} y} T_{mn}^w(y), \quad -h \leq y \leq 0 \quad (5.99)$$

$$B_z^{\text{II}}(x, y, z) = \sum_{m=-M}^M \sum_{n=-N}^N e^{j\xi_m x} e^{jk_n z} S_{mn}^y e^{-\kappa_{mn} y} \frac{jk_n}{\kappa_{mn}^2} \frac{dT_{mn}^w(y)}{dy}, \quad -h \leq y \leq 0 \quad (5.100)$$

where from (5.74) the derivative of the transmission function with respect to y can be easily obtained as

$$\frac{dT_{mn}^w(y)}{dy} = 2\kappa_{mn} \left[\frac{\alpha_{mn}(\beta_{mn} - \kappa_{mn})e^{(\alpha_{mn}y - \beta_{mn}h)} - \beta_{mn}(\alpha_{mn} - \kappa_{mn})e^{(\beta_{mn}y - \alpha_{mn}h)}}{Q_{mn}} \right] \quad (5.101)$$

5.6.3.2. Solution for the reflected flux density

Similarly using (5.16), (5.58) and (5.80)-(5.81) the reflected flux density components of region I can be written in terms of the incident source y -component magnetic flux density as given below

$$B_x^{\text{I},r}(x, y, z) = - \sum_{m=-M}^M \sum_{n=-N}^N e^{j\xi_m x} e^{jk_n z} S_{mn}^y e^{-\kappa_{mn} y} \frac{j\xi_m}{\kappa_{mn}} R_{mn}^w(y), \quad 0 \leq y \leq g \quad (5.102)$$

$$B_y^{\text{I},r}(x, y, z) = \sum_{m=-M}^M \sum_{n=-N}^N e^{j\xi_m x} e^{jk_n z} S_{mn}^y e^{-\kappa_{mn} y} R_{mn}^w(y), \quad 0 \leq y \leq g \quad (5.103)$$

$$B_z^{\text{I},r}(x, y, z) = - \sum_{m=-M}^M \sum_{n=-N}^N e^{j\xi_m x} e^{jk_n z} S_{mn}^y e^{-\kappa_{mn} y} \frac{jk_n}{\kappa_{mn}} R_{mn}^w(y), \quad 0 \leq y \leq g \quad (5.104)$$

Using (5.50), (5.61) and (5.62) and defining the source flux density at $y=0$ as

$$B_{x,mn}^{\text{I},s}(x, 0, z) = \sum_{m=-M}^M \sum_{n=-N}^N e^{j\xi_m x} e^{jk_n z} S_{mn}^y e^{-\kappa_{mn} g} \frac{j\xi_m}{\kappa_{mn}} \quad (5.105)$$

$$B_{y,mn}^{I,s}(x, 0, z) = e^{j\xi_m x} e^{jk_n z} S_{mn}^y e^{-\kappa_{mn} g} \quad (5.106)$$

$$B_{z,mn}^{I,s}(x, 0, z) = \sum_{m=-M}^M \sum_{n=-N}^N e^{j\xi_m x} e^{jk_n z} S_{mn}^y e^{-\kappa_{mn} g} \frac{jk_n}{\kappa_{mn}} \quad (5.107)$$

The reflected flux density components (5.102)-(5.104) can also be written in terms of the respective source flux density components as follows

$$B_x^{I,r}(x, y, z) = - \sum_{m=-M}^M \sum_{n=-N}^N B_{x,mn}^{I,s}(x, 0, z) R_{mn}^w(y), \quad 0 \leq y \leq g \quad (5.108)$$

$$B_y^{I,r}(x, y, z) = \sum_{m=-M}^M \sum_{n=-N}^N B_{y,mn}^{I,s}(x, 0, z) R_{mn}^w(y), \quad 0 \leq y \leq g \quad (5.109)$$

and

$$B_z^{I,r}(x, y, z) = - \sum_{m=-M}^M \sum_{n=-N}^N B_{z,mn}^{I,s}(x, 0, z) R_{mn}^w(y), \quad 0 \leq y \leq g \quad (5.110)$$

The reflected flux density given by (5.108)-(5.110) can also be written in a more compact form using (5.106) as

$$\mathbf{B}^{I,r} = \sum_{m=-M}^M \sum_{n=-N}^N B_{y,mn}^{I,s}(x, 0, z) R_{mn}^w(y) \left[-\frac{j\xi_m}{\kappa_{mn}} \hat{x} + \hat{y} - \frac{jk_n}{\kappa_{mn}} \hat{z} \right], \quad 0 \leq y \leq g \quad (5.111)$$

$$\mathbf{B}^{I,r} = \sum_{m=-M}^M \sum_{n=-N}^N B_{y,mn}^{I,s}(x, 0, z) R_{mn}^w(y) \left[-j \cos \varphi \hat{x} + \hat{y} - j \sin \varphi \hat{z} \right], \quad 0 \leq y \leq g \quad (5.112)$$

where

$$\varphi = \tan^{-1}(k_n / \xi_m) \quad (5.113)$$

5.7. Calculation of Electromagnetic Force

The electromagnetic forces acting on the magnetic source will be calculated using two approaches. The first approach uses Maxwell's stress tensor [112, 115, 143] using

the reflected field of region I whereas the second approach is based on fictitious magnetic charge [197].

5.7.1. Calculation using Maxwell's Stress Tensor

Maxwell's stress tensor method [112, 115, 143] will be used to calculate the thrust, lift and lateral forces acting on the conductive plate using

$$F_x = \frac{1}{2\mu_0} \operatorname{Re} \left\{ \int_x \int_z B_x^{\text{II}} B_y^{\text{II}*} dx dz \right\} \text{ at } y = 0 \quad (5.114)$$

$$F_y = \frac{1}{4\mu_0} \operatorname{Re} \left\{ \int_x \int_z (B_y^{\text{II}} B_y^{\text{II}*} - B_x^{\text{II}} B_x^{\text{II}*} - B_z^{\text{II}} B_z^{\text{II}*}) dx dz \right\} \text{ at } y = 0 \quad (5.115)$$

$$F_z = \frac{1}{2\mu_0} \operatorname{Re} \left\{ \int_x \int_z B_z^{\text{II}} B_y^{\text{II}*} dx dz \right\} \text{ at } y = 0 \quad (5.116)$$

where the integration is performed over the entire top surface of the conductive plate at $y=0$ and '*' denotes complex conjugate. The limits of integration with respect to x and z are $-l/2$ to $l/2$ and $-w/2$ to $w/2$. It must be noted that (5.114)-(5.116) produce the force acting on the plate. Hence in order to find the force acting on the magnetic source, a negative sign should be added in front of the force equations.

Using (5.23) and (5.24) the thrust tensor given by (5.114) becomes

$$F_x = \frac{1}{2\mu_0} \operatorname{Re} \left\{ \int_x \int_z (B_x^{\text{I},s} + B_x^{\text{I},r}) (B_y^{\text{I},s} + B_y^{\text{I},r})^* dx dz \right\} \text{ at } y = 0 \quad (5.117)$$

Adding the x -component of the reflected and source flux density of region I given by (5.61) and (5.102) at $y=0$ and using (5.81) gives

$$B_x^{I,s} + B_x^{I,r} = \sum_{m=-M}^M \sum_{n=-N}^N e^{j\xi_m x} e^{jk_n z} S_{mn}^y e^{-\kappa_{mn} g} \frac{j\xi_m (2 - T_{mn}^w(0))}{\kappa_{mn}}, \text{ at } y = 0 \quad (5.118)$$

Evaluating (5.99) at $y=0$ gives the total y -component magnetic flux density on the top surface of the conductive plate as

$$B_y^{I,s} + B_y^{I,r} = \sum_{m=-M}^M \sum_{n=-N}^N e^{j\xi_m x} e^{jk_n z} S_{mn}^y e^{-\kappa_{mn} g} T_{mn}^w(0), \text{ at } y = 0 \quad (5.119)$$

Substituting (5.118) and complex conjugate of (5.119) into (5.117) and performing the double integral, the thrust force is easily evaluated to be

$$F_x = \frac{lw}{2\mu_0} \text{Re} \left\{ \sum_{m=-M}^M \sum_{n=-N}^N |S_{mn}^y|^2 e^{-2\kappa_{mn} g} \frac{j\xi_m}{\kappa_{mn}} T_{mn}^{w*}(0) (2 - T_{mn}^w(0)) \right\} \quad (5.120)$$

Since,

$$\text{Re} \left\{ j T_{mn}^{w*}(0) T_{mn}^w(0) \right\} = 0 \quad (5.121)$$

the thrust force becomes

$$F_x = \frac{lw}{\mu_0} \text{Re} \left\{ \sum_{m=-M}^M \sum_{n=-N}^N |S_{mn}^y|^2 e^{-2\kappa_{mn} g} \frac{j\xi_m}{\kappa_{mn}} T_{mn}^{w*}(0) \right\} \quad (5.122)$$

On further simplification, the thrust force acting on the source can be written as

$$F_x = -\frac{lw}{\mu_0} \text{Im} \left\{ \sum_{m=-M}^M \sum_{n=-N}^N |S_{mn}^y|^2 e^{-2\kappa_{mn} g} \frac{\xi_m}{\kappa_{mn}} T_{mn}^w(0) \right\} \quad (5.123)$$

Using the relation between the reflection and transmission coefficient given by (5.82), (5.123) can be written as

$$F_x = -\frac{lw}{\mu_0} \text{Im} \left\{ \sum_{m=-M}^M \sum_{n=-N}^N |S_{mn}^y|^2 e^{-2\kappa_{mn}g} \frac{\xi_m}{\kappa_{mn}} R_{mn}^w(0) \right\} \quad (5.124)$$

Equation (5.124) obtains the thrust force from the y -component of the source magnetic flux density.

Similarly substituting (5.24) and (5.25) into (5.116) the lateral stress tensor can be written in terms of the reflected and source magnetic flux density as follows

$$F_z = \frac{1}{2\mu_0} \text{Re} \left\{ \int_x \int_z (B_z^{l,s} + B_z^{l,r})(B_y^{l,s} + B_y^{l,r})^* dx dz \right\}, \text{ at } y=0 \quad (5.125)$$

Adding (5.62) and (5.104) at $y=0$ gives the total z -component magnetic flux density on the top surface of the conductive plate

$$B_z^{l,s} + B_z^{l,r} = \sum_{m=-M}^M \sum_{n=-N}^N e^{j\xi_m x} e^{jk_n z} S_{mn}^y e^{-\kappa_{mn}g} \frac{jk_n (2 - T_{mn}^w(0))}{\kappa_{mn}}, \text{ at } y=0 \quad (5.126)$$

Substituting (5.126) and complex conjugate of (5.119) into (5.125) and integrating with respect to x and z yields

$$F_z = \frac{lw}{2\mu_0} \text{Re} \left\{ \sum_{m=-M}^M \sum_{n=-N}^N |S_{mn}^y|^2 e^{-2\kappa_{mn}g} \frac{jk_n}{\kappa_{mn}} T_{mn}^{w*}(0) (2 - T_{mn}^w(0)) \right\} \quad (5.127)$$

Using (5.121), the lateral force acting on the source becomes

$$F_z = -\frac{lw}{\mu_0} \text{Re} \left\{ \sum_{m=-M}^M \sum_{n=-N}^N |S_{mn}^y|^2 e^{-2\kappa_{mn}g} \frac{jk_n}{\kappa_{mn}} T_{mn}^{w*}(0) \right\} \quad (5.128)$$

Or,

$$F_z = -\frac{lw}{\mu_0} \text{Im} \left\{ \sum_{m=-M}^M \sum_{n=-N}^N |S_{mn}^y|^2 e^{-2\kappa_{mn}g} \frac{k_n}{\kappa_{mn}} T_{mn}^w(0) \right\} \quad (5.129)$$

Using (5.82), the lateral force can be written as

$$F_z = -\frac{lw}{\mu_0} \text{Im} \left\{ \sum_{m=-M}^M \sum_{n=-N}^N |S_{mn}^y|^2 e^{-2\kappa_{mn}g} \frac{k_n}{\kappa_{mn}} R_{mn}^w(0) \right\} \quad (5.130)$$

Substituting (5.23)-(5.25) into the expression of the lift tensor given by (5.115) and splitting the integrand into three parts with each part due to a separate flux density component, (5.115) can be written as

$$F_y = F_{y1} - F_{y2} - F_{y3} \quad (5.131)$$

where

$$F_{y1} = \frac{1}{4\mu_0} \text{Re} \left\{ \int_x \int_z (B_y^{1,s} + B_y^{1,r})(B_y^{1,s} + B_y^{1,r})^* dx dz \right\}, \text{ at } y=0 \quad (5.132)$$

$$F_{y2} = \frac{1}{4\mu_0} \text{Re} \left\{ \int_x \int_z (B_x^{1,s} + B_x^{1,r})(B_x^{1,s} + B_x^{1,r})^* dx dz \right\}, \text{ at } y=0 \quad (5.133)$$

$$F_{y3} = \frac{1}{4\mu_0} \text{Re} \left\{ \int_x \int_z (B_z^{1,s} + B_z^{1,r})(B_z^{1,s} + B_z^{1,r})^* dx dz \right\}, \text{ at } y=0 \quad (5.134)$$

Substituting (5.119) and its complex conjugate into (5.132) and integrating yields

$$F_{y1} = \frac{lw}{4\mu_0} \text{Re} \left\{ \sum_{m=-M}^M \sum_{n=-N}^N |S_{mn}^y|^2 e^{-2\kappa_{mn}g} |T_{mn}^w(0)|^2 \right\} \quad (5.135)$$

On substitution of (5.118) and its complex conjugate into (5.133) and integrating one obtains

$$F_{y2} = \frac{lw}{4\mu_0} \sum_{m=-M}^M \sum_{n=-N}^N \frac{\xi_m^2}{\kappa_{mn}} |S_{mn}^y|^2 e^{-2\kappa_{mn}g} (2 - T_{mn}^w(0))(2 - T_{mn}^w(0))^* \quad (5.136)$$

Further rearranging gives

$$F_{y2} = \frac{lw}{4\mu_0} \sum_{m=-M}^M \sum_{n=-N}^N \frac{\xi_m^2}{\kappa_{mn}^2} |S_{mn}^y|^2 e^{-2\kappa_{mn}g} \left[4 - 2T_{mn}^{w*}(0) - 2T_{mn}^w(0) + |T_{mn}^w(0)|^2 \right] \quad (5.137)$$

Finally substituting (5.126) and its complex conjugate into (5.134) and integrating one finds

$$F_{y3} = \frac{lw}{4\mu_0} \sum_{m=-M}^M \sum_{n=-N}^N \frac{k_n^2}{\kappa_{mn}^2} |S_{mn}^y|^2 e^{-2\kappa_{mn}g} \left[4 - 2T_{mn}^{w*}(0) - 2T_{mn}^w(0) + |T_{mn}^w(0)|^2 \right] \quad (5.138)$$

Substituting (5.135), (5.137) and (5.138) into (5.131) and using (5.48) gives the lift force acting on the magnetic source as

$$F_y = -\frac{lw}{\mu_0} \operatorname{Re} \left\{ \sum_{m=-M}^M \sum_{n=-N}^N |S_{mn}^y|^2 e^{-2\kappa_{mn}g} (T_{mn}^w(0) - 1) \right\} \quad (5.139)$$

Using (5.82), the lift force can be written as

$$F_y = -\frac{lw}{\mu_0} \operatorname{Re} \left\{ \sum_{m=-M}^M \sum_{n=-N}^N |S_{mn}^y|^2 e^{-2\kappa_{mn}g} R_{mn}^w(0) \right\} \quad (5.140)$$

In the next subsection electromagnetic force calculation using magnetic charge will be discussed.

5.7.2. Calculation using Fictitious Magnetic Charge

In electrostatics, the work done to bring a surface charge distribution, ρ_e , from infinity to an existing electric field of potential V is given by [115]

$$U_e = \int_S \rho_e V dS \quad (5.141)$$

Extending the concept to magnetostatics, assuming a fictitious magnetic charge distribution (due to the magnetic source) on the surface at $y=0$ in the presence of the reflected magnetic scalar potential, the work done or the total energy of the system is given by

$$U_m = \frac{1}{2} \operatorname{Re} \left\{ \int_{-l/2}^{l/2} \int_{-w/2}^{w/2} \rho_m^s \phi^{I,r} dx dz \right\}, \text{ at } y=0 \quad (5.142)$$

The charge density is twice the normal component of the flux density [76]. Hence from (5.50)

$$\rho_m^s(x, y, z) \Big|_{y=0} = 2 \sum_{m=-M}^M \sum_{n=-N}^N e^{j\xi_m x} e^{jk_n z} S_{mn}^y e^{-\kappa_{mn} g} \quad (5.143)$$

Using (2.5) the reflected scalar potential can be obtained from the reflected y -component flux density given by (5.103) as

$$\phi^{I,r}(x, y, z) = \frac{1}{\mu_0} \sum_{m=-M}^M \sum_{n=-N}^N e^{j\xi_m x} e^{jk_n z} S_{mn}^y e^{-\kappa_{mn} g} \frac{R_{mn}^w(y)}{\kappa_{mn}}, \quad 0 \leq y \leq g \quad (5.144)$$

The electromagnetic forces acting on the magnetic source are given by

$$\mathbf{F} = \nabla U_m \Big|_{\rho_m^s = \text{constant}} \quad (5.145)$$

Substituting (5.142) into (5.145), the force components are obtained as

$$F_x = \frac{1}{2} \operatorname{Re} \left\{ \int_{-l/2}^{l/2} \int_{-w/2}^{w/2} \rho_m^s \frac{\partial \phi^{I,r}}{\partial x} dx dz \right\}, \text{ at } y=0 \quad (5.146)$$

$$F_y = \frac{1}{2} \operatorname{Re} \left\{ \int_{-l/2}^{l/2} \int_{-w/2}^{w/2} \rho_m^s \frac{\partial \phi^{I,r}}{\partial y} dx dz \right\}, \text{ at } y=0 \quad (5.147)$$

$$F_z = \frac{1}{2} \operatorname{Re} \left\{ \int_{-l/2}^{l/2} \int_{-w/2}^{w/2} \rho_m^s \frac{\partial \phi^{l,r}}{\partial z} dx dz \right\}, \text{ at } y=0 \quad (5.148)$$

Utilizing (2.5), the forces can be written in a more compact form as [197]

$$\mathbf{F} = -\frac{1}{2\mu_0} \operatorname{Re} \left\{ \int_{-l/2}^{l/2} \int_{-w/2}^{w/2} \rho_m^s \mathbf{B}^{l,r} dx dz \right\}, \text{ at } y=0 \quad (5.149)$$

Substituting the charge density given by (5.143) and the reflected scalar field given by (5.144) into (5.146) and integrating with respect to x and z gives

$$F_x = \frac{lw}{\mu_0} \operatorname{Re} \left\{ \sum_{m=-M}^M \sum_{n=-N}^N |S_{mn}^y|^2 e^{-2\kappa_{mn}g} \frac{j\xi_m R_{mn}^w(0)}{\kappa_{mn}} \right\} \quad (5.150)$$

or,

$$F_x = -\frac{lw}{\mu_0} \operatorname{Im} \left\{ \sum_{m=-M}^M \sum_{n=-N}^N |S_{mn}^y|^2 e^{-2\kappa_{mn}g} \frac{\xi_m}{\kappa_{mn}} R_{mn}^w(0) \right\} \quad (5.151)$$

which is same as (5.124).

Similarly substituting (5.143) and (5.144) into (5.147) and (5.148) yields respectively the normal and lateral force as given by

$$F_y = -\frac{lw}{\mu_0} \operatorname{Re} \left\{ \sum_{m=-M}^M \sum_{n=-N}^N |S_{mn}^y|^2 e^{-2\kappa_{mn}g} R_{mn}^w(0) \right\} \quad (5.152)$$

and

$$F_z = -\frac{lw}{\mu_0} \operatorname{Im} \left\{ \sum_{m=-M}^M \sum_{n=-N}^N |S_{mn}^y|^2 e^{-2\kappa_{mn}g} \frac{k_n}{\kappa_{mn}} R_{mn}^w(0) \right\} \quad (5.153)$$

which are same as (5.140) and (5.130) respectively.

Noting the similarity among the force expressions given by (5.151)-(5.153) and defining

$$f_{mn} = -\frac{lw}{\mu_0} |S_{mn}^y|^2 e^{-2\kappa_{mn}g} R_{mn}^w(0) \quad (5.154)$$

then the electromagnetic forces can be written in a more compact form as

$$F_y = \text{Re} \left\{ \sum_{m=-M}^M \sum_{n=-N}^N f_{mn} \right\} \quad (5.155)$$

$$F_x = \text{Im} \left\{ \sum_{m=-M}^M \sum_{n=-N}^N \frac{\xi_m}{\kappa_{mn}} f_{mn} \right\} \quad (5.156)$$

$$F_z = \text{Im} \left\{ \sum_{m=-M}^M \sum_{n=-N}^N \frac{k_n}{\kappa_{mn}} f_{mn} \right\} \quad (5.157)$$

Taking divergence on both sides of (5.149) and noting (3.3), it is observed that

$$\nabla \cdot \mathbf{F} = 0 \quad (5.158)$$

5.8. Power Transfer Calculation

Differentiating the energy given by (5.142) with respect to time, the total power transfer from the magnetic source to the conductive plate can be calculated as follows

$$P_{transfer} = \left. \frac{\partial U_m}{\partial t} \right|_{\rho_m^s = \text{const} \tan t}, \text{ at } y=0 \quad (5.159)$$

It is noted from (5.159) that the power absorbed by the plate is designated as positive.

Substituting (5.142) into (5.159) gives

$$P_{transfer} = \frac{1}{2} \text{Re} \left\{ \int_{-l/2}^{l/2} \int_{-w/2}^{w/2} \rho_m^{s*} \frac{\partial \phi^{l,r}}{\partial t} dx dz \right\}, \text{ at } y=0 \quad (5.160)$$

In steady state (5.160) can be written as

$$P_{transfer} = -\frac{1}{2} \text{Re} \left\{ j\omega_e \int_{-l/2}^{l/2} \int_{-w/2}^{w/2} \rho_m^{s*} \phi^{l,r} dx dz \right\}, \text{ at } y=0 \quad (5.161)$$

Substituting (5.143) and (5.144) into (5.161) and integrating gives

$$P_{transfer} = -\frac{l\omega\omega_e}{\mu_0} \operatorname{Re} \left\{ j \sum_{m=-M}^M \sum_{n=-N}^N |S_{mn}^y|^2 e^{-2\kappa_{mn}g} \frac{R_{mn}^w(0)}{\kappa_{mn}} \right\} \quad (5.162)$$

or,

$$P_{transfer} = \frac{l\omega\omega_e}{\mu_0} \operatorname{Im} \left\{ \sum_{m=-M}^M \sum_{n=-N}^N |S_{mn}^y|^2 e^{-2\kappa_{mn}g} \frac{R_{mn}^w(0)}{\kappa_{mn}} \right\} \quad (5.163)$$

5.9. Electromagnetic Torque Calculation

The electromagnetic torque acting on the source is another useful parameter which can be derived using

$$T_{em} = \frac{P_{transfer}}{\omega_m} = \frac{P_{transfer}}{(\omega_e / P)} \quad (5.164)$$

where ω_m is the mechanical angular speed [rads^{-1}] and P is number of pole-pairs of the source. Substituting (5.163) into (5.164), the torque is calculated to be

$$T_{em} = \frac{l\omega P}{\mu_0} \operatorname{Im} \left\{ \sum_{m=-M}^M \sum_{n=-N}^N |S_{mn}^y|^2 e^{-2\kappa_{mn}g} \frac{R_{mn}^w(0)}{\kappa_{mn}} \right\} \quad (5.165)$$

5.10. Power Loss Calculation

One part of the transferred power to the conductive plate is lost as heat and the other part contributes to moving the source with velocity v_x , v_y and v_z . Therefore the power loss can be obtained as

$$P_{loss} = P_{transfer} - F_x v_x - F_y v_y - F_z v_z \quad (5.166)$$

Substituting thrust, lift and lateral force from (5.150), (5.152) and (5.153) respectively and power transfer from (5.162) into (5.166) and noting that

$$-\text{Im}\{R_{mn}^w(0)\} = \text{Re}\{jR_{mn}^w(0)\} \quad (5.167)$$

the following is obtained

$$P_{loss} = -\frac{lw}{\mu_0} \text{Re} \left\{ \sum_{m=-M}^M \sum_{n=-N}^N |S_{mn}^y|^2 e^{-2\kappa_{mn}g} \frac{R_{mn}^w(0)}{\kappa_{mn}} (j\omega_e + j\xi_m v_x + jk_n v_z - \kappa_{mn} v_y) \right\} \quad (5.168)$$

There is a striking similarity between the analytic force, power transfer, torque and power loss expressions derived in this chapter with the ones obtained in the 2-D analytic based steady state analysis conducted by Paudel [14]. This should be expected as this current chapter discusses eddy current modeling for a large conductive plate which, in many respects, resembles the 2-D model developed by Paudel [14].

Figure 5.8 shows a flowchart of the developed SOVP based steady state analytic model to compute the eddy current forces, torque and power transfer.

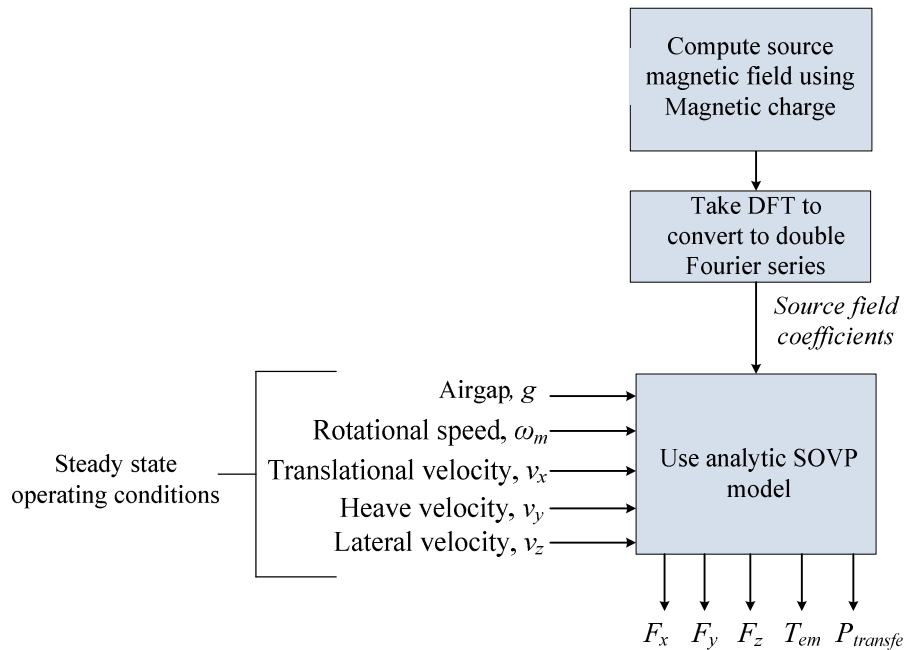


Figure 5.8. Flowchart of the presented analytic SOVP model to compute forces, torque and power transfer

5.11. Electromagnetic Stiffness Constant Calculation

The stiffness constant is defined as the negative of the derivative of the force with respect to the displacement [198]. The stiffness matrix for a 3-D model can be obtained by taking derivatives of the thrust, lift and lateral forces acting on the source with respect to x , y and z -axis displacements respectively.

$$\begin{bmatrix} k_{xx} & k_{xy} & k_{xz} \\ k_{yx} & k_{yy} & k_{yz} \\ k_{zx} & k_{zy} & k_{zz} \end{bmatrix} = - \begin{bmatrix} \frac{dF_x}{dx} & \frac{dF_x}{dy} & \frac{dF_x}{dz} \\ \frac{dF_y}{dx} & \frac{dF_y}{dy} & \frac{dF_y}{dz} \\ \frac{dF_z}{dx} & \frac{dF_z}{dy} & \frac{dF_z}{dz} \end{bmatrix} \quad (5.169)$$

Observing the force expressions given by (5.146)-(5.148), it can be noticed that

$$\frac{dF_x}{dy} = \frac{dF_y}{dx} \quad (5.170)$$

$$\frac{dF_x}{dz} = \frac{dF_z}{dx} \quad (5.171)$$

$$\frac{dF_y}{dz} = \frac{dF_z}{dy} \quad (5.172)$$

Differentiating the thrust force given by (5.146) with respect to y and substituting (5.143) and (5.144) into it and integrating with respect to x and z at $y=0$ yields for k_{xy} as

$$k_{xy} = -\frac{lw}{\mu_0} \text{Im} \left\{ \sum_{m=-M}^M \sum_{n=-N}^N \xi_m \left| S_{mn}^y \right|^2 e^{-2\kappa_{mn}g} R_{mn}^w(0) \right\} \quad (5.173)$$

Similarly differentiating (5.146) with respect to z and substituting (5.143) and (5.144) into it and then integrating at $y=0$ yields for k_{xz} as

$$k_{xz} = \frac{lw}{\mu_0} \operatorname{Re} \left\{ \sum_{m=-M}^M \sum_{n=-N}^N \xi_m k_n \left| S_{mn}^y \right|^2 e^{-2\kappa_{mn}g} \frac{R_{mn}^w(0)}{\kappa_{mn}} \right\} \quad (5.174)$$

Differentiating (5.147) with respect to z and substituting (5.143) and (5.144) into it and then integrating at $y=0$ yields for k_{yz} as

$$k_{yz} = -\frac{lw}{\mu_0} \operatorname{Im} \left\{ \sum_{m=-M}^M \sum_{n=-N}^N k_n \left| S_{mn}^y \right|^2 e^{-2\kappa_{mn}g} R_{mn}^w(0) \right\} \quad (5.175)$$

For the diagonal elements of the stiffness matrix the thrust, lift and lateral forces are differentiated with respect to x , y and z –displacements respectively and are given by

$$k_{xx} = \frac{lw}{\mu_0} \operatorname{Re} \left\{ \sum_{m=-M}^M \sum_{n=-N}^N \xi_m^2 \left| S_{mn}^y \right|^2 e^{-2\kappa_{mn}g} \frac{R_{mn}^w(0)}{\kappa_{mn}} \right\} \quad (5.176)$$

$$k_{yy} = -\frac{lw}{\mu_0} \operatorname{Re} \left\{ \sum_{m=-M}^M \sum_{n=-N}^N \kappa_{mn} \left| S_{mn}^y \right|^2 e^{-2\kappa_{mn}g} R_{mn}^w(0) \right\} \quad (5.177)$$

$$k_{zz} = \frac{lw}{\mu_0} \operatorname{Re} \left\{ \sum_{m=-M}^M \sum_{n=-N}^N k_n^2 \left| S_{mn}^y \right|^2 e^{-2\kappa_{mn}g} \frac{R_{mn}^w(0)}{\kappa_{mn}} \right\} \quad (5.178)$$

From (5.176)-(5.178) it is noted that

$$k_{xx} + k_{yy} + k_{zz} = 0 \quad (5.179)$$

This is another consequence of (5.158).

5.12. Electromagnetic Damping Constant Calculation

The damping constant is defined as the negative derivative of force with respect to the velocity [199]. Unlike the stiffness constants, the electromagnetic damping constants depend on the transmission function. The damping coefficients matrix for the 3-D model

can be determined by differentiating (5.155)-(5.157) with respect to the source velocities along the x , y and z - directions as given by

$$\begin{bmatrix} D_{xx} & D_{xy} & D_{xz} \\ D_{yx} & D_{yy} & D_{yz} \\ D_{zx} & D_{zy} & D_{zz} \end{bmatrix} = - \begin{bmatrix} \frac{dF_x}{dv_x} & \frac{dF_x}{dv_y} & \frac{dF_x}{dv_z} \\ \frac{dF_y}{dv_x} & \frac{dF_y}{dv_y} & \frac{dF_y}{dv_z} \\ \frac{dF_z}{dv_x} & \frac{dF_z}{dv_y} & \frac{dF_z}{dv_z} \end{bmatrix} \\ = - \begin{bmatrix} \text{Im} \sum_m \sum_n \frac{\xi_m}{\kappa_{mn}} \frac{\partial f_{mn}}{\partial v_x} & \text{Im} \sum_m \sum_n \frac{\xi_m}{\kappa_{mn}} \frac{\partial f_{mn}}{\partial v_y} & \text{Im} \sum_m \sum_n \frac{\xi_m}{\kappa_{mn}} \frac{\partial f_{mn}}{\partial v_z} \\ \text{Re} \sum_m \sum_n \frac{\partial f_{mn}}{\partial v_x} & \text{Re} \sum_m \sum_n \frac{\partial f_{mn}}{\partial v_y} & \text{Re} \sum_m \sum_n \frac{\partial f_{mn}}{\partial v_z} \\ \text{Im} \sum_m \sum_n \frac{k_n}{\kappa_{mn}} \frac{\partial f_{mn}}{\partial v_x} & \text{Im} \sum_m \sum_n \frac{k_n}{\kappa_{mn}} \frac{\partial f_{mn}}{\partial v_y} & \text{Im} \sum_m \sum_n \frac{k_n}{\kappa_{mn}} \frac{\partial f_{mn}}{\partial v_z} \end{bmatrix} \quad (5.180)$$

Observing the expression of f_{mn} given by (5.154), it is noticed that only the reflection coefficient, $R_{mn}^w(0)$, depends on the velocity. Its derivative with respect to v_x , v_y and v_z can be calculated analytically. Substituting (5.154), the damping matrix, \mathbf{D}_{em} , can be written as

$$[\mathbf{D}_{em}] = \frac{lw}{\mu_0} \text{Re} \sum_m \sum_n \left| S_{mn}^y \right|^2 e^{-2\kappa_{mn}g} \\ \cdot \begin{bmatrix} -\frac{j\xi_m}{\kappa_{mn}} \frac{\partial R_{mn}^w(0)}{\partial v_x} & -\frac{j\xi_m}{\kappa_{mn}} \frac{\partial R_{mn}^w(0)}{\partial v_y} & -\frac{j\xi_m}{\kappa_{mn}} \frac{\partial R_{mn}^w(0)}{\partial v_z} \\ \frac{\partial R_{mn}^w(0)}{\partial v_x} & \frac{\partial R_{mn}^w(0)}{\partial v_y} & \frac{\partial R_{mn}^w(0)}{\partial v_z} \\ -\frac{jk_n}{\kappa_{mn}} \frac{\partial R_{mn}^w(0)}{\partial v_x} & -\frac{jk_n}{\kappa_{mn}} \frac{\partial R_{mn}^w(0)}{\partial v_y} & -\frac{jk_n}{\kappa_{mn}} \frac{\partial R_{mn}^w(0)}{\partial v_z} \end{bmatrix} \quad (5.181)$$

The followings are defined

$$\tau_{mn} = \kappa_{mn} v_y + j(w_e + \xi_m v_x + k_n v_z) \quad (5.182)$$

$$d_{mn} = 2\kappa_{mn}^2 - j\mu_0\sigma(w_e + \xi_m v_x + k_n v_z) + 2\kappa_{mn}\varsigma_{mn}\coth(\varsigma_{mn}h) \quad (5.183)$$

Differentiating $R_{mn}^w(0)$ given by (5.95) with respect to v_x yields

$$\frac{\partial R_{mn}^w(0)}{\partial v_x} = \frac{\partial}{\partial v_x} \left[\frac{\mu_0\sigma(\kappa_{mn}v_y + j(w_e + \xi_m v_x + k_n v_z))}{2\kappa_{mn}^2 - j\mu_0\sigma(w_e + \xi_m v_x + k_n v_z) + 2\kappa_{mn}\varsigma_{mn}\coth(\varsigma_{mn}h)} \right] \quad (5.184)$$

Using (5.183), (5.184) can be written as

$$\frac{\partial R_{mn}^w(0)}{\partial v_x} = \frac{I_1^x - I_2^x - I_3^x - I_4^x}{d_{mn}^2} \quad (5.185)$$

where,

$$I_1^x = d_{mn} \frac{\partial}{\partial v_x} [\mu_0\sigma(\kappa_{mn}v_y + j(w_e + \xi_m v_x + k_n v_z))] \quad (5.186)$$

$$I_1^x = j\mu_0\sigma\xi_m d_{mn} \quad (5.187)$$

$$\text{Then,} \quad I_2^x = \mu_0\sigma\tau_{mn} \frac{\partial}{\partial v_x} [-j\mu_0\sigma(w_e + \xi_m v_x + k_n v_z)] \quad (5.188)$$

$$\text{or,} \quad I_2^x = -j\mu_0^2\sigma^2\xi_m\tau_{mn} \quad (5.189)$$

$$\text{Then,} \quad I_3^x = 2\mu_0\sigma\tau_{mn}\kappa_{mn}\coth(\varsigma_{mn}h) \frac{\partial\varsigma_{mn}}{\partial v_x} \quad (5.190)$$

Differentiating (5.85) with respect to v_x yields

$$\frac{\partial\varsigma_{mn}}{\partial v_x} = - \frac{j\mu_0\sigma\xi_m}{\sqrt{(\mu_0\sigma v_y)^2 + 4(\xi_m^2 + k_n^2 - j\mu_0\sigma(\omega_e + v_x\xi_m + v_zk_n))}} \quad (5.191)$$

Using (5.85), above can be written as

$$\frac{\partial \varsigma_{mn}}{\partial v_x} = -\frac{j\mu_0\sigma\xi_m}{2\varsigma_{mn}} \quad (5.192)$$

Substituting (5.192) into (5.190) yields

$$I_3^x = -j\mu_0^2\sigma^2\tau_{mn}\kappa_{mn}\xi_m \coth(\varsigma_{mn}h) / \varsigma_{mn} \quad (5.193)$$

Finally,

$$I_4^x = 2\mu_0\sigma\tau_{mn}\kappa_{mn}\varsigma_{mn} \frac{\partial \coth(\varsigma_{mn}h)}{\partial v_x} \quad (5.194)$$

Applying chain rule of differentiation,

$$I_4^x = j\mu_0^2\sigma^2\tau_{mn}\kappa_{mn}\xi_m h \operatorname{cosech}^2(\varsigma_{mn}h) \quad (5.195)$$

Substituting (5.187), (5.189), (5.193) and (5.195) into (5.185) gives

$$\frac{\partial R_{mn}^w(0)}{\partial v_x} = \frac{j\mu_0\sigma\xi_m \left[d_{mn} + \mu_0\sigma\tau_{mn}\kappa_{mn} \coth(\varsigma_{mn}h) / \varsigma_{mn} + \mu_0\sigma\tau_{mn} - \mu_0\sigma\tau_{mn}\kappa_{mn} h \operatorname{cosech}^2(\varsigma_{mn}h) \right]}{d_{mn}^2} \quad (5.196)$$

Similarly, derivative of the reflection function with respect to v_z can be obtained as

$$\frac{\partial R_{mn}^w(0)}{\partial v_z} = \frac{j\mu_0\sigma k_n \left[d_{mn} + \mu_0\sigma\tau_{mn}\kappa_{mn} \coth(\varsigma_{mn}h) / \varsigma_{mn} + \mu_0\sigma\tau_{mn} - \mu_0\sigma\tau_{mn}\kappa_{mn} h \operatorname{cosech}^2(\varsigma_{mn}h) \right]}{d_{mn}^2} \quad (5.197)$$

The derivative of the reflection function with respect to v_y can be obtained using

$$\frac{\partial R_{mn}^w(0)}{\partial v_y} = \frac{\partial}{\partial v_y} \left[\frac{\mu_0\sigma (\kappa_{mn}v_y + j(w_e + \xi_m v_x + k_n v_z))}{2\kappa_{mn}^2 - j\mu_0\sigma(w_e + \xi_m v_x + k_n v_z) + 2\kappa_{mn}\varsigma_{mn} \coth(\varsigma_{mn}h)} \right] \quad (5.198)$$

Using (5.183), above can be written as

$$\frac{\partial R_{mn}^w(0)}{\partial v_y} = \frac{I_1^y - I_2^y - I_3^y}{d_{mn}^2} \quad (5.199)$$

where,
$$I_1^y = d_{mn} \frac{\partial}{\partial v_y} [\mu_0 \sigma (\kappa_{mn} v_y + j(\omega_e + \xi_m v_x + k_n v_z))] \quad (5.200)$$

$$I_1^y = \mu_0 \sigma \kappa_{mn} d_{mn} \quad (5.201)$$

Then,
$$I_2^y = 2\mu_0 \sigma \tau_{mn} \kappa_{mn} \coth(\varsigma_{mn} h) \frac{\partial \varsigma_{mn}}{\partial v_y} \quad (5.202)$$

Differentiating (5.85) with respect to v_y and using (5.42) produces

$$\frac{\partial \varsigma_{mn}}{\partial v_y} = \frac{1}{2} \frac{\mu_0 \sigma v_y}{\sqrt{(\mu_0 \sigma v_y)^2 + 4(\xi_m^2 + k_n^2 - j\mu_0 \sigma (\omega_e + v_x \xi_m + v_z k_n))}} \quad (5.203)$$

Using (5.85), above can be written as

$$\frac{\partial \varsigma_{mn}}{\partial v_y} = \frac{\mu_0 \sigma v_y}{4\varsigma_{mn}} \quad (5.204)$$

Substituting (5.204) into (5.202)

$$I_2^y = 0.5\mu_0^2 \sigma^2 v_y \tau_{mn} \kappa_{mn} \coth(\varsigma_{mn} h) / \varsigma_{mn} \quad (5.205)$$

Finally,

$$I_3^y = 2\mu_0 \sigma \tau_{mn} \kappa_{mn} \varsigma_{mn} \frac{\partial \coth(\varsigma_{mn} h)}{\partial v_y} \quad (5.206)$$

or,
$$I_3^y = -0.5\mu_0^2 \sigma^2 \tau_{mn} \kappa_{mn} v_y h \operatorname{cosech}^2(\varsigma_{mn} h) \quad (5.207)$$

Substituting (5.201), (5.205) and (5.207) into (5.199) gives

$$\frac{\partial R_{mn}^w(0)}{\partial v_y} = \frac{\mu_0 \sigma \kappa_{mn} \left[d_{mn} - 0.5 \mu_0 \sigma v_y \tau_{mn} \left(\coth(\varsigma_{mn} h) / \varsigma_{mn} - h \operatorname{cosech}^2(\varsigma_{mn} h) \right) \right]}{d_{mn}^2} \quad (5.208)$$

Substituting (5.196), (5.197) and (5.208) into (5.181) the electromagnetic damping coefficients can be computed.

In order to calculate torque damping, the electromagnetic torque acting on the source given by (5.165) is differentiated with respect to mechanical rotational speed, ω_m , of the source to yield

$$D_{torque} = -\frac{\partial T_{em}}{\partial \omega_m} = -\frac{\partial T_{em}}{\partial \omega_e} \frac{\partial \omega_e}{\partial \omega_m} = -P \frac{\partial T_{em}}{\partial \omega_e} \left(\because \omega_e = P \omega_m \right) \quad (5.209)$$

Substituting (5.165) into (5.209) gives

$$D_{torque} = -\frac{l w P^2}{\mu_0} \operatorname{Im} \left\{ \sum_{m=-M}^M \sum_{n=-N}^N \left| S_{mn}^y \right|^2 \frac{e^{-2\kappa_{mn} g}}{\kappa_{mn}} \frac{\partial R_{mn}^w(0)}{\partial \omega_e} \right\} \quad (5.210)$$

Differentiating $R_{mn}^w(0)$ given by (5.95) with respect to ω_e yields

$$\frac{\partial R_{mn}^w(0)}{\partial \omega_e} = \frac{\partial}{\partial \omega_e} \left[\frac{\mu_0 \sigma \left(\kappa_{mn} v_y + j(\omega_e + \xi_m v_x + k_n v_z) \right)}{2\kappa_{mn}^2 - j\mu_0 \sigma (\omega_e + \xi_m v_x + k_n v_z) + 2\kappa_{mn} \varsigma_{mn} \coth(\varsigma_{mn} h)} \right] \quad (5.211)$$

or, using (5.183),

$$\frac{\partial R_{mn}^w(0)}{\partial \omega_e} = \frac{I_1^T - I_2^T - I_3^T - I_4^T}{d_{mn}^2} \quad (5.212)$$

where,

$$I_1^T = d_{mn} \frac{\partial}{\partial \omega_e} \left[\mu_0 \sigma \left(\kappa_{mn} v_y + j(\omega_e + \xi_m v_x + k_n v_z) \right) \right] \quad (5.213)$$

or,

$$I_1^T = j\mu_0 \sigma d_{mn} \quad (5.214)$$

Then,

$$I_2^T = \mu_0 \sigma \tau_{mn} \frac{\partial}{\partial w_e} [-j\mu_0 \sigma (w_e + \xi_m v_x + k_n v_z)] \quad (5.215)$$

or,

$$I_2^T = -j\mu_0^2 \sigma^2 \tau_{mn} \quad (5.216)$$

Then,

$$I_3^T = 2\mu_0 \sigma \tau_{mn} \kappa_{mn} \coth(\varsigma_{mn} h) \frac{\partial \varsigma_{mn}}{\partial w_e} \quad (5.217)$$

Differentiating (5.85) with respect to ω_e yields

$$\frac{\partial \varsigma_{mn}}{\partial w_e} = - \frac{j\mu_0 \sigma}{\sqrt{(\mu_0 \sigma v_y)^2 + 4(\xi_m^2 + k_n^2 - j\mu_0 \sigma (\omega_e + v_x \xi_m + v_z k_n))}} \quad (5.218)$$

Again using (5.85), above equation can be rewritten as

$$\frac{\partial \varsigma_{mn}}{\partial w_e} = - \frac{j\mu_0 \sigma}{2\varsigma_{mn}} \quad (5.219)$$

Substituting (5.219) into (5.217) gives

$$I_3^T = -j\kappa_{mn} \mu_0^2 \sigma^2 \frac{\tau_{mn}}{\varsigma_{mn}} \coth(\varsigma_{mn} h) \quad (5.220)$$

Finally,

$$I_4^T = 2\mu_0 \sigma \tau_{mn} \kappa_{mn} \varsigma_{mn} \frac{\partial \coth(\varsigma_{mn} h)}{\partial w_e} \quad (5.221)$$

Applying chain rule of differentiation,

$$I_4^T = j\mu_0^2 \sigma^2 h \kappa_{mn} \tau_{mn} \operatorname{cosech}^2(\varsigma_{mn} h) \quad (5.222)$$

Substituting (5.214), (5.216), (5.220) and (5.222) into (5.212) yields

$$\frac{\partial R_{mn}^w(0)}{\partial \omega_e} = \frac{j\mu_0\sigma \left[d_{mn} + \mu_0\sigma\tau_{mn} + \mu_0\sigma\kappa_{mn}\tau_{mn} \left(\coth(\varsigma_{mn}h) / \varsigma_{mn} - h\text{cosech}^2(\varsigma_{mn}h) \right) \right]}{d_{mn}^2} \quad (5.223)$$

Substituting (5.223) into (5.210) the electromagnetic torque damping is obtained

$$D_{torque} = -\frac{lwP^2}{\mu_0} \text{Im} \sum_{m=-M}^M \sum_{n=-N}^N \left| S_{mn}^y \right|^2 \frac{e^{-2\kappa_{mn}g} j\mu_0\sigma}{\kappa_{mn} d_{mn}^2} \left[d_{mn} + \mu_0\sigma\tau_{mn} + \mu_0\sigma\kappa_{mn}\tau_{mn} \left(\coth(\varsigma_{mn}h) / \varsigma_{mn} - h\text{cosech}^2(\varsigma_{mn}h) \right) \right] \quad (5.224)$$

$$D_{torque} = -lw\sigma P^2 \text{Re} \sum_{m=-M}^M \sum_{n=-N}^N \left| S_{mn}^y \right|^2 \frac{e^{-2\kappa_{mn}g}}{\kappa_{mn} d_{mn}^2} \left[d_{mn} + \mu_0\sigma\tau_{mn} + \mu_0\sigma\kappa_{mn}\tau_{mn} \left(\coth(\varsigma_{mn}h) / \varsigma_{mn} - h\text{cosech}^2(\varsigma_{mn}h) \right) \right] \quad (5.225)$$

5.13. Model Validation

For validation purpose a segmented Halbach rotor moving over a conductive plate, as shown in Figure 5.1, has been considered. The accuracy of this analytic model highly depends on the source field modeling of the Halbach rotor. But as already discussed in chapter 2 the source field can be accurately, for engineering purposes, modeled using planar magnetic charge sheet. Hence in this chapter the Halbach rotor field will not be validated.

In this section, the magnetic fields in the conductive region will be compared with a previously developed steady state FEA model where the Halbach rotor was modeled using a novel current sheet approach [75]. In addition to this FEA model, the FEA model based on a magnetic charge source modeling approach, as discussed in chapter 3, will be

used for force and power loss comparison. Results for different plate width will be compared and it will be shown that as the plate width reduces the analytic model fails to calculate the correct result.

5.13.1. Field Validation

The simulation parameters used for the field validation are given in Table 5.1. Figure 5.9 shows the subdomain plots of the induced magnetic flux density in the conductive plate obtained from the FEA model [75]. The field comparisons are performed at 15 ms^{-1} translational velocity and 25 ms^{-1} slip speed. The slip speed is defined as

$$s_l = \omega_m r_o - v_x \quad (1.1)$$

Figure 5.10 illustrates a comparison between the analytically computed (using (5.96) and (5.97)) and FEA calculated x and z components of the magnetic vector potential. The induced magnetic flux density components are compared in Figure 5.11. A relatively close match has been obtained.

Table 5.1 : Parameters for simulation without heave velocity and large plate width

	Description	Value	Unit
Magnetic Rotor	Outer radius, r_o	50	mm
	Inner radius, r_i	34.2	mm
	Width, w_o	50	mm
	Remnant magnetic flux density, B_{rem}	1.42	T
	Relative permeability, μ_r	1.055	-
	Pole pairs, P	4	-
Conductive plate	Conductivity, σ	2.459×10^7	Sm^{-1}
	Width, w	150	mm
	Length, l	200	mm
	Thickness, h	6.3	mm
	Air-gap between rotor and plate, g	9.5	mm

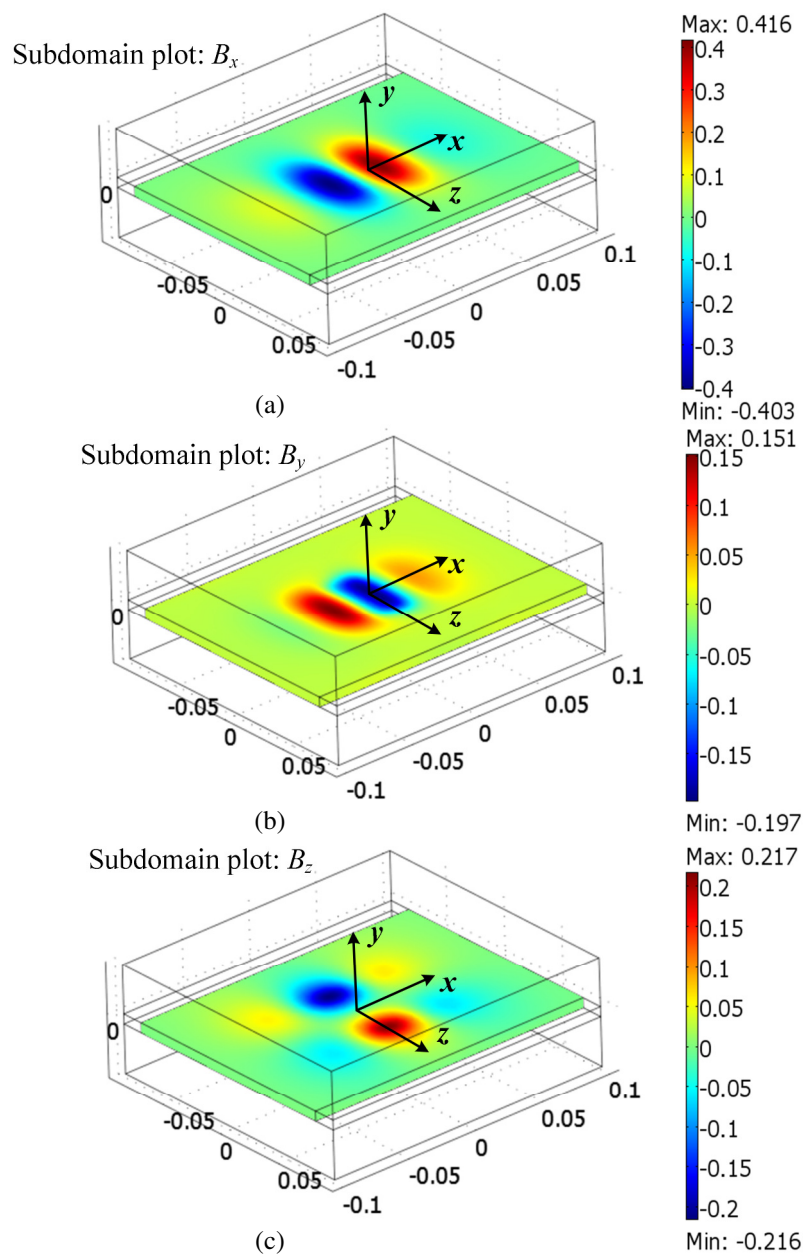


Figure 5.9. Plots of (a) B_x , (b) B_y and (c) B_z magnetic flux density components induced in the conductive plate due to a Halbach rotor moving at 15ms^{-1} translational velocity and 25ms^{-1} slip speed above the plate. The plots are obtained from FEA steady state model with current sheet based Halbach rotor field modeling approach. The model was written using Comsol v3.5a and Matlab. The rotor is located at the center of the plate

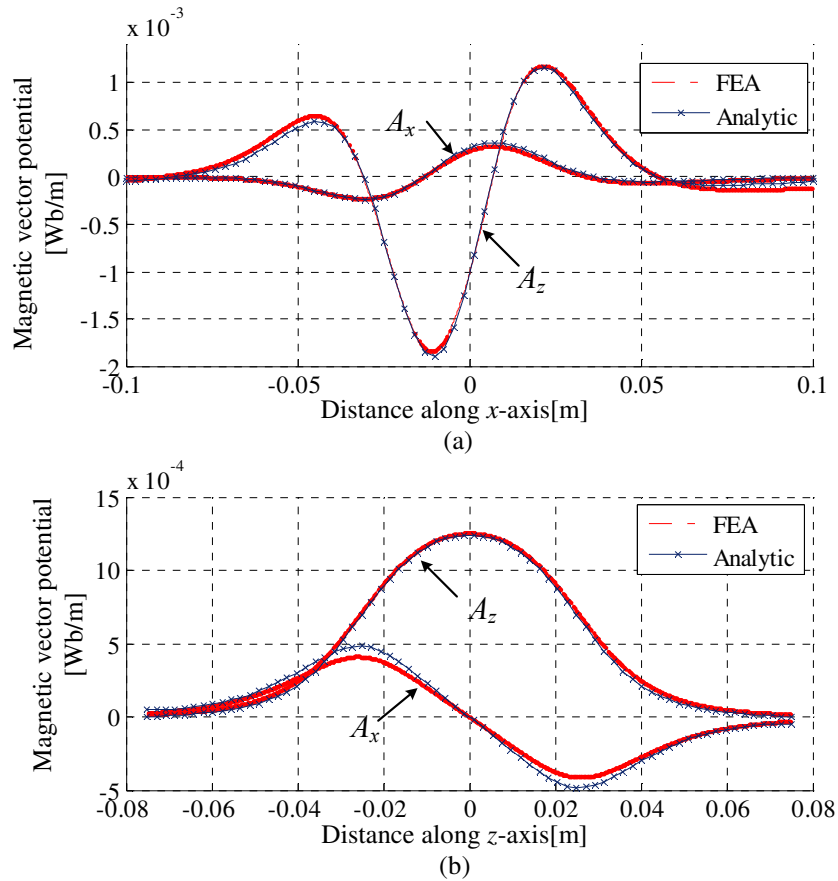


Figure 5.10. Comparison of the x and z components of the magnetic vector potential on the top surface of the conductive plate between the analytic and current sheet based Comsol finite element model (a) across x -axis for $z = -10\text{mm}$; (b) across z -axis for $x = 20\text{mm}$. The rotor is located at the center of the plate

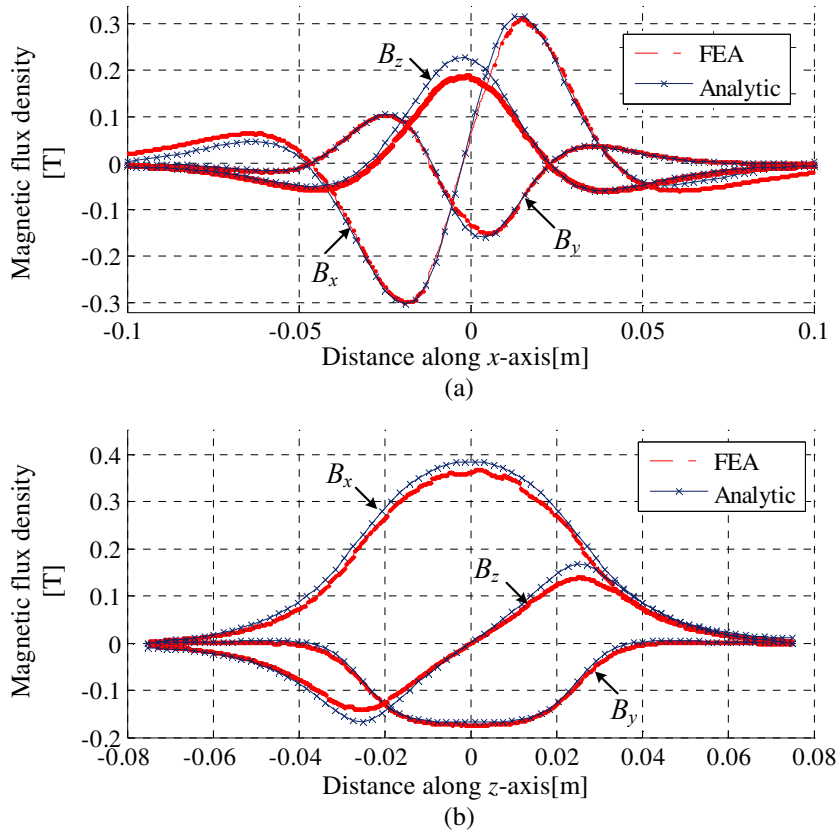


Figure 5.11. Comparison of the x , y and z components of the magnetic flux density on the top surface of the conductive plate between the analytic and current sheet based Comsol finite element model (a) across x -axis for $z = 20\text{mm}$; (b) across z -axis for $x = 10\text{mm}$. The rotor is located at the center of the plate

5.13.2. Force and Power Loss Validation

Using the parameters given in Table 5.1, the force and power loss comparison as a function of slip speed for the analytic and FEA models are illustrated in Figure 5.12.

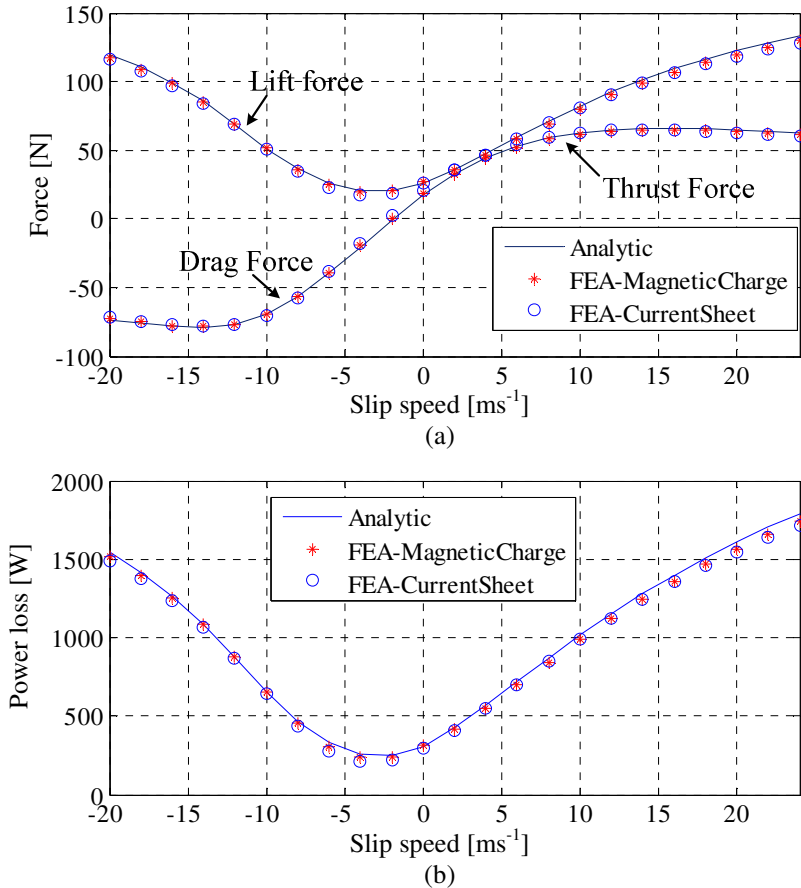


Figure 5.12. (a) Force and (b) power loss comparison among analytic and FEA models based on current sheet and magnetic charge modeling techniques for $(v_x, v_y) = (15, 0)$ ms⁻¹. The rotor is located at the center of the plate

The average computation time involved in calculating the force and power loss results for a single slip speed value by the FEA and analytic models are listed in Table 5.2. As expected, the analytic model reduces the computation time by approximately an order of 1000.

Table 5.2. : Computation time for analytic and finite element steady state models

Model type	Computation time	Unit
Magnetic charge based steady state model using Comsol v3.5a	160	s
Current sheet based steady state model using Comsol v3.5a	440	s
Analytic SOVP model	0.038	s

The Comsol finite element model using current sheet approach does not include the heave velocity in the formulation [75]. Thus for comparisons in the presence of the heave velocity of the rotor, the FEA model with magnetic charge based source modeling

approach (discussed in chapter 3) has been used. Table 5.3 lists the parameters used for the comparison and Figure 5.13 shows the force and power loss comparison between the analytic and FEA model. Again a very good match was obtained.

Table 5.3. : Parameters for simulation with heave velocity and large plate width

	Description	Value	Unit
Magnetic Rotor	Outer radius, r_o	26	mm
	Inner radius, r_i	9.62	mm
	Width, w_o	52	mm
	Remnant magnetic flux density, B_{rem}	1.42	T
	Relative permeability, μ_r	1.108	-
	Pole pairs, P	2	-
Conductive plate	Conductivity, σ	2.459×10^7	Sm^{-1}
	Width, w	150	mm
	Length, l	200	mm
	Thickness, h	6.3	mm
	Air-gap between rotor and plate, g	9.5	mm

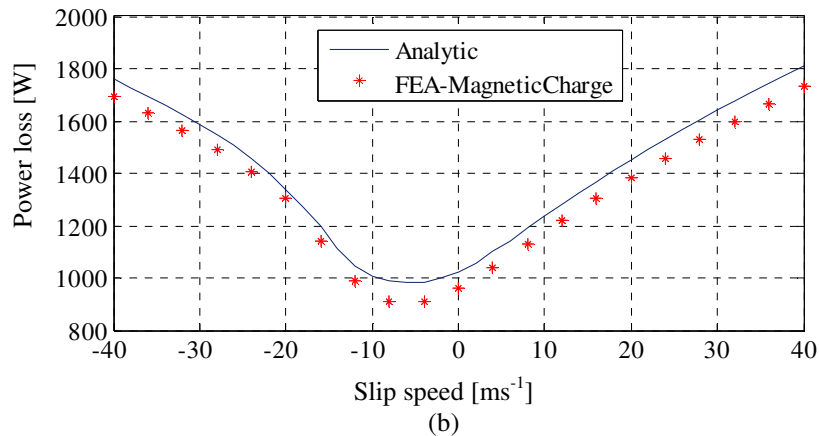
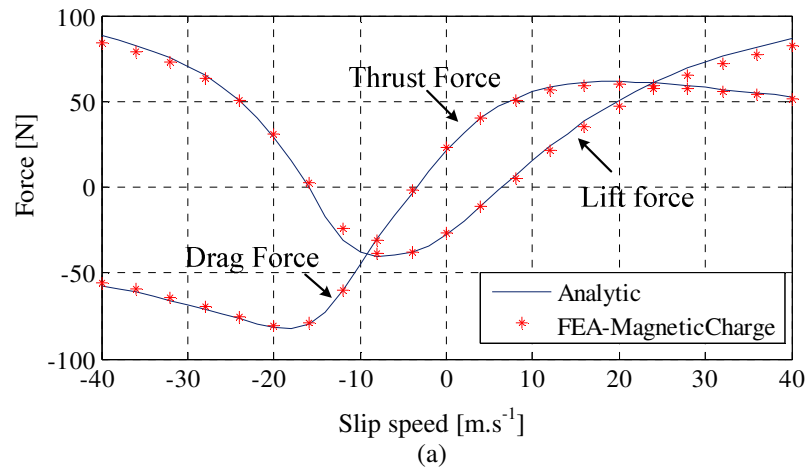


Figure 5.13. (a) Force and (b) power loss comparison between analytic and FEA model based on magnetic charge source modeling techniques for $(v_x, v_y) = (20, 2) \text{ ms}^{-1}$. The rotor is located at the center of the plate.

In the following comparisons, the plate width has been reduced to 77mm to study the performance of the analytic model when a reduced conductive plate width is used. A width of 77mm is chosen as this is the width of the experimental guideway wheel that is being used (shown in Figure 1.20). Figure 5.14 shows excellent results from the analytic model even for the reduced plate width when the rotor is located at the center of the plate (laterally). Also, in the presence of the heave velocity the analytic model performs extremely well for reduced plate width as is evident from Figure 5.15. Table 5.4 compares the average accuracy of the developed SOVP based steady state analytic model with respect to the Comsol based steady state FEA models for 77 mm guideway width, 15ms^{-1} translational velocity and zero heave velocity.

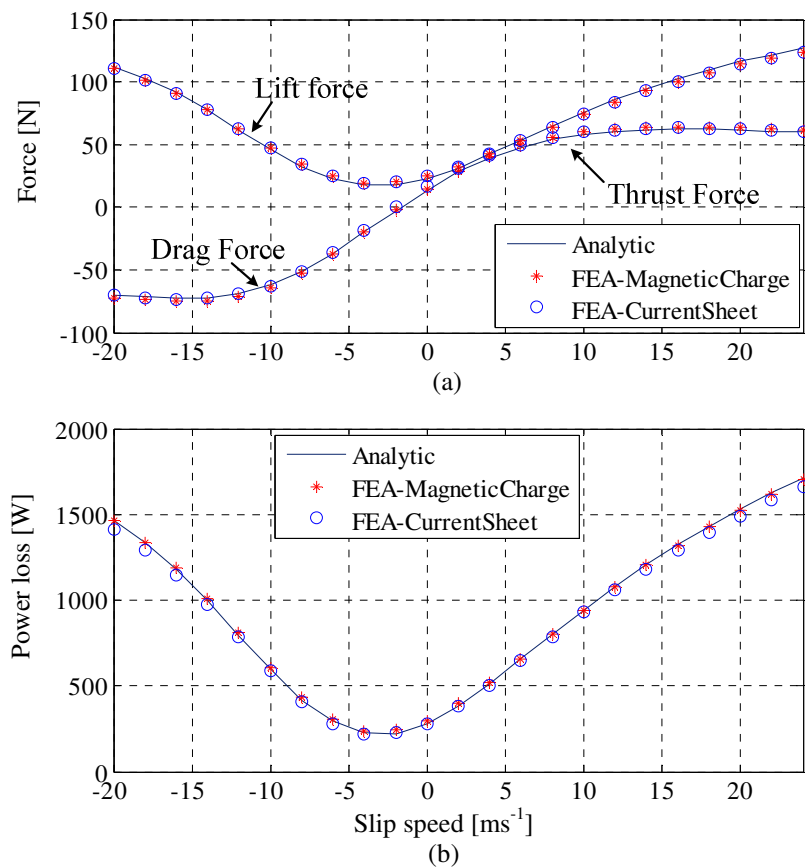
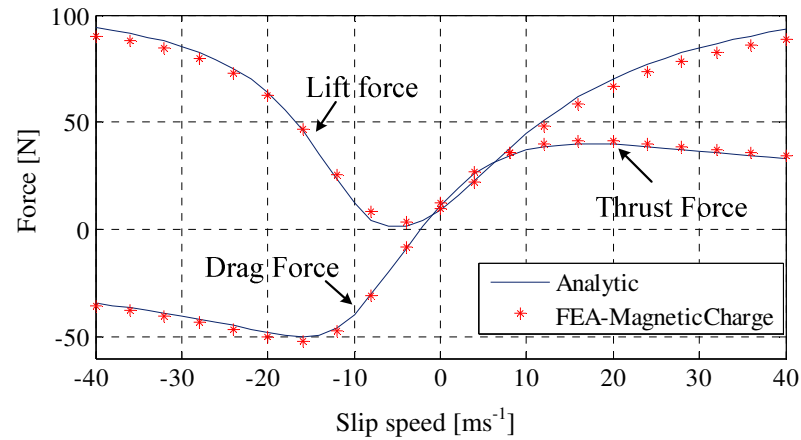


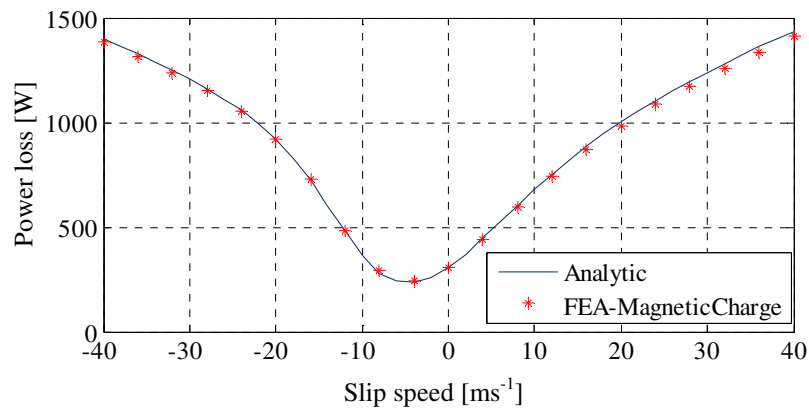
Figure 5.14. (a) Force and (b) power loss comparison among analytic and FEA models based on current sheet and magnetic charge source modeling techniques for $(v_x, v_y) = (15, 0) \text{ms}^{-1}$. The rotor is located at the center of the plate.

Table 5.4 : Accuracy of the developed SOVP based analytic steady state model

Parameter	Error with FEA magnetic charge [%]	Error with FEA current sheet [%]
Thrust force	2.92	1.35
Lift force	0.42	0.48
Power loss	0.22	2.08



(a)



(b)

Figure 5.15. (a) Force and (b) power loss comparison between analytic and FEA model based on magnetic charge source modeling techniques for $(v_x, v_y) = (15, 2) \text{ ms}^{-1}$. The rotor is located at the center of the plate.

The analytical model performs very well for a reduced plate width in which the plate is wider than the rotor, however, when the rotor is laterally offset (along z -axis), the model fails to calculate the correct result. Figure 5.16 (a) and (b) show that the analytic thrust force and power loss values are different from the FEA counterparts by a large

margin for a lateral offset of 25mm. The main shortcoming of the presented analytic model is in the calculation of the lateral force which is compared in Figure 5.16 (c).

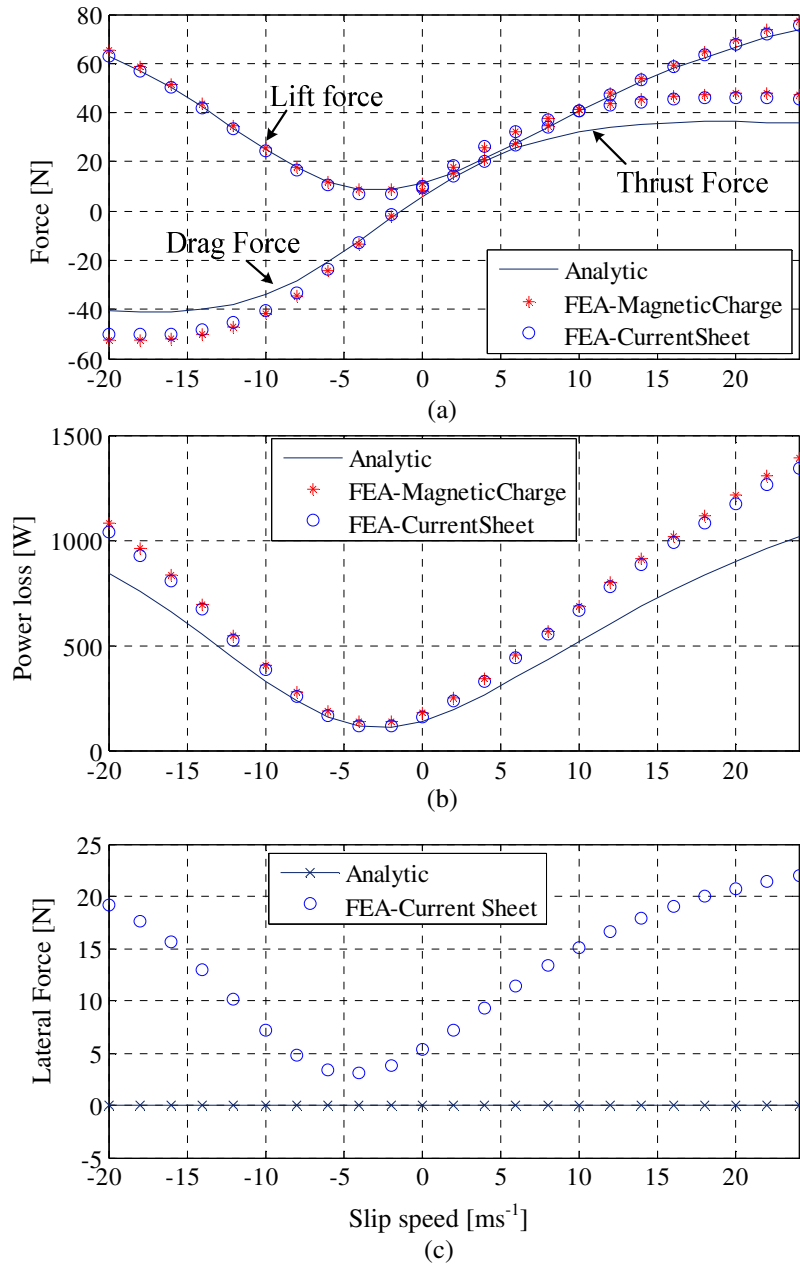


Figure 5.16. (a) Thrust/ drag and lift force; (b) power loss and (c) lateral force comparison among the analytic and FEA models based on current sheet and magnetic charge source modeling techniques for $(v_x, v_y) = (15, 0) \text{ ms}^{-1}$. The rotor is laterally offset from the center of the plate by 25mm.

5.14. Stiffness and Damping Coefficients Results

Using the parameters given in Table 5.3, the lift and drag force as a function of translational velocity for the case when $\omega_e = 0 \text{ rads}^{-1}$ and $(v_z, v_y) = (0, 0) \text{ ms}^{-1}$ is shown in

Figure 5.17. The lateral force, F_z , is insignificant at $v_z=0$ and without lateral offset of the rotor, thus F_z is not shown in Figure 5.17.

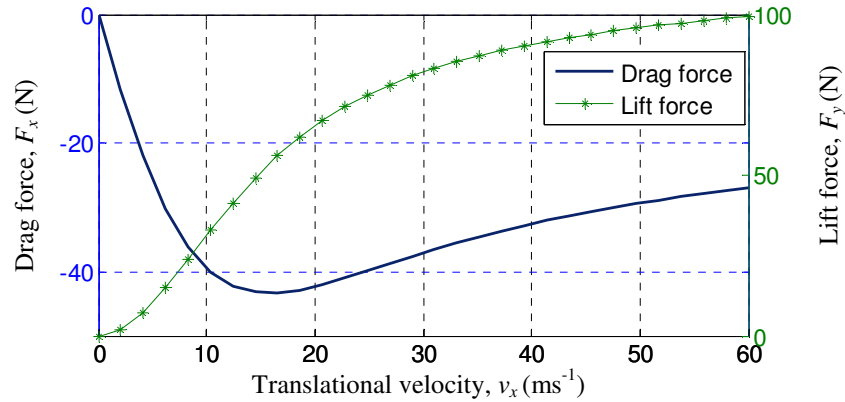


Figure 5.17. Electrodynamic F_x and F_y as a function of translational velocity for $(\omega_e, v_y, v_z) = (0 \text{ rads}^{-1}, 0 \text{ ms}^{-1}, 0 \text{ ms}^{-1})$. As $\omega_e=0 \text{ rads}^{-1}$ the F_x force is a drag force.

The stiffness coefficients as functions of translational velocity, v_x , are shown in Figure 5.18. The lateral force, F_z , is insignificant at $v_z=0$ and without lateral offset of the rotor, thus F_z is not shown in Figure 5.18. The stiffness coefficients k_{yy} is positive for increase in translational velocity. It implies that when the rotor comes close to the conductive plate, it will be pushed back because of a positive stiffness which is a necessary condition for stability. The stability exists in the direction of positive stiffness if the reaction force acts to oppose perturbation in displacements [200]. Also Figure 5.18(a) proves the validity of (5.158). The negative stiffness k_{xy} results as the drag force decreases with height. The off-diagonal stiffness terms with respect to the z -direction i.e. k_{xz} (or k_{zx}) and k_{yz} (or k_{zy}) are negligibly small for large plate width assumption and zero lateral offset of the rotor and hence not shown.

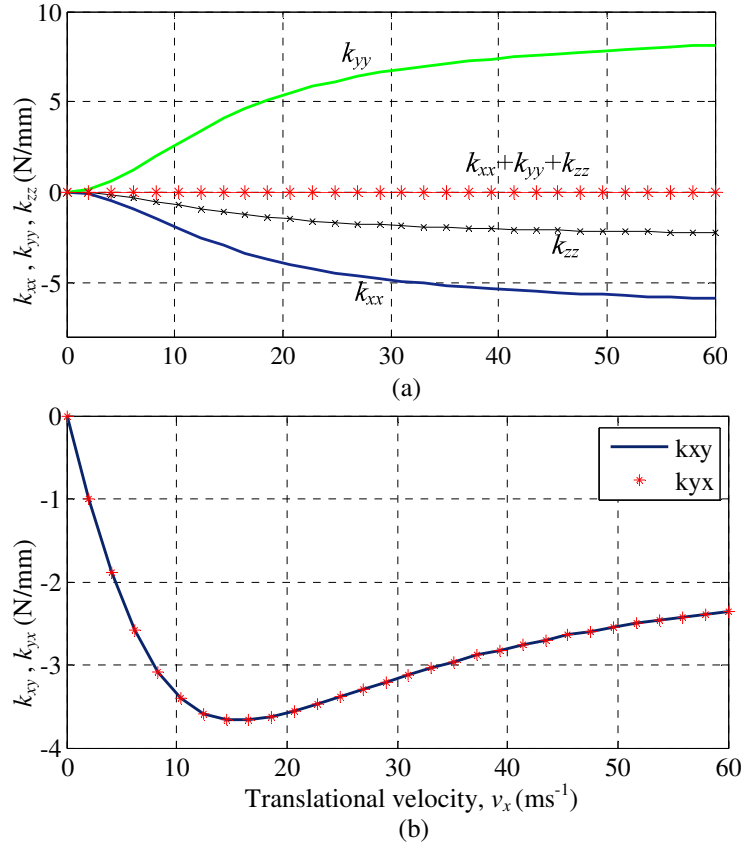


Figure 5.18. The electrodynamic stiffness coefficients as a function of translational velocity for $(\omega_e, v_y, v_z) = (0 \text{ rads}^{-1}, 0 \text{ ms}^{-1}, 0 \text{ ms}^{-1})$.

Figure 5.19 shows linear variation in the lift and drag forces for small change in the heave velocity, v_y . As the lateral force, F_z , is insignificant at the chosen operating condition, it is not shown in Figure 5.19. Figure 5.20 and Figure 5.21 show the horizontal and vertical damping constants calculated using (5.181), (5.196)-(5.208). The damping coefficient D_{xx} is positive at $v_x=0\text{m/s}$ and becomes zero when the drag force reaches its peak value (as shown in Figure 5.17) and becomes negative with further increase in the translational velocity, v_x resulting in decreasing drag force. From the perspective of energy, positive damping means energy is taken away from the system whereas negative damping implies adding energy to the system [201]. The damping coefficient D_{yx} as shown in Figure 5.20 can be understood from the slope of the lift force vs. v_x curve

shown in Figure 5.17. Since the lift force increases with increase in v_x (see Figure 5.17), energy is being added to the system, hence, the damping coefficient D_{yx} is negative.

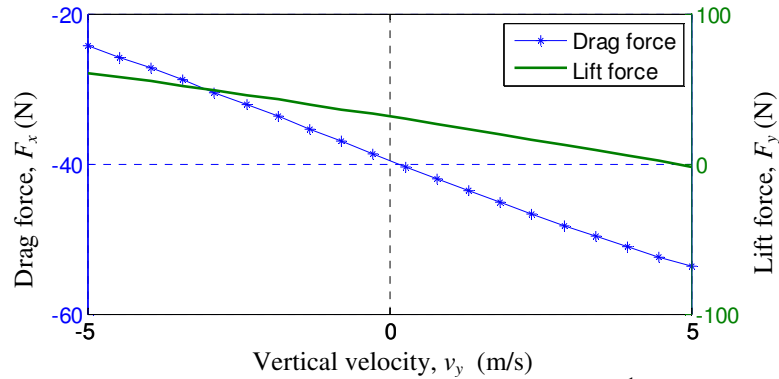


Figure 5.19 Lift, F_y and drag force, F_x vs. heave velocity, v_y , for $\omega_e = 0 \text{ rads}^{-1}$ and $(v_x, v_z) = (10, 0) \text{ ms}^{-1}$

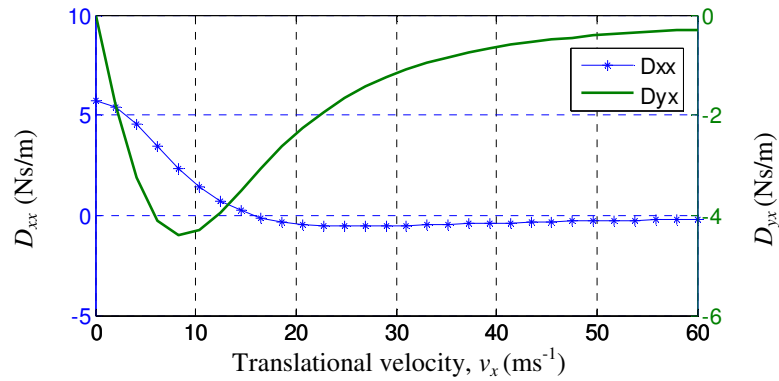


Figure 5.20 The electrodynamic damping terms, D_{xx} and D_{yx} .

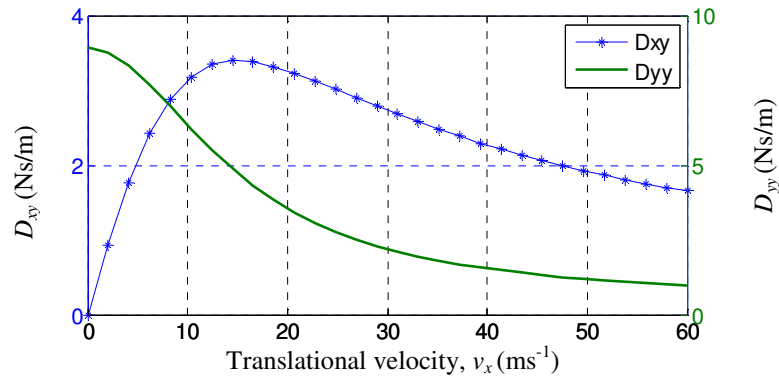


Figure 5.21 The electrodynamic damping terms, D_{xy} and D_{yy} .

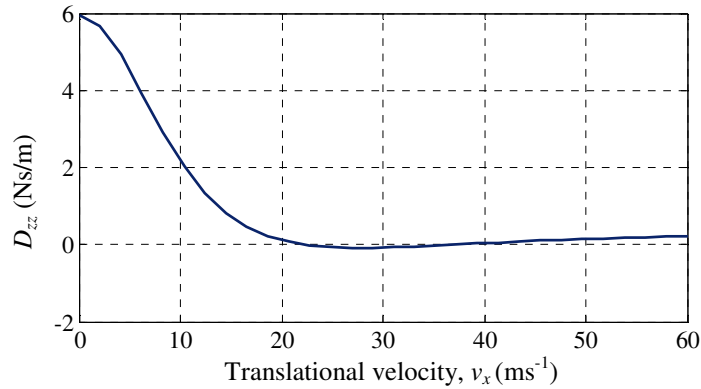


Figure 5.22 The electrodynamic damping term D_{zz} .

Both drag and lift force decrease with increase in heave velocity (see Figure 5.19), thus the energy is being taken away from the system. Therefore, the damping coefficients D_{xy} and D_{yy} are both positive. The vertical damping coefficient, D_{yy} decreases and becomes almost zero with increase in translational velocity. However, the damping coefficient D_{xy} is initially zero and increases to its maximum value and decreases with further increase in translational speed. These damping characteristics shown in Figure 5.21 agree with the calculations performed by Yoshida [202], Urankar [203] and Ooi [204] in which no negative vertical damping was calculated. Figure 5.22 shows that D_{zz} damping term is significant only at low translational velocity and at high-speed it practically becomes negligible. The remaining off-diagonal damping terms are negligibly small for large plate width assumption and zero lateral offset of the rotor and hence not shown.

For the case when $\omega_e \neq 0$, a slip will be present as defined by (1.1). Depending on the slip value the F_x can be either a thrust or a drag force as shown in Figure 5.23. The F_x and F_y as function of slip and translational speed are shown in Figure 5.24 while Figure 5.25 shows the stiffness contour plots. From Figure 5.25 it is observed that k_{xx} and k_{zz} are almost always negative and thus leads to instability whereas k_{yy} is always positive and the

coupling term k_{xy} is positive for positive slip values and changes sign with negative slip speeds. Hence, judging from the stiffness constants it can be stated that the Halbach rotor moving above a conductive plate is stable along the y -direction but unstable along the forward x lateral z -directions.

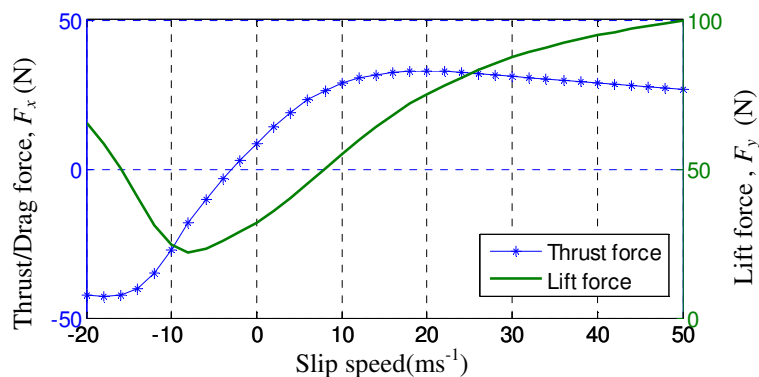


Figure 5.23 F_x and F_y force as function of slip when $(v_x, v_y, v_z) = (20, 0, 0) \text{ ms}^{-1}$

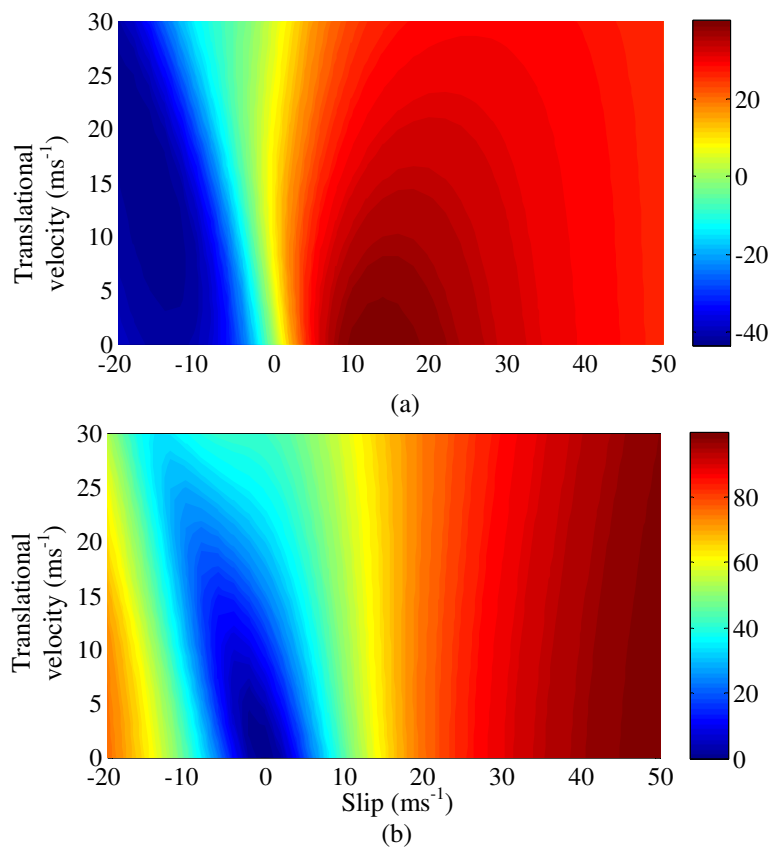


Figure 5.24 (a) Thrust force and (b) lift force function of slip and translational velocity at $(v_x, v_z) = (0, 0) \text{ ms}^{-1}$.

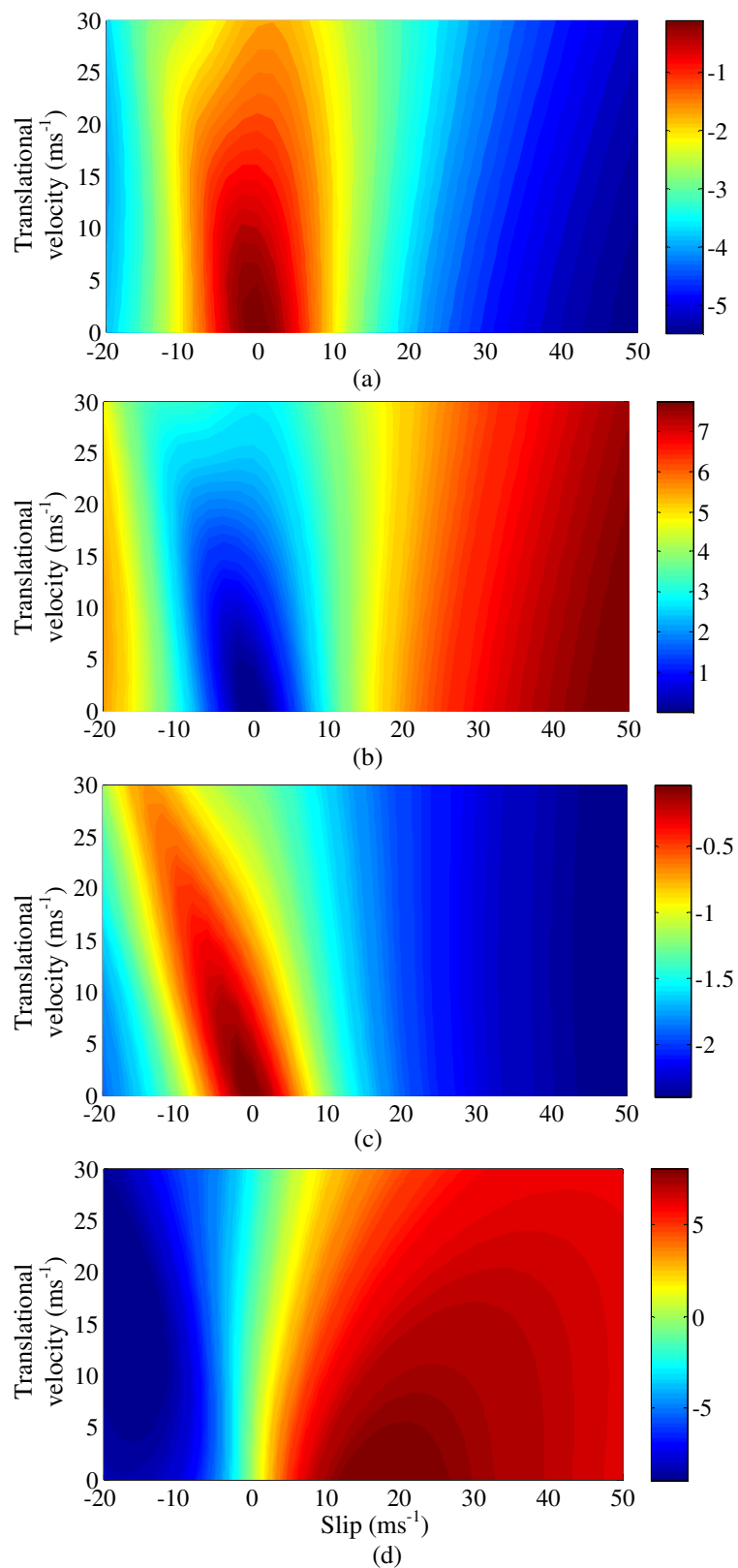


Figure 5.25 The stiffness coefficients (a) k_{xx} , (b) k_{yy} , (c) k_{zz} and (d) k_{xy} (or k_{yx}) as a function of slip and translational velocity at $(v_y, v_z) = (0, 0)$ ms⁻¹.

The damping constants are shown in Figure 5.26 and Figure 5.27. Unlike in Figure 5.20, the horizontal damping coefficient, D_{xx} , becomes positive when both the translational and rotational speed are included. The magnitude of D_{xx} however decreases with increase in slip value as shown in Figure 5.26(a). It can be noted that the vertical damping, D_{yy} , is always positive but decreases with slip value. Lateral damping D_{zz} decreases with increasing slip speed and translational velocity. The off-diagonal damping term D_{yx} is positive for positive slip values whereas the other off-diagonal damping term D_{xy} is negative in that slip region and therefore this term is likely to create instabilities at positive slip condition. The decrease of the magnetic damping values at positive slip values suggests that the inherent magnetic damping is insufficient and therefore active control of an electrodynamic maglev system is essential.

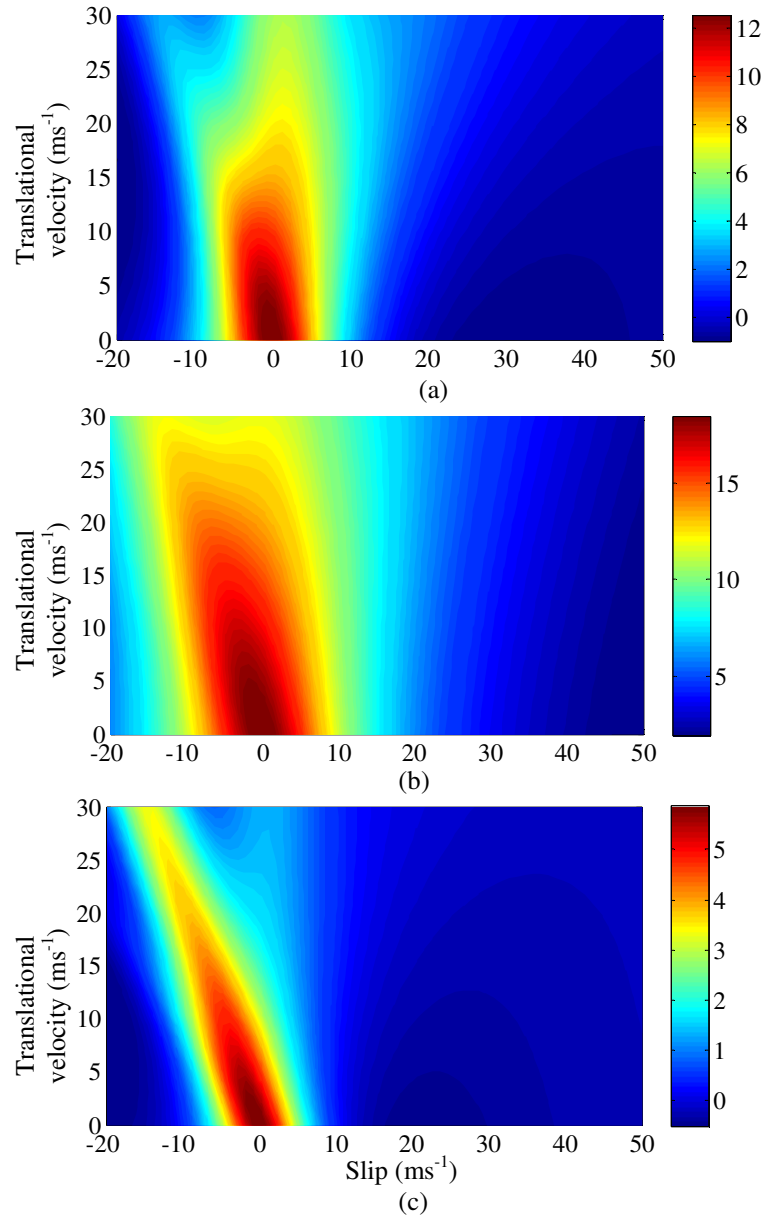


Figure 5.26 Damping coefficient (a) D_{xx} (b) D_{yy} and (c) D_{zz} as a function of slip and translational velocity at $g=5\text{mm}$ and $(v_y, v_z)=(0,0)\text{ms}^{-1}$.

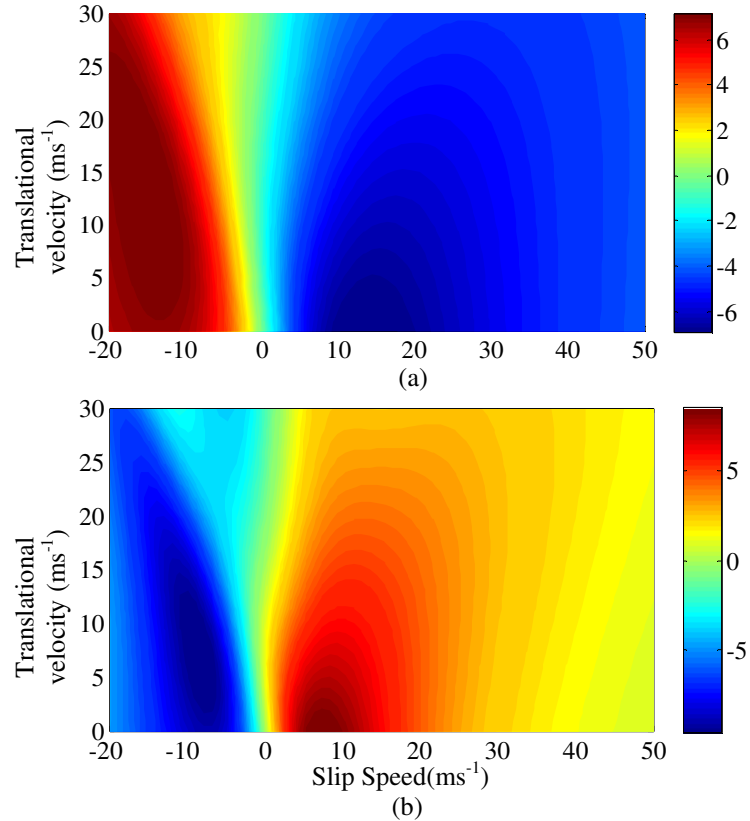


Figure 5.27 Damping coefficient (a) D_{xy} and (b) D_{yx} as a function of slip and translational velocity at $g=5\text{mm}$ and $(v_y, v_z)=(0,0)\text{ms}^{-1}$.

5.15. Summary

An analytic steady state modeling approach to study the eddy current distributions, force and power loss in a conductive plate of infinite dimension has been presented. The key points of the developed model are outlined in Table 5.5. The model is based on the SOVP and thus only one scalar potential namely the TE potential is required to formulate the entire problem region and thus it is computationally very fast. Computation time has been compared with FEA models. Also an electromagnetic force and power loss comparison has been made to suggest that the model can be very useful for plate width of at least one and half times that of the source.

However, the proposed analytic approach fails to model the eddy current distribution when the source is laterally offset towards the edge of the plate. Therefore there is clearly

a need for finding a new model to account for the edge effect of the finite width conductive plate. This will be discussed in the next chapter.

Table 5.5 : Summary of the presented 3-D analytic steady state model using SOVP

Model assumptions	Model characteristics
<ul style="list-style-type: none"> • Conductive plate is linear, simply connected and homogenous • Conductive plate has constant conductivity and is non-magnetic • Frequency is low • Conductive plate is infinitely long and wide, but has finite thickness 	<ul style="list-style-type: none"> • Models the conductive and nonconductive domains using TE potential of the SOVP. • Can be applicable for any magnetic source • Computes the source field using magnetic charge sheet • Models translational, heave, lateral as well as rotational motion of the source • Computationally very fast • Accurate when the plate dimension is large compared to the source dimension. In other words, it is accurate when the induced eddy currents do not see the edge of the plate. • Model has been developed in Matlab

CHAPTER 6 : 3-D ANALYTIC EDDY CURRENT MODELING FOR FINITE WIDTH CONDUCTIVE PLATE

6.1. Introduction

As pointed out in the previous chapter, the assumption of an infinitely large width for the conductive plate fails to model the eddy current distribution when the source is moved towards the edge of the plate. This chapter will present two 3-D analytic eddy current modeling techniques using magnetic vector potential (MVP) for a conductive plate of finite width and thickness. In the first analytic model only two-components of the magnetic vector potential will be used with the assumption of small plate thickness whereas the second model does not assume small thickness and uses all three components of the magnetic vector potential. The length of the plate will be assumed to be large. The models will include the translational and heave motion of the magnetic source. This chapter will compare the fields induced in the plate and forces acting on the source for different lateral positions of the source with finite element models.

Consider a maglev application [13, 74, 75] where the magnetic source, which is a special type of magnetic rotor called a Halbach, as shown in Figure 6.1, is moved and rotated over a plate made of conductive and non-magnetic material, such as aluminum. Figure 6.2 shows the x - y and z - y view of the problem regions. The conductive plate, region Ω_{II} , has a length l , width, w , and height, h and the magnetic rotor is located at a distance g above the conductive plate. Also the source velocities in the x and y -directions

as well as rotational speed ω_m are shown in the figure. It must be noted here that although Figure 6.1 and Figure 6.2 display a magnetic rotor as the source, the field and force equations derived in the proposed model are applicable to any kind of magnetic source.

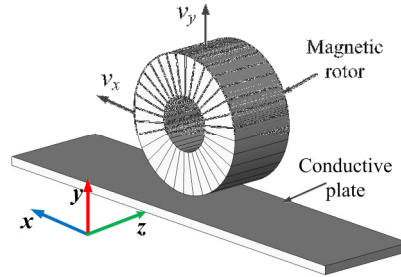


Figure 6.1. 3-D schematic of a magnetic rotor rotating and translationally moving over a conductive, non-magnetic plate.

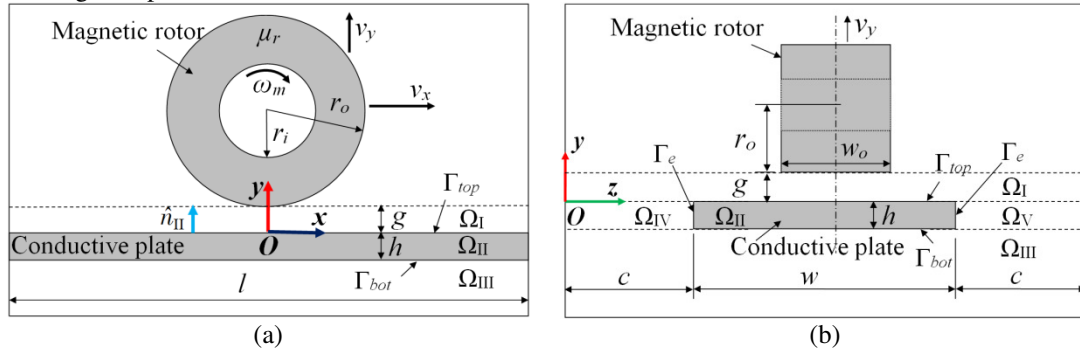


Figure 6.2. (a) x - y view and (b) z - y view of the problem regions. The rotor is at the center of the conductive region located at $(x_c, y_c, z_c) = (0, r_o + g, c + w/2)$.

The conductive medium is located at $y=0$ of the Cartesian coordinate system which creates five regions as shown in Figure 6.2:

- Region I (Ω_I) is the air or nonconductive region between the magnetic source and conductive plate located at $0 \leq y \leq g$, $0 \leq z \leq 2c + w$
- Region II (Ω_{II}) is the conductive region located at $-h \leq y \leq 0$, $c \leq z \leq c + w$
- Region III (Ω_{III}) is the air or nonconductive region below the conductive plate located at $y \leq -h$, $0 \leq z \leq 2c + w$.
- Region IV (Ω_{IV}) is the air or nonconductive region to the side of the conductive plate located at $-h \leq y \leq 0$, $0 \leq z \leq c$

- Region V (Ω_V) is the air or nonconductive region to the side of the conductive plate located at $-h \leq y \leq 0$, $c + w \leq z \leq 2c + w$

The assumptions of the analytic models presented in this chapter are:

- The plate length, l , is infinite but width, w , is finite
- The plate has finite thickness, h .
- For 2-component vector potential model it is assumed that the plate thickness, h , is small. Thus fields in regions Ω_{IV} and Ω_V are not modeled. However, in 3-component vector potential model this assumption is alleviated and fields in Ω_{IV} and Ω_V are modeled.
- The plate is continuous with constant conductivity and non-magnetic.
- The magnetic source has translational and heave motion along with rotational motion.
- The frequency is sufficiently low in order for the quasi-static approximation to be valid.

This chapter presents a two-component analytic MVP model in section 6.3-section 6.9 and an improved three-component model in section 6.10. The chapter is organized as follows: section 6.2 will describe the governing equations for all the problem regions outlined above and section 6.3 will discuss the boundary conditions; section 6.4 will derive the general solution for different problem regions; section 6.5 will talk about the source field modeling; electromagnetic fields will be calculated in section 6.6; electromagnetic forces will be derived in section 6.7 which will be followed by power loss and electromagnetic torque calculation in section 6.8; model validation will be performed in section 6.9; the limitations of the developed two-component MVP model

will be discussed and a three-component analytic MVP model will be presented in section 6.10 and finally a summary of the chapter will be provided in section 6.11.

6.2. Governing Equation Formulation

In the proposed model the conductive and nonconductive regions will be modeled using the magnetic vector potential. The finite width of the conductive plate will be taken into account by choosing appropriate Fourier series expansion for the vector potentials and source fields. The governing equation modeling in terms of the magnetic vector potential is given by (3.23) in chapter 3 and here it is reproduced for convenience

$$\nabla^2 \mathbf{A} = \mu_0 \sigma \left(\frac{\partial \mathbf{A}}{\partial t} + (\mathbf{v} \cdot \nabla) \mathbf{A} \right) \quad (3.23)$$

where μ_0 is the permeability [Hm^{-1}] of the free-space, σ is conductivity [Sm^{-1}] of the conductive plate and \mathbf{v} is the velocity [ms^{-1}] of the source. In the steady state the vector potential can be assumed to have the following solution

$$\mathbf{A}(x, y, z, t) = \mathbf{A}(x, y, z) e^{-j\omega_e t} \quad (3.58)$$

where ω_e is the electrical angular frequency [rads^{-1}] of the source. It can be due to excitation current frequency or angular speed of the rotor.

6.2.1. Conductive Region (Ω_{II})

As the induced eddy current flows parallel to the plate when the source is at the center of the plate, the y -component of the induced eddy current is negligible [141, 182, 185]. Also as the thickness is assumed to be small, the y -component of the eddy current and also the magnetic vector potential is assumed to be negligible even when the source moves towards the edge of the plate (refer to Figure 3.16 and Figure 3.17). With this

assumption, the magnetic vector potential can be written in terms of only the x and z -components as follows

$$\mathbf{A}^{\text{II}}(x, y, z) = A_x^{\text{II}}(x, y, z)\hat{x} + A_z^{\text{II}}(x, y, z)\hat{z} \quad (6.1)$$

where \hat{x} and \hat{z} are the normal vectors along the x and z directions respectively and superscript ‘II’ indicates region II. Assuming the source has velocities along the x and y -directions, (3.23) can be decomposed into the following scalar equations

$$\nabla^2 A_i^{\text{II}} = -\mu_0 \sigma \left(j\omega_e A_i^{\text{II}} + v_x \frac{\partial A_i^{\text{II}}}{\partial x} + v_y \frac{\partial A_i^{\text{II}}}{\partial y} \right), \quad i = x, z \quad (6.2)$$

6.2.2. Nonconductive Regions I and III (Ω_{I} and Ω_{III})

In the nonconductive region I the total vector potential is composed of the source field and reflected field due to induced eddy currents in the plate. Also if the lateral dimension of the plate is almost equal to that of the source or if source is laterally shifted towards the edge, the total vector potential in region III is composed of the source field and transmitted field due to induced eddy current in the plate. Hence

$$\mathbf{A}^{\text{I}} = \mathbf{A}^{\text{I},s} + \mathbf{A}^{\text{I},r} \quad (6.3)$$

$$\mathbf{A}^{\text{III}} = \mathbf{A}^{\text{III},s} + \mathbf{A}^{\text{III},t} \quad (6.4)$$

In (6.3) and (6.4) superscripts ‘ s ’, ‘ r ’ and ‘ t ’ indicate the source, reflected and transmitted fields respectively. Equation (6.4) does not have the source term if the source is located at the center of the plate and its lateral dimension is much smaller than that of the plate.

However, unlike [166, 167, 169-171] the computation of the source fields in terms of the vector potential $\mathbf{A}^{\text{I},s}$ and $\mathbf{A}^{\text{III},s}$ in the nonconductive regions can be avoided by noting that only knowledge of the source field on the conductive plate surface is required in

order to calculate the eddy current field within the conductive region [185, 188]. Hence the governing equation within the nonconductive regions I and III only needs to be formulated in terms of the reflected and transmitted magnetic vector potential respectively which follow the following Laplace's equation

$$\nabla^2 \mathbf{A}^{l,r} = 0 \quad (6.5)$$

$$\nabla^2 \mathbf{A}^{III,t} = 0 \quad (6.6)$$

6.2.3. Nonconductive Regions IV and V (Ω_{IV} and Ω_V)

It is assumed that the vector potential, A_z , does not exist within nonconductive side regions Ω_{IV} and Ω_V [141]. Also due to the small thickness of the conductive plate it is reasonable to assume that the A_x vector potential is zero in these regions. This thereby eliminates the need to formulate the vector potential in the side regions Ω_{IV} and Ω_V .

6.3. Boundary Conditions

The boundary conditions will be written assuming the lateral dimension of the source is comparable to that of the plate or the source is located near the edge of the plate. Based on these assumptions, the source field will be included in the boundary conditions for the top and bottom conductive region boundaries at $y = 0$ and $y = -h$ respectively. In order to obtain the field and force solutions when the aforementioned assumptions do not hold true, the source term on the bottom conductive surface can simply be neglected.

From the continuity of the tangential magnetic field and the normal component of the magnetic flux density at $y=0$ and $y = -h$ and noting the fact that the conductive material is non-magnetic, the following must hold true at the interfaces at $y=0$ and $y=-h$

$$B_x^{II} = B_x^{I,s} + B_x^{I,r}, \text{ at } y = 0 \quad (6.7)$$

$$B_y^{\text{II}} = B_y^{\text{I},s} + B_y^{\text{I},r}, \text{ at } y = 0 \quad (6.8)$$

$$B_z^{\text{II}} = B_z^{\text{I},s} + B_z^{\text{I},r}, \text{ at } y = 0 \quad (6.9)$$

and

$$B_x^{\text{II}} = B_x^{\text{III},s} + B_x^{\text{III},t}, \text{ at } y = -h \quad (6.10)$$

$$B_y^{\text{II}} = B_y^{\text{III},s} + B_y^{\text{III},t}, \text{ at } y = -h \quad (6.11)$$

$$B_z^{\text{II}} = B_z^{\text{III},s} + B_z^{\text{III},t}, \text{ at } y = -h \quad (6.12)$$

Using (3.7), (3.9) and ignoring the y -component magnetic vector potential, (5.23) and (5.25) become

$$\frac{\partial A_z^{\text{II}}}{\partial y} = \frac{\partial A_z^{\text{I},r}}{\partial y} + B_x^s, \text{ at } y = 0 \quad (6.13)$$

$$\frac{\partial A_x^{\text{II}}}{\partial y} = \frac{\partial A_x^{\text{I},r}}{\partial y} - B_z^s, \text{ at } y = 0 \quad (6.14)$$

where, for example, B_x^s is the x -component of the source magnetic flux density. Substituting (3.8) into (5.24), the continuity of the normal component flux density at $y = 0$ becomes

$$\left(\frac{\partial A_x^{\text{II}}}{\partial z} - \frac{\partial A_x^{\text{I},r}}{\partial z} \right) - \left(\frac{\partial A_z^{\text{II}}}{\partial x} - \frac{\partial A_z^{\text{I},r}}{\partial x} \right) = B_y^s, \text{ at } y = 0 \quad (6.15)$$

It is seen that the normal boundary condition (6.15) couples the A_x and A_z field terms together which can significantly complicate the solution. However, the A_x and A_z field terms can be decoupled by noting that the Coulomb gauge [112]

$$\nabla \cdot \mathbf{A}^{\text{II}} = 0 \quad (6.16)$$

applies on the boundary [112, 140, 169]. Therefore the Coulomb gauge boundary condition at $y=0$ is

$$\left(\frac{\partial A_x^{\text{II}}}{\partial x} - \frac{\partial A_x^{\text{I},r}}{\partial x} \right) + \left(\frac{\partial A_z^{\text{II}}}{\partial z} - \frac{\partial A_z^{\text{I},r}}{\partial z} \right) = 0, \text{ at } y = 0 \quad (6.17)$$

By taking the partial derivative of (6.15) with respect to x and subtracting it from the partial derivative of (6.17) with respect to z , one obtains

$$\frac{\partial^2}{\partial z^2} [A_z^{\text{II}} - A_z^{\text{I},r}] + \frac{\partial^2}{\partial x^2} [A_z^{\text{II}} - A_z^{\text{I},r}] = -\frac{\partial B_y^s}{\partial x}, \text{ at } y = 0 \quad (6.18)$$

Following the same procedure, for A_x yields at $y=0$

$$\frac{\partial^2}{\partial z^2} [A_x^{\text{II}} - A_x^{\text{I},r}] + \frac{\partial^2}{\partial x^2} [A_x^{\text{II}} - A_x^{\text{I},r}] = \frac{\partial B_y^s}{\partial z}, \text{ at } y = 0 \quad (6.19)$$

The coupled boundary condition (6.15) can now be replaced with the two decoupled boundary conditions (6.18) and (6.19) thereby enabling equations for A_x and A_z to be solved separately [169]. Analogous decoupled equations at $y = -h$ can be obtained such that:

$$\frac{\partial A_z^{\text{II}}}{\partial y} = \frac{\partial A_z^{\text{III},t}}{\partial y} + B_x^s, \text{ at } y = -h \quad (6.20)$$

$$\frac{\partial A_x^{\text{II}}}{\partial y} = \frac{\partial A_x^{\text{III},t}}{\partial y} - B_z^s, \text{ at } y = -h \quad (6.21)$$

$$\frac{\partial^2}{\partial z^2} [A_z^{\text{II}} - A_z^{\text{III},t}] + \frac{\partial^2}{\partial x^2} [A_z^{\text{II}} - A_z^{\text{III},t}] = -\frac{\partial B_y^s}{\partial x}, \text{ at } y = -h \quad (6.22)$$

$$\frac{\partial^2}{\partial z^2} [A_x^{\text{II}} - A_x^{\text{III},t}] + \frac{\partial^2}{\partial x^2} [A_x^{\text{II}} - A_x^{\text{III},t}] = \frac{\partial B_y^s}{\partial z}, \text{ at } y = -h \quad (6.23)$$

In order to ensure the uniqueness of the solution

$$\hat{n}_{\text{II}} \cdot \mathbf{A}^{\text{II}} = 0 \quad (6.24)$$

must also be enforced on the conductive region boundaries [139, 140] where \hat{n}_{II} is the unit normal vector on the conductive boundary as shown in Figure 6.2(a). Equation (6.24) implies the following boundary conditions

$$A_x = 0, \text{ on } x = 0, l \quad (6.25)$$

$$A_z = 0, \text{ on } z = c, c + w \quad (6.26)$$

The outer nonconductive boundaries are assumed to be sufficiently large that the following holds true

$$\mathbf{A}^{\text{I},r} = \mathbf{A}^{\text{III},t} = 0, \text{ on } \Gamma_o \quad (6.27)$$

6.4. Derivation of General Solutions

6.4.1. Conductive Region (Ω_{II})

Using the separation of variables method [132], the x and z -components of the magnetic vector potential in Ω_{II} can be written as

$$A_i^{\text{II}}(x, y, z) = X_i(x)Y_i(y)Z_i(z), \quad i = x, z \quad (6.28)$$

For the conductive region, substituting (6.28) into (6.2) and dividing both sides by $X_i(x)Y_i(y)Z_i(z)$ (assuming they are non-zero functions of spatial variables) yields

$$\frac{X_i''}{X_i} + \frac{Y_i''}{Y_i} + \frac{Z_i''}{Z_i} = -\mu_0\sigma \left(j\omega_e + v_x \frac{X_i'}{X_i} + v_y \frac{Y_i'}{Y_i} \right), \quad i = x, z \quad (6.29)$$

where the superscript prime indicates differentiation.

Let

$$X_i(x) = e^{j\xi_m x}, \quad i = x, z \quad (6.30)$$

with the spatial frequency with respect to x defined as

$$\xi_m = \frac{2\pi m}{l}, \quad -\infty \leq m \leq \infty \quad (6.31)$$

As the conductive medium is assumed to have a large length, the field is not forced to zero at $x = 0$ and l boundaries. Substituting (6.30) into (6.29) gives for all m

$$-\xi_m^2 + \frac{Y_i''}{Y_i} + \frac{Z_i''}{Z_i} = -\mu_0 \sigma \left(j\omega_e + jv_x \xi_m + v_y \frac{Y_i'}{Y} \right), \quad i = x, z \quad (6.32)$$

Rearranging (6.32)

$$\frac{Z_i''}{Z_i} = \xi_m^2 - j\mu_0 \sigma (\omega_e + v_x \xi_m) - \frac{Y_i''}{Y_i} - \mu_0 \sigma v_y \frac{Y_i'}{Y}, \quad i = x, z \quad (6.33)$$

In (6.33) derivatives of two independent functions are equal to each other. Hence both sides must be equal to a constant. Say each side of (6.33) is equal to $-k_n^2$. Hence from (6.33)

$$\xi_m^2 - j\mu_0 \sigma (\omega_e + v_x \xi_m) - \frac{Y_i''}{Y_i} - \mu_0 \sigma v_y \frac{Y_i'}{Y} = -k_n^2, \quad i = x, z \quad (6.34)$$

and

$$\frac{Z_i''}{Z_i} = -k_n^2, \quad i = x, z \quad (6.35)$$

The general solution of (6.35) is

$$Z_i(z) = A_n^i \sin(k_n z) + B_n^i \cos(k_n z), \quad i = x, z \quad (6.36)$$

However, in order to satisfy (6.26) the A_z field should have only sine term whereas the A_x field should have only cosine terms of (6.36) as written below

$$Z_z(z) = A_n^z \sin(k_n(z - c)), \quad 1 \leq n \leq \infty, \text{ for } A_z \quad (6.37)$$

$$Z_x(z) = A_n^x \cos(k_n(z - c)), \quad 0 \leq n \leq \infty, \text{ for } A_x \quad (6.38)$$

and the spatial frequency, k_n , can be defined as

$$k_n = \frac{\pi n}{w} \quad (6.39)$$

From (6.34)

$$\frac{Y_i''}{Y_i} + \mu_0 \sigma v_y \frac{Y_i'}{Y_i} - \xi_m^2 - k_n^2 + j\mu_0 \sigma (\omega_e + v_x \xi_m) = 0, \quad i = x, z \quad (6.40)$$

Or,

$$\frac{Y_i''}{Y_i} + \mu_0 \sigma v_y \frac{Y_i'}{Y_i} - \gamma_{mn}^2 = 0, \quad i = x, z \quad (6.41)$$

where

$$\gamma_{mn}^2 = \xi_m^2 + k_n^2 - j\mu_0 \sigma (\omega_e + v_x \xi_m) \quad (6.42)$$

The roots of (6.41) are

$$\alpha_{mn} = 0.5(-\mu_0 \sigma v_y + \sqrt{(\mu_0 \sigma v_y)^2 + 4\gamma_{mn}^2}) \quad (6.43)$$

$$\beta_{mn} = 0.5(-\mu_0 \sigma v_y - \sqrt{(\mu_0 \sigma v_y)^2 + 4\gamma_{mn}^2}) \quad (6.44)$$

Hence the general solution for $Y_i(y)$ is

$$Y_i(y) = C_{mn}^{\text{II},i} e^{\alpha_{mn} y} + D_{mn}^{\text{II},i} e^{\beta_{mn} y}, \quad i = x, z \quad (6.45)$$

Substituting (6.30), (6.38) and (6.45) into (6.28) for $i = x$ the general solution for the A_x vector potential in the conductive region is obtained as

$$A_x^{\text{II}} = \sum_{m=-M}^M \sum_{n=0}^N e^{j\xi_m x} \cos(k_n(z-c)) \left(C_{mn}^{\text{II},x} e^{\alpha_{mn} y} + D_{mn}^{\text{II},x} e^{\beta_{mn} y} \right) \quad (6.46)$$

Similarly substituting (6.30), (6.37) and (6.45) into (6.28) for $i = z$ the general solution for the A_z vector potential in the conductive region is obtained as

$$A_z^{\text{II}} = \sum_{m=-M}^M \sum_{n=1}^N e^{j\xi_m x} \sin(k_n(z-c)) \left(C_{mn}^{\text{II},z} e^{\alpha_{mn} y} + D_{mn}^{\text{II},z} e^{\beta_{mn} y} \right) \quad (6.47)$$

The Fourier series of (6.46) and (6.47) has M and N harmonics in the x and z -directions respectively. The error introduced by this series truncation can be eliminated by simply choosing a sufficient number of harmonics.

6.4.2. Nonconductive Regions I and III (Ω_{I} and Ω_{III})

Applying the separation of variables method to (6.5) and noting that the field must decay for increasing distance away from the conductive plate the x and z -components of the vector potentials in Ω_{I} are

$$A_x^{\text{I},r} = \sum_{m=-M}^M \sum_{n=0}^N e^{j\xi_m x} \cos(k_n(z-c)) C_{mn}^{\text{I},x} e^{-\kappa_{mn} y} \quad (6.48)$$

$$A_z^{\text{I},r} = \sum_{m=-M}^M \sum_{n=1}^N e^{j\xi_m x} \sin(k_n(z-c)) C_{mn}^{\text{I},z} e^{-\kappa_{mn} y} \quad (6.49)$$

where

$$\kappa_{mn} = \sqrt{\xi_m^2 + k_n^2} \quad (6.50)$$

In (6.48) and (6.49), the Fourier frequencies with respect to z i.e. k_n makes sure that term-by-term matching with conductive region is possible while applying boundary conditions (6.13), (6.14), (6.18) and (6.19).

The vector potential in region Ω_{III} must decay with increasing negative y direction and therefore the solution to (6.6) for the x and z -components of the potential are

$$A_x^{III,t} = \sum_{m=-M}^M \sum_{n=0}^N e^{j\xi_m x} \cos(k_n(z-c)) C_{mn}^{III,x} e^{\kappa_{mn}(y+h)} \quad (6.51)$$

$$A_z^{III,t} = \sum_{m=-M}^M \sum_{n=1}^N e^{j\xi_m x} \sin(k_n(z-c)) C_{mn}^{III,z} e^{\kappa_{mn}(y+h)} \quad (6.52)$$

Again in (6.51) and (6.52), the Fourier frequencies with respect to z i.e. k_n makes sure that term-by-term matching with conductive region is possible while applying boundary conditions (6.20) - (6.23).

6.5. Source Field Formulation

As seen in section 6.3, the source field appears in the boundary conditions at $y = 0$ and $y = -h$ in the form of magnetic flux density. After taking note of the A_x and A_z expressions given by (6.46), (6.47) and the boundary conditions given in section 6.3, it can be observed that in order to enable one to match the source field with the induced field term-by-term, the source flux density must have the same eigenvalues, k_n , along the z -axis and ξ_m along the x -axis as the vector potential in the conductive region. Hence the source flux densities should be represented in the following form on the top surface of the conductive plate

$$B_x^{l,s}(x, 0, z) = \sum_{m=-M}^M \sum_{n=1}^N e^{j\xi_m x} \sin(k_n(z-c)) S_{mn}^{x,top}, \text{ at } y = 0 \quad (6.53)$$

$$B_y^{I,s}(x, 0, z) = \sum_{m=-M}^M \sum_{n=1}^N e^{j\xi_m x} \sin(k_n(z-c)) S_{mn}^{y,top}, \text{ at } y=0 \quad (6.54)$$

$$B_z^{I,s}(x, 0, z) = \sum_{m=-M}^M \sum_{n=0}^N e^{j\xi_m x} \cos(k_n(z-c)) S_{mn}^{z,top}, \text{ at } y=0 \quad (6.55)$$

Here, the superscript ‘I,s’ indicates the source field in region I and ‘x,top’ indicates the x -component source field on the top conductive plate surface.

Similarly, on the bottom surface at $y = -h$

$$B_x^{III,s}(x, -h, z) = \sum_{m=-M}^M \sum_{n=1}^N e^{j\xi_m x} \sin(k_n(z-c)) S_{mn}^{x,bot}, \text{ at } y=-h \quad (6.56)$$

$$B_y^{III,s}(x, -h, z) = \sum_{m=-M}^M \sum_{n=1}^N e^{j\xi_m x} \sin(k_n(z-c)) S_{mn}^{y,bot}, \text{ at } y=-h \quad (6.57)$$

$$B_z^{III,s}(x, -h, z) = \sum_{m=-M}^M \sum_{n=0}^N e^{j\xi_m x} \cos(k_n(z-c)) S_{mn}^{z,bot}, \text{ at } y=-h \quad (6.58)$$

Here, the superscript ‘III,s’ indicates the source field in region III and ‘x,bot’ indicates the x -component source field on the bottom conductive plate surface.

Modeling of magnetic source field using cylindrical charge sheet, as shown in Figure 6.3, has been discussed in chapter 2 and also in [76]. The charge sheet has a radius of r_o and width w_o and it completely encloses the magnetic source. $A(r_o, \theta_o, z_o)$ is any point on the charge sheet and $M(x, y, z)$ is any external point. Magnetic flux density derivation at any external point due to the cylindrical charge sheet has been provided in chapter 2.

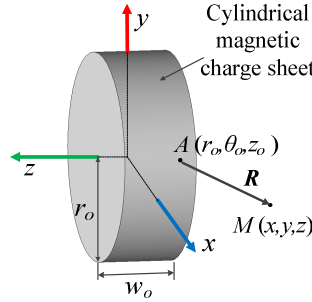


Figure 6.3. Cylindrical magnetic charge sheet with origin located at (x_c, y_c, z_c) .

The coordinate system shown in Figure 6.3 is located at the center of the rotor. However, since the conductive plate coordinate origin location is different, as shown in Figure 6.2, the source field coordinate origins must be offset by $(x_c, y_c, z_c) = (0, r_o + g, c + w/2)$. Taking this into account and noting that on the cylindrical surface the radial component is the normal component of the flux density, the x , y and z -flux density components given by (2.21)-(2.23) become

$$B_x^s = \frac{B_r^s(r_o, \theta_o) r_o}{2\pi} \int_0^{2\pi} \frac{(x - r_o \cos \theta_o)}{r^2} \left[\frac{2z + w_o}{\sqrt{4r^2 + (2z + w_o)^2}} - \frac{2z - w_o}{\sqrt{4r^2 + (2z - w_o)^2}} \right] d\theta_o \quad (6.59)$$

$$B_y^s = \frac{B_r^s(r_o, \theta_o) r_o}{2\pi} \int_0^{2\pi} \frac{(y - y_c - r_o \sin \theta_o)}{r^2} \left[\frac{2z + w_o}{\sqrt{4r^2 + (2z + w_o)^2}} - \frac{2z - w_o}{\sqrt{4r^2 + (2z - w_o)^2}} \right] d\theta_o \quad (6.60)$$

$$B_z^s = \frac{B_r^s(r_o, \theta_o) r_o}{\pi} \int_0^{2\pi} \left[\frac{1}{\sqrt{4r^2 + (2z - w_o)^2}} - \frac{1}{\sqrt{4r^2 + (2z + w_o)^2}} \right] d\theta_o \quad (6.61)$$

where

$$r^2 = x^2 + (y - y_c)^2 + r_o^2 - 2r_o (x \cos \theta_o + (y - y_c) \sin \theta_o) \quad (6.62)$$

The integration with respect to θ_o is accomplished numerically. In (6.59)-(6.61) superscript 's' indicates original source field and $B_r^s(r_o, \theta_o)$ is the variation of the radial flux density due to the source on the charge sheet surface along the θ_o and z_o directions which can be obtained either analytically or from finite element analysis (FEA) as described in chapter 2.

The double Fourier series coefficients of (6.53) - (6.55) are obtained by substituting (6.59)-(6.61) evaluated at $y = 0$ into

$$S_{mn}^{x,top} = \frac{2}{lw} \int_c^{c+w} \int_{-l/2}^{l/2} e^{-j\xi_m x} \sin(k_n(z-c)) B_x^{s,o}(x, 0, z) dx dz \quad (6.63)$$

$$S_{mn}^{y,top} = \frac{2}{lw} \int_c^{c+w} \int_{-l/2}^{l/2} e^{-j\xi_m x} \sin(k_n(z-c)) B_y^{s,o}(x, 0, z) dx dz \quad (6.64)$$

$$S_{mn}^{z,top} = \frac{(2 - \delta_{n0})}{lw} \int_c^{c+w} \int_{-l/2}^{l/2} e^{-j\xi_m x} \cos(k_n(z-c)) B_z^{s,o}(x, 0, z) dx dz \quad (6.65)$$

where

$$\delta_{n0} = \begin{cases} 0, & n \neq 0 \\ 1, & n = 0 \end{cases} \quad (6.66)$$

Figure 6.4 and Figure 6.5 illustrate the idea in which the source field is truncated in order to satisfy the conductive region interface vector potential boundary conditions on a term-by-term basis.

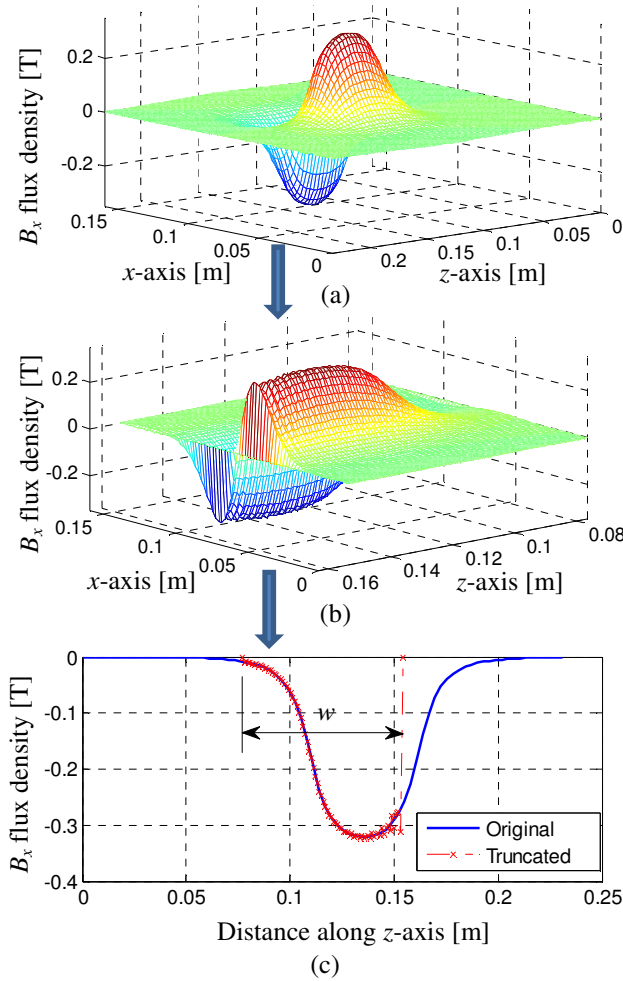


Figure 6.4. (a) The B_x^s source flux density distribution over the length of l and width of $2c+w$ as obtained from (6.59) (b) B_x^s field reconstructed using (6.53) over the length l and width of w of conductive plate. (c) Comparison between original and truncated B_x^s at $x=90$ mm.

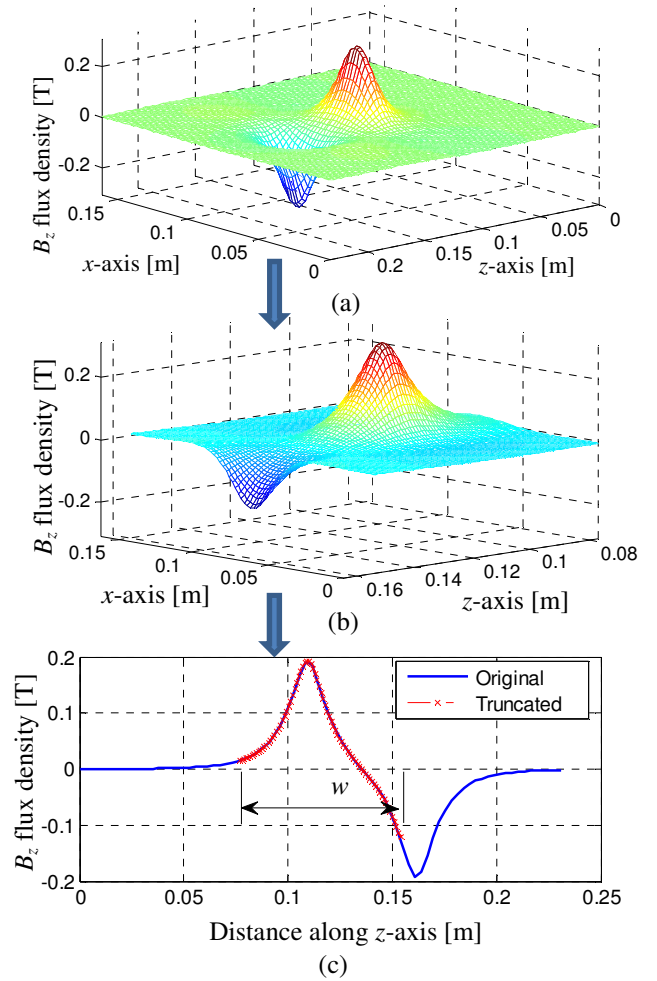


Figure 6.5. (a) The B_z^s source flux density distribution over the length of l and width of $2c+w$ as obtained from (6.61) (b) B_z^s field reconstructed using (6.55) over the length l and width w of conductive plate. (c) Comparison between original and truncated B_z^s at $x=90$ mm.

The Fourier coefficients, $S_{mn}^{x,bot}$, $S_{mn}^{y,bot}$, $S_{mn}^{z,bot}$ are obtained by evaluating (6.63) - (6.65) at $y = -h$.

6.6. Field Solution

The unknowns in the general solutions (6.46) - (6.52) can be obtained by using the boundary conditions (6.13), (6.14), (6.18) and (6.19) at $y = 0$ and (6.20) - (6.23) at $y = -h$.

First the magnetic vector potential components will be derived and then solutions for the flux density components will be obtained.

6.6.1. Solution for the Magnetic Vector Potential

6.6.1.1. Solution for the x-component Magnetic Vector Potential

Substituting the x -component vector potential equations (6.46), (6.48) at $y=0$ and the z -component magnetic flux density due to the source on the top surface (6.55) into the boundary condition (6.14) and eliminating common terms yields for all m, n

$$\alpha_{mn} C_{mn}^{\text{II},x} + \beta_{mn} D_{mn}^{\text{II},x} = -\kappa_{mn} C_{mn}^{\text{I},x} - S_{mn}^{z,top} \quad (6.67)$$

Similarly substituting the x -component vector potential equations (6.46), (6.48) at $y = 0$ and y -component magnetic flux density due to the source on the top surface (6.54) into the boundary condition (6.19) and using (6.50) yields for all m, n

$$C_{mn}^{\text{II},x} + D_{mn}^{\text{II},x} = C_{mn}^{\text{I},x} - \frac{k_n}{\kappa_{mn}^2} S_{mn}^{y,top} \quad (6.68)$$

Substituting (6.46), (6.51) and the z and y -components of the source flux densities on the bottom plate surface from (6.58) and (6.57) respectively into the boundary conditions (6.21) and (6.23) yields for all m, n

$$\alpha_{mn} C_{mn}^{\text{II},x} e^{-\alpha_{mn}h} + \beta_{mn} D_{mn}^{\text{II},x} e^{-\beta_{mn}h} = \kappa_{mn} C_{mn}^{\text{III},x} - S_{mn}^{z,bot} \quad (6.69)$$

and

$$C_{mn}^{\text{II},x} e^{-\alpha_{mn}h} + D_{mn}^{\text{II},x} e^{-\beta_{mn}h} = C_{mn}^{\text{III},x} - \frac{k_n}{\kappa_{mn}^2} S_{mn}^{y,bot} \quad (6.70)$$

respectively. Eliminating $C_{mn}^{\text{I},x}$ from (6.67) and (6.68) gives

$$(\alpha_{mn} + \kappa_{mn}) C_{mn}^{\text{II},x} + (\beta_{mn} + \kappa_{mn}) D_{mn}^{\text{II},x} = - \left(S_{mn}^{z,top} + \frac{k_n}{\kappa_{mn}} S_{mn}^{y,top} \right) \quad (6.71)$$

Similarly eliminating $C_{mn}^{III,x}$ from (6.69) and (6.70) gives

$$(\alpha_{mn} - \kappa_{mn})C_{mn}^{II,x} e^{-\alpha_{mn}h} + (\beta_{mn} - \kappa_{mn})D_{mn}^{II,x} e^{-\beta_{mn}h} = -\left(S_{mn}^{z,bot} - \frac{k_n}{\kappa_{mn}} S_{mn}^{y,bot} \right) \quad (6.72)$$

Solving (6.71) and (6.72) for $C_{mn}^{II,x}$ and $D_{mn}^{II,x}$ yields

$$C_{mn}^{II,x} = \frac{\left(S_{mn}^{z,bot} - \frac{k_n}{\kappa_{mn}} S_{mn}^{y,bot} \right) (\beta_{mn} + \kappa_{mn}) - \left(S_{mn}^{z,top} + \frac{k_n}{\kappa_{mn}} S_{mn}^{y,top} \right) (\beta_{mn} - \kappa_{mn}) e^{-\beta_{mn}h}}{Q_{mn}} \quad (6.73)$$

$$D_{mn}^{II,x} = \frac{\left(S_{mn}^{z,top} + \frac{k_n}{\kappa_{mn}} S_{mn}^{y,top} \right) (\alpha_{mn} - \kappa_{mn}) e^{-\alpha_{mn}h} - \left(S_{mn}^{z,bot} - \frac{k_n}{\kappa_{mn}} S_{mn}^{y,bot} \right) (\alpha_{mn} + \kappa_{mn})}{Q_{mn}} \quad (6.74)$$

where

$$Q_{mn} = (\alpha_{mn} + \kappa_{mn})(\beta_{mn} - \kappa_{mn}) e^{-\beta_{mn}h} - (\beta_{mn} + \kappa_{mn})(\alpha_{mn} - \kappa_{mn}) e^{-\alpha_{mn}h} \quad (6.75)$$

Substituting (6.73) and (6.74) into (6.46) yields

$$A_x^{II} = \sum_{m=-M}^M \sum_{n=0}^N e^{j\xi_m x} \cos(k_n(z-c)) \left[S_{mn}^{A_x,top} T_{mn}^{top}(y) + S_{mn}^{A_x,bot} T_{mn}^{bot}(y) \right] \quad (6.76)$$

where the source terms on the top and bottom of the conductive plate are respectively

$$S_{mn}^{A_x,top} = S_{mn}^{z,top} + (k_n / \kappa_{mn}) S_{mn}^{y,top} \quad (6.77)$$

$$S_{mn}^{A_x,bot} = S_{mn}^{z,bot} - (k_n / \kappa_{mn}) S_{mn}^{y,bot} \quad (6.78)$$

and the transmission functions for the top and bottom surfaces of the conductive plate are respectively

$$T_{mn}^{top}(y) = \frac{1}{Q_{mn}} \left[(\alpha_{mn} - \kappa_{mn}) e^{(\beta_{mn}y - \alpha_{mn}h)} - (\beta_{mn} - \kappa_{mn}) e^{(\alpha_{mn}y - \beta_{mn}h)} \right] \quad (6.79)$$

$$T_{mn}^{bot}(y) = \frac{1}{Q_{mn}} \left[(\beta_{mn} + \kappa_{mn}) e^{\alpha_{mn}y} - (\alpha_{mn} + \kappa_{mn}) e^{\beta_{mn}y} \right] \quad (6.80)$$

The transmission functions given by (6.79), (6.80) can also be written as

$$T_{mn}^{top}(y) = \frac{[\lambda + (\gamma_{nm} - \kappa_{nm})] e^{-\gamma_{nm}(y+h)} - [\lambda - (\gamma_{nm} + \kappa_{nm})] e^{\gamma_{nm}(y+h)}}{[\lambda^2 - (\gamma_{nm} + \kappa_{nm})^2] e^{\gamma_{nm}h} - [\lambda^2 - (\gamma_{nm} - \kappa_{nm})^2] e^{-\gamma_{nm}h}} e^{\lambda y} \quad (6.81)$$

$$T_{mn}^{bot}(y) = \frac{[\lambda - (\gamma_{nm} - \kappa_{nm})] e^{\gamma_{nm}y} - [\lambda + (\gamma_{nm} + \kappa_{nm})] e^{-\gamma_{nm}y}}{[\lambda^2 - (\gamma_{nm} + \kappa_{nm})^2] e^{\gamma_{nm}h} - [\lambda^2 - (\gamma_{nm} - \kappa_{nm})^2] e^{-\gamma_{nm}h}} e^{\lambda(y+h)} \quad (6.82)$$

where

$$\lambda = 0.5\mu_0\sigma v_y \quad (6.83)$$

It is worth noting that as the transmission functions are source independent; this solution is valid for any magnetic source located at any location above the conductive region.

Using (6.68), the reflected x -component vector potential coefficients for region I are

$$C_{mn}^{I,x} = C_{mn}^{II,x} + D_{mn}^{II,x} + \frac{k_n}{\kappa_{mn}} \frac{S_{mn}^{y,top}}{2} \quad (6.84)$$

Substituting (6.73) and (6.74) into (6.84) gives

$$C_{mn}^{I,x} = \left(S_{mn}^{z,top} + \frac{k_n}{\kappa_{mn}} S_{mn}^{y,top} \right) T_{mn}^{top}(0) + \left(S_{mn}^{z,bot} - \frac{k_n}{\kappa_{mn}} S_{mn}^{y,bot} \right) T_{mn}^{bot}(0) + \frac{k_n}{\kappa_{mn}} \frac{S_{mn}^{y,top}}{2} \quad (6.85)$$

where $T_{mn}^{top}(0)$ and $T_{mn}^{bot}(0)$ are the top and bottom surface transmission functions evaluated at $y=0$ respectively. Rearranging (6.85) yields

$$\begin{aligned}
C_{mn}^{I,x} = & S_{mn}^{z,top} T_{mn}^{top}(0) + \left(\kappa_{mn} T_{mn}^{top}(0) + 1 \right) \frac{k_n}{\kappa_{mn}} S_{mn}^{y,top} \\
& + \left(S_{mn}^{z,bot} - \frac{k_n}{\kappa_{mn}} S_{mn}^{y,bot} \right) T_{mn}^{bot}(0)
\end{aligned} \tag{6.86}$$

Substituting (6.86) into (6.48) gives the reflected x -component magnetic vector potential in region I

$$\begin{aligned}
A_x^{I,r} = & \sum_{m=-M}^M \sum_{n=0}^N e^{j\xi_m x} \cos(k_n(z-c)) e^{-\kappa_{mn} y} \left[S_{mn}^{z,top} T_{mn}^{top}(0) + \left(\kappa_{mn} T_{mn}^{top}(0) + 1 \right) \frac{k_n}{\kappa_{mn}} S_{mn}^{y,top} \right. \\
& \left. + \left(S_{mn}^{z,bot} - \frac{k_n}{\kappa_{mn}} S_{mn}^{y,bot} \right) T_{mn}^{bot}(0) \right]
\end{aligned} \tag{6.87}$$

Transmitted vector potential coefficients in region III can be obtained from (6.70)

$$C_{mn}^{III,x} = C_{mn}^{II,x} e^{-\alpha_{mn} h} + D_{mn}^{II,x} e^{-\beta_{mn} h} + \frac{k_n}{\kappa_{mn}} S_{mn}^{y,bot} \tag{6.88}$$

Substituting (6.73) and (6.74) into (6.88) one finds

$$\begin{aligned}
C_{mn}^{III,x} = & \frac{1}{Q_{mn}} \left(S_{mn}^{z,top} + \frac{k_n}{\kappa_{mn}} S_{mn}^{y,top} \right) e^{-(\alpha_{mn} + \beta_{mn})h} [(\alpha_{mn} - \kappa_{mn}) - (\beta_{mn} - \kappa_{mn})] \\
& + \frac{1}{Q_{mn}} \left(S_{mn}^{z,bot} - \frac{k_n}{\kappa_{mn}} S_{mn}^{y,bot} \right) e^{-(\alpha_{mn} + \beta_{mn})h} [(\beta_{mn} + \kappa_{mn}) e^{-\alpha_{mn} h} - (\alpha_{mn} + \kappa_{mn}) e^{-\beta_{mn} h}] \\
& + \frac{k_n}{\kappa_{mn}} S_{mn}^{y,bot}
\end{aligned} \tag{6.89}$$

Using the transmission functions for the top and bottom surfaces (6.79) and (6.80), (6.89) can be written as

$$C_{mn}^{III,x} = \left(S_{mn}^{z,top} + \frac{k_n}{\kappa_{mn}} S_{mn}^{y,top} \right) T_{mn}^{top}(-h) + \left(S_{mn}^{z,bot} - \frac{k_n}{\kappa_{mn}} S_{mn}^{y,bot} \right) T_{mn}^{bot}(-h) + \frac{k_n}{\kappa_{mn}^2} S_{mn}^{y,bot} \quad (6.90)$$

After rearranging terms (6.90) gives

$$C_{mn}^{III,x} = \left(S_{mn}^{z,top} + \frac{k_n}{\kappa_{mn}} S_{mn}^{y,top} \right) T_{mn}^{top}(-h) + S_{mn}^{z,bot} T_{mn}^{bot}(-h) - \left(\kappa_{mn} T_{mn}^{bot}(-h) - 1 \right) \frac{k_n}{\kappa_{mn}^2} S_{mn}^{y,bot} \quad (6.91)$$

Substituting (6.91) into (6.51) gives the transmitted x -component magnetic vector potential in region III

$$A_x^{III,t} = \sum_{m=-M}^M \sum_{n=0}^N e^{j\xi_m x} \cos(k_n(z-c)) e^{\kappa_{mn}(y+h)} \left[\left(S_{mn}^{z,top} + \frac{k_n}{\kappa_{mn}} S_{mn}^{y,top} \right) T_{mn}^{top}(-h) + S_{mn}^{z,bot} T_{mn}^{bot}(-h) - \left(\kappa_{mn} T_{mn}^{bot}(-h) - 1 \right) \frac{k_n}{\kappa_{mn}^2} S_{mn}^{y,bot} \right] \quad (6.92)$$

If the magnetic source is located away from the edges of the plate or lateral dimension of the plate is much larger than that of the source, the source and transmission functions for the bottom surface must be neglected in (6.76), (6.87) and (6.92).

6.6.1.2. Solution for the z -component Magnetic Vector Potential

Substituting the z -component vector potential equations (6.47), (6.49) at $y = 0$ and x and y -component magnetic flux density due to the source on the top surface (6.53) and (6.54) respectively into the boundary conditions (6.13) and (6.18) yields for all m, n

$$\alpha_{mn} C_{mn}^{II,z} + \beta_{mn} D_{mn}^{II,z} = -\kappa_{mn} C_{mn}^{I,z} + S_{mn}^{x,top} \quad (6.93)$$

and

$$C_{mn}^{II,z} + D_{mn}^{II,z} = C_{mn}^{I,z} + \frac{j\xi_m}{\kappa_{mn}^2} S_{mn}^{y,top} \quad (6.94)$$

respectively.

Substituting (6.47), (6.52) and the x and y -components of the source flux densities on the bottom plate surface from (6.56) and (6.57) respectively into the boundary conditions (6.20) and (6.22) yields for all m, n

$$\alpha_{mn} C_{mn}^{\text{II},z} e^{-\alpha_{mn}h} + \beta_{mn} D_{mn}^{\text{II},z} e^{-\beta_{mn}h} = \kappa_{mn} C_{mn}^{\text{III},z} + S_{mn}^{x,bot} \quad (6.95)$$

and

$$C_{mn}^{\text{II},z} e^{-\alpha_{mn}h} + D_{mn}^{\text{II},z} e^{-\beta_{mn}h} = C_{mn}^{\text{III},z} + \frac{j\xi_m}{\kappa_{mn}} S_{mn}^{y,bot} \quad (6.96)$$

respectively. Eliminating $C_{mn}^{\text{I},z}$ from (6.93) and (6.94) gives

$$(\alpha_{mn} + \kappa_{mn})C_{mn}^{\text{II},z} + (\beta_{mn} + \kappa_{mn})D_{mn}^{\text{II},z} = \left(S_{mn}^{x,top} + \frac{j\xi_m}{\kappa_{mn}} S_{mn}^{y,top} \right) \quad (6.97)$$

Similarly eliminating $C_{mn}^{\text{III},z}$ from (6.95) and (6.96) gives

$$(\alpha_{mn} - \kappa_{mn})C_{mn}^{\text{II},z} e^{-\alpha_{mn}h} + (\beta_{mn} - \kappa_{mn})D_{mn}^{\text{II},z} e^{-\beta_{mn}h} = \left(S_{mn}^{x,bot} - \frac{j\xi_m}{\kappa_{mn}} S_{mn}^{y,bot} \right) \quad (6.98)$$

Solving (6.97) and (6.98) for $C_{mn}^{\text{II},z}$ and $D_{mn}^{\text{II},z}$ yields

$$C_{mn}^{\text{II},z} = \frac{\left(S_{mn}^{x,top} + \frac{j\xi_m}{\kappa_{mn}} S_{mn}^{y,top} \right) (\beta_{mn} - \kappa_{mn}) e^{-\beta_{mn}h} - \left(S_{mn}^{x,bot} - \frac{j\xi_m}{\kappa_{mn}} S_{mn}^{y,bot} \right) (\beta_{mn} + \kappa_{mn})}{Q_{mn}} \quad (6.99)$$

$$D_{mn}^{\text{II},z} = \frac{\left(S_{mn}^{x,bot} - \frac{j\xi_m}{\kappa_{mn}} S_{mn}^{y,bot} \right) (\alpha_{mn} + \kappa_{mn}) - \left(S_{mn}^{x,top} + \frac{j\xi_m}{\kappa_{mn}} S_{mn}^{y,top} \right) (\alpha_{mn} - \kappa_{mn}) e^{-\alpha_{mn}h}}{Q_{mn}} \quad (6.100)$$

where Q_{mn} is defined by (6.75). Substituting (6.99) and (6.100) into (6.47) yields

$$A_z^{\text{II}} = - \sum_{m=-M}^M \sum_{n=1}^N e^{j\xi_m x} \sin(k_n(z-c)) \left[S_{mn}^{A_z, \text{top}} T_{mn}^{\text{top}}(y) + S_{mn}^{A_z, \text{bot}} T_{mn}^{\text{bot}}(y) \right] \quad (6.101)$$

where the source terms on the top and bottom of the conductive plate are respectively

$$S_{mn}^{A_z, \text{top}} = S_{mn}^{x, \text{top}} + (j\xi_m / \kappa_{mn}) S_{mn}^{y, \text{top}} \quad (6.102)$$

$$S_{mn}^{A_z, \text{bot}} = S_{mn}^{x, \text{bot}} - (j\xi_m / \kappa_{mn}) S_{mn}^{y, \text{bot}} \quad (6.103)$$

and the transmission functions for the top and bottom of the conductive plate are defined by (6.79) and (6.80) respectively. Like the A_x field equation, this solution is valid for any magnetic source located at any location above the conductive region.

Reflected A_z field coefficients are found from (6.94)

$$C_{mn}^{\text{I}, z} = C_{mn}^{\text{II}, z} + D_{mn}^{\text{II}, z} - \frac{j\xi_m}{\kappa_{mn}} S_{mn}^{y, \text{top}} \quad (6.104)$$

Substituting (6.99) and (6.100) into (6.104) gives

$$C_{mn}^{\text{I}, z} = - \left(S_{mn}^{x, \text{top}} + \frac{j\xi_m}{\kappa_{mn}} S_{mn}^{y, \text{top}} \right) T_{mn}^{\text{top}}(0) - \left(S_{mn}^{x, \text{bot}} - \frac{j\xi_m}{\kappa_{mn}} S_{mn}^{y, \text{bot}} \right) T_{mn}^{\text{bot}}(0) - \frac{j\xi_m}{\kappa_{mn}} S_{mn}^{y, \text{top}} \quad (6.105)$$

Rearranging terms

$$C_{mn}^{\text{I}, z} = -S_{mn}^{x, \text{top}} T_{mn}^{\text{top}}(0) - \left(\kappa_{mn} T_{mn}^{\text{top}}(0) + 1 \right) \frac{j\xi_m}{\kappa_{mn}} S_{mn}^{y, \text{top}} - \left(S_{mn}^{x, \text{bot}} - \frac{j\xi_m}{\kappa_{mn}} S_{mn}^{y, \text{bot}} \right) T_{mn}^{\text{bot}}(0) \quad (6.106)$$

Substituting (6.106) into (6.49) gives the reflected z -component vector potential in region

I as follows

$$A_z^{I,r} = - \sum_{m=-M}^M \sum_{n=1}^N e^{j\xi_m x} \sin(k_n(z-c)) e^{-\kappa_{mn}y} \left[S_{mn}^{x,top} T_{mn}^{top}(0) + \left(\kappa_{mn} T_{mn}^{top}(0) + 1 \right) \frac{j\xi_m}{\kappa_{mn}} S_{mn}^{y,top} + \left(S_{mn}^{x,bot} - \frac{j\xi_m}{\kappa_{mn}} S_{mn}^{y,bot} \right) T_{mn}^{bot}(0) \right] \quad (6.107)$$

The transmitted field coefficients can be obtained from (6.96) as

$$C_{mn}^{III,z} = C_{mn}^{II,z} e^{-\alpha_{mn}h} + D_{mn}^{II,z} e^{-\beta_{mn}h} - \frac{j\xi_m}{\kappa_{mn}} S_{mn}^{y,bot} \quad (6.108)$$

Substituting (6.99) and (6.100) into (6.108) gives

$$C_{mn}^{III,z} = - \left(S_{mn}^{x,top} + \frac{j\xi_m}{\kappa_{mn}} S_{mn}^{y,top} \right) T_{mn}^{top}(-h) - \left(S_{mn}^{x,bot} - \frac{j\xi_m}{\kappa_{mn}} S_{mn}^{y,bot} \right) T_{mn}^{bot}(-h) - \frac{j\xi_m}{\kappa_{mn}} S_{mn}^{y,bot} \quad (6.109)$$

After rearranging

$$C_{mn}^{III,z} = - \left(S_{mn}^{x,top} + \frac{j\xi_m}{\kappa_{mn}} S_{mn}^{y,top} \right) T_{mn}^{top}(-h) - S_{mn}^{x,bot} T_{mn}^{bot}(-h) + \left(\kappa_{mn} T_{mn}^{bot}(-h) - 1 \right) \frac{j\xi_m}{\kappa_{mn}} S_{mn}^{y,bot} \quad (6.110)$$

Substituting (6.110) into (6.52) gives the transmitted z -component magnetic vector potential in region III as follows

$$A_z^{III,t} = - \sum_{m=-M}^M \sum_{n=1}^N e^{j\xi_m x} \sin(k_n(z-c)) e^{\kappa_{mn}(y+h)} \left[\left(S_{mn}^{x,top} + \frac{j\xi_m}{\kappa_{mn}} S_{mn}^{y,top} \right) T_{mn}^{top}(-h) + S_{mn}^{x,bot} T_{mn}^{bot}(-h) - \left(\kappa_{mn} T_{mn}^{bot}(-h) - 1 \right) \frac{j\xi_m}{\kappa_{mn}} S_{mn}^{y,bot} \right] \quad (6.111)$$

If the magnetic source is located away from the edges of the plate or lateral dimension of the plate is much larger than that of the source, the source and transmission functions for the bottom surface must be neglected in (6.101), (6.107) and (6.111).

6.6.2. Solution for the Magnetic Flux Density

Using the following relationships (3.7)-(3.9) derived in chapter 3, the magnetic flux density components can be obtained in terms of the magnetic vector potential.

6.6.2.1. Solution for the transmitted flux density in Region II

Substituting (6.76), (6.101) into (3.7)-(3.9) and noting that the A_y component is zero in the presented analytic model, the flux density components in region II are obtained as

$$B_x^{\text{II}} = - \sum_{m=-M}^M \sum_{n=1}^N e^{j\xi_m x} \sin(k_n(z-c)) \left[S_{mn}^{A_z, \text{top}} \frac{\partial T_{mn}^{\text{top}}}{\partial y} + S_{mn}^{A_z, \text{bot}} \frac{\partial T_{mn}^{\text{bot}}}{\partial y} \right] \quad (6.112)$$

$$B_y^{\text{II}} = - \sum_{m=-M}^M \sum_{n=0}^N e^{j\xi_m x} \sin(k_n(z-c)) \left[\left(k_n S_{mn}^{A_x, \text{top}} - j\xi_m S_{mn}^{A_z, \text{top}} \right) T_{mn}^{\text{top}} + \left(k_n S_{mn}^{A_x, \text{bot}} - j\xi_m S_{mn}^{A_z, \text{bot}} \right) T_{mn}^{\text{bot}} \right] \quad (6.113)$$

$$B_z^{\text{II}} = - \sum_{m=-M}^M \sum_{n=0}^N e^{j\xi_m x} \cos(k_n(z-c)) \left[S_{mn}^{A_x, \text{top}} \frac{\partial T_{mn}^{\text{top}}}{\partial y} + S_{mn}^{A_x, \text{bot}} \frac{\partial T_{mn}^{\text{bot}}}{\partial y} \right] \quad (6.114)$$

where

$$\frac{\partial T_{mn}^{\text{top}}}{\partial y} = \frac{1}{Q_{mn}} \left[\beta_{mn} (\alpha_{mn} - \kappa_{mn}) e^{(\beta_{mn} y - \alpha_{mn} h)} - \alpha_{mn} (\beta_{mn} - \kappa_{mn}) e^{(\alpha_{mn} y - \beta_{mn} h)} \right] \quad (6.115)$$

and

$$\frac{\partial T_{mn}^{\text{top}}}{\partial y} = \frac{1}{Q_{mn}} \left[\alpha_{mn} (\beta_{mn} + \kappa_{mn}) e^{\alpha_{mn} y} - \beta_{mn} (\alpha_{mn} + \kappa_{mn}) e^{\beta_{mn} y} \right] \quad (6.116)$$

6.6.2.2. Solution for the reflected flux density in Region I

The reflected x -component magnetic flux density in region I can be obtained by substituting (6.87) and (6.107) into (3.7) which gives

$$\begin{aligned}
B_x^{l,r} = & \sum_{m=-M}^M \sum_{n=1}^N e^{j\xi_m x} \sin(k_n(z-c)) e^{-\kappa_{mn}y} \kappa_{mn} \left[\left(\kappa_{mn} T_{mn}^{top}(0) + 1 \right) \frac{j\xi_m}{\kappa_{mn}^2} S_{mn}^{y,top} \right. \\
& \left. + S_{mn}^{x,top} T_{mn}^{top}(0) + \left(S_{mn}^{x,bot} - \frac{j\xi_m}{\kappa_{mn}} S_{mn}^{y,bot} \right) T_{mn}^{bot}(0) \right]
\end{aligned} \tag{6.117}$$

In order to find the reflected y-component flux density, (6.87) and (6.107) are substituted into (3.8) to yield

$$\begin{aligned}
B_y^{l,r} = & - \sum_{m=-M}^M \sum_{n=0}^N e^{j\xi_m x} \sin(k_n(z-c)) e^{-\kappa_{mn}y} \left[\left(k_n S_{mn}^{z,top} - j\xi_m S_{mn}^{x,top} \right) T_{mn}^{top}(0) \right. \\
& + \left(\kappa_{mn} T_{mn}^{top}(0) + 1 \right) \frac{k_n^2 + \xi_m^2}{\kappa_{mn}^2} S_{mn}^{y,top} \\
& + \left(k_n S_{mn}^{z,bot} - j\xi_m S_{mn}^{x,bot} \right) T_{mn}^{bot}(0) \\
& \left. - \frac{k_n^2 + \xi_m^2}{\kappa_{mn}} S_{mn}^{y,bot} T_{mn}^{bot}(0) \right]
\end{aligned} \tag{6.118}$$

Using (6.50), (6.118) becomes

$$\begin{aligned}
B_y^{l,r} = & - \sum_{m=-M}^M \sum_{n=0}^N e^{j\xi_m x} \sin(k_n(z-c)) e^{-\kappa_{mn}y} \left[\left(k_n S_{mn}^{z,top} - j\xi_m S_{mn}^{x,top} + \kappa_{mn} S_{mn}^{y,top} \right) T_{mn}^{top}(0) \right. \\
& \left. + S_{mn}^{y,top} + \left(k_n S_{mn}^{z,bot} - j\xi_m S_{mn}^{x,bot} - \kappa_{mn} S_{mn}^{y,bot} \right) T_{mn}^{bot}(0) \right]
\end{aligned} \tag{6.119}$$

Similarly substituting (6.87) into (3.9), the z-component flux density is obtained as

$$\begin{aligned}
B_z^{l,r} = & \sum_{m=-M}^M \sum_{n=0}^N e^{j\xi_m x} \cos(k_n(z-c)) e^{-\kappa_{mn}y} \kappa_{mn} \left[\left(\kappa_{mn} T_{mn}^{top}(0) + 1 \right) \frac{k_n}{\kappa_{mn}^2} S_{mn}^{y,top} \right. \\
& \left. + S_{mn}^{z,top} T_{mn}^{top}(0) + \left(S_{mn}^{z,bot} - \frac{k_n}{\kappa_{mn}} S_{mn}^{y,bot} \right) T_{mn}^{bot}(0) \right]
\end{aligned} \tag{6.120}$$

6.6.2.3. Solution for the transmitted flux density in Region III

In order to derive the x -component transmitted magnetic flux density in region III,

(6.111) is substituted into (3.7) to yield

$$B_x^{\text{III},t} = - \sum_{m=-M}^M \sum_{n=1}^N e^{j\xi_m x} \sin(k_n(z-c)) e^{\kappa_{mn}(y+h)} \kappa_{mn} \left[\left(S_{mn}^{x,top} + \frac{j\xi_m}{\kappa_{mn}} S_{mn}^{y,top} \right) T_{mn}^{top}(-h) \right. \\ \left. + S_{mn}^{x,bot} T_{mn}^{bot}(-h) - \left(\kappa_{mn} T_{mn}^{bot}(-h) - 1 \right) \frac{j\xi_m}{\kappa_{mn}^2} S_{mn}^{y,bot} \right] \quad (6.121)$$

The y -component flux density in region III is obtained by substituting (6.92) and (6.111) into (3.8)

$$B_y^{\text{III},t} = - \sum_{m=-M}^M \sum_{n=0}^N e^{j\xi_m x} \sin(k_n(z-c)) e^{\kappa_{mn}(y+h)} \left[\left(k_n S_{mn}^{z,top} - j\xi_m S_{mn}^{x,top} \right) T_{mn}^{top}(-h) \right. \\ \left. + \frac{k_n^2 + \xi_m^2}{\kappa_{mn}} S_{mn}^{y,top} T_{mn}^{top}(-h) \right. \\ \left. + \left(k_n S_{mn}^{z,bot} - j\xi_m S_{mn}^{x,bot} \right) T_{mn}^{bot}(-h) \right. \\ \left. - \left(\kappa_{mn} T_{mn}^{bot}(-h) - 1 \right) \frac{k_n^2 + \xi_m^2}{\kappa_{mn}^2} S_{mn}^{y,bot} \right] \quad (6.122)$$

Using (6.50), (6.122) becomes

$$B_y^{\text{III},t} = \sum_{m=-M}^M \sum_{n=0}^N e^{j\xi_m x} \sin(k_n(z-c)) e^{\kappa_{mn}(y+h)} \left[\left(j\xi_m S_{mn}^{x,top} - k_n S_{mn}^{z,top} - \kappa_{mn} S_{mn}^{y,top} \right) T_{mn}^{top}(-h) \right. \\ \left. - \left(k_n S_{mn}^{z,bot} - j\xi_m S_{mn}^{x,bot} - \kappa_{mn} S_{mn}^{y,bot} \right) T_{mn}^{bot}(-h) + S_{mn}^{y,bot} \right] \quad (6.123)$$

Substituting (6.92) into (3.9) gives the z -component transmitted flux density

$$\begin{aligned}
B_z^{\text{III},t} = & - \sum_{m=-M}^M \sum_{n=0}^N e^{j\xi_m x} \cos(k_n(z-c)) e^{\kappa_{mn}(y+h)} \kappa_{mn} \left[\left(S_{mn}^{z,top} + \frac{k_n}{\kappa_{mn}} S_{mn}^{y,top} \right) T_{mn}^{top}(-h) \right. \\
& \left. + S_{mn}^{z,bot} T_{mn}^{bot}(-h) - \left(\kappa_{mn} T_{mn}^{bot}(-h) - 1 \right) \frac{k_n}{\kappa_{mn}} S_{mn}^{y,bot} \right]
\end{aligned} \tag{6.124}$$

6.7. Calculation of Electromagnetic Force

The electromagnetic forces acting on the magnetic source will be calculated using Maxwell's stress tensor [112, 115, 143] and Lorentz method [143].

6.7.1. Calculation using Maxwell's Stress Tensor

The thrust, lift and lateral forces are given by [143]

$$F_x = \frac{1}{2\mu_0} \text{Re} \left\{ \int_{\Gamma_{top}} B_x^{\text{II}} B_y^{\text{II}*} dx dz - \int_{\Gamma_{bot}} B_x^{\text{II}} B_y^{\text{II}*} dx dz \right\} \tag{6.125}$$

$$\begin{aligned}
F_y = \frac{1}{4\mu_0} \text{Re} \left\{ \int_{\Gamma_{top}} \left(B_y^{\text{II}} B_y^{\text{II}*} - B_x^{\text{II}} B_x^{\text{II}*} - B_z^{\text{II}} B_z^{\text{II}*} \right) dx dz \right. \\
\left. - \int_{\Gamma_{bot}} \left(B_y^{\text{II}} B_y^{\text{II}*} - B_x^{\text{II}} B_x^{\text{II}*} - B_z^{\text{II}} B_z^{\text{II}*} \right) dx dz \right\}
\end{aligned} \tag{6.126}$$

$$F_z = \frac{1}{2\mu_0} \text{Re} \left\{ \int_{\Gamma_{top}} B_z^{\text{II}} B_y^{\text{II}*} dx dz - \int_{\Gamma_{bot}} B_z^{\text{II}} B_y^{\text{II}*} dx dz \right\} \tag{6.127}$$

where Γ_{top} and Γ_{bot} are the conductive plate surfaces at $y = 0$ and $y = -h$ respectively as shown in Figure 6.2. Integration over Γ_{bot} is not necessary as the source is located at the center of the plate or its lateral dimension is much smaller than that of the plate. Maxwell's stress tensor will be calculated using the reflected fields in regions I and transmitted fields in region III.

Substituting (6.53) and (6.117) into (6.7) gives at $y = 0$

$$B_x^{\text{II}} = \sum_{m=-M}^M \sum_{n=1}^{\infty} e^{j\xi_m x} \sin(k_n(z-c)) \left[\left(\kappa_{mn} T_{mn}^{\text{top}}(0) + 1 \right) \left(S_{mn}^{x,\text{top}} + \frac{j\xi_m}{\kappa_{mn}} S_{mn}^{y,\text{top}} \right) + \kappa_{mn} \left(S_{mn}^{x,\text{bot}} - \frac{j\xi_m}{\kappa_{mn}} S_{mn}^{y,\text{bot}} \right) T_{mn}^{\text{bot}}(0) \right] \quad (6.128)$$

Adding (6.54) with (6.119) and substituting into (6.8) gives at $y = 0$

$$B_y^{\text{II}} = - \sum_{m=-M}^M \sum_{n=1}^{\infty} e^{j\xi_m x} \sin(k_n(z-c)) \left[\left(k_n S_{mn}^{z,\text{top}} - j\xi_m S_{mn}^{x,\text{top}} + \kappa_{mn} S_{mn}^{y,\text{top}} \right) T_{mn}^{\text{top}}(0) + \left(k_n S_{mn}^{z,\text{bot}} - j\xi_m S_{mn}^{x,\text{bot}} - \kappa_{mn} S_{mn}^{y,\text{bot}} \right) T_{mn}^{\text{bot}}(0) \right] \quad (6.129)$$

Similarly substituting (6.55) and (6.120) into (6.9) gives at $y = 0$

$$B_z^{\text{II}} = \sum_{m=-M}^M \sum_{n=0}^{\infty} e^{j\xi_m x} \cos(k_n(z-c)) \left[\left(\kappa_{mn} T_{mn}^{\text{top}}(0) + 1 \right) \left(S_{mn}^{z,\text{top}} + \frac{k_n}{\kappa_{mn}} S_{mn}^{y,\text{top}} \right) + \kappa_{mn} \left(S_{mn}^{z,\text{bot}} - \frac{k_n}{\kappa_{mn}} S_{mn}^{y,\text{bot}} \right) T_{mn}^{\text{bot}}(0) \right] \quad (6.130)$$

Equations (6.128) - (6.130) will be used for force calculation using tensor method on the top plate surface.

For the bottom conductive plate surface, substituting (6.56) and (6.121) into (6.10) at $y = -h$ gives

$$B_x^{\text{II}} = - \sum_{m=-M}^M \sum_{n=1}^N e^{j\xi_m x} \sin(k_n(z-c)) \left[\left(\kappa_{mn} T_{mn}^{\text{bot}}(-h) - 1 \right) \left(S_{mn}^{x,\text{bot}} - \frac{j\xi_m}{\kappa_{mn}} S_{mn}^{y,\text{bot}} \right) + \kappa_{mn} \left(S_{mn}^{x,\text{top}} + \frac{j\xi_m}{\kappa_{mn}} S_{mn}^{y,\text{top}} \right) T_{mn}^{\text{top}}(-h) \right] \quad (6.131)$$

Substituting (6.57) and (6.123) into (6.11) gives at $y = -h$

$$B_y^{\text{II}} = - \sum_{m=-M}^M \sum_{n=0}^N e^{j\xi_m x} \sin(k_n(z-c)) \left[\left(k_n S_{mn}^{z,\text{bot}} - j\xi_m S_{mn}^{x,\text{bot}} - \kappa_{mn} S_{mn}^{y,\text{bot}} \right) T_{mn}^{\text{bot}}(-h) + \left(k_n S_{mn}^{z,\text{top}} - j\xi_m S_{mn}^{x,\text{top}} + \kappa_{mn} S_{mn}^{y,\text{top}} \right) T_{mn}^{\text{top}}(-h) \right]$$

And finally substituting (6.58) and (6.124) into (6.12) gives at $y = -h$

$$B_z^{\text{II}} = - \sum_{m=-M}^M \sum_{n=0}^N e^{j\xi_m x} \cos(k_n(z-c)) \left[\left(\kappa_{mn} T_{mn}^{\text{bot}}(-h) - 1 \right) \left(S_{mn}^{z,\text{bot}} - \frac{k_n}{\kappa_{mn}} S_{mn}^{y,\text{bot}} \right) + \kappa_{mn} \left(S_{mn}^{z,\text{top}} + \frac{k_n}{\kappa_{mn}} S_{mn}^{y,\text{top}} \right) T_{mn}^{\text{top}}(-h) \right] \quad (6.133)$$

Equations (6.131) - (6.133) will be used for tensor force calculations on the bottom plate surface.

The thrust force is calculated using (6.125). Substituting (6.128) and conjugate of (6.129) into the first term of (6.125) and (6.131), conjugate of (6.132) into the second term of (6.125) gives the thrust force.

Similarly substituting (6.128) - (6.130) and their conjugate into the first term of (6.126), (6.131) - (6.133) and their conjugate into the second term of (6.126), the lift force can be calculated analytically.

Finally, for the lateral force computation (6.130), conjugate of (6.129) are substituted into the first term of (6.127) for integration over Γ_{top} and (6.133), conjugate of (6.132) are substituted into the second term of (6.127) for integration over Γ_{bot} . The latter is subtracted from the former to give the net lateral force.

6.7.2. Simplified Stress Tensor Calculation

Considerable simplification in the force calculation can be achieved when the induced eddy current field region in the conductive medium is narrow compared to the width of the plate. This happens when the magnetic source is not laterally offset and/or the width of the source is small compared to that of the plate.

Noting that

$$\nabla \cdot \mathbf{B}^s = 0 \quad (3.3)$$

the following relations hold true

$$S_{mn}^{x,top} = j\xi_m S_{mn}^{y,top} / \kappa_{mn} \quad (6.134)$$

$$S_{mn}^{z,top} = k_n S_{mn}^{y,top} / \kappa_{mn} \quad (6.135)$$

The associated source terms in (6.76) and (6.101) for the top surface of the conductive plate using (6.134)-(6.135) are

$$S_{mn}^{A_x,top} = -(k_n / \kappa_{mn}^2) S_{mn}^{y,top} \quad (6.136)$$

$$S_{mn}^{A_z,top} = j(\xi_m / \kappa_{mn}^2) S_{mn}^{y,top} \quad (6.137)$$

and the transmission function of the conductive plate is modified into

$$T_{mn}(y) = 2\kappa_{mn} \frac{[\lambda - (\gamma_{mn} + \kappa_{mn})] - [\lambda + (\gamma_{mn} - \kappa_{mn})]e^{-2\gamma_{mn}(y+h)}}{[\lambda^2 - (\gamma_{mn} + \kappa_{mn})^2] - [\lambda^2 - (\gamma_{mn} - \kappa_{mn})^2]e^{-2\gamma_{mn}h}} e^{(\lambda + \gamma_{mn})y} \quad (6.138)$$

The reflected fields in Ω_1 as given by (6.87) and (6.107) are modified into

$$A_x^{I,r}(x, y, z) = - \sum_{m=-M}^M \sum_{n=0}^N \frac{k_n}{\kappa_{mn}} S_{mn}^{y,top} R_{mn}(0) e^{-\kappa_{mn}y} \cos[k_n(z-c)] e^{j\xi_m x} \quad (6.139)$$

$$A_z^{I,r}(x, y, z) = \sum_{m=-M}^M \sum_{n=1}^N \frac{j\xi_m}{\kappa_{mn}} S_{mn}^{y,top} R_{mn}(0) e^{-\kappa_{mn}y} \sin[k_n(z-c)] e^{j\xi_m x} \quad (6.140)$$

where $R_{mn}(0)$ is the reflection coefficient and is related to the transmission coefficient by

$$R_{mn}(0) + 1 = T_{mn}(0) \quad (6.141)$$

Substituting (6.138) into (6.141) and rearranging gives

$$R_{mn}(0) = \frac{(\lambda + \gamma_{mn} - \kappa_{mn})(\lambda - \gamma_{mn} - \kappa_{mn})(e^{-2\gamma_{mn}h} - 1)}{[\lambda^2 - (\gamma_{mn} + \kappa_{mn})^2] - [\lambda^2 - (\gamma_{mn} - \kappa_{mn})^2]e^{-2\gamma_{mn}h}} \quad (6.142)$$

For the case when $v_y = 0$, (6.142) simplifies down to

$$R_{mn}(0) = \Phi_{mn} \frac{1 - e^{-2\gamma_{mn}h}}{1 - \Phi_{mn}^2 e^{-2\gamma_{mn}h}} \quad (6.143)$$

where

$$\Phi_{mn} = \frac{1 - (\gamma_{mn} / \kappa_{mn})}{1 + (\gamma_{mn} / \kappa_{mn})} \quad (6.144)$$

This form of the reflection coefficient has previously been derived by a number of other authors [205-211]. The reflected flux density components evaluated at $y=0$, as given by (6.117) and (6.119) are simplified into

$$B_x^{l,r}(x, 0, z) = -\operatorname{Re} \left[\sum_{m=-M}^M \sum_{n=1}^N \frac{j\xi_m}{\kappa_{mn}} S_{mn}^{y,top} R_{mn}(0) \sin[k_n(z - c)] e^{j\xi_m x} \right] \quad (6.145)$$

$$B_y^{l,r}(x, 0, z) = \operatorname{Re} \left[\sum_{m=-M}^M \sum_{n=0}^N S_{mn}^{y,top} R_{mn}(0) \sin[k_n(z - c)] e^{j\xi_m x} \right] \quad (6.146)$$

However, as the fields in Ω_I are governed by the magnetostatic equations, the forces can also be computed using the fictitious surface magnetic charge approach [212, 213]. In this case the force within the air region due to a source magnetic charge can be computed using

$$\mathbf{F} = -\frac{1}{2\mu_0} \operatorname{Re} \left[\oint_S \rho_m^* \mathbf{B}^r dS \right], \text{ at } y=0 \quad (6.147)$$

where ‘*’ superscript indicates complex conjugation. The magnetic charge sheet density $\rho_m(x,z)$ is equal to twice the normal component of the source magnetic flux density [76].

$$\rho_m(x, z) = 2B_{y, mn}^s(x, 0, z), \text{ at } y=0 \quad (6.148)$$

Substituting (6.146) into (6.148)

$$\rho_m(x, z) = 2 \sum_{m=-M}^M \sum_{n=1}^N S_{mn}^{y, top} \sin[k_n(z - c)] e^{j\xi_m x}, \text{ at } y=0 \quad (6.149)$$

Substituting (6.149) and (6.145) into (6.147) yields thrust force as

$$F_x = \frac{lw}{2\mu_0} \operatorname{Re} \left[\sum_{m=-M}^M \sum_{n=1}^N \frac{j\xi_m}{\kappa_{mn}} \left| B_{y, mn}^s(x, 0, z) \right|^2 R_{mn}(0) \right] \quad (6.150)$$

Noting that $\operatorname{Re}[jR_{mn}(0)] = -\operatorname{Im}[R_{mn}(0)]$, (6.150) can be also written as

$$F_x = -\frac{lw}{2\mu_0} \operatorname{Im} \left[\sum_{m=-M}^M \sum_{n=1}^N \frac{\xi_m}{\kappa_{mn}} \left| B_{y, mn}^s(x, 0, z) \right|^2 R_{mn}(0) \right] \quad (6.151)$$

Similarly substituting (6.149) and (6.146) into (6.147) yields lift force as

$$F_y = -\frac{lw}{2\mu_0} \operatorname{Re} \left[\sum_{m=-M}^M \sum_{n=1}^N \left| B_{y, mn}^s(x, 0, z) \right|^2 R_{mn}(0) \right] \quad (6.152)$$

6.7.3. Calculation using Lorentz method

In the Lorentz method, the forces are given by [143]

$$\mathbf{F} = \frac{1}{2} \operatorname{Re} \int_{\Omega_{\text{II}}} \left(\mathbf{J}^{\text{II}} \times \mathbf{B}^{\text{II}*} \right) d\Omega_{\text{II}} \quad (6.153)$$

In (6.153) the integration is performed over the entire region II. From (6.153) the thrust, lift and lateral forces are

$$F_x = -\frac{1}{2} \operatorname{Re} \left[\int_{x=-l/2}^{l/2} \int_{y=-h}^0 \int_{z=c}^{c+w} J_z^{\text{II}} B_y^{\text{II}*} dz dy dx \right] \quad (6.154)$$

$$F_y = \frac{1}{2} \operatorname{Re} \left[\int_{x=-l/2}^{l/2} \int_{y=-h}^0 \int_{z=c}^{c+w} (J_z^{\text{II}} B_x^{\text{II}*} - J_x^{\text{II}} B_z^{\text{II}*}) dz dy dx \right] \quad (6.155)$$

$$.F_z = \frac{1}{2} \operatorname{Re} \left[\int_{x=-l/2}^{l/2} \int_{y=-h}^0 \int_{z=c}^{c+w} J_x^{\text{II}} B_y^{\text{II}*} dz dy dx \right]. \quad (6.156)$$

The relationships between the induced eddy current density, \mathbf{J} , and the magnetic vector potential, \mathbf{A} , are given by (3.17)-(3.19) in chapter 3. The relationships for the x and z -components are rewritten here for convenience

$$J_x = -\sigma \left(\frac{\partial A_x}{\partial t} + v_x \frac{\partial A_x}{\partial x} + v_y \frac{\partial A_x}{\partial y} \right) \quad (3.17)$$

$$J_z = -\sigma \left(\frac{\partial A_z}{\partial t} + v_x \frac{\partial A_z}{\partial x} + v_y \frac{\partial A_z}{\partial y} \right) \quad (3.19)$$

Substituting the transmitted flux density of region II given by (6.112)-(6.114) and induced eddy current density given by (3.17), (3.19) into (6.154)-(6.156), the electromagnetic forces can be obtained.

6.8. Power Loss, Total Power Transfer and Torque Calculation

The power loss in the conductive plate in the form of heat is calculated using Ohm's law

$$P_{loss} = \frac{1}{2\sigma} \operatorname{Re} \left[\int_{\Omega_{\text{II}}} (J_x^{\text{II}} J_x^{\text{II}*} + J_z^{\text{II}} J_z^{\text{II}*}) d\Omega_{\text{II}} \right] \quad (6.157)$$

Substituting (3.17), (3.19) and their conjugate into (6.157) and integrating over the conductive plate domain, the power loss can be analytically computed. In order to find the total power transfer from the magnetic source, following relation can be used

$$P_{transfer} = P_{loss} + F_x v_x + F_y v_y \quad (6.158)$$

In (6.158) power required to move the magnetic source with constant velocity v_x and v_y has been added to the power loss to obtain total input power required or total power transfer. Thrust and lift force are substituted from (6.125) and (6.126) (using stress tensor method) or (6.154) - (6.155) (using Lorentz method) and power loss from (6.157) into (6.158) to obtain the total power transfer.

Electromagnetic torque acting on the source can be obtained by simply using

$$T_{em} = \frac{P_{transfer}}{\omega_m} = \frac{P_{transfer}}{(\omega_e / P)} \quad (6.159)$$

where ω_m is the mechanical angular speed [rads⁻¹] and P is number of pole pairs of the source.

Figure 6.6 shows a flowchart of the developed 2-component MVP based steady state analytic model to compute the eddy current forces, torque and power loss.

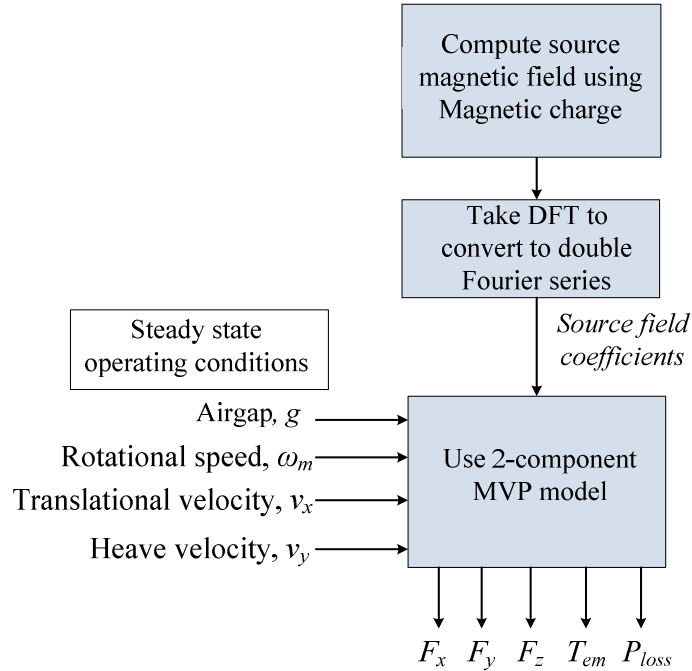


Figure 6.6. Flowchart of the presented analytic 2-component MVP model

6.9. Model Validation

In section 6.9.1 eddy current fields will be validated whereas in section 6.9.2 eddy current forces and joule loss will be compared with FEA models.

6.9.1. Field Validation

In this chapter the presented analytic model is validated with commercially available finite element analysis (FEA) software and also with a previously developed 3-D steady state FEA model [75]. For validation purposes a Halbach magnetized 2 pole pair rotor has been used as the source. The conductive plate and Halbach rotor geometric information is shown in

Table 6.1. It was assumed that the rotor was located 5 mm above the conductive plate. For computational purposes the number of harmonics along the x and z -axes are chosen to be 32 i.e. $M = N = 32$. A comparison of the magnetic vector potential and flux density

with FEA for zero translational velocity and zero lateral offset of the rotor is shown in Figure 6.7 and Figure 6.8. Good match of fields was obtained.

Table 6.1 : Halbach rotor and conductive plate parameters

	Description	Value	Unit
Magnetic Rotor	Outer radius, r_o	26	mm
	Inner radius, r_i	9.62	mm
	Width, w_o	52	mm
	Remnant magnetic flux density, B_{rem}	1.42	T
	Relative permeability, μ_r	1.108	-
	Pole pairs, P	2	-
	Rotational speed	5000	RPM
	Translational velocity, v_x	0	ms^{-1}
	Heave velocity, v_y	0	ms^{-1}
	Conductive plate	Conductivity, σ	2.459×10^7
Width, w		77	mm
Length, l		200	mm
Thickness, h		6.3	mm
Air-gap between rotor and plate, g		5	mm

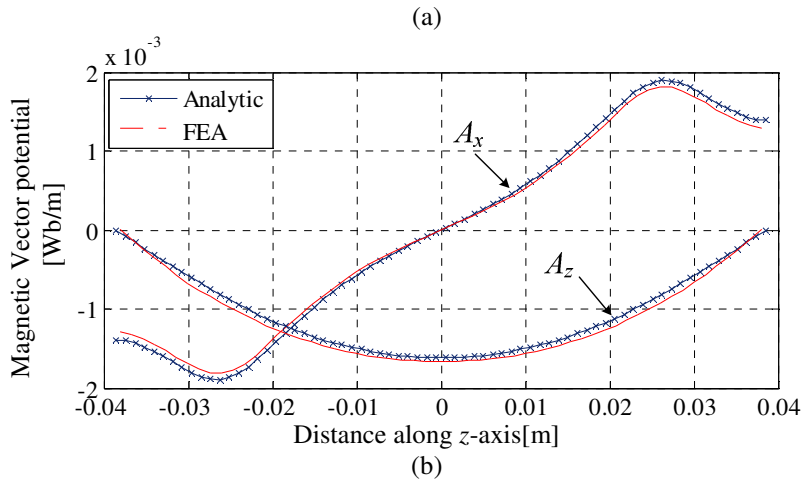
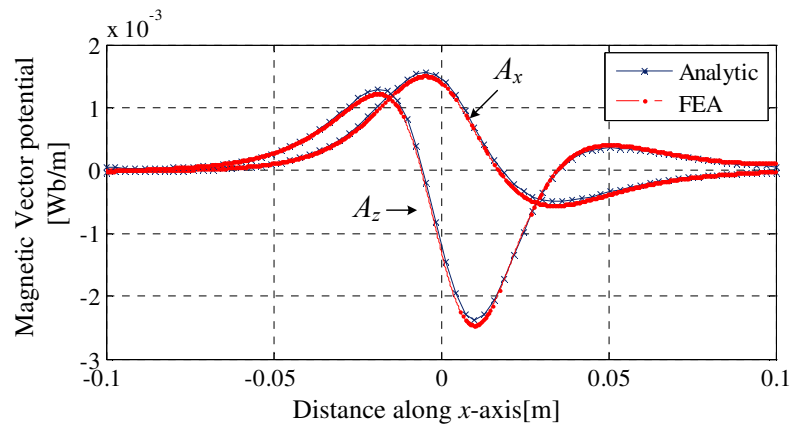


Figure 6.7. The A_x and A_z magnetic vector potential comparison with Comsol FEA model (a) along $(y, z) =$

(0, 20)mm coordinate axis (b) along $(x, y) = (0, 0)$ mm coordinate axis. The rotor is located at the center of the plate.

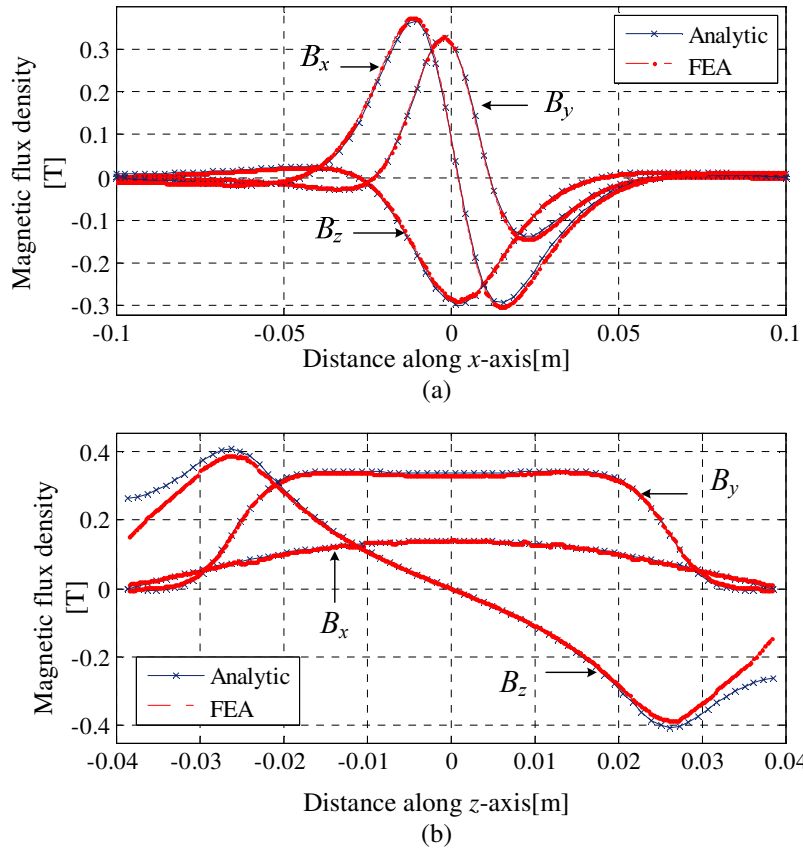


Figure 6.8. The B_x , B_y and B_z magnetic flux density comparison with Comsol FEA model (a) along $(y, z) = (0, 20)$ mm coordinate axis (b) along $(x, y) = (0, 0)$ mm coordinate axis. The rotor is located at the center of the plate.

Surface plot of the induced vector potentials in the conductive plate obtained from current sheet based steady state FEA model [75] is shown in Figure 6.9 while Figure 6.10 shows surface plot obtained from the developed analytic model. Similarly, Figure 6.11 and Figure 6.12 show the surface plot of the induced magnetic flux density in the conductive plate from the FEA and presented analytic model respectively.

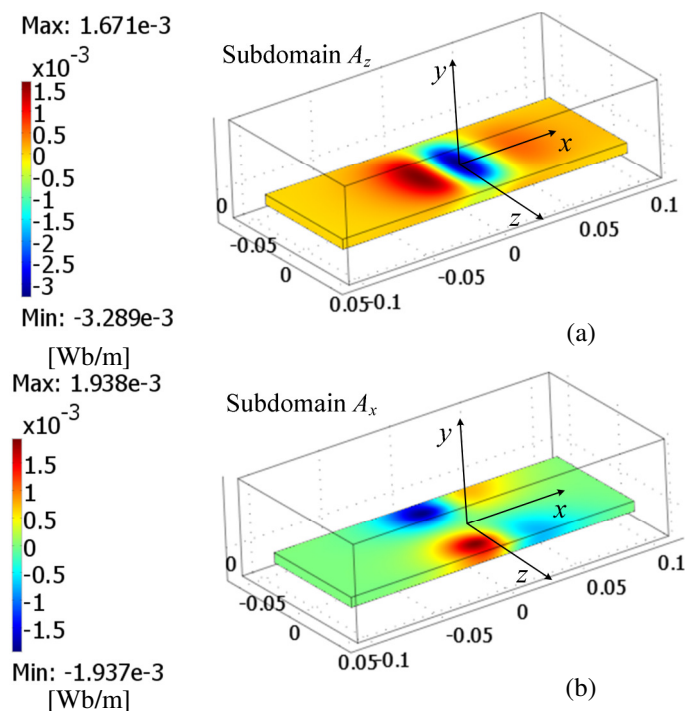


Figure 6.9. Plot of the (a) A_z and (b) A_x magnetic vector potential in the conductive plate computed using current sheet based FEA model. The rotor is located at the center of the plate.

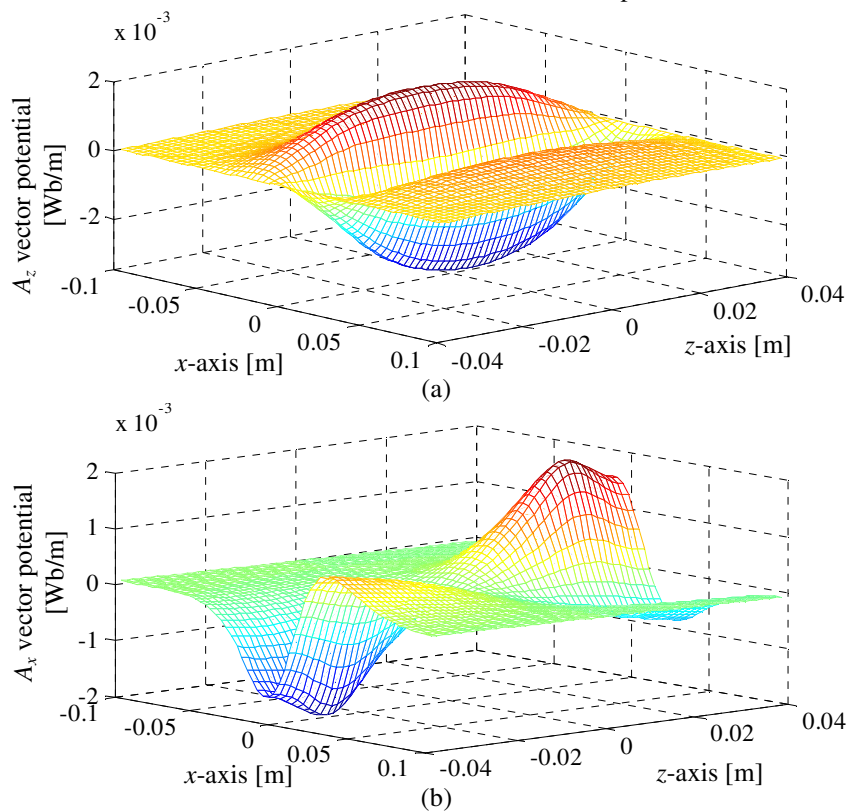


Figure 6.10. Surface plot of the analytically computed (a) A_z and (b) A_x magnetic vector potential on the conductive plate top surface. The rotor is located at the center of the plate.

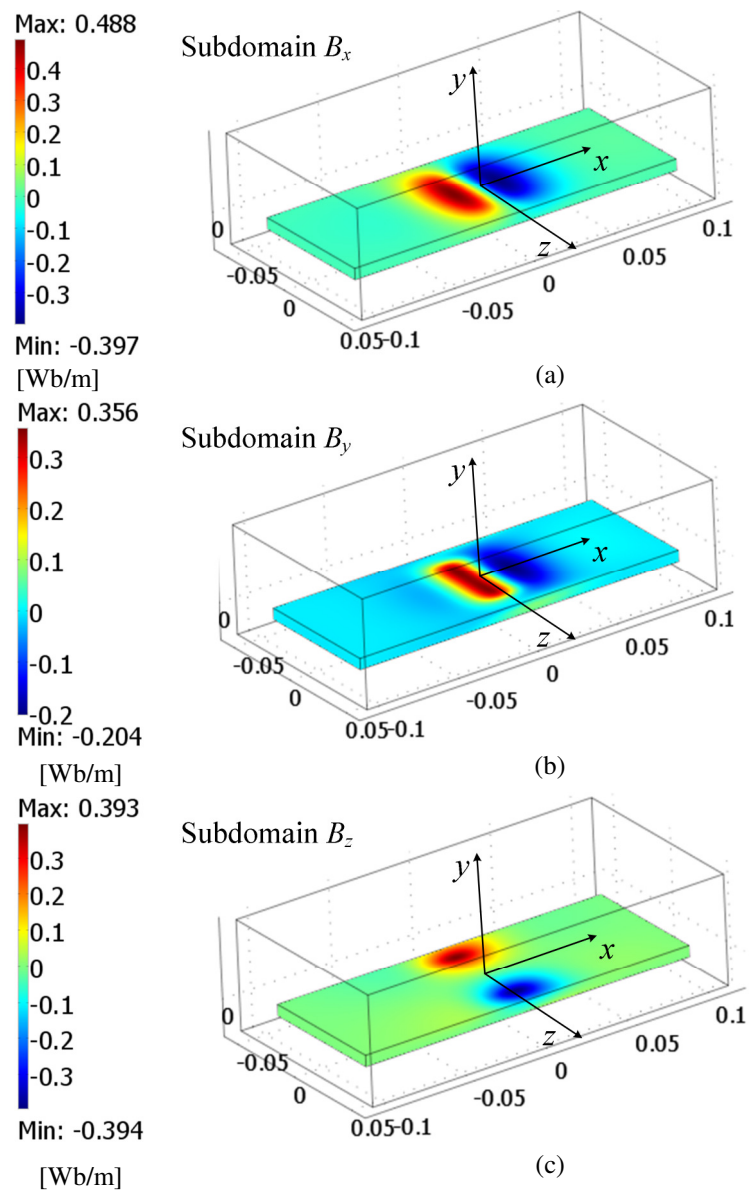


Figure 6.11. Plot of the induced (a) B_x , (b) B_y , and (c) B_z magnetic flux density in the conductive plate computed using current sheet based FEA model. The rotor is located at the center of the plate.

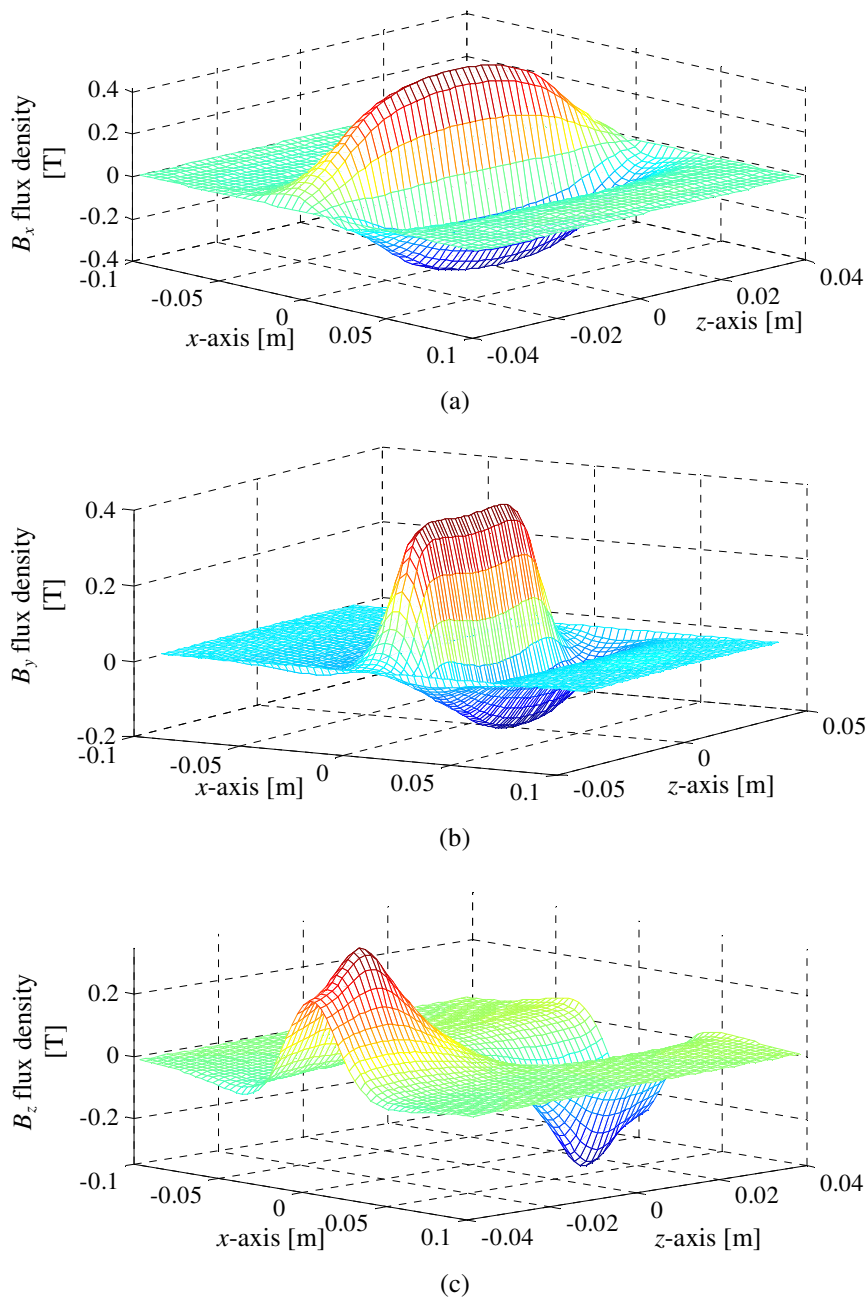


Figure 6.12. Surface plot of the analytically computed induced (a) B_x , (b) B_y and (c) B_z magnetic flux density on the conductive plate top surface. The rotor is located at the center of the plate.

Magnetic vector potential and flux density comparison when the rotor is moved towards the conductive plate edge by 20mm are shown in Figure 6.13 and Figure 6.14 respectively. Figure 6.15 and Figure 6.16 show the surface plots of the induced magnetic

vector potentials obtained from the FEA [75] and analytic model respectively. Again a close match of fields was obtained.

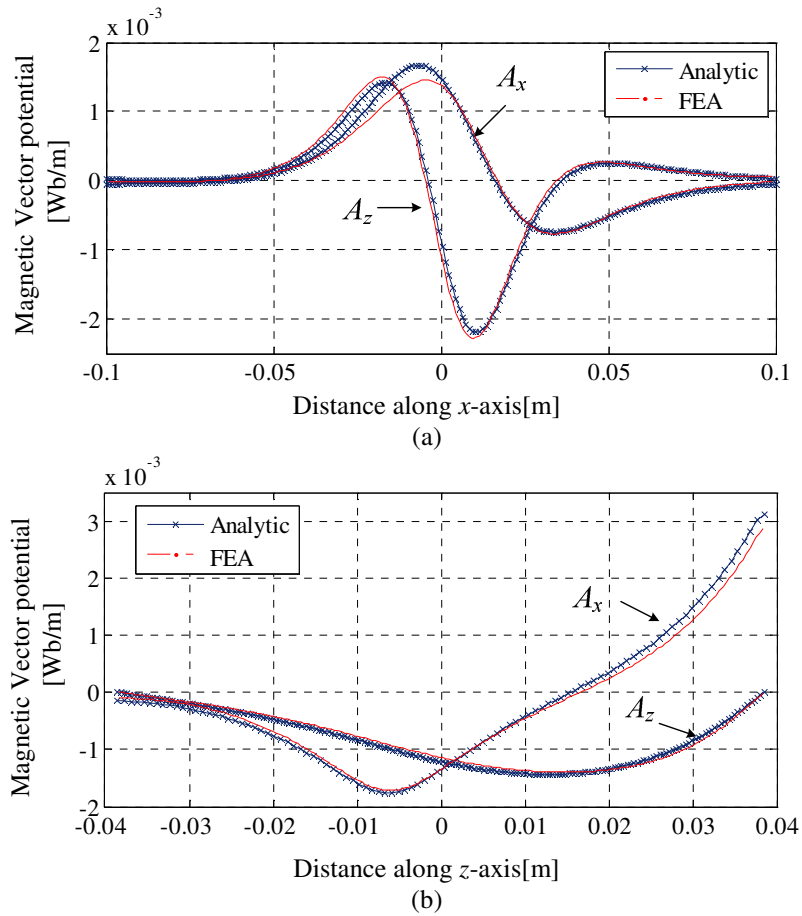


Figure 6.13. The A_x and A_z magnetic vector potential comparison with current sheet based Comsol FEA model (a) along $(y, z) = (0, 30)$ mm coordinate axis (b) along $(x, y) = (0, 0)$ mm coordinate axis. The rotor is shifted from the center of the plate by 20mm.

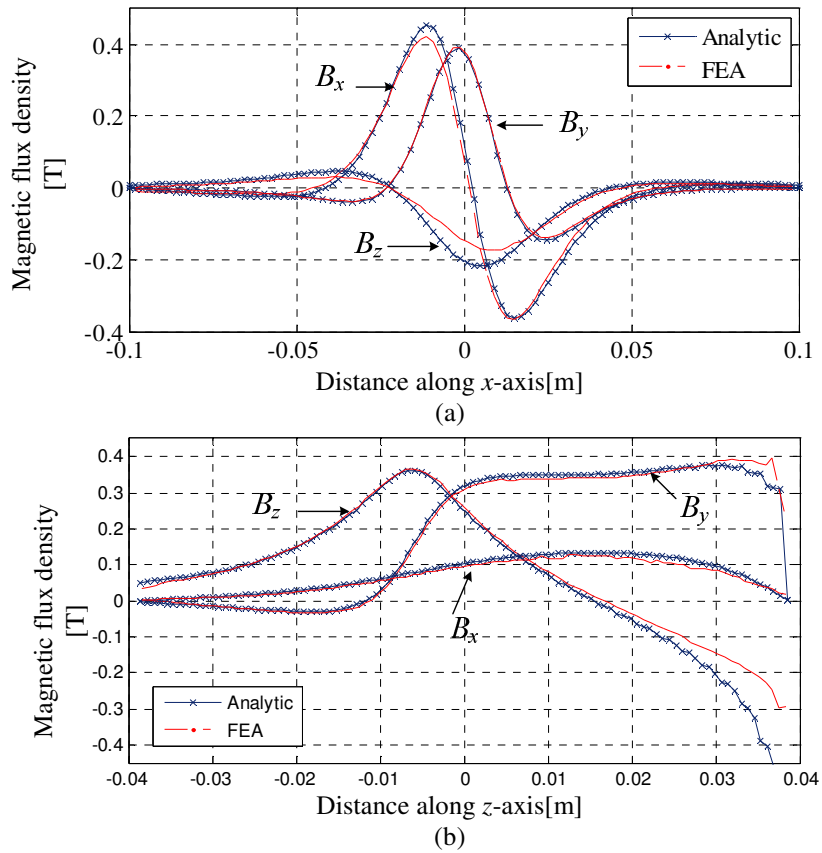


Figure 6.14. The B_x , B_y and B_z magnetic flux density comparison with Comsol FEA model (a) along $(y, z) = (0, 20)$ mm coordinate axis (b) along $(x, y) = (0, 0)$ mm coordinate axis. The rotor is shifted from the center of the plate by 20mm.

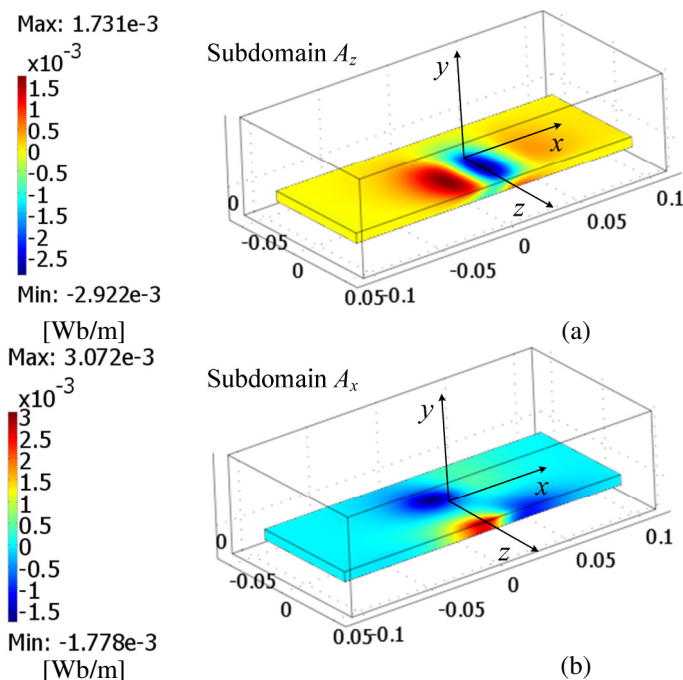


Figure 6.15. Plot of the (a) A_z and (b) A_x magnetic vector potential in the conductive plate computed using FEA. The rotor is shifted from the center of the plate by 20mm

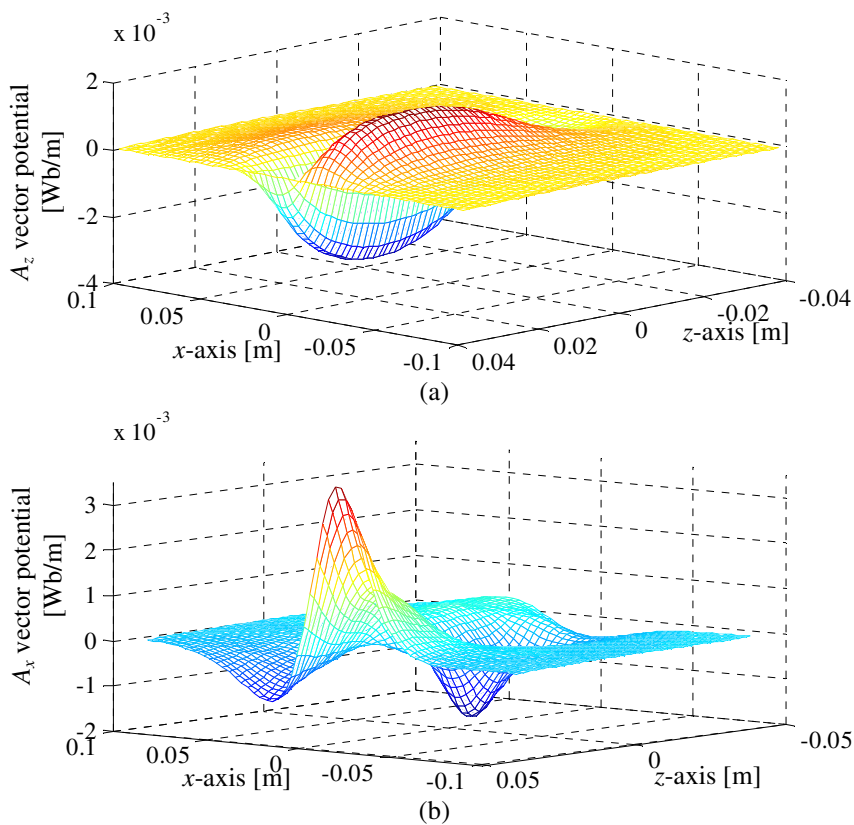
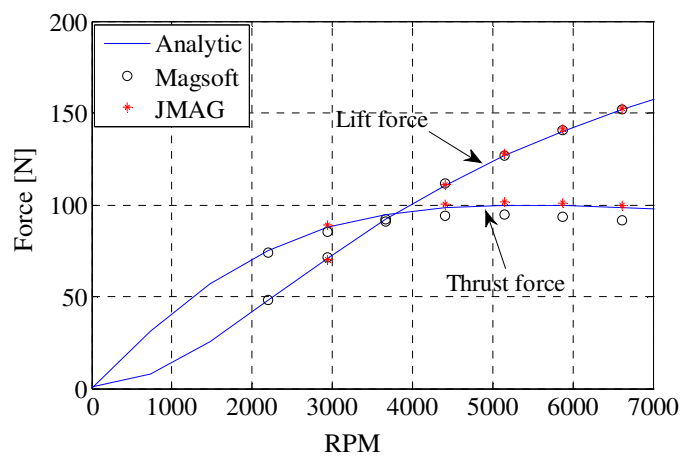


Figure 6.16. Surface plot of the analytically calculated (a) A_z and (b) A_x magnetic vector potential on the conductive plate surface. The rotor is shifted from the center of the plate by 20mm.

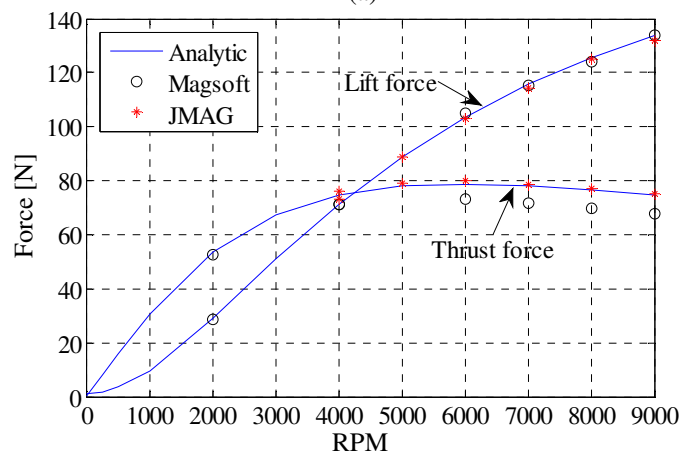
6.9.2. Force and Power Loss Validation

Using the parameters listed in

Table 6.1, a 3-D transient FEA model was created in JMAG and Magsoft Flux 3-D in order to further validate the analytic model. Due to the limitations of JMAG and Magsoft the Halbach rotor was rotated over the conductive plate without additional translational motion. The size of the air region and mesh size in the conductive region have been chosen carefully to minimize numerical errors. In addition the FEA model presented in [75] has been used for force and power loss comparison when there is non-zero translational velocity. Thrust and lift force comparison for the zero and non-zero translational speeds are shown in Figure 6.17 and Figure 6.18 respectively while Figure 6.19 shows the power loss comparison. The figures show that the analytical model achieves a close match with the FEA models.

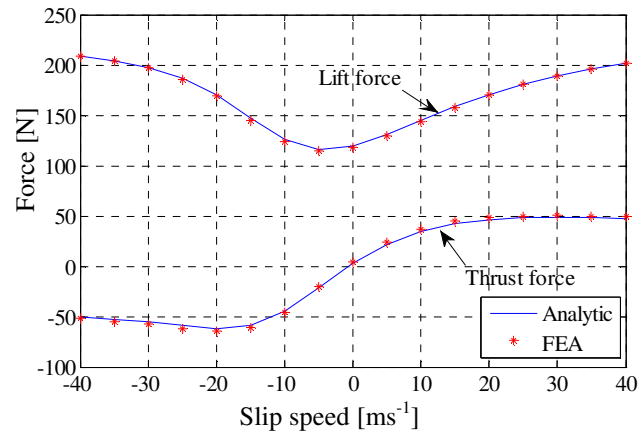


(a)

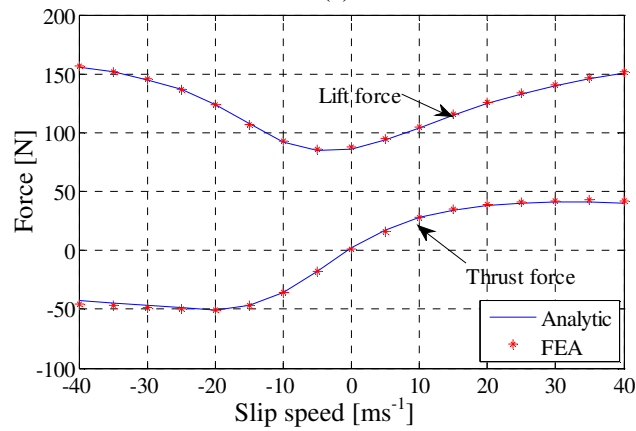


(b)

Figure 6.17 Thrust and lift force comparison between the 3-D analytic model and FEA for zero translational velocity when the rotor is (a) at the center and (b) shifted from the center of the conductive plate by 15mm.



(a)



(b)

Figure 6.18 Thrust and lift force comparison between 3-D analytic model and FEA model for $v_x=20\text{ms}^{-1}$ translational velocity and $v_y=5\text{ms}^{-1}$ heave velocity when the rotor is (a) at the center and (b) shifted from the center of the conductive plate by 20mm.

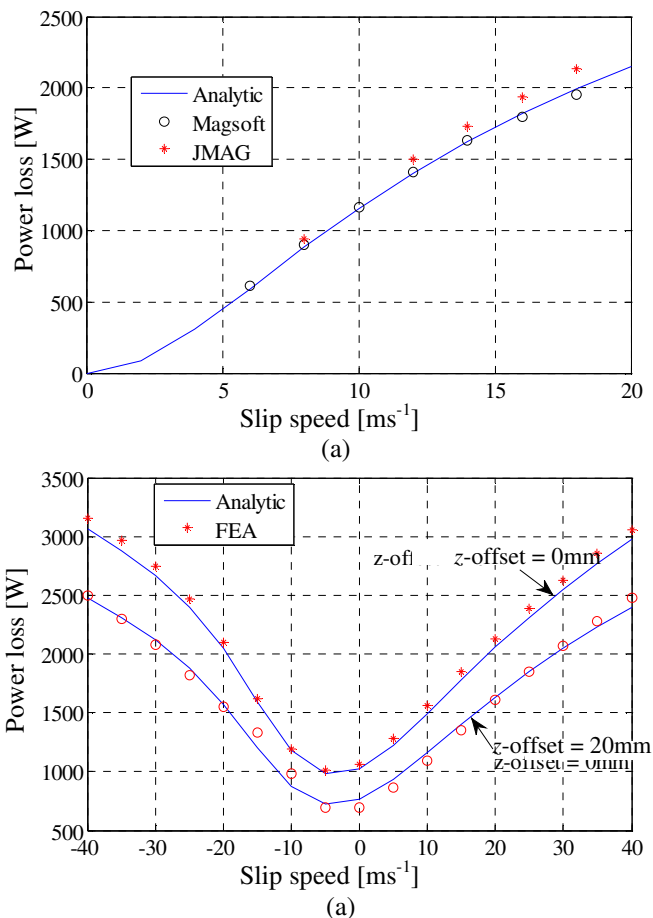


Figure 6.19 Power loss comparison between analytic and FEA models for (a) $v_x=0\text{ms}^{-1}$ translational velocity and (b) $v_x=20\text{ms}^{-1}$ translational velocity and $v_y=5\text{ms}^{-1}$ heave velocity.

Figure 6.20 shows the perspective and x - z view of the rotor with a pitch angle. Figure 6.21 shows the thrust, lateral and lift force comparison of the developed 2-component analytic model with a Magsoft Flux FEA model for different pitch angle values.

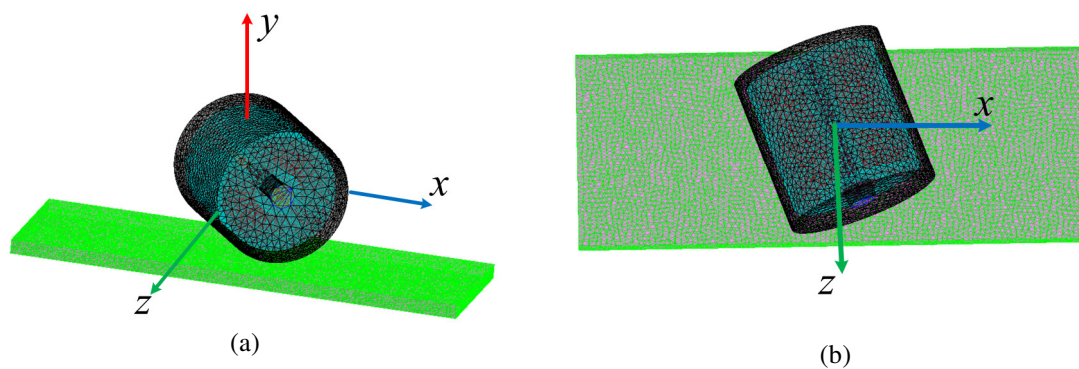


Figure 6.20. The (a) perspective and (b) x - z view of the Halbach rotor in the presence of pitch angle

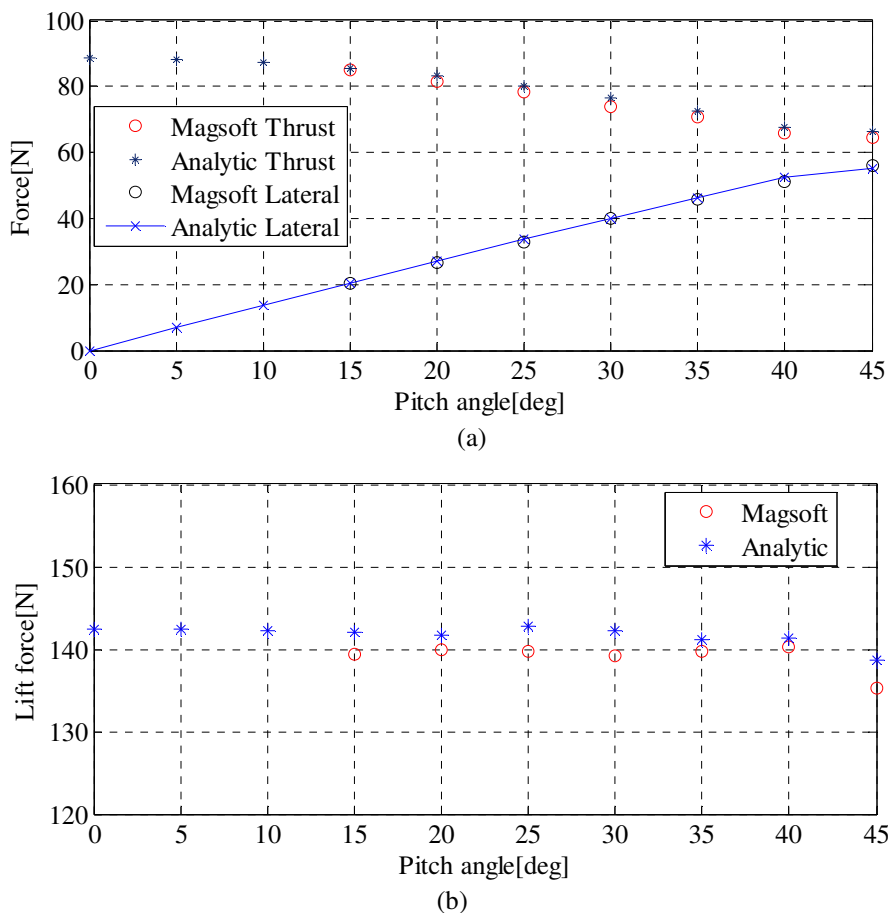


Figure 6.21 (a) Thrust and lateral force comparison, (b) lift force comparison between Magsoft Flux FEA and analytic model for zero translational velocity when the rotor is at the center of the plate. Rotational speed of the rotor is 7000 RPM. Comparison is performed for varying pitch angle of the rotor.

Figure 6.22 shows the perspective and y - z view of the rotor with a roll angle whereas

Table 6.2 shows the thrust, lateral and lift force comparison with Magsoft Flux FEA model for a roll angle value of 15 degree.

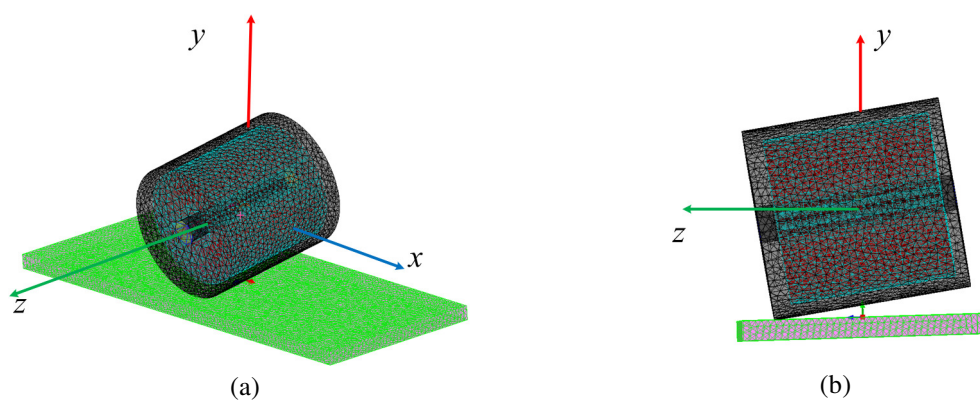


Figure 6.22 The (a) perspective and (b) y - z view of the Halbach rotor with 15 degree roll angle

Table 6.2. : Force comparison between analytic and Magsoft Flux FEA models

Model	Thrust force (N)	Lift force (N)	Lateral force (N)
Magsoft Flux	26.19	51.79	1.808
2-component analytic model	28.02	51.71	1.202

The average computation time involved in calculating the force and power loss results for a single rotational speed value by the FEA and analytic model are listed in Table 6.3. As expected, the analytic model reduces the computation time by a large extent.

Table 6.3 : Computation time for 2-component analytic and FEA models

Model type	Computation time
JMAG transient	5 hr 40 min
Magsoft flux transient	5 hr 21 min
Current sheet based steady state model using Comsol v3.5a	8 min
Analytic 2-component vector potential model	0.544 s

6.10. Limitation of the Proposed Model and Improved 3-Component Vector Potential Model

The limitation of the presented analytic model is its inability to calculate the correct lateral force as shown in Figure 6.23 which shows the lateral force comparison for lateral offset of the rotor by 10 and 20mm.

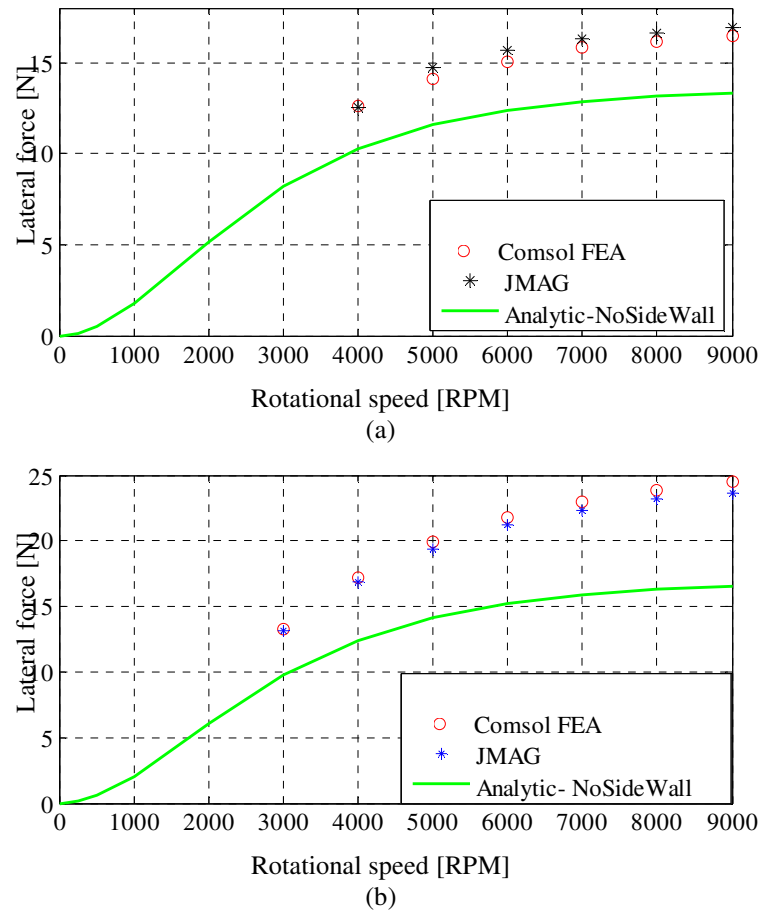


Figure 6.23. Lateral force comparison among Comsol, analytic and JMAG FEA models for (a) 10mm lateral offset and (b) 20mm lateral offset. The comparison was made at $(v_x, v_y, v_z)=(0,0,0)$ ms^{-1} .

In addition to incorrect lateral force, the thrust and lift force accuracy of the presented analytic model degrades with the increased plate thickness. This is due to the fact that the interaction of the magnetic source with the edge surface, Γ_e , of the plate has been ignored so far due to the assumption of a small plate thickness, h , and thus the vector potential fields in Ω_V have not been modeled. However, with increased plate thickness, h , and in the presence of lateral source field offset, d , it becomes essential to consider the effect of the source field in Ω_V on the induced eddy current distribution in the conductive plate region Ω_{II} .

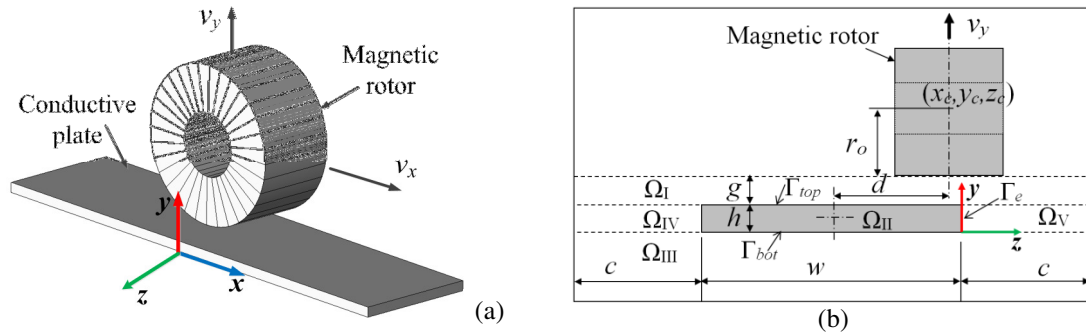


Figure 6.24. (a) 3-D schematic of a single rotor on conductive aluminum plate; (b) z-y view of the problem regions. The rotor is laterally offset from the center of the plate.

This is demonstrated in Figure 6.25 and Figure 6.26 which show the induced A_x and A_z vector potential within a 15mm thick finite with conductive plate when a Halbach rotor source field is applied and not applied to the edges of the plate. The figures are obtained using a previously presented finite element analysis (FEA) steady-state model [75]. By comparing the magnitude of the induced A_x field in Figure 6.25 and Figure 6.26, the importance of the source-plate interaction through Γ_e can be noticed. On the other hand, the figures show that the source flux linkage through Γ_e does not increase the A_z component in Ω_{II} significantly. Hence this component has been omitted while studying the edge effect. In the previous analysis it was shown that the A_y component was not required to determine the correct thrust/drag, F_x and lift, F_y , force for a small plate thickness. Thus the A_y is only significant when the source flux linkage through Γ_e is considered.

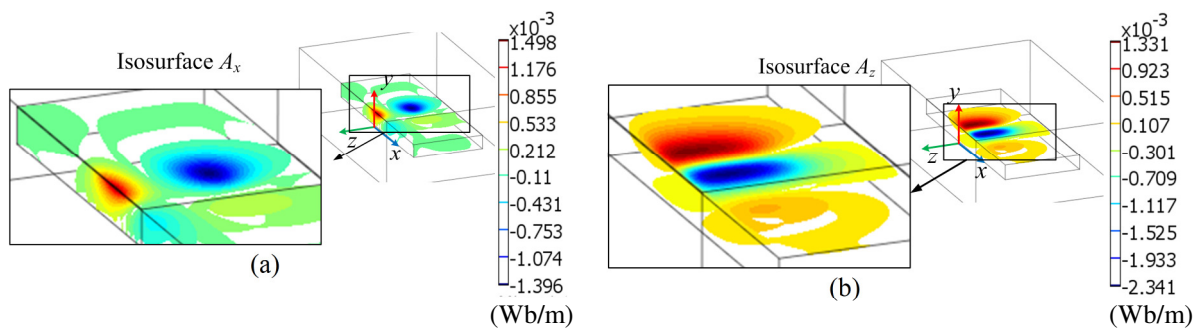


Figure 6.25. (a) The A_x and (b) A_z magnetic vector potential in a conductive plate of thickness 15mm when a magnetic rotor is laterally shifted by 25mm and the source field is applied on Γ_{top} , Γ_{bot} but *not* on Γ_e

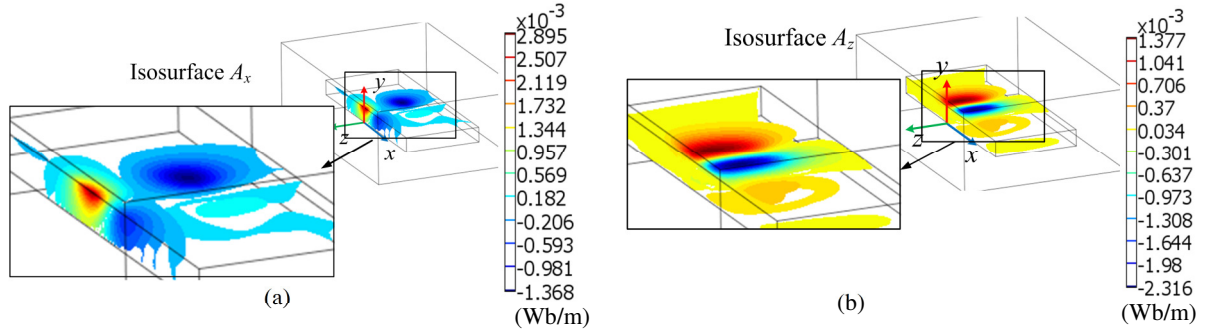


Figure 6.26 (a) The A_x and (b) A_z magnetic vector potential in a conductive plate of thickness 15mm when a magnetic rotor is laterally shifted by 25mm and the source field is applied on Γ_e as well as Γ_{top} and Γ_{bot}

Based on this analysis and using the superposition principle the total magnetic vector potential in the conductive plate, Ω_{II} , can be written as the summation of the fields induced due to the source-plate interaction through Γ_{top} , Γ_{bot} and edge boundary, Γ_e , such that

$$A_x^{II} = A_x^{II,t} + A_x^{II,e} \quad (6.160)$$

$$A_y^{II} = A_y^{II,e} \quad (6.161)$$

$$A_z^{II} = A_z^{II,t} \quad (6.162)$$

where the superscript 't' and 'e' denote top and edge field contributions. The goal of this section is to determine the induced $A_x^{II,e}$ and $A_y^{II,e}$ field due to the source-plate interaction through edge Γ_e . Due to the inclusion of the A_y component, the current analytic model can be called 3-component model. The derived field will then be added to the field contribution from the top and bottom of the conductor that was obtained in section 6.6 to determine the total thrust/drag and lift force. The approach will be compared with an FEA model [75].

6.10.1. Governing Equations and Boundary Conditions

The x and y -component of the vector potential in Ω_{II} satisfies the following governing equation [214]

$$\nabla^2 A_i^{II,e} = \mu_0 \sigma \left(j\omega_e A_i^{II,e} + v_x \frac{\partial A_i^{II,e}}{\partial x} + v_y \frac{\partial A_i^{II,e}}{\partial y} \right), \quad i = x, y, \text{ in } \Omega_{II} \quad (6.163)$$

where v_x and v_y are the source velocity in the x and y -directions, σ is the plate conductivity (S/m). Also in order to satisfy current flow continuity

$$\hat{n}_{II} \cdot \mathbf{A}^{II,e} = 0 \quad (6.164)$$

must be satisfied on the boundaries of Ω_{II} [214] where \hat{n}_{II} is a unit vector normal to the conductive plate. Utilizing the real and complex Fourier analysis technique the general solution of (6.163) is

$$A_x^{II,e}(x, y, z) = \sum_{m=-M}^M \sum_{n=0}^N C_{mn}^{x,e} e^{j\xi_m x} \cos(u_n y) e^{\tau_{mn}^{II} z}, \text{ in } \Omega_{II} \quad (6.165)$$

$$A_y^{II,e}(x, y, z) = \sum_{m=-M}^M \sum_{n=1}^N C_{mn}^{y,e} e^{j\xi_m x} \sin(u_n y) e^{\tau_{mn}^{II} z}, \text{ in } \Omega_{II} \quad (6.166)$$

where

$$\xi_m = 2m\pi / l \quad (6.167)$$

$$u_n = n\pi / h \quad (6.168)$$

$$\tau_{mn}^{II} = 0.5\mu_0\sigma v_y + \sqrt{(0.5\mu_0\sigma v_y)^2 + (\tau_{mn}^V)^2 + j\mu_0\sigma(\omega_e + \xi_m v_x)} \quad (6.169)$$

$$\tau_{mn}^V = \sqrt{u_n^2 + \xi_m^2} \quad (6.170)$$

ω_e = electrical frequency (rads⁻¹). It is assumed that the plate-width, w , is large enough to ignore any reflection from the plate surface at $z=-w$. Hence, region Ω_{IV} is not required in this formulation. The vector potentials in Ω_V satisfies the following Laplace equation

$$\nabla^2 A_i^V = 0, \quad i = x, y, \text{ in } \Omega_V \quad (6.171)$$

which yields the following general solutions

$$A_x^V(x, y, z) = \sum_{m=-M}^M \sum_{n=0}^N D_{mn}^x e^{j\xi_m x} \cos(u_n y) e^{-\tau_{mn}^V z}, \text{ in } \Omega_V \quad (6.172)$$

$$A_y^V(x, y, z) = \sum_{m=-M}^M \sum_{n=1}^N D_{mn}^y e^{j\xi_m x} \sin(u_n y) e^{-\tau_{mn}^V z}, \text{ in } \Omega_V \quad (6.173)$$

From the continuity of the tangential components of the magnetic field intensity and normal components of the flux density at $z=0$ and the continuity of the Coulomb gauge

$$\nabla \cdot \mathbf{A} = 0 \quad (3.22)$$

the following boundary conditions are derived

$$-\frac{\partial A_y^{\text{II,e}}}{\partial z} = -\frac{\partial A_y^V}{\partial z} + B_x^s(x, y, z), \text{ at } z=0 \quad (6.174)$$

$$\frac{\partial A_x^{\text{II,e}}}{\partial z} = \frac{\partial A_x^V}{\partial z} + B_y^s(x, y, z), \text{ at } z=0 \quad (6.175)$$

$$\frac{\partial^2 A_y^{\text{II,e}}}{\partial x^2} + \frac{\partial^2 A_y^{\text{II,e}}}{\partial y^2} = \frac{\partial^2 A_y^V}{\partial x^2} + \frac{\partial^2 A_y^V}{\partial y^2} + \frac{\partial B_z^s(x, y, z)}{\partial x}, \text{ at } z=0 \quad (6.176)$$

$$\frac{\partial^2 A_x^{\text{II,e}}}{\partial x^2} + \frac{\partial^2 A_x^{\text{II,e}}}{\partial y^2} = \frac{\partial^2 A_x^V}{\partial x^2} + \frac{\partial^2 A_x^V}{\partial y^2} - \frac{\partial B_z^s(x, y, z)}{\partial y}, \text{ at } z=0 \quad (6.177)$$

6.10.2. Source Field Modeling

Following the treatment presented in section 6.5 the source field on the edge surface, Γ_e , can be represented as the following Fourier series

$$B_x^s(x, y, 0) = \sum_{m=-M}^M \sum_{n=1}^N S_{mn}^{x,s} \sin(u_n y) e^{j\xi_m x}, \text{ at } z=0 \quad (6.178)$$

$$B_y^s(x, y, 0) = \sum_{m=-M}^M \sum_{n=0}^N S_{mn}^{y,s} \cos(u_n y) e^{j\xi_m x}, \text{ at } z=0 \quad (6.179)$$

$$B_z^s(x, y, 0) = \sum_{m=-M}^M \sum_{n=1}^N S_{mn}^{z,s} \sin(u_n y) e^{j\xi_m x}, \text{ at } z=0 \quad (6.180)$$

The coefficients in (6.178)-(6.180) are determined by using the standard procedure of computing the Fourier series coefficients [132, 214].

6.10.3. Field Solution

The induced magnetic fields due to the presence of the edge source field can be determined by substituting (6.165),(6.166),(6.172),(6.173) and (6.178)-(6.180) into (6.174)-(6.177). Then utilizing (3.7)-(3.9) the field solution is

$$B_x^{\text{II},e}(x, y, z) = \sum_{m=-M}^M \sum_{n=1}^N e^{j\xi_m x} \sin(u_n y) e^{\tau_{mn}^{\text{II}} z} \frac{[S_{mn}^{x,s} + (j\xi_m S_{mn}^{z,s} / \tau_{mn}^{\text{V}})]}{[1 + \tau_{mn}^{\text{V}} / \tau_{mn}^{\text{II}}]} \quad (6.181)$$

$$B_y^{\text{II},e}(x, y, z) = \sum_{m=-M}^M \sum_{n=0}^N e^{j\xi_m x} \cos(u_n y) e^{\tau_{mn}^{\text{II}} z} \frac{[S_{mn}^{y,s} + (u_n S_{mn}^{z,s} / \tau_{mn}^{\text{V}})]}{[1 + \tau_{mn}^{\text{V}} / \tau_{mn}^{\text{II}}]} \quad (6.182)$$

$$B_z^{\text{II},e}(x, y, z) = \sum_{m=-M}^M \sum_{n=1}^N e^{j\xi_m x} \sin(u_n y) e^{\tau_{mn}^{\text{II}} z} \frac{[u_n S_{mn}^{y,s} - j\xi_m S_{mn}^{x,s} + \tau_{mn}^{\text{V}} S_{mn}^{z,s}]}{[\tau_{mn}^{\text{II}} (1 + \tau_{mn}^{\text{V}} / \tau_{mn}^{\text{II}})]} \quad (6.183)$$

6.10.4. Model Validation

The presented analytic model has been validated with a previously developed 3-D steady state FEA model [75]. The simulation parameters are shown in

Table 6.1. The forces were calculated using Maxwell's stress tensor [115] where the net flux density in Ω_{II} has been considered which is obtained by adding (6.181)-(6.183) with the contribution from the source field applied on Γ_{top} and Γ_{bot} as derived in section 6.6.2. Figure 6.27-Figure 6.29 show the force comparison when using the FEA model [75] as well as a previously presented 2-component model of section 6.7 and the modified 3-component vector potential model. The percentage error in the force calculation using the 3-component and 2-component vector potential model has been displayed. The inclusion of the edge effect components has reduced the analytic force calculation error.

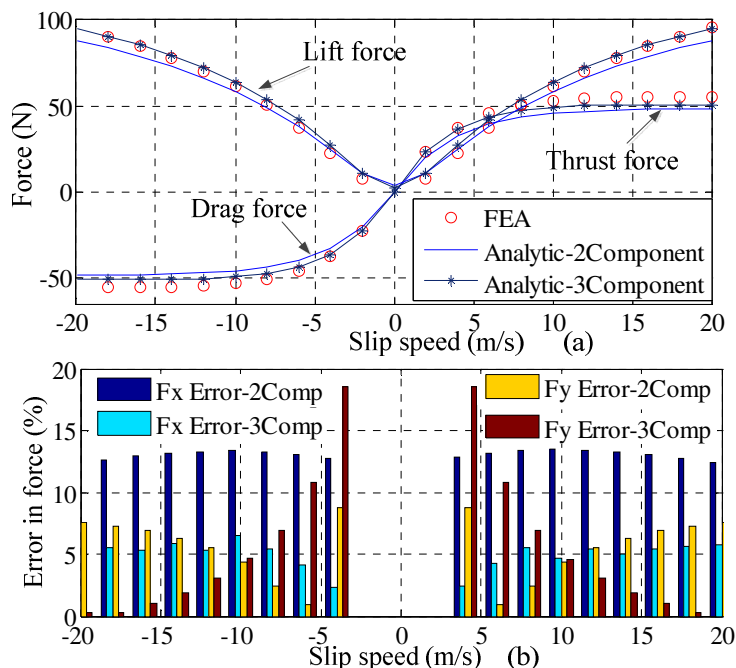


Figure 6.27. (a) Force comparison at $v_x=0\text{m/s}$ and $(d, h) = (25, 15)\text{mm}$; (b) percentage error in force calculation

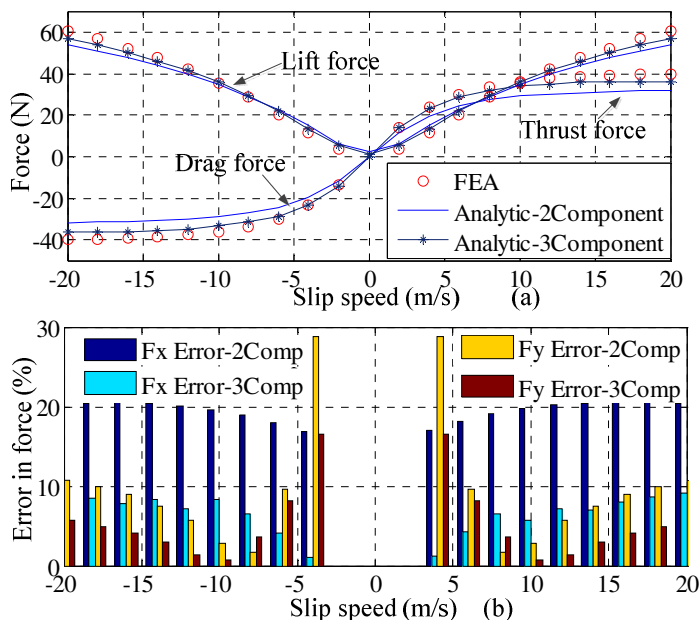


Figure 6.28 (a) Force comparison at $v_x=0\text{m/s}$ and $(d, h)=(35, 15)\text{mm}$; (b) percentage error in force calculation

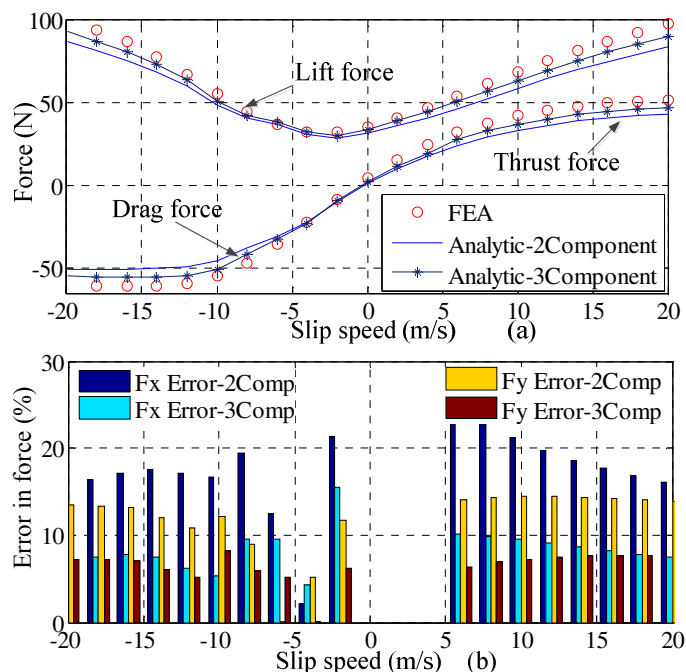


Figure 6.29. (a) Force comparison at $v_x=15\text{m/s}$ and $(d, h)=(25, 25)\text{mm}$; (b) percentage error in force calculation

The flux density comparison for 15mm thick plate and 35mm lateral offset of the rotor along the z -axis is provided in Figure 6.30 and Figure 6.31. From the plots it is observed that towards the edge (i.e. $z=0\text{mm}$) the error in analytically calculated B_y and B_z field increases which results in inaccurate lateral force calculation. Hence the presented

3-component model has improved the thrust and lift force computation for increased plate thickness, however, it is still an approximate model.

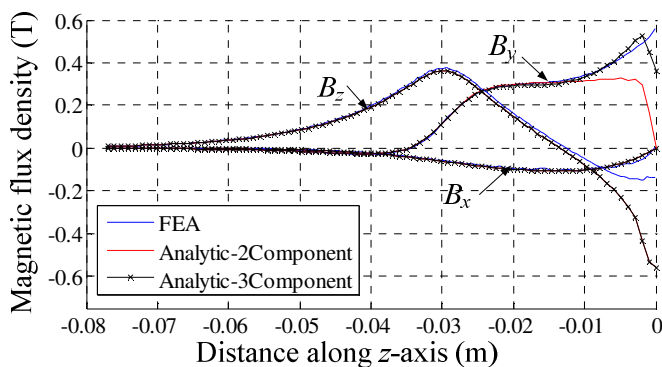


Figure 6.30. Flux density comparison at $x=0\text{mm}$ on the top plate surface

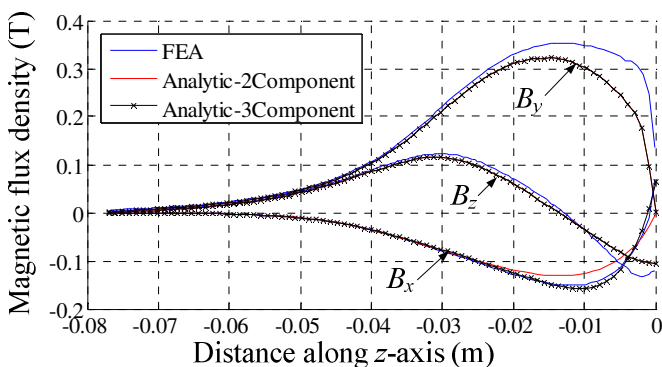


Figure 6.31 Flux density comparison at $x=-20\text{mm}$ on the top plate surface

The average computation time involved in calculating the force and power loss results for a single rotational speed value by the FEA and 3-component MVP based analytic model are listed in Table 6.4. By comparing with Table 6.3 it is observed that the 3-component MVP model is slower than its 2-component counterpart due to the added boundary conditions at the edges of the conductive plate and extra component of the magnetic vector potential.

Table 6.4 : Computation time for 3-component analytic and FEA models

Model type	Computation time
JMAG transient	5 hr 40 min
Magsoft flux transient	5 hr 21 min
Current sheet based steady state model using Comsol v3.5a	8 min
Analytic 3-component vector potential model	6 s

6.11. Summary

Analytic 3-D steady state modeling approach to study eddy current distribution in a conductive plate of finite width and thickness has been presented. The 2-component model is formulated in terms of decoupled set of equations using the magnetic vector potential in the nonconductive and conductive regions. It is computationally efficient. Computation time has been compared with FEA models. Also electromagnetic forces and power loss comparison has been made to suggest that the model can be very useful to calculate thrust, lift force and power loss in the plate when the dimension of the plate is comparable to that the source or when the source is laterally offset towards the edge of the plate. However the drawback of this model is its inability to calculate correct lateral force and is applicable to only plate of small thickness. An improved 3-component vector potential model has also been presented for a plate of arbitrary thickness. However, the 3-component model is also an approximate model as it lacks the accuracy in the magnetic fields near the plate edge. The key points of the proposed two and three component MVP models are summarized in Table 6.5 and Table 6.6 respectively.

The presented approximate analytic models using magnetic vector potential are of great interest due to quick computation of the induced fields and/or thrust and lift force due to finite width and thickness conductive plate. However the accurate treatment of the eddy current analysis in a conductive plate of finite width is a tedious process as will be described in the next chapter.

Table 6.5 : Summary of the presented 3-D analytic steady state model using 2-component MVP

Model assumptions	Model characteristics
<ul style="list-style-type: none"> • Conductive plate is linear, simply connected, homogenous and non-magnetic • Conductive plate is infinitely long, but has finite width • Plate has finite but small thickness • A_y component of the MVP is ignored • Frequency is low 	<ul style="list-style-type: none"> • Models the conductive and nonconductive domains using 2-components of the MVP. • Decoupled boundary conditions lead to simple model derivation • Can be applicable for any magnetic source • Computes the source field using magnetic charge sheet • Models translational, heave as well as rotational motion of the source • Computationally faster than FEA but inferior to the analytic SOVP model • Not accurate for plate with large but finite thickness • Fails to produce correct lateral force in the presence of lateral offset of the source. • Model has been developed in Matlab

Table 6.6 : Summary of the presented 3-D analytic steady state model using 3-component MVP

Model assumptions	Model characteristics
<ul style="list-style-type: none"> • Conductive plate is linear, simply connected, homogenous and non-magnetic • Conductive plate is infinitely long, but has finite width • Plate has finite and arbitrary thickness • Frequency is low 	<ul style="list-style-type: none"> • Models the conductive and nonconductive domains using the MVP. All three components are used in the plate domain. • Can be applicable for any magnetic source • Computes the source field using magnetic charge sheet • Models translational, heave as well as rotational motion of the source • Computationally faster than FEA but inferior to the 2-component MVP model. • Accuracy is better than the 2-component MVP model for plate with large thickness. • Fails to produce correct lateral force in the presence of lateral offset of the source. • Model has been developed in Matlab

CHAPTER 7 : 3-D ANALYTIC EDDY CURRENT MODELING FOR FINITE PLATE WIDTH INCLUDING EDGE-EFFECT

7.1. Introduction

As pointed out in the previous chapter, the source field interaction through the edge of a conductive plate should be taken into account in order to analytically derive the correct lateral force (F_z). To account for the edge effect, in the previous chapter the side-air regions have been modeled using the magnetic vector potentials. This resulted in an improved thrust and lift force which is applicable to a plate of any thickness. In other words, modeling the magnetic vector potentials in the edge regions removed the assumption of the small but finite plate thickness. However, from the flux density comparisons provided in chapter chapter 6, it is observed that in the presence of lateral offset of the magnetic source, the B_y and B_z flux components of the analytic model do not match quite well with the FEA counterparts. This results mainly in an inaccurate lateral force.

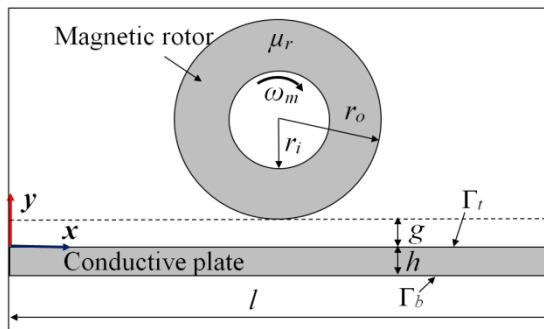


Figure 7.1. x-y view of the problem domain

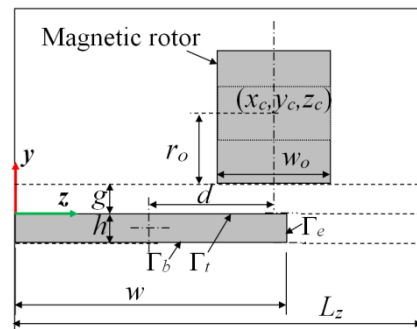


Figure 7.2. y-z view of the problem domain

The x - y and y - z view of the problem domain are shown in Figure 7.1 and Figure 7.2 respectively. In order to achieve coupling between the fields in the plate, Ω_{II} , and side region, Ω_V , in a mathematically elegant way the fields in these regions can be modeled as Fourier series with eigenvalues determined by applying appropriate boundary conditions at the interface boundary, Γ_e . As the problem domain (originally infinite) is being truncated in the x and z -directions by applying suitable boundary conditions, this approach is referred to in the literature as *truncated region eigenfunction expansion* (TREE) [117, 118, 149, 151, 192].

Previously the TREE approach has been used to study the eddy current distribution in a conductive medium with flaw or crack for nondestructive testing applications [117, 118, 141, 148, 149, 151, 192, 215]. However, to date such models have been developed for a plate of infinite thickness with a borehole with finite or infinite depth in order to study the impedance variation near the bore hole. The contribution of this chapter is to apply the TREE approach to a conductive plate of finite thickness and to analytically derive the eddy current fields and forces.

The assumptions of the analytic model presented in this chapter are:

- The plate length, l , is infinite but width, w , and thickness, h , are finite
- The plate is continuous, non-magnetic, linear and homogenous.
- The magnetic source has only rotational motion.
- Frequency is low.

The rest of the chapter is arranged as follows: section 7.2 will describe the governing equations for all the problem regions and section 7.3 will discuss the boundary

conditions; section 7.4 will derive the analytic eddy current forces; model validation will be performed in section 7.5 and a summary of the chapter will be provided in section 7.6.

7.2. Governing Equation Formulation

The magnetostatic field of the magnetic rotor is required only in the boundary condition of boundary Γ_t in order to determine the transmitted and reflected fields. Hence, the following simplified problem domain can be derived from Figure 7.1 and Figure 7.2 by omitting the magnetic rotor.

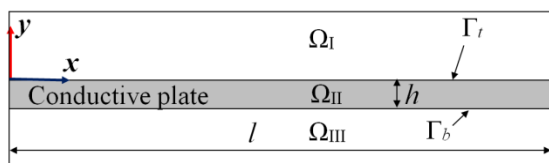


Figure 7.3. x - y view of the problem domain with different problem regions

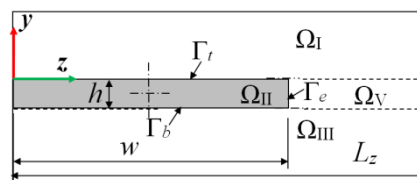


Figure 7.4. y - z view of the problem domain with different problem regions

In this chapter the induced and reflected fields in the conductive region Ω_{II} and nonconductive region Ω_V are modeled using the second order vector potential (SOVP) while the fields in the nonconductive regions Ω_I and Ω_{III} are modeled using the magnetic scalar potential. Due to such choice of potentials the number of unknowns in the problem domain has been kept to a minimum. For simplicity it has been assumed that the magnetic source does not have any motion along the x , y and z directions.

As stated before, in the presented formulation the solution domain has been truncated along the x and z -directions while it is unconstrained along the y -axis. Thus the solution domain extends from 0 to l in the x -direction and from 0 to L_z in the z -direction. There is a wide choice of possible combinations of boundary conditions at the four truncation boundaries. The possible boundary conditions include perfect magnetic conductor (PMC), $B_t=0$ (subscript t stands for tangential component) and perfect electric conductor (PEC), $B_n=0$ (subscript n stands for normal component). For the problem domain

geometry considered here the conductive plate edge at $z=w$ is located sufficiently far from the truncation boundaries and hence the choice of the boundary conditions on the truncation boundary have a negligible effect on the numerical values of the field in the solution domain. In this chapter, a PMC condition has been applied at $x=0$ and PEC condition has been applied at $x=l$ i.e.

$$B_i = 0, \quad i = y, z, \quad \text{at } x=0 \quad (7.1)$$

$$B_x = 0, \quad \text{at } x=l \quad (7.2)$$

Along the z -direction, a PMC condition is satisfied at $z=0$ and $z=L_z$ i.e.

$$B_i = 0, \quad i = x, y, \quad \text{at } z=0, L_z \quad (7.3)$$

This choice of boundary conditions yields Fourier series with respect to both x and z axes without zero frequency terms. The absence of zero frequency terms greatly simplifies the solution procedure.

7.2.1. Conductive Region (Ω_{II})

The SOVP has been utilized in Ω_{II} region which is denoted as \mathbf{W} and defined as [141, 182, 183]

$$\mathbf{A} = \nabla \times \mathbf{W} \quad (3.64)$$

$$\mathbf{B} = \nabla \times \nabla \times \mathbf{W} \quad (5.11)$$

As discussed in chapter 4, \mathbf{W} can be split into TE, W_a , and TM, W_b , scalar potentials with z -preferred direction as follows [117, 118, 192]

$$\mathbf{W} = \hat{z}W_a + \hat{z} \times \nabla W_b \quad (7.4)$$

Here \hat{z} is the unit vector along the z -direction. From (5.7) it is noticed that the TE and TM potentials satisfy the following in the absence of translational velocity terms

$$\frac{\partial^2 W_i^{\text{II}}}{\partial x^2} + \frac{\partial^2 W_i^{\text{II}}}{\partial y^2} + \frac{\partial^2 W_i^{\text{II}}}{\partial z^2} = \varepsilon^2 W_i^{\text{II}}, \quad i = a, b \quad (7.5)$$

where

$$\varepsilon^2 = -\mu_0 \sigma j \omega_e \quad (7.6)$$

Unlike chapter 5, in (7.4) the unit vector is chosen along the z -axis for the following reason.

Substituting (7.4) into (3.64) and using (7.5) yields

$$A_x^{\text{II}} = \frac{\partial W_a^{\text{II}}}{\partial y} \quad (7.7)$$

$$A_y^{\text{II}} = -\frac{\partial W_a^{\text{II}}}{\partial x} \quad (7.8)$$

$$A_z^{\text{II}} = \varepsilon^2 W_b^{\text{II}} \quad (7.9)$$

The normal component of the eddy current or the magnetic vector potential should be zero at $z=0$ and $z=w$ i.e.

$$A_z = 0, \quad \text{at } z=0, w \quad (7.10)$$

From (7.9) it is noticed that with the z -preferred direction of the SOVP, the A_z component is function of the W_b potential only. Hence the boundary condition (7.10) can be easily satisfied by choosing suitable Fourier series representation of only the W_b potential.

For the magnetic flux density, substituting (7.4) into (5.11) gives

$$B_x^{\text{II}} = \frac{\partial^2 W_a^{\text{II}}}{\partial z \partial x} + \varepsilon^2 \frac{\partial W_b^{\text{II}}}{\partial y} \quad (7.11)$$

$$B_y^{\text{II}} = \frac{\partial^2 W_a^{\text{II}}}{\partial z \partial y} - \varepsilon^2 \frac{\partial W_b^{\text{II}}}{\partial x} \quad (7.12)$$

$$B_z^{\text{II}} = \frac{\partial^2 W_a^{\text{II}}}{\partial z^2} - \varepsilon^2 W_a^{\text{II}} \quad (7.13)$$

Using the separation of variables method [132]

$$W_i^{\text{II}}(x, y, z) = X_i(x)Y_i(y)Z_i(z), \quad i = a, b \quad (7.14)$$

and using the boundary conditions (7.1) and (7.2) yields for the x -dependency of the TE and TM potentials as follows

$$X_a(x) = \sin(\xi_m x) \quad (7.15)$$

$$X_b(x) = \cos(\xi_m x) \quad (7.16)$$

where

$$\xi_m = \frac{\pi(2m-1)}{2l}, \quad 1 \leq m \leq \infty \quad (7.17)$$

Substituting (7.15) or (7.16) into (7.5),

$$\frac{\partial^2 W_i^{\text{II}}}{\partial y^2} + \frac{\partial^2 W_i^{\text{II}}}{\partial z^2} = \varepsilon^2 W_i^{\text{II}} + \xi_m^2 W_i^{\text{II}}, \quad i = a, b \quad (7.18)$$

Dividing both sides by $X_i(x)Y_i(y)Z_i(z)$

$$\frac{Y_i''}{Y_i} + \frac{Z_i''}{Z_i} = \varepsilon^2 + \xi_m^2 \quad (7.19)$$

Noting the boundary condition (7.3) and (7.10), the following z -dependency can be obtained for the W_a and W_b potentials

$$Z_a(z) = \cos(q_n z) \quad (7.20)$$

$$Z_b(z) = \sin(r_n z) \quad (7.21)$$

where
$$r_n = n\pi / w, 1 \leq n \leq \infty \quad (7.22)$$

The eigenvalues q_n are determined from the continuity condition of the magnetic flux density and field intensity at $z=w$ interface, Γ_e , and will be discussed in section 7.3.1. The choice of r_n as given by (7.22) makes sure that the boundary condition (7.10) is satisfied. Substituting (7.20) into (7.19) gives

$$\frac{Y_a''}{Y_a} = \xi_m^2 + q_n^2 + \varepsilon^2 \quad (7.23)$$

Hence for the TE potential

$$Y_a(y) = C_{mn}^a e^{\alpha_{mn}y} + D_{mn}^a e^{-\alpha_{mn}y} \quad (7.24)$$

where
$$\alpha_{mn} = \sqrt{\xi_m^2 + q_n^2 + \varepsilon^2} \quad (7.25)$$

Similarly for the TM potential

$$Y_b(y) = C_{mn}^b e^{\beta_{mn}y} + D_{mn}^b e^{-\beta_{mn}y} \quad (7.26)$$

where
$$\beta_{mn} = \sqrt{\xi_m^2 + r_n^2 + \varepsilon^2} \quad (7.27)$$

Using (7.15), (7.20) and (7.24), the general solutions for the conductive region are

$$W_a^{\text{II}}(x, y, z) = \sum_{m=1}^M \sum_{n=1}^{N_z} \sin(\xi_m x) \cos(q_n z) \left(C_{mn}^a e^{\alpha_{mn}y} + D_{mn}^a e^{-\alpha_{mn}y} \right) \quad (7.28)$$

$$W_b^{\text{II}}(x, y, z) = \sum_{m=1}^M \sum_{n=1}^{N_r} \cos(\xi_m x) \sin(r_n z) \left(C_{mn}^b e^{\beta_{mn}y} + D_{mn}^b e^{-\beta_{mn}y} \right) \quad (7.29)$$

It is noted that the Fourier series of (7.28) and (7.29) have finite number of harmonics. The error introduced by this series truncation can be eliminated by choosing sufficient number of harmonics. More discussion on the selection of the number of harmonics is

presented in section 7.3.1. It must also be noted that (7.28) and (7.29) have different number of harmonics along the z -axis. The logic behind this selection will be discussed in section 7.3.1.

Substituting (7.28)-(7.29) into (7.11)-(7.13) the following general solutions are obtained for the flux density components

$$B_x^{\text{II}} = - \sum_{m=1}^M \sum_{n=1}^{N_z} \cos(\xi_m x) \sin(q_n z) \xi_m q_n \left(C_{mn}^a e^{\alpha_{mn} y} + D_{mn}^a e^{-\alpha_{mn} y} \right) + \varepsilon^2 \sum_{m=1}^M \sum_{n=1}^{N_r} \cos(\xi_m x) \sin(r_n z) \beta_{mn} \left(C_{mn}^b e^{\beta_{mn} y} - D_{mn}^b e^{-\beta_{mn} y} \right) \quad (7.30)$$

$$B_y^{\text{II}} = - \sum_{m=1}^M \sum_{n=1}^{N_z} \sin(\xi_m x) \sin(q_n z) q_n \alpha_{mn} \left(C_{mn}^a e^{\alpha_{mn} y} - D_{mn}^a e^{-\alpha_{mn} y} \right) + \varepsilon^2 \sum_{m=1}^M \sum_{n=1}^{N_r} \sin(\xi_m x) \sin(r_n z) \xi_m \left(C_{mn}^b e^{\beta_{mn} y} + D_{mn}^b e^{-\beta_{mn} y} \right) \quad (7.31)$$

$$B_z^{\text{II}} = - \sum_{m=1}^M \sum_{n=1}^{N_z} \sin(\xi_m x) \cos(q_n z) p_n^2 \left(C_{mn}^a e^{\alpha_{mn} y} + D_{mn}^a e^{-\alpha_{mn} y} \right) \quad (7.32)$$

7.2.2. Nonconductive Region (Ω_V)

The TM potential does not contribute to the magnetic field in nonconductive region Ω_V [118, 192]. Thus it is not modeled in Ω_V . The following general solution for the TE potential can be obtained which satisfies (7.1), (7.2) and (7.3)

$$W_a^{\text{V}}(x, y, z) = \sum_{m=1}^M \sum_{n=1}^{N_z} \sin(\xi_m x) \cos(p_n (L_z - z)) \left(C_{mn}^{\text{V}} e^{\gamma_{mn} y} + D_{mn}^{\text{V}} e^{-\gamma_{mn} y} \right) \quad (7.33)$$

where
$$\varpi_{mn} = \sqrt{\xi_m^2 + p_n^2} \quad (7.34)$$

and eigenvalues p_n need to be determined from the boundary condition at $z=w$ as described in section 7.3.1.

However, to match the conductive region Ω_{II} with the nonconductive region Ω_{V} on a term-by-term basis, their y -dependency can be chosen to be the same i.e

$$\varpi_{mn} = \alpha_{mn} \quad (7.35)$$

and also the TE potential coefficients of Ω_{V} can be expressed linearly in terms of the coefficients of Ω_{II}

$$C_{mn}^{\text{V}} = a_{mn} C_{mn}^{\text{a}} \quad (7.36)$$

$$D_{mn}^{\text{V}} = a_{mn} D_{mn}^{\text{a}} \quad (7.37)$$

where a_{mn} is linear factor and will be determined in section 7.3.1. Using (7.35)-(7.37), (7.33) becomes

$$W_a^{\text{V}}(x, y, z) = \sum_{m=1}^M \sum_{n=1}^{N_z} \sin(\xi_m x) \cos(p_n(L_z - z)) a_{mn} \left(C_{mn}^{\text{a}} e^{\alpha_{mn} y} + D_{mn}^{\text{a}} e^{-\alpha_{mn} y} \right) \quad (7.38)$$

Equation (7.35) implies that

$$p_n^2 = q_n^2 + \varepsilon^2 \quad (7.39)$$

Equation (7.39) relates the eigenvalues of Ω_{II} and Ω_{V} .

Since conductivity is zero in Ω_{V} , the following is obtained from (7.11)-(7.13)

$$B_x^{\text{V}} = \frac{\partial^2 W_a^{\text{V}}}{\partial z \partial x} \quad (7.40)$$

$$B_y^{\text{V}} = \frac{\partial^2 W_a^{\text{V}}}{\partial z \partial y} \quad (7.41)$$

$$B_z^{\text{V}} = \frac{\partial^2 W_a^{\text{V}}}{\partial z^2} \quad (7.42)$$

Substituting (7.38) into (7.40)-(7.42) the following general solutions are obtained for the flux density components in Ω_V

$$B_x^V = \sum_{m=1}^M \sum_{n=1}^{N_z} \cos(\xi_m x) \sin(p_n(L_z - z)) \xi_m p_n a_{mn} \left(C_{mn}^a e^{\alpha_{mn} y} + D_{mn}^a e^{-\alpha_{mn} y} \right) \quad (7.43)$$

$$B_y^V = \sum_{m=1}^M \sum_{n=1}^{N_z} \sin(\xi_m x) \sin(p_n(L_z - z)) p_n \alpha_{mn} a_{mn} \left(C_{mn}^a e^{\alpha_{mn} y} - D_{mn}^a e^{-\alpha_{mn} y} \right) \quad (7.44)$$

$$B_z^V = -\sum_{m=1}^M \sum_{n=1}^{N_z} \sin(\xi_m x) \cos(p_n(L_z - z)) p_n^2 a_{mn} \left(C_{mn}^a e^{\alpha_{mn} y} + D_{mn}^a e^{-\alpha_{mn} y} \right) \quad (7.45)$$

7.2.3. Nonconductive Regions Ω_I and Ω_{III}

The fields in Ω_I are modeled using the magnetic scalar potential. In the absence of free current the magnetic scalar potential satisfies the following Laplace equation in Ω_I

$$\mu_0 \nabla^2 \phi = 0 \quad (3.32)$$

From the discussion presented in section 5.5 and using the relation between the TE potential, W_a , and magnetic scalar potential, ϕ , given by (5.18) the source field in Ω_I can be written as

$$\phi^s(x, y, z) = \sum_{m=1}^M \sum_{n=1}^{N_z} \sin(\xi_m x) \sin(k_n z) e^{\kappa_{mn} y} S_{mn}^\phi, \quad y < g \quad (7.46)$$

where

$$k_n = n\pi / L_z \quad (7.47)$$

$$\kappa_{mn} = \sqrt{k_n^2 + \xi_m^2} \quad (7.48)$$

The choice of eigenvalues along the x and z -axis satisfies boundary conditions (7.1)-(7.3). Here it has been assumed that the charge sheet has been kept at $y=0$. Equation (7.46) is valid for region below the magnetic source i.e. for $y < g$. The y -dependency makes sure

that the source field increases towards the magnetic source while it decreases away from the source.

The reflected field can be written as

$$\phi^I(x, y, z) = \sum_{m=1}^M \sum_{n=1}^{N_z} \sin(\xi_m x) \sin(k_n z) e^{-\kappa_{mn} y} A_{mn}^I \quad (7.49)$$

The y-dependency of (7.49) is chosen to decay the reflected field with distance away from the conductive surface at $y=0$.

The transmitted field in this region satisfies governing equation (3.32) and boundary conditions (7.1)-(7.3) and is given by

$$\phi^{III}(x, y, z) = \sum_{m=1}^M \sum_{n=1}^{N_z} \sin(\xi_m x) \sin(k_n z) e^{\kappa_{mn}(y+h)} A_{mn}^{III} \quad (7.50)$$

The y-dependency is chosen to decay the field with distance away from the conductive medium.

The flux density is obtained from the scalar potential using

$$\mathbf{B} = -\mu_0 \nabla \phi \quad (2.5)$$

Substituting (7.46) into (2.5) the source flux density components are

$$B_x^s(x, y, z) = -\mu_0 \sum_{m=1}^M \sum_{n=1}^{N_z} \cos(\xi_m x) \sin(k_n z) e^{\kappa_{mn} y} \xi_m S_{mn}^\phi, \quad y < g \quad (7.51)$$

$$B_y^s(x, y, z) = -\mu_0 \sum_{m=1}^M \sum_{n=1}^{N_z} \sin(\xi_m x) \sin(k_n z) e^{\kappa_{mn} y} \kappa_{mn} S_{mn}^\phi, \quad y < g \quad (7.52)$$

$$B_z^s(x, y, z) = -\mu_0 \sum_{m=1}^M \sum_{n=1}^{N_z} \sin(\xi_m x) \cos(k_n z) e^{\kappa_{mn} y} k_n S_{mn}^\phi, \quad y < g \quad (7.53)$$

Similarly substituting (7.49) into (2.5) gives the reflected flux density components

$$B_x^I(x, y, z) = -\mu_0 \sum_{m=1}^M \sum_{n=1}^{N_z} \cos(\xi_m x) \sin(k_n z) e^{-\kappa_{mn} y} \xi_m A_{mn}^I \quad (7.54)$$

$$B_y^I(x, y, z) = \mu_0 \sum_{m=1}^M \sum_{n=1}^{N_z} \sin(\xi_m x) \sin(k_n z) e^{-\kappa_{mn} y} \kappa_{mn} A_{mn}^I \quad (7.55)$$

$$B_z^I(x, y, z) = -\mu_0 \sum_{m=1}^M \sum_{n=1}^{N_z} \sin(\xi_m x) \cos(k_n z) e^{-\kappa_{mn} y} k_n A_{mn}^I \quad (7.56)$$

Finally on substitution of (7.50) into (2.5) the transmitted flux density components are obtained

$$B_x^{III}(x, y, z) = -\mu_0 \sum_{m=1}^M \sum_{n=1}^{N_z} \cos(\xi_m x) \sin(k_n z) e^{\kappa_{mn}(y+h)} \xi_m A_{mn}^{III} \quad (7.57)$$

$$B_y^{III}(x, y, z) = -\mu_0 \sum_{m=1}^M \sum_{n=1}^{N_z} \sin(\xi_m x) \sin(k_n z) e^{\kappa_{mn}(y+h)} \kappa_{mn} A_{mn}^{III} \quad (7.58)$$

$$B_z^{III}(x, y, z) = -\mu_0 \sum_{m=1}^M \sum_{n=1}^{N_z} \sin(\xi_m x) \cos(k_n z) e^{\kappa_{mn}(y+h)} k_n A_{mn}^{III} \quad (7.59)$$

7.3. Boundary Condition and Field Solution

7.3.1. Determination of Unknown Eigenvalues

In order to determine the unknown eigenvalues p_n and q_n , the continuity condition of the magnetic flux density and field intensity is applied at $z=w$ interface, Γ_e . From the continuity of the normal component flux density, B_z yields

$$\cos(q_n w) = \cos(p_n(L_z - w)) a_{mn} \quad (7.60)$$

From the continuity of the tangential component (B_x and B_y) of the flux density (noting unity relative permeability throughout in the problem domain)

$$-\sin(q_n w)q_n = \sin(p_n(L_z - w))p_n a_{mn} \quad (7.61)$$

Dividing (7.61) by (7.60)

$$\tan(q_n w)q_n + \tan(p_n(L_z - w))p_n = 0 \quad (7.62)$$

using (7.39), (7.62) can be written as

$$\sqrt{p_n^2 - \varepsilon^2} \tan\left(w\sqrt{p_n^2 - \varepsilon^2}\right) + p_n \tan(p_n(L_z - w)) = 0 \quad (7.63)$$

Equation (7.63) is solved numerically to find p_n . Equations (7.39) and (7.60) are then used to determine q_n and a_{mn} respectively.

The complex eigenvalues p_n need to be calculated precisely. In this root finding algorithm, two sets of calculations are performed. In the first set, the width of the plate, w , is decreased from $w=L_z$ to its value in small decrementing steps and in the second set, the width w is increased from $w=0$ to its value in small incrementing steps. The incrementing and decrementing processes yield two sets of eigenvalues. Finally, the two sets are merged to form the final set of eigenvalues p_n [148, 192]. The decrementing and incrementing processes are described in brief below.

In the decrementing calculation, initially w is set equal to L_z . From (7.63) it is noticed that for $w=L_z$ the eigenvalues p_n are given by

$$p_n^0 = \sqrt{k_n^2 + \varepsilon^2} \quad \text{for } w=L_z \quad (7.64)$$

The superscript '0' indicates first step of root calculation. Then w is decreased by small steps Δw till its value becomes equal to the width of the plate. In each step, the Newton-Raphson iteration scheme [216] is used to compute the eigenvalues for that particular w

until the difference in the eigenvalues between two successive steps becomes smaller than a specified tolerance. The iterative change in the eigenvalue is written as [148, 216]

$$p_n^{i+1} = p_n^i - \frac{f(p_n)}{\partial f(p_n) / \partial p_n} \Big|_i \quad (7.65)$$

where

$$f(p_n) = q_n \tan(wq_n) + p_n \tan(p_n(L_z - w)) \quad (7.66)$$

$$\begin{aligned} \frac{\partial f(p_n)}{\partial p_n} = & \tan(p_n(L_z - w)) + p_n(L_z - w) \sec^2(p_n(L_z - w)) \\ & + p_n \tan(q_n w) / q_n + p_n w \sec^2(q_n w) \end{aligned} \quad (7.67)$$

Here i is the number of iterations. In the incrementing process, initially w is set equal to 0. For this value of w , from (7.63) it is observed that the eigenvalues are

$$p_n^0 = k_n \quad (7.68)$$

Then w is increased by small steps Δw till its value becomes equal to the width of the plate. In each step, the Newton-Raphson iteration scheme [216] is used to compute the eigenvalues for that particular w until the difference in the eigenvalues between two successive steps becomes smaller than a specified tolerance. With this method, the eigenvalues can be computed very accurately.

Figure 7.5 shows the eigenvalues obtained using parameters listed in Table 7.1 applying the decrementing and incrementing processes. The two sets produce the same eigenvalues for large index n . The calculations have been performed in MATLAB.

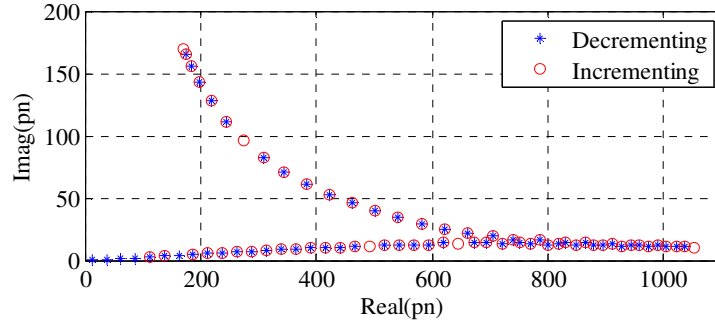


Figure 7.5. Complex roots p_n calculated using incrementing and decrementing process for $L_z=200\text{mm}$ and plate width= 77mm

Table 7.1: Parameters used for root calculation

Description	Value	Unit
Width, w	77	mm
Domain width, L_z	200	mm
Conductivity, σ	2.459×10^7	Sm^{-1}
Rotational speed of rotor, ω_m	9000	RPM

Another numerical aspect of this formulation is the choice of N_z and N_r . The choice of N_z depends on the value of L_z . Generally the larger the problem domain, the greater the number of terms necessary [148]. For the simulations presented in this chapter N_z has been chosen to be 64 for $L_z=200\text{mm}$. It is observed that choosing $N_r \sim N_z$ may make the system of equations ill-conditioned. Hence choosing the ratio of $N_r/N_z \sim w/L_z$ keep the condition number sufficiently low [149].

7.3.2. Determination of Unknown Coefficients

In order to determine the unknown Fourier series coefficients of the fields, boundary condition is applied at $y=0$ and $-h$.

From the continuity of B_x at $y=0$ for each m

$$-\mu_0 \sum_{n=1}^{N_z} \sin(k_n z) \xi_m \left(S_{mn}^\phi + A_{mn}^I \right) = \begin{cases} -\sum_{n=1}^{N_z} \sin(q_n z) \xi_m q_n \left(C_{mn}^a + D_{mn}^a \right) \\ + \varepsilon^2 \sum_{n=1}^{N_r} \sin(r_n z) \beta_{mn} \left(C_{mn}^b - D_{mn}^b \right), & 0 < z < w \\ \sum_{n=1}^{N_z} \sin(p_n (L_z - z)) \xi_m p_n a_{mn} \left(C_{mn}^a + D_{mn}^a \right), & w < z < L_z \end{cases} \quad (7.69)$$

Multiplying both sides by $\sin(k_i z)$ and integrating from $z=0$ to L_z gives

$$-\mu_0 0.5 L_z \xi_m (\bar{\mathbf{S}}_m^\phi + \bar{\mathbf{A}}_m^I) = \xi_m \mathbf{M}^{(1)} (\bar{\mathbf{C}}_m^a + \bar{\mathbf{D}}_m^a) + \varepsilon^2 \mathbf{M}^{(2)} \mathbf{b}_m (\bar{\mathbf{C}}_m^b - \bar{\mathbf{D}}_m^b) \quad (7.70)$$

where

$$\mathbf{M}_{in}^{(1)} = -q_n \int_0^w \sin(k_i z) \sin(q_n z) dz + p_n a_{mn} \int_w^{L_z} \sin(k_i z) \sin[p_n (L_z - z)] dz, \quad [N_z \times N_z] \quad (7.71)$$

$$\mathbf{M}_{in}^{(2)} = \int_0^w \sin(k_i z) \sin(r_n z) dz, \quad [N_z \times N_r] \quad (7.72)$$

$$\mathbf{b}_m = \text{diag}[\beta_{mn}], \quad [N_r \times N_r] \quad (7.73)$$

And $\bar{\mathbf{S}}_m^\phi$, $\bar{\mathbf{A}}_m^I$, $\bar{\mathbf{C}}_m^a$, $\bar{\mathbf{D}}_m^a$ are vector quantities of dimension $[N_z \times 1]$ whereas $\bar{\mathbf{C}}_m^b$, $\bar{\mathbf{D}}_m^b$ are vector of dimension $[N_r \times 1]$. From the continuity of B_y at $y=0$, one derives for each m

$$-\mu_0 \sum_{n=1}^{N_z} \sin(k_n z) \kappa_{mn} (S_{mn}^\phi - A_{mn}^I) = \begin{cases} -\sum_{n=1}^{N_z} \sin(q_n z) q_n \alpha_{mn} (C_{mn}^a - D_{mn}^a) \\ + \varepsilon^2 \sum_{n=1}^{N_r} \sin(r_n z) \xi_m (C_{mn}^b + D_{mn}^b), & 0 < z < w \\ \sum_{n=1}^{N_z} \sin(p_n (L_z - z)) p_n \alpha_{mn} a_{mn} (C_{mn}^a - D_{mn}^a), & w < z < L_z \end{cases} \quad (7.74)$$

Multiplying both sides by $\sin(k_i z)$ and integrating from $z=0$ to L_z gives

$$-\mu_0 0.5 L_z \mathbf{k}_m (\bar{\mathbf{S}}_m^\phi - \bar{\mathbf{A}}_m^I) = \mathbf{M}^{(1)} \mathbf{a}_m (\bar{\mathbf{C}}_m^a - \bar{\mathbf{D}}_m^a) + \varepsilon^2 \xi_m \mathbf{M}^{(2)} (\bar{\mathbf{C}}_m^b + \bar{\mathbf{D}}_m^b) \quad (7.75)$$

$$\mathbf{k}_m = \text{diag}[\kappa_{mn}], \quad [N_z \times N_z] \quad (7.76)$$

$$\mathbf{a}_m = \text{diag}[\alpha_{mn}], \quad [N_z \times N_z] \quad (7.77)$$

From the continuity of B_z at $y=0$, one derives for each m

$$-\mu_0 \sum_{n=1}^{N_z} \cos(k_n z) k_n (S_{mn}^\phi + A_{mn}^I) = \begin{cases} -\sum_{n=1}^{N_z} \cos(q_n z) p_n^2 (C_{mn}^a + D_{mn}^a), & 0 < z < w \\ -\sum_{n=1}^{N_z} \cos(p_n (L_z - z)) p_n^2 a_{mn} (C_{mn}^a + D_{mn}^a), & w < z < L_z \end{cases} \quad (7.78)$$

Multiplying both sides by $\cos(k_i z)$ and integrating from $z=0$ to L_z ,

$$-\mu_0 0.5 L_z \mathbf{K} (\bar{\mathbf{S}}_m^\phi + \bar{\mathbf{A}}_m^I) = \mathbf{M}^{(3)} (\bar{\mathbf{C}}_m^a + \bar{\mathbf{D}}_m^a) \quad (7.79)$$

where

$$\mathbf{K} = \text{diag}[k_n], \quad [N_z \times N_z] \quad (7.80)$$

$$\mathbf{M}_{in}^{(3)} = -p_n^2 \int_0^w \cos(k_i z) \cos(q_n z) dz - p_n^2 a_{mn} \int_w^{L_z} \cos(k_i z) \cos[p_n (L_z - z)] dz \quad (7.81)$$

Next, boundary conditions are applied at $y=-h$. Applying the continuity of the B_x at $y=-h$ yields

$$-\mu_0 \sum_{n=1}^{N_z} \sin(k_n z) \xi_m A_{mn}^{\text{III}} = \begin{cases} -\sum_{n=1}^{N_z} \sin(q_n z) \xi_m q_n (C_{mn}^a e^{-\alpha_{mn} h} + D_{mn}^a e^{\alpha_{mn} h}) \\ + \varepsilon^2 \sum_{n=1}^{N_r} \sin(r_n z) \beta_{mn} (C_{mn}^b e^{-\beta_{mn} h} - D_{mn}^b e^{\beta_{mn} h}), & 0 < z < w \\ \sum_{n=1}^{N_z} \sin(p_n (L_z - z)) \xi_m p_n a_{mn} (C_{mn}^a e^{-\alpha_{mn} h} + D_{mn}^a e^{\alpha_{mn} h}), & w < z < L_z \end{cases} \quad (7.82)$$

Multiplying both sides by $\sin(k_i z)$ and integrating from $z=0$ to L_z gives

$$-\mu_0 0.5 L_z \xi_m \bar{\mathbf{A}}_m^{\text{III}} = \xi_m \mathbf{M}^{(1)} (\bar{\mathbf{C}}_m^a \mathbf{e}^{-\mathbf{a}_m h} + \bar{\mathbf{D}}_m^a \mathbf{e}^{\mathbf{a}_m h}) + \varepsilon^2 \mathbf{M}^{(2)} \mathbf{b}_m (\bar{\mathbf{C}}_m^b \mathbf{e}^{-\mathbf{b}_m h} - \bar{\mathbf{D}}_m^b \mathbf{e}^{\mathbf{b}_m h}) \quad (7.83)$$

where

$$\mathbf{e}^{-\mathbf{a}_m h} = \text{diag}[e^{-\alpha_{mn} h}], \quad [N_z \times N_z] \quad (7.84)$$

$$\mathbf{e}^{-\mathbf{b}_m h} = \text{diag}[e^{-\alpha_{mn} h}], \quad [N_r \times N_r] \quad (7.85)$$

From the continuity of B_y at $y=-h$ the following is obtained

$$-\mu_0 \sum_{n=1}^{N_z} \sin(k_n z) \kappa_{mn} A_{mn}^{\text{III}} = \begin{cases} -\sum_{n=1}^{N_z} \sin(q_n z) q_n \alpha_{mn} \left(C_{mn}^a e^{-\alpha_{mn} h} - D_{mn}^a e^{-\alpha_{mn} h} \right) \\ + \varepsilon^2 \sum_{n=1}^{N_r} \sin(r_n z) \xi_m \left(C_{mn}^b e^{-\beta_{mn} h} + D_{mn}^b e^{-\beta_{mn} h} \right), & 0 < z < w \\ \sum_{n=1}^{N_z} \sin(p_n (L_z - z)) p_n \alpha_{mn} a_{mn} \left(C_{mn}^a e^{-\alpha_{mn} h} - D_{mn}^a e^{-\alpha_{mn} h} \right), & w < z < L_z \end{cases} \quad (7.86)$$

Multiplying both sides by $\sin(k_i z)$ and integrating from $z=0$ to L_z gives

$$-\mu_0 0.5 L_z \mathbf{k}_m \bar{\mathbf{A}}_m^{\text{III}} = \mathbf{M}^{(1)} \mathbf{a}_m (\bar{\mathbf{C}}_m^a e^{-\mathbf{a}_m h} - \bar{\mathbf{D}}_m^a e^{\mathbf{a}_m h}) + \varepsilon^2 \xi_m \mathbf{M}^{(2)} (\bar{\mathbf{C}}_m^b e^{-\mathbf{b}_m h} + \bar{\mathbf{D}}_m^b e^{\mathbf{b}_m h}) \quad (7.87)$$

From the continuity of B_z field at $y=-h$

$$-\mu_0 \sum_{n=1}^{N_z} \cos(k_n z) k_n A_{mn}^{\text{III}} = \begin{cases} -\sum_{n=1}^{N_z} \cos(q_n z) p_n^2 \left(C_{mn}^a e^{-\alpha_{mn} h} + D_{mn}^a e^{\alpha_{mn} h} \right), & 0 < z < w \\ -\sum_{n=1}^{N_z} \cos(p_n (L_z - z)) p_n^2 a_{mn} \left(C_{mn}^a e^{-\alpha_{mn} h} + D_{mn}^a e^{\alpha_{mn} h} \right), & w < z < L_z \end{cases} \quad (7.88)$$

Multiplying both sides by $\cos(k_i z)$ and integrating from $z=0$ to L_z ,

$$-\mu_0 0.5 L_z \mathbf{K} \bar{\mathbf{A}}_m^{\text{III}} = \mathbf{M}^{(3)} (\bar{\mathbf{C}}_m^a e^{-\mathbf{a}_m h} + \bar{\mathbf{D}}_m^a e^{\mathbf{a}_m h}) \quad (7.89)$$

From (7.79)

$$\bar{\mathbf{A}}_m^{\text{I}} = -\bar{\mathbf{S}}_m^\phi - \frac{2}{\mu_0 L_z} \mathbf{K}^{-1} \mathbf{M}^{(3)} (\bar{\mathbf{C}}_m^a + \bar{\mathbf{D}}_m^a) \quad (7.90)$$

Substituting (7.90) into (7.70) yields

$$0.5 \xi_m L_z \left(\frac{2}{L_z} \mathbf{K}^{-1} \mathbf{M}^{(3)} (\bar{\mathbf{C}}_m^a + \bar{\mathbf{D}}_m^a) \right) = \xi_m \mathbf{M}^{(1)} (\bar{\mathbf{C}}_m^a + \bar{\mathbf{D}}_m^a) + \varepsilon^2 \mathbf{M}^{(2)} \mathbf{b}_m (\bar{\mathbf{C}}_m^b - \bar{\mathbf{D}}_m^b) \quad (7.91)$$

$$\text{or,} \quad \xi_m \left[\mathbf{K}^{-1} \mathbf{M}^{(3)} - \mathbf{M}^{(1)} \right] (\bar{\mathbf{C}}_m^a + \bar{\mathbf{D}}_m^a) - \varepsilon^2 \mathbf{M}^{(2)} \mathbf{b}_m (\bar{\mathbf{C}}_m^b - \bar{\mathbf{D}}_m^b) = 0 \quad (7.92)$$

Defining

$$\mathbf{A}_1 = \xi_m [\mathbf{K}^{-1}\mathbf{M}^{(3)} - \mathbf{M}^{(1)}] \quad (7.93)$$

$$\mathbf{B}_1 = -\varepsilon^2 \mathbf{M}^{(2)} \mathbf{b}_m \quad (7.94)$$

(7.92) can be written as

$$\mathbf{A}_1(\bar{\mathbf{C}}_m^a + \bar{\mathbf{D}}_m^a) + \mathbf{B}_1(\bar{\mathbf{C}}_m^b - \bar{\mathbf{D}}_m^b) = 0 \quad (7.95)$$

Again substituting (7.90) into (7.75) yields

$$0.5L_z \mathbf{k}_m \left(-\mu_0 2\bar{\mathbf{S}}_m^\phi - \frac{2}{L_z} \mathbf{K}^{-1}\mathbf{M}^{(3)}(\bar{\mathbf{C}}_m^a + \bar{\mathbf{D}}_m^a) \right) = \mathbf{M}^{(1)} \mathbf{a}_m (\bar{\mathbf{C}}_m^a - \bar{\mathbf{D}}_m^a) + \varepsilon^2 \xi_m \mathbf{M}^{(2)} (\bar{\mathbf{C}}_m^b + \bar{\mathbf{D}}_m^b) \quad (7.96)$$

or,

$$-\mu_0 L_z \mathbf{k}_m \bar{\mathbf{S}}_m^\phi = [\mathbf{k}_m \mathbf{K}^{-1}\mathbf{M}^{(3)} + \mathbf{M}^{(1)} \mathbf{a}_m] \bar{\mathbf{C}}_m^a + [\mathbf{k}_m \mathbf{K}^{-1}\mathbf{M}^{(3)} - \mathbf{M}^{(1)} \mathbf{a}_m] \bar{\mathbf{D}}_m^a + \varepsilon^2 \xi_m \mathbf{M}^{(2)} (\bar{\mathbf{C}}_m^b + \bar{\mathbf{D}}_m^b) \quad (7.97)$$

Defining

$$\mathbf{A}_{2c} = [\mathbf{k}_m \mathbf{K}^{-1}\mathbf{M}^{(3)} + \mathbf{M}^{(1)} \mathbf{a}_m] \quad (7.98)$$

$$\mathbf{A}_{2d} = [\mathbf{k}_m \mathbf{K}^{-1}\mathbf{M}^{(3)} - \mathbf{M}^{(1)} \mathbf{a}_m] \quad (7.99)$$

$$\mathbf{B}_2 = \varepsilon^2 \xi_m \mathbf{M}^{(2)} \quad (7.100)$$

equation (7.97) can be written as

$$-\mu_0 L_z \mathbf{k}_m \bar{\mathbf{S}}_m^\phi = \mathbf{A}_{2c} \bar{\mathbf{C}}_m^a + \mathbf{A}_{2d} \bar{\mathbf{D}}_m^a + \mathbf{B}_2 (\bar{\mathbf{C}}_m^b + \bar{\mathbf{D}}_m^b) \quad (7.101)$$

Similarly substituting (7.89) into (7.83) yields

$$\xi_m \mathbf{K}^{-1}\mathbf{M}^{(3)} (\mathbf{e}^{-\mathbf{a}_m^h} \bar{\mathbf{C}}_m^a + \mathbf{e}^{\mathbf{a}_m^h} \bar{\mathbf{D}}_m^a) = \xi_m \mathbf{M}^{(1)} (\mathbf{e}^{-\mathbf{a}_m^h} \bar{\mathbf{C}}_m^a + \mathbf{e}^{\mathbf{a}_m^h} \bar{\mathbf{D}}_m^a) + \varepsilon^2 \mathbf{M}^{(2)} \mathbf{b}_m (\mathbf{e}^{-\mathbf{b}_m^h} \bar{\mathbf{C}}_m^b - \mathbf{e}^{\mathbf{b}_m^h} \bar{\mathbf{D}}_m^b) \quad (7.102)$$

$$\xi_m [\mathbf{K}^{-1}\mathbf{M}^{(3)} - \mathbf{M}^{(1)}] (\mathbf{e}^{-\mathbf{a}_m^h} \bar{\mathbf{C}}_m^a + \mathbf{e}^{\mathbf{a}_m^h} \bar{\mathbf{D}}_m^a) - \varepsilon^2 \mathbf{M}^{(2)} \mathbf{b}_m (\mathbf{e}^{-\mathbf{b}_m^h} \bar{\mathbf{C}}_m^b - \mathbf{e}^{\mathbf{b}_m^h} \bar{\mathbf{D}}_m^b) = 0 \quad (7.103)$$

Utilizing (7.93)-(7.94), (7.103) can be written as

$$\mathbf{A}_1(\mathbf{e}^{-\mathbf{a}_m h} \bar{\mathbf{C}}_m^a + \mathbf{e}^{\mathbf{a}_m h} \bar{\mathbf{D}}_m^a) + \mathbf{B}_1(\mathbf{e}^{-\mathbf{b}_m h} \bar{\mathbf{C}}_m^b - \mathbf{e}^{\mathbf{b}_m h} \bar{\mathbf{D}}_m^b) = 0 \quad (7.104)$$

Again substituting (7.89) into (7.87) gives

$$\begin{aligned} \mathbf{k}_m \mathbf{K}^{-1} \mathbf{M}^{(3)}(\mathbf{e}^{-\mathbf{a}_m h} \bar{\mathbf{C}}_m^a + \mathbf{e}^{\mathbf{a}_m h} \bar{\mathbf{D}}_m^a) &= \mathbf{M}^{(1)} \mathbf{a}_m (\mathbf{e}^{-\mathbf{a}_m h} \bar{\mathbf{C}}_m^a - \mathbf{e}^{\mathbf{a}_m h} \bar{\mathbf{D}}_m^a) \\ &+ \varepsilon^2 \xi_m \mathbf{M}^{(2)}(\mathbf{e}^{-\mathbf{b}_m h} \bar{\mathbf{C}}_m^b + \mathbf{e}^{\mathbf{b}_m h} \bar{\mathbf{D}}_m^b) \end{aligned} \quad (7.105)$$

$$\begin{aligned} [\mathbf{k}_m \mathbf{K}^{-1} \mathbf{M}^{(3)} - \mathbf{M}^{(1)} \mathbf{a}_m] \mathbf{e}^{-\mathbf{a}_m h} \bar{\mathbf{C}}_m^a + [\mathbf{k}_m \mathbf{K}^{-1} \mathbf{M}^{(3)} + \mathbf{M}^{(1)} \mathbf{a}_m] \mathbf{e}^{\mathbf{a}_m h} \bar{\mathbf{D}}_m^a \\ - \varepsilon^2 \xi_m \mathbf{M}^{(2)}(\mathbf{e}^{-\mathbf{b}_m h} \bar{\mathbf{C}}_m^b + \mathbf{e}^{\mathbf{b}_m h} \bar{\mathbf{D}}_m^b) = 0 \end{aligned} \quad (7.106)$$

Using (7.98)-(7.100), above equation can be written as

$$\mathbf{A}_{2d} \mathbf{e}^{-\mathbf{a}_m h} \bar{\mathbf{C}}_m^a + \mathbf{A}_{2c} \mathbf{e}^{\mathbf{a}_m h} \bar{\mathbf{D}}_m^a - \mathbf{B}_2(\mathbf{e}^{-\mathbf{b}_m h} \bar{\mathbf{C}}_m^b + \mathbf{e}^{\mathbf{b}_m h} \bar{\mathbf{D}}_m^b) = 0 \quad (7.107)$$

Equations (7.95), (7.101), (7.104) and (7.107) can be written in the following matrix form:

$$\mathbf{A} \bar{\mathbf{x}} = \bar{\mathbf{b}} \quad (7.108)$$

where

$$\mathbf{A} = \begin{bmatrix} \mathbf{A}_1 & \mathbf{A}_1 & \mathbf{B}_1 & -\mathbf{B}_1 \\ \mathbf{A}_{2c} & \mathbf{A}_{2d} & \mathbf{B}_2 & \mathbf{B}_2 \\ \mathbf{A}_1 \mathbf{e}^{-\mathbf{a}_m h} & \mathbf{A}_1 \mathbf{e}^{\mathbf{a}_m h} & \mathbf{B}_1 \mathbf{e}^{-\mathbf{b}_m h} & -\mathbf{B}_1 \mathbf{e}^{\mathbf{b}_m h} \\ \mathbf{A}_{2d} \mathbf{e}^{-\mathbf{a}_m h} & \mathbf{A}_{2c} \mathbf{e}^{\mathbf{a}_m h} & -\mathbf{B}_2 \mathbf{e}^{-\mathbf{b}_m h} & -\mathbf{B}_2 \mathbf{e}^{\mathbf{b}_m h} \end{bmatrix} \quad (7.109)$$

$$\bar{\mathbf{x}} = \begin{bmatrix} \bar{\mathbf{C}}_m^a \\ \bar{\mathbf{D}}_m^a \\ \bar{\mathbf{C}}_m^b \\ \bar{\mathbf{D}}_m^b \end{bmatrix} \quad (7.110)$$

and

$$\bar{\mathbf{b}} = \begin{bmatrix} 0 \\ -\mu_0 L_z \mathbf{k}_m \bar{\mathbf{S}}_m^\phi \\ 0 \\ 0 \end{bmatrix} \quad (7.111)$$

Matrix \mathbf{A} is of dimension $[4N_z \times 2(N_z + N_r)]$ whereas vectors $\bar{\mathbf{x}}$ and $\bar{\mathbf{b}}$ have dimension of $[2(N_z + N_r) \times 1]$ and $[4N_z \times 1]$. Matrix \mathbf{A} is asymmetric, but it has full column rank.

Thus its left pseudo-inverse is fairly accurate representation of its true inverse and $\bar{\mathbf{x}}$ can be obtained by solving

$$\bar{\mathbf{x}} = \mathbf{A}^+ \bar{\mathbf{b}} \quad (7.112)$$

where \mathbf{A}^+ is the pseudo-inverse of \mathbf{A} . It is computed in MATLAB.

7.4. Force Calculation

Maxwell stress tensor using the magnetic flux induced in the conductive medium is used to calculate the forces. The derivation of the thrust (F_x), lift (F_y) and lateral (F_z) force will be discussed next.

7.4.1. Thrust Force Calculation

Thrust force is calculated using

$$F_x = \frac{1}{2\mu_0} \left[\int_0^l \int_0^w B_x^{\text{II}} B_y^{\text{II}*} \Big|_{y=0} dz dx - \int_0^l \int_0^w B_x^{\text{II}} B_y^{\text{II}*} \Big|_{y=-h} dz dx \right] + \frac{1}{2\mu_0} \left[\int_0^l \int_{-h}^0 B_x^{\text{II}} B_z^{\text{II}*} \Big|_{z=w} dy dx \right] \quad (7.113)$$

The first two integrals calculate force from Γ_t and Γ_b whereas the third one computes force from Γ_e . Each of them will be computed separately below.

Substituting (7.30) and (7.31) evaluated at $y=0$ into the first integrand of (7.113) yields

$$F_x^{\text{top}} = \frac{1}{2\mu_0} \int_0^l \int_0^w B_x^{\text{II}} B_y^{\text{II}*} \Big|_{y=0} dz dx \quad (7.114)$$

or,

$$\begin{aligned}
F_x^{top} = \frac{1}{2\mu_0} \int_0^l \int_0^w \left[\right. & \left. - \sum_{m=1}^M \sum_{n=1}^{N_z} \cos(\xi_m x) \sin(q_n z) \xi_m q_n (C_{mn}^a + D_{mn}^a) \right. \\
& \left. + \varepsilon^2 \sum_{m=1}^M \sum_{n=1}^{N_r} \cos(\xi_m x) \sin(r_n z) \beta_{mn} (C_{mn}^b - D_{mn}^b) \right] \\
& \left[- \sum_{m=1}^M \sum_{n=1}^{N_z} \sin(\xi_m x) \sin(q_n^* z) q_n^* \alpha_{mn}^* (C_{mn}^{a*} - D_{mn}^{a*}) \right. \\
& \left. + \varepsilon^2 \sum_{m=1}^M \sum_{n=1}^{N_r} \sin(\xi_m x) \sin(r_n z) \xi_m (C_{mn}^{b*} + D_{mn}^{b*}) \right] dz dx
\end{aligned} \tag{7.115}$$

or,

$$\begin{aligned}
F_x^{top} = & \frac{1}{2\mu_0} \int_0^l \int_0^w \left[\sum_{m=1}^M \sum_{n=1}^{N_z} \cos(\xi_m x) \sin(q_n z) \xi_m q_n (C_{mn}^a + D_{mn}^a) \right. \\
& \left. + \sum_{i=1}^M \sum_{l=1}^{N_z} \sin(\xi_i x) \sin(q_l^* z) q_l^* \alpha_{il}^* (C_{il}^{a*} - D_{il}^{a*}) \right. \\
& - \varepsilon^{2*} \sum_{m=1}^M \sum_{n=1}^{N_z} \cos(\xi_m x) \sin(q_n z) \xi_m q_n (C_{mn}^a + D_{mn}^a) \sum_{i=1}^M \sum_{l=1}^{N_r} \sin(\xi_i x) \sin(r_l z) \xi_i (C_{il}^{b*} + D_{il}^{b*}) \\
& - \varepsilon^2 \sum_{m=1}^M \sum_{n=1}^{N_r} \cos(\xi_m x) \sin(r_n z) \beta_{mn} (C_{mn}^b - D_{mn}^b) \sum_{i=1}^M \sum_{l=1}^{N_z} \sin(\xi_i x) \sin(q_l^* z) q_l^* \alpha_{il}^* (C_{il}^{a*} - D_{il}^{a*}) \\
& \left. + \varepsilon^2 \varepsilon^{2*} \sum_{m=1}^M \sum_{n=1}^{N_r} \cos(\xi_m x) \sin(r_n z) \beta_{mn} (C_{mn}^b - D_{mn}^b) \sum_{i=1}^M \sum_{l=1}^{N_r} \sin(\xi_i x) \sin(r_l z) \xi_i (C_{il}^{b*} + D_{il}^{b*}) \right] dz dx
\end{aligned} \tag{7.116}$$

or,

$$\begin{aligned}
F_x^{top} = \frac{1}{2\mu_0} \left[\sum_{m=1}^M \sum_{n=1}^{N_z} \sum_{i=1}^M \sum_{l=1}^{N_z} I_{mi}^x I_{nl}^{z1} \xi_m q_n (C_{mn}^a + D_{mn}^a) q_l^* \alpha_{il}^* (C_{il}^{a*} - D_{il}^{a*}) \right. \\
- \varepsilon^{2*} \sum_{m=1}^M \sum_{n=1}^{N_z} \sum_{i=1}^M \sum_{l=1}^{N_r} I_{mi}^x I_{nl}^{z2} \xi_m q_n (C_{mn}^a + D_{mn}^a) \xi_i (C_{il}^{b*} + D_{il}^{b*}) \\
- \varepsilon^2 \sum_{m=1}^M \sum_{n=1}^{N_r} \sum_{i=1}^M \sum_{l=1}^{N_z} I_{mi}^x I_{nl}^{z3} \beta_{mn} (C_{mn}^b - D_{mn}^b) q_l^* \alpha_{il}^* (C_{il}^{a*} - D_{il}^{a*}) \\
\left. + \varepsilon^2 \varepsilon^{2*} \sum_{m=1}^M \sum_{n=1}^{N_r} \sum_{i=1}^M \sum_{l=1}^{N_r} I_{mi}^x I_{nl}^{z4} \beta_{mn} (C_{mn}^b - D_{mn}^b) \xi_i (C_{il}^{b*} + D_{il}^{b*}) \right]
\end{aligned} \tag{7.117}$$

where

$$\begin{aligned}
I_{mi}^x &= \int_{x=0}^l \cos(\xi_m x) \sin(\xi_i x) dx \\
&= 0.5 \int_0^l \sin[(\xi_i + \xi_m)x] + \sin[(\xi_i - \xi_m)x] dx \\
&= \begin{cases} 0.5 \left[\frac{1 - \cos[(\xi_i + \xi_m)l]}{(\xi_i + \xi_m)} + \frac{1 - \cos[(\xi_i - \xi_m)l]}{(\xi_i - \xi_m)} \right], & \xi_i \neq \xi_m \\ 0.5 \left[\frac{1 - \cos[(\xi_i + \xi_m)l]}{(\xi_i + \xi_m)} \right], & \xi_i = \xi_m \end{cases}
\end{aligned} \tag{7.118}$$

$$\begin{aligned}
I_{nl}^{z1} &= \int_{z=0}^w \sin(q_n z) \sin(q_l^* z) dz \\
&= 0.5 \int_0^w \cos[(q_n - q_l^*)z] - \cos[(q_n + q_l^*)z] dz \\
&= 0.5 \left[\frac{\sin[(q_n - q_l^*)w]}{(q_n - q_l^*)} - \frac{\sin[(q_n + q_l^*)w]}{(q_n + q_l^*)} \right]
\end{aligned} \tag{7.119}$$

$$\begin{aligned}
I_{nl}^{z2} &= \int_{z=0}^w \sin(q_n z) \sin(r_l z) dz \\
&= 0.5 \int_0^w \cos[(q_n - r_l)z] - \cos[(q_n + r_l)z] dz \\
&= 0.5 \left[\frac{\sin[(q_n - r_l)w]}{(q_n - r_l)} - \frac{\sin[(q_n + r_l)w]}{(q_n + r_l)} \right]
\end{aligned} \tag{7.120}$$

$$\begin{aligned}
I_{nl}^{z3} &= \int_{z=0}^w \sin(r_n z) \sin(q_l^* z) dz \\
&= 0.5 \int_0^w \cos[(r_n - q_l^*)z] - \cos[(r_n + q_l^*)z] dz \\
&= 0.5 \left[\frac{\sin[(r_n - q_l^*)w]}{(r_n - q_l^*)} - \frac{\sin[(r_n + q_l^*)w]}{(r_n + q_l^*)} \right]
\end{aligned} \tag{7.121}$$

$$\begin{aligned}
I_{nl}^{z4} &= \int_{z=0}^w \sin(r_n z) \sin(r_l z) dz \\
&= 0.5 \int_{z=0}^w \cos[(r_n - r_l)z] - \cos[(r_n + r_l)z] dz \\
&= \begin{cases} 0, & r_n \neq r_l \\ w/2, & r_n = r_l \end{cases}
\end{aligned} \tag{7.122}$$

Next, the force from the bottom surface Γ_b is computed

$$F_x^{bot} = \frac{1}{2\mu_0} \int_0^l \int_0^w B_x^{\text{II}} B_y^{\text{II}*} \Big|_{y=-h} dz dx \tag{7.123}$$

Equation (7.123) can be easily computed from (7.117) by simply replacing C_{mn}^a , D_{mn}^a , C_{mn}^b and D_{mn}^b with $C_{mn}^a e^{-\alpha_{mn}h}$, $D_{mn}^a e^{\alpha_{mn}h}$, $C_{mn}^b e^{-\beta_{mn}h}$ and $D_{mn}^b e^{\beta_{mn}h}$ respectively. The following computes the thrust force from Γ_e

$$F_x^{side} = \frac{1}{2\mu_0} \int_0^l \int_{-h}^0 B_x^{\text{II}} B_z^{\text{II}*} \Big|_{z=w} dy dx \tag{7.124}$$

Substituting (7.30) and (7.32) into (7.124)

$$\begin{aligned}
F_x^{side} &= \frac{1}{2\mu_0} \int_0^l \int_{-h}^0 \left[\sum_{m=1}^M \sum_{n=1}^{N_z} \cos(\xi_m x) \sin(q_n w) \xi_m q_n \left(C_{mn}^a e^{\alpha_{mn}y} + D_{mn}^a e^{-\alpha_{mn}y} \right) \right. \\
&\quad \left. \sum_{i=1}^M \sum_{l=1}^{N_z} \sin(\xi_l x) \cos(q_l^* w) P_l^{2*} \left(C_{il}^a e^{\alpha_{il}y} + D_{il}^a e^{-\alpha_{il}y} \right)^* \right] dy dx
\end{aligned} \tag{7.125}$$

or,

$$\begin{aligned}
F_x^{side} &= \frac{1}{2\mu_0} \sum_{m=1}^M \sum_{n=1}^{N_z} \sum_{i=1}^M \sum_{l=1}^{N_z} I_{mi}^x \sin(q_n w) \xi_m q_n \cos(q_l^* w) P_l^{2*} \int_{-h}^0 \left\{ C_{mn}^a C_{il}^{a*} e^{(\alpha_{mn} + \alpha_{il}^*)y} \right. \\
&\quad \left. + C_{mn}^a D_{il}^{a*} e^{(\alpha_{mn} - \alpha_{il}^*)y} + D_{mn}^a C_{il}^{a*} e^{-(\alpha_{mn} - \alpha_{il}^*)y} + D_{mn}^a D_{il}^{a*} e^{-(\alpha_{mn} + \alpha_{il}^*)y} \right\} dy
\end{aligned} \tag{7.126}$$

or,

$$F_x^{side} = \frac{1}{2\mu_0} \sum_{m=1}^M \sum_{n=1}^{N_z} \sum_{i=1}^M \sum_{l=1}^{N_z} I_{mi}^x \sin(q_n w) \xi_m q_n \cos(q_l^* w) P_l^{2*} \left[C_{mn}^a C_{il}^{a*} \frac{1 - e^{-(\alpha_{mn} + \alpha_{il}^*)h}}{(\alpha_{mn} + \alpha_{il}^*)} \right. \\ \left. + C_{mn}^a D_{il}^{a*} \frac{1 - e^{-(\alpha_{mn} - \alpha_{il}^*)h}}{(\alpha_{mn} - \alpha_{il}^*)} - D_{mn}^a C_{il}^{a*} \frac{1 - e^{(\alpha_{mn} - \alpha_{il}^*)h}}{(\alpha_{mn} - \alpha_{il}^*)} - D_{mn}^a D_{il}^{a*} \frac{1 - e^{(\alpha_{mn} + \alpha_{il}^*)h}}{(\alpha_{mn} + \alpha_{il}^*)} \right] \quad (7.127)$$

Substituting (7.117), (7.123) and (7.127) into (7.113) the net thrust force acting on the conductive plate can be determined.

7.4.2. Lift Force Calculation

Lift force is calculated using

$$F_y = \frac{1}{4\mu_0} \int_0^l \int_0^w (B_y^{\text{II}} B_y^{\text{II}*} - B_x^{\text{II}} B_x^{\text{II}*} - B_z^{\text{II}} B_z^{\text{II}*}) \Big|_{y=0} dz dx \\ - \frac{1}{4\mu_0} \int_0^l \int_0^w (B_y^{\text{II}} B_y^{\text{II}*} - B_x^{\text{II}} B_x^{\text{II}*} - B_z^{\text{II}} B_z^{\text{II}*}) \Big|_{y=-h} dz dx \quad (7.128) \\ + \frac{1}{2\mu_0} \left[\int_0^l \int_{-h}^0 B_y^{\text{II}} B_z^{\text{II}*} \Big|_{z=w} dy dx \right]$$

In order to calculate lift force from Γ_t the following integration is performed

$$F_y^{top} = \frac{1}{4\mu_0} \int_0^l \int_0^w (B_y^{\text{II}} B_y^{\text{II}*} - B_x^{\text{II}} B_x^{\text{II}*} - B_z^{\text{II}} B_z^{\text{II}*}) \Big|_{y=0} dz dx \quad (7.129)$$

Substituting (7.31) into the first term of (7.129)

$$\begin{aligned}
& \int_{x=0}^l \int_{z=0}^w B_y^{\text{II}} B_y^{\text{II}*} dx dz \\
&= \int_{z=0}^w \left[\frac{l}{2} \sum_{m=1}^M \sum_{n=1}^{N_z} \sum_{l=1}^{N_z} \sin(q_n z) q_n \alpha_{mn} (C_{mn}^a - D_{mn}^a) \sin(q_l^* z) q_l^* \alpha_{ml}^* (C_{ml}^a - D_{ml}^a)^* \right. \\
&\quad - \varepsilon^{2*} \frac{l}{2} \sum_{m=1}^M \sum_{n=1}^{N_z} \sum_{l=1}^{N_r} \sin(q_n z) q_n \alpha_{mn} (C_{mn}^a - D_{mn}^a) \sin(r_l z) \xi_m (C_{ml}^b + D_{ml}^b)^* \\
&\quad \left. - \varepsilon^2 \frac{l}{2} \sum_{m=1}^M \sum_{n=1}^{N_r} \sum_{l=1}^{N_z} \sin(r_n z) \xi_m (C_{mn}^b + D_{mn}^b) \sin(q_l^* z) q_l^* \alpha_{ml}^* (C_{ml}^a - D_{ml}^a)^* \right] dz \\
&\quad + \varepsilon^2 \varepsilon^{2*} \frac{lw}{4} \sum_{m=1}^M \sum_{n=1}^{N_r} \xi_m^2 (C_{mn}^b + D_{mn}^b) (C_{mn}^b + D_{mn}^b)^*
\end{aligned} \tag{7.130}$$

or,

$$\begin{aligned}
& \int_{x=0}^l \int_{z=0}^w B_y^{\text{II}} B_y^{\text{II}*} dx dz \\
&= \frac{l}{2} \sum_{m=1}^M \sum_{n=1}^{N_z} \sum_{l=1}^{N_z} I_{nl}^z q_n \alpha_{mn} (C_{mn}^a - D_{mn}^a) q_l^* \alpha_{ml}^* (C_{ml}^a - D_{ml}^a)^* \\
&\quad - \varepsilon^{2*} \frac{l}{2} \sum_{m=1}^M \sum_{n=1}^{N_z} \sum_{l=1}^{N_r} I_{nl}^{z2} q_n \alpha_{mn} (C_{mn}^a - D_{mn}^a) \xi_m (C_{ml}^b + D_{ml}^b)^* \\
&\quad - \varepsilon^2 \frac{l}{2} \sum_{m=1}^M \sum_{n=1}^{N_r} \sum_{l=1}^{N_z} I_{nl}^{z3} \xi_m (C_{mn}^b + D_{mn}^b) q_l^* \alpha_{ml}^* (C_{ml}^a - D_{ml}^a)^* \\
&\quad + \varepsilon^2 \varepsilon^{2*} \frac{lw}{4} \sum_{m=1}^M \sum_{n=1}^{N_r} \xi_m^2 (C_{mn}^b + D_{mn}^b) (C_{mn}^b + D_{mn}^b)^*
\end{aligned} \tag{7.131}$$

Substituting (7.30) into the second term of (7.129) yields

$$\begin{aligned}
& \int_{x=0}^l \int_{z=0}^w B_x^{\text{II}} B_x^{\text{II}*} dx dz \\
&= \int_{z=0}^w \left[\frac{l}{2} \sum_{m=1}^M \sum_{n=1}^{N_z} \sum_{l=1}^{N_z} \sin(q_n z) \xi_m q_n (C_{mn}^a + D_{mn}^a) \sin(q_l^* z) \xi_m q_l^* (C_{ml}^a + D_{ml}^a)^* \right. \\
&\quad - \varepsilon^{2*} \frac{l}{2} \sum_{m=1}^M \sum_{n=1}^{N_z} \sum_{l=1}^{N_r} \sin(q_n z) \xi_m q_n (C_{mn}^a + D_{mn}^a) \sin(r_l z) \beta_{ml}^* (C_{ml}^b - D_{ml}^b)^* \\
&\quad \left. - \varepsilon^2 \frac{l}{2} \sum_{m=1}^M \sum_{n=1}^{N_r} \sum_{l=1}^{N_z} \sin(r_n z) \beta_{mn} (C_{mn}^b - D_{mn}^b) \sin(q_l^* z) q_l^* \xi_m (C_{ml}^a + D_{ml}^a)^* \right] dz \\
&\quad + \varepsilon^2 \varepsilon^{2*} \frac{lw}{4} \sum_{m=1}^M \sum_{n=1}^{N_r} |\beta_{mn}|^2 (C_{mn}^b - D_{mn}^b) (C_{mn}^b - D_{mn}^b)^*
\end{aligned} \tag{7.132}$$

or,

$$\begin{aligned}
& \int_{x=0}^l \int_{z=0}^w B_x^{\text{II}} B_x^{\text{II}*} dx dz \\
&= \frac{l}{2} \sum_{m=1}^M \sum_{n=1}^{N_z} \sum_{l=1}^{N_z} I_{nl}^z \xi_m q_n (C_{mn}^a + D_{mn}^a) \xi_m q_l^* (C_{ml}^a + D_{ml}^a)^* \\
&\quad - \varepsilon^{2*} \frac{l}{2} \sum_{m=1}^M \sum_{n=1}^{N_z} \sum_{l=1}^{N_z} I_{nl}^{z2} \xi_m q_n (C_{mn}^a + D_{mn}^a) \beta_{ml}^* (C_{ml}^b - D_{ml}^b)^* \\
&\quad - \varepsilon^2 \frac{l}{2} \sum_{m=1}^M \sum_{n=1}^{N_z} \sum_{l=1}^{N_z} I_{nl}^{z3} \beta_{mn} (C_{mn}^b - D_{mn}^b) q_l^* \xi_m (C_{ml}^a + D_{ml}^a)^* \\
&\quad + \varepsilon^2 \varepsilon^{2*} \frac{lw}{4} \sum_{m=1}^M \sum_{n=1}^{N_z} |\beta_{mn}|^2 (C_{mn}^b - D_{mn}^b) (C_{mn}^b - D_{mn}^b)^*
\end{aligned} \tag{7.133}$$

Finally substituting (7.32) into the third term of (7.129) yields

$$\begin{aligned}
& \int_{x=0}^l \int_{z=0}^w B_z^{\text{II}} B_z^{\text{II}*} dx dz \\
&= \int_{z=0}^w \frac{l}{2} \sum_{m=1}^M \sum_{n=1}^{N_z} \sum_{l=1}^{N_z} \cos(q_n z) P_n^2 (C_{mn}^a + D_{mn}^a) \cos(q_l^* z) P_l^{2*} (C_{ml}^a + D_{ml}^a)^* dz \\
&= \frac{l}{2} \sum_{m=1}^M \sum_{n=1}^{N_z} \sum_{l=1}^{N_z} I_{nl}^{z5} P_n^2 (C_{mn}^a + D_{mn}^a) P_l^{2*} (C_{ml}^a + D_{ml}^a)^*
\end{aligned} \tag{7.134}$$

where

$$\begin{aligned}
I_{nl}^{z5} &= \int_{z=0}^w \cos(q_n z) \cos(q_l^* z) dz \\
&= 0.5 \int_{z=0}^w \cos[(q_n - q_l^*)z] + \cos[(q_n + q_l^*)z] dz \\
&= 0.5 \left[\frac{\sin[(q_n - q_l^*)w]}{(q_n - q_l^*)} + \frac{\sin[(q_n + q_l^*)w]}{(q_n + q_l^*)} \right]
\end{aligned} \tag{7.135}$$

Lift force can be computed from the bottom surface Γ_b by replacing C_{mn}^a , D_{mn}^a , C_{mn}^b and

D_{mn}^b with $C_{mn}^a e^{-\alpha_{mn}h}$, $D_{mn}^a e^{\alpha_{mn}h}$, $C_{mn}^b e^{-\beta_{mn}h}$ and $D_{mn}^b e^{\beta_{mn}h}$ respectively.

Substituting (7.31) and (7.32) into the third integral of (7.128) gives

$$F_y^{side} = \frac{l}{4\mu_0} \int_{-h}^0 \left[\sum_{m=1}^M \sum_{n=1}^{N_z} \sum_{l=1}^{N_z} \sin(q_n w) q_n \alpha_{mn} \left(C_{mn}^a e^{\alpha_{mn} y} - D_{mn}^a e^{-\alpha_{mn} y} \right) \right. \\ \left. \cdot \cos(q_l^* w) P_l^{2*} \left(C_{ml}^{a*} e^{\alpha_{ml}^* y} + D_{ml}^{a*} e^{-\alpha_{ml}^* y} \right) \right] dy \quad (7.136)$$

or,

$$F_y^{side} = \frac{l}{4\mu_0} \sum_{m=1}^M \sum_{n=1}^{N_z} \sum_{l=1}^{N_z} \sin(q_n w) q_n \alpha_{mn} \cos(q_l^* w) P_l^{2*} \int_{-h}^0 \left[C_{mn}^a C_{ml}^{a*} e^{(\alpha_{mn} + \alpha_{ml}^*) y} \right. \\ \left. + C_{mn}^a D_{ml}^{a*} e^{(\alpha_{mn} - \alpha_{ml}^*) y} - D_{mn}^a C_{ml}^{a*} e^{-(\alpha_{mn} - \alpha_{ml}^*) y} - D_{mn}^a D_{ml}^{a*} e^{-(\alpha_{mn} + \alpha_{ml}^*) y} \right] dy \quad (7.137)$$

or,

$$F_y^{side} = \frac{l}{4\mu_0} \sum_{m=1}^M \sum_{n=1}^{N_z} \sum_{l=1}^{N_z} \sin(q_n w) q_n \alpha_{mn} \cos(q_l^* w) P_l^{2*} \left[C_{mn}^a C_{ml}^{a*} \frac{1 - e^{-(\alpha_{mn} + \alpha_{ml}^*) h}}{(\alpha_{mn} + \alpha_{ml}^*)} \right. \\ \left. + C_{mn}^a D_{ml}^{a*} \frac{1 - e^{-(\alpha_{mn} - \alpha_{ml}^*) h}}{(\alpha_{mn} - \alpha_{ml}^*)} + D_{mn}^a C_{ml}^{a*} \frac{1 - e^{(\alpha_{mn} - \alpha_{ml}^*) h}}{(\alpha_{mn} - \alpha_{ml}^*)} + D_{mn}^a D_{ml}^{a*} \frac{1 - e^{(\alpha_{mn} + \alpha_{ml}^*) h}}{(\alpha_{mn} + \alpha_{ml}^*)} \right] \quad (7.138)$$

7.4.3. Lateral Force Calculation

Lateral force is calculated using

$$F_z = \frac{1}{2\mu_0} \left[\int_0^l \int_0^w B_z^{\text{II}} B_y^{\text{II}*} \Big|_{y=0} dz dx - \int_0^l \int_0^w B_z^{\text{II}} B_y^{\text{II}*} \Big|_{y=-h} dz dx \right] \\ + \frac{1}{4\mu_0} \left[\int_0^l \int_{-h}^0 (B_z^{\text{II}} B_z^{\text{II}*} - B_x^{\text{II}} B_x^{\text{II}*} - B_y^{\text{II}} B_y^{\text{II}*}) \Big|_{z=w} dy dx \right] \quad (7.139)$$

Substituting (7.32) and (7.31) into the integral for the top plate surface Γ_t gives

$$F_z^{top} = \frac{1}{2\mu_0} \int_0^l \int_0^w B_z^{\text{II}} B_y^{\text{II}*} \Big|_{y=0} dz dx \quad (7.140)$$

or,

$$F_z^{top} = \frac{l}{4\mu_0} \int_0^w \left[\sum_{m=1}^M \sum_{n=1}^{N_z} \sum_{l=1}^{N_z} \cos(q_n z) p_n^2 (C_{mn}^a + D_{mn}^a) \sin(q_l^* z) q_l^* \alpha_{ml}^* (C_{ml}^a - D_{ml}^a)^* \right. \\ \left. - \varepsilon^{2*} \sum_{m=1}^M \sum_{n=1}^{N_z} \sum_{l=1}^{N_r} \cos(q_n z) p_n^2 (C_{mn}^a + D_{mn}^a) \sin(r_l z) \xi_m (C_{ml}^b + D_{ml}^b)^* \right] dz \quad (7.141)$$

or,

$$F_z^{top} = \frac{l}{4\mu_0} \left[\sum_{m=1}^M \sum_{n=1}^{N_z} \sum_{l=1}^{N_z} I_{nl}^{z6} p_n^2 (C_{mn}^a + D_{mn}^a) q_l^* \alpha_{ml}^* (C_{ml}^a - D_{ml}^a)^* \right. \\ \left. - \varepsilon^{2*} \sum_{m=1}^M \sum_{n=1}^{N_z} \sum_{l=1}^{N_r} I_{nl}^{z7} p_n^2 \xi_m (C_{mn}^a + D_{mn}^a) (C_{ml}^b + D_{ml}^b)^* \right] \quad (7.142)$$

where

$$I_{nl}^{z6} = \int_{z=0}^w \cos(q_n z) \sin(q_l^* z) dz \\ = 0.5 \int_{z=0}^w \sin[(q_n + q_l^*)z] - \sin[(q_n - q_l^*)z] dz \\ = 0.5 \left[\frac{1 - \cos[(q_n + q_l^*)w]}{(q_n + q_l^*)} - \frac{1 - \cos[(q_n - q_l^*)w]}{(q_n - q_l^*)} \right] \quad (7.143)$$

$$I_{nl}^{z7} = \int_{z=0}^w \cos(q_n z) \sin(r_l z) dz \\ = 0.5 \int_{z=0}^w \sin[(q_n + r_l)z] - \sin[(q_n - r_l)z] dz \\ = 0.5 \left[\frac{1 - \cos[(q_n + r_l)w]}{(q_n + r_l)} - \frac{1 - \cos[(q_n - r_l)w]}{(q_n - r_l)} \right] \quad (7.144)$$

Similarly lateral force from the bottom surface Γ_b can be easily computed.

$$\text{Now,} \quad F_z^{side} = \frac{1}{4\mu_0} \left[\int_{-l/2-h}^{l/2} \int_0^w (B_z^{\text{II}} B_z^{\text{II}*} - B_x^{\text{II}} B_x^{\text{II}*} - B_y^{\text{II}} B_y^{\text{II}*}) \Big|_{z=w} dy dx \right] \quad (7.145)$$

Substituting (7.32) into the first integrand of (7.145) yields

$$\int_0^l \int_{-h}^0 B_z^{\text{II}} B_z^{\text{II}*} \Big|_{z=w} dy dx = \frac{l}{2} \sum_{m=1}^M \sum_{n=1}^{N_z} \sum_{l=1}^{N_z} \cos(q_n w) p_n^2 \cos(q_l^* w) p_l^{2*} \cdot \int_{-h}^0 \left(C_{mn}^a e^{\alpha_{mn} y} + D_{mn}^a e^{-\alpha_{mn} y} \right) \left(C_{ml}^a e^{\alpha_{ml} y} + D_{ml}^a e^{-\alpha_{ml} y} \right)^* dy \quad (7.146)$$

or,

$$\int_0^l \int_{-h}^0 B_z^{\text{II}} B_z^{\text{II}*} \Big|_{z=w} dy dx = \frac{l}{2} \sum_{m=1}^M \sum_{n=1}^{N_z} \sum_{l=1}^{N_z} \cos(q_n w) p_n^2 \cos(q_l^* w) p_l^{2*} \left[C_{mn}^a C_{ml}^{a*} \frac{1 - e^{-(\alpha_{mn} + \alpha_{ml}^*)h}}{\alpha_{mn} + \alpha_{ml}^*} + C_{mn}^a D_{ml}^{a*} \frac{1 - e^{-(\alpha_{mn} - \alpha_{ml}^*)h}}{\alpha_{mn} - \alpha_{ml}^*} - D_{mn}^a C_{ml}^{a*} \frac{1 - e^{(\alpha_{mn} - \alpha_{ml}^*)h}}{\alpha_{mn} - \alpha_{ml}^*} - D_{mn}^a D_{ml}^{a*} \frac{1 - e^{(\alpha_{mn} + \alpha_{ml}^*)h}}{\alpha_{mn} + \alpha_{ml}^*} \right] \quad (7.147)$$

Substituting (7.31) into the second integrand of (7.145) yields

$$\int_0^l \int_{-h}^0 B_y^{\text{II}} B_y^{\text{II}*} \Big|_{z=w} dy dx = \frac{l}{2} \sum_{m=1}^M \sum_{n=1}^{N_z} \sum_{l=1}^{N_z} \sin(q_n w) q_n \alpha_{mn} \sin(q_l^* w) q_l^* \alpha_{ml}^* \cdot \int_{-h}^0 \left(C_{mn}^a e^{\alpha_{mn} y} - D_{mn}^a e^{-\alpha_{mn} y} \right) \left(C_{ml}^a e^{\alpha_{ml} y} - D_{ml}^a e^{-\alpha_{ml} y} \right)^* dy \quad (7.148)$$

or,

$$\int_0^l \int_{-h}^0 B_y^{\text{II}} B_y^{\text{II}*} \Big|_{z=w} dy dx = \frac{l}{2} \sum_{m=1}^M \sum_{n=1}^{N_z} \sum_{l=1}^{N_z} \sin(q_n w) q_n \alpha_{mn} \sin(q_l^* w) q_l^* \alpha_{ml}^* \int_{-h}^0 \left\{ C_{mn}^a C_{ml}^{a*} e^{(\alpha_{mn} + \alpha_{ml}^*)y} - C_{mn}^a D_{ml}^{a*} e^{(\alpha_{mn} - \alpha_{ml}^*)y} - D_{mn}^a C_{ml}^{a*} e^{-(\alpha_{mn} - \alpha_{ml}^*)y} + D_{mn}^a D_{ml}^{a*} e^{-(\alpha_{mn} + \alpha_{ml}^*)y} \right\} dy \quad (7.149)$$

or,

$$\int_0^l \int_{-h}^0 B_y^{\text{II}} B_y^{\text{II}*} \Big|_{z=w} dy dx = \frac{l}{2} \sum_{m=1}^M \sum_{n=1}^{N_z} \sum_{l=1}^{N_z} \sin(q_n w) q_n \alpha_{mn} \sin(q_l^* w) q_l^* \alpha_{ml}^* \left\{ C_{mn}^a C_{ml}^{a*} \frac{1 - e^{-(\alpha_{mn} + \alpha_{ml}^*)h}}{\alpha_{mn} + \alpha_{ml}^*} - C_{mn}^a D_{ml}^{a*} \frac{1 - e^{-(\alpha_{mn} - \alpha_{ml}^*)h}}{\alpha_{mn} - \alpha_{ml}^*} + D_{mn}^a C_{ml}^{a*} \frac{1 - e^{(\alpha_{mn} - \alpha_{ml}^*)h}}{\alpha_{mn} - \alpha_{ml}^*} + D_{mn}^a D_{ml}^{a*} \frac{1 - e^{(\alpha_{mn} + \alpha_{ml}^*)h}}{\alpha_{mn} + \alpha_{ml}^*} \right\} \quad (7.150)$$

Substituting (7.30) into the third integrand of (7.145) yields

$$\int_0^l \int_{-h}^0 B_x^{\text{II}} B_x^{\text{II}*} \Big|_{z=w} dy dx = \frac{l}{2} \sum_{m=1}^M \sum_{n=1}^{N_z} \xi_m^2 \sin(q_n z) q_n \sin(q_l^* z) q_l^* \cdot \int_{-h}^0 \left(C_{mn}^a e^{\alpha_{mn} y} + D_{mn}^a e^{-\alpha_{mn} y} \right) \left(C_{ml}^a e^{\alpha_{ml} y} + D_{ml}^a e^{-\alpha_{ml} y} \right)^* dy \quad (7.151)$$

or,

$$\int_0^l \int_{-h}^0 B_x^{\text{II}} B_x^{\text{II}*} \Big|_{z=w} dy dx = \frac{l}{2} \sum_{m=1}^M \sum_{n=1}^{N_z} \xi_m^2 \sin(q_n z) q_n \sin(q_l^* z) q_l^* \int_{-h}^0 \left[C_{mn}^a C_{ml}^{a*} e^{(\alpha_{mn} + \alpha_{ml}^*)y} + C_{mn}^a D_{ml}^{a*} e^{(\alpha_{mn} - \alpha_{ml}^*)y} + D_{mn}^a C_{ml}^{a*} e^{-(\alpha_{mn} - \alpha_{ml}^*)y} + D_{mn}^a D_{ml}^{a*} e^{-(\alpha_{mn} + \alpha_{ml}^*)y} \right] dy \quad (7.152)$$

or,

$$\int_0^l \int_{-h}^0 B_x^{\text{II}} B_x^{\text{II}*} \Big|_{z=w} dy dx = \frac{l}{2} \sum_{m=1}^M \sum_{n=1}^{N_z} \xi_m^2 \sin(q_n z) q_n \sin(q_l^* z) q_l^* \left[C_{mn}^a C_{ml}^{a*} \frac{1 - e^{-(\alpha_{mn} + \alpha_{ml}^*)h}}{\alpha_{mn} + \alpha_{ml}^*} + C_{mn}^a D_{ml}^{a*} \frac{1 - e^{-(\alpha_{mn} - \alpha_{ml}^*)h}}{\alpha_{mn} - \alpha_{ml}^*} - D_{mn}^a C_{ml}^{a*} \frac{1 - e^{(\alpha_{mn} - \alpha_{ml}^*)h}}{\alpha_{mn} - \alpha_{ml}^*} - D_{mn}^a D_{ml}^{a*} \frac{1 - e^{(\alpha_{mn} + \alpha_{ml}^*)h}}{\alpha_{mn} + \alpha_{ml}^*} \right] \quad (7.153)$$

Figure 7.6 shows a flowchart of the developed SOVP based steady state analytic model to compute the eddy current forces.

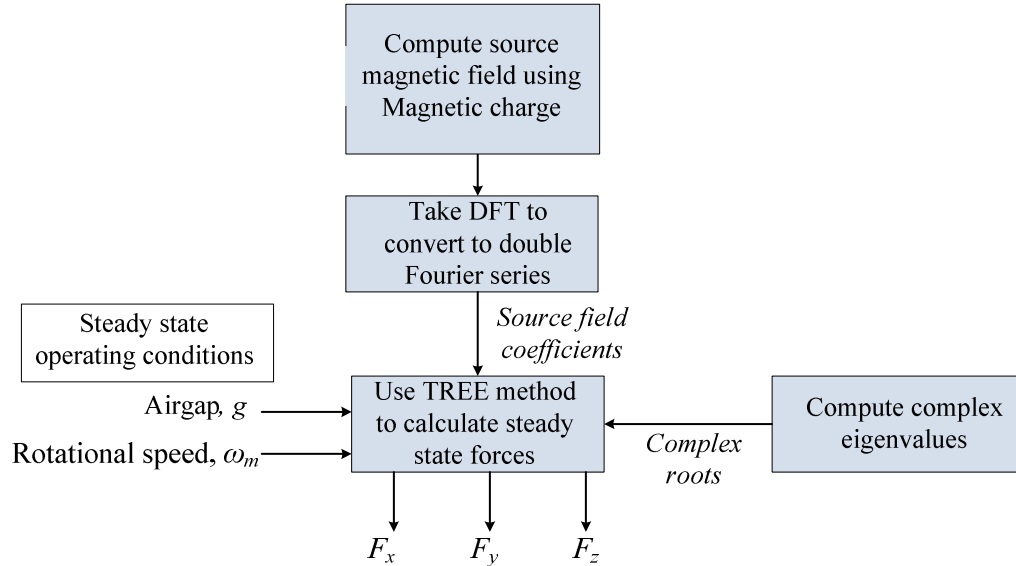


Figure 7.6. Flowchart of the presented TREE method using SOVP

7.5. Model Validation

7.5.1. Field Validation

Like previous chapters, for validation purposes a Halbach rotor has been used. The geometric and material properties of the rotor and conductive plate are listed in Table 7.2. The induced magnetic flux density in the conductive region has been compared against a previously developed 3-D FEA steady state model [13, 75] for 25mm lateral offset of the rotor. Figure 7.7 shows the flux density comparison on the top surface of the conductive plate across z -axis. An excellent field match has been obtained.

Table 7.2: Simulation Parameters

	Description	Value	Unit
Magnetic Rotor	Outer radius, r_o	26	mm
	Inner radius, r_i	9.62	mm
	Width, w_o	52	mm
	Remnant magnetic flux density, B_{rem}	1.42	T
	Relative permeability, μ_r	1.108	-
	Pole pairs, P	2	-
Conductive plate	Conductivity, σ	2.459×10^7	Sm^{-1}
	Width, w	77	mm
	Length, l	200	mm
	Thickness, h	6.3	mm
	Air-gap between rotor and plate, g	9.5	mm

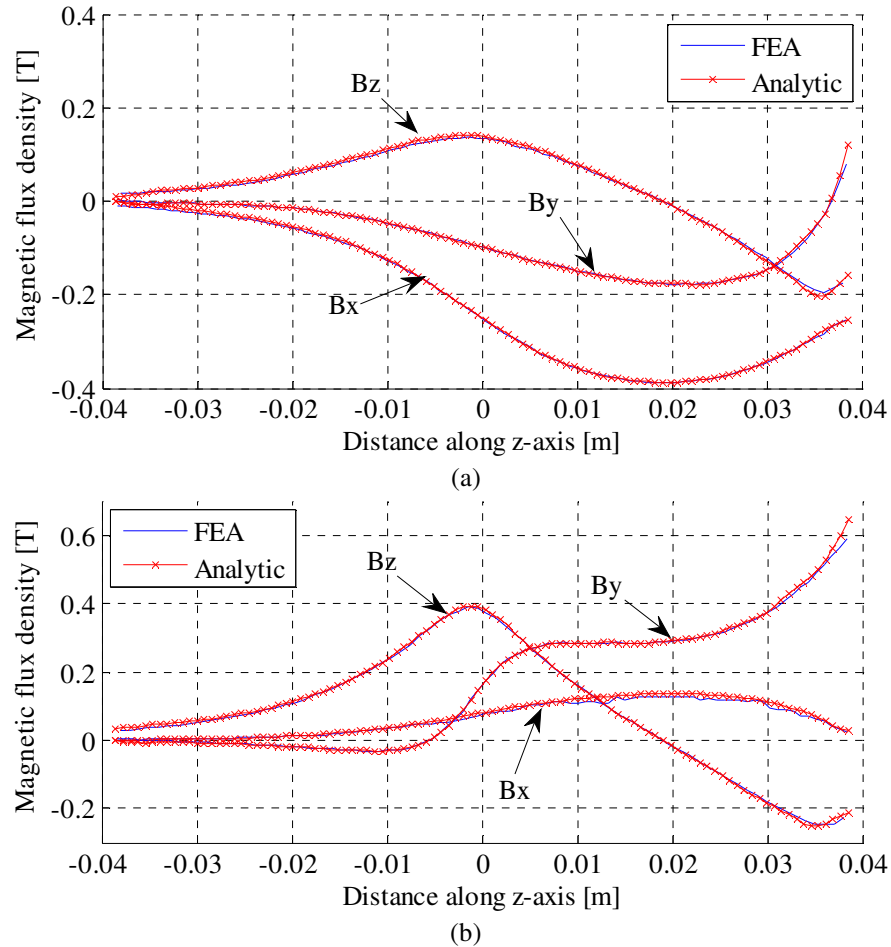


Figure 7.7. Induced magnetic flux density comparison on the top surface of the conductive plate at (a) $x=20\text{mm}$ and (b) $x=0\text{mm}$ for 25mm lateral offset of the rotor at zero translational velocity and 8000 RPM rotational velocity.

7.5.2. Force Validation

Electromagnetic forces are compared with FEA steady state model developed using COMSOL [13, 75] and JMAG for different lateral offset and rotational speed values and shown in Figure 7.9-Figure 7.10. A very good match of the forces has been achieved.

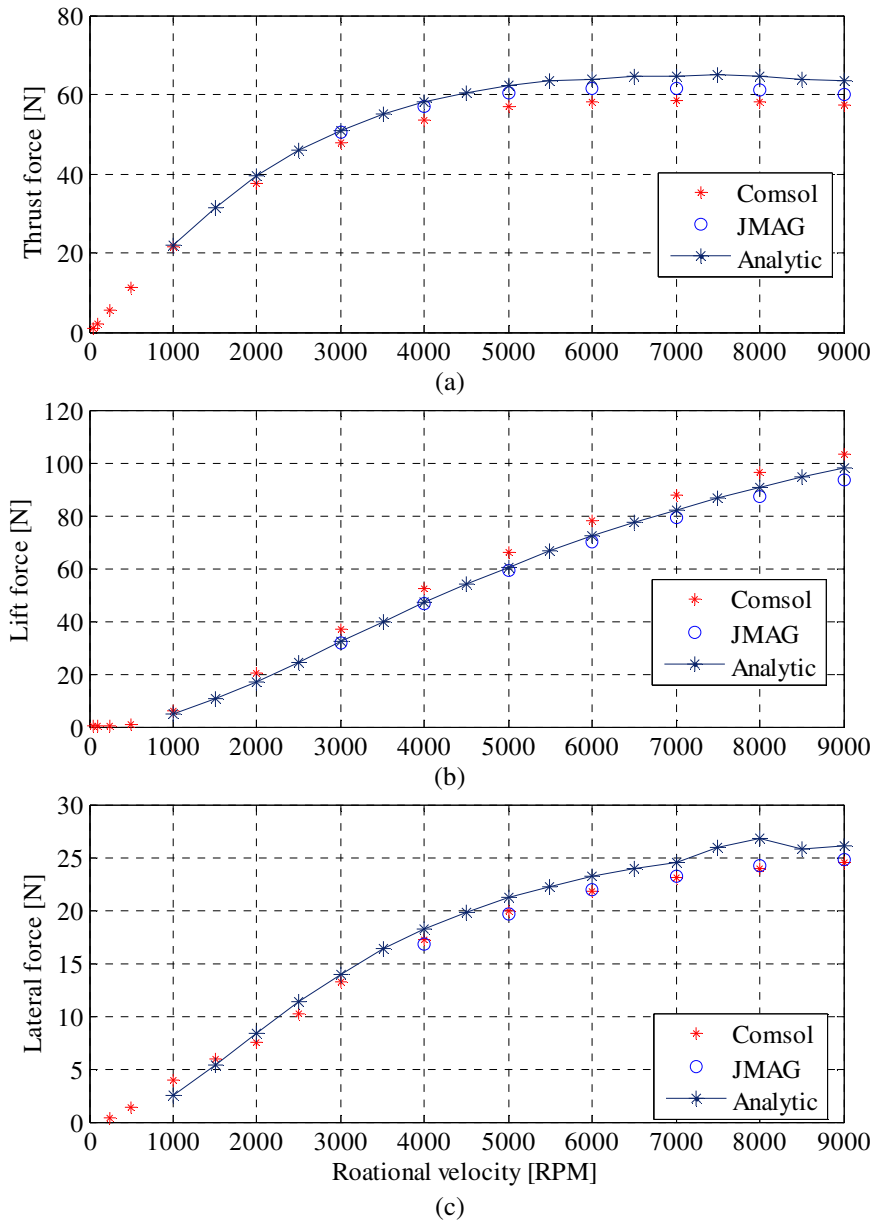


Figure 7.8. Comparisons of (a) F_x , (b) F_y and (c) F_z for 25mm lateral offset of the rotor at zero translational velocity.

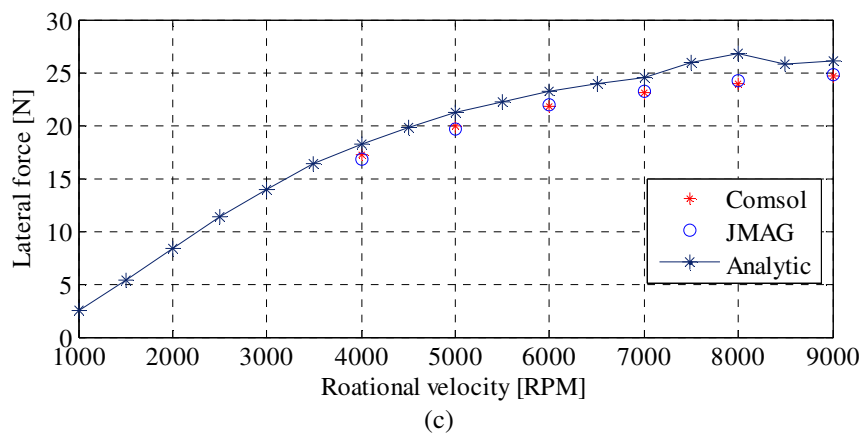
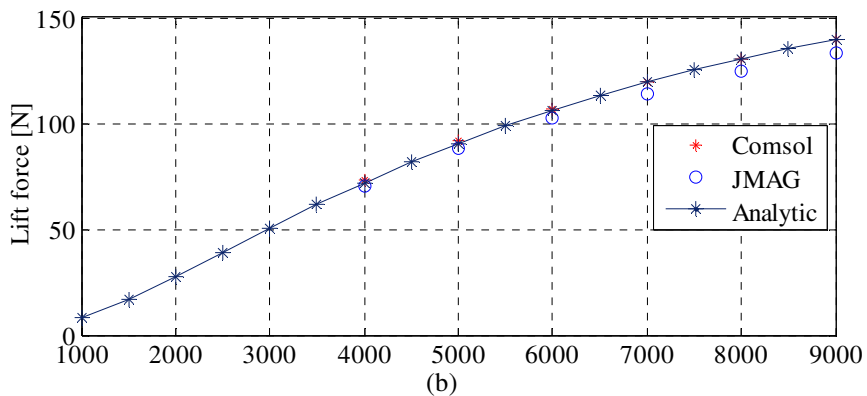
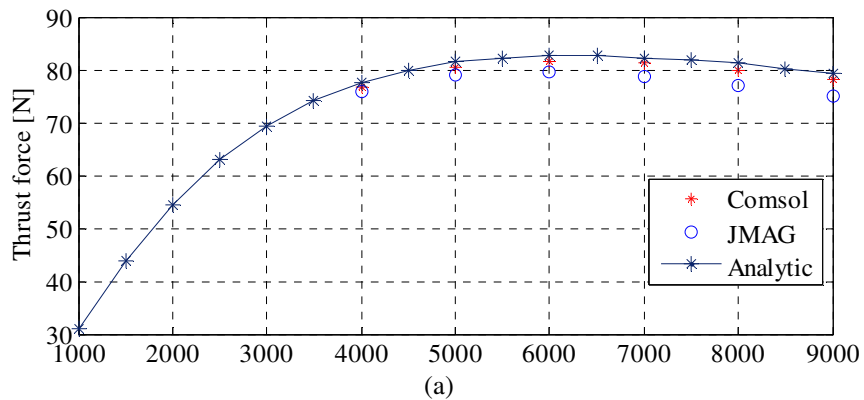


Figure 7.9. Comparisons of (a) F_x , (b) F_y and (c) F_z for 15mm lateral offset of the rotor at zero translational velocity.

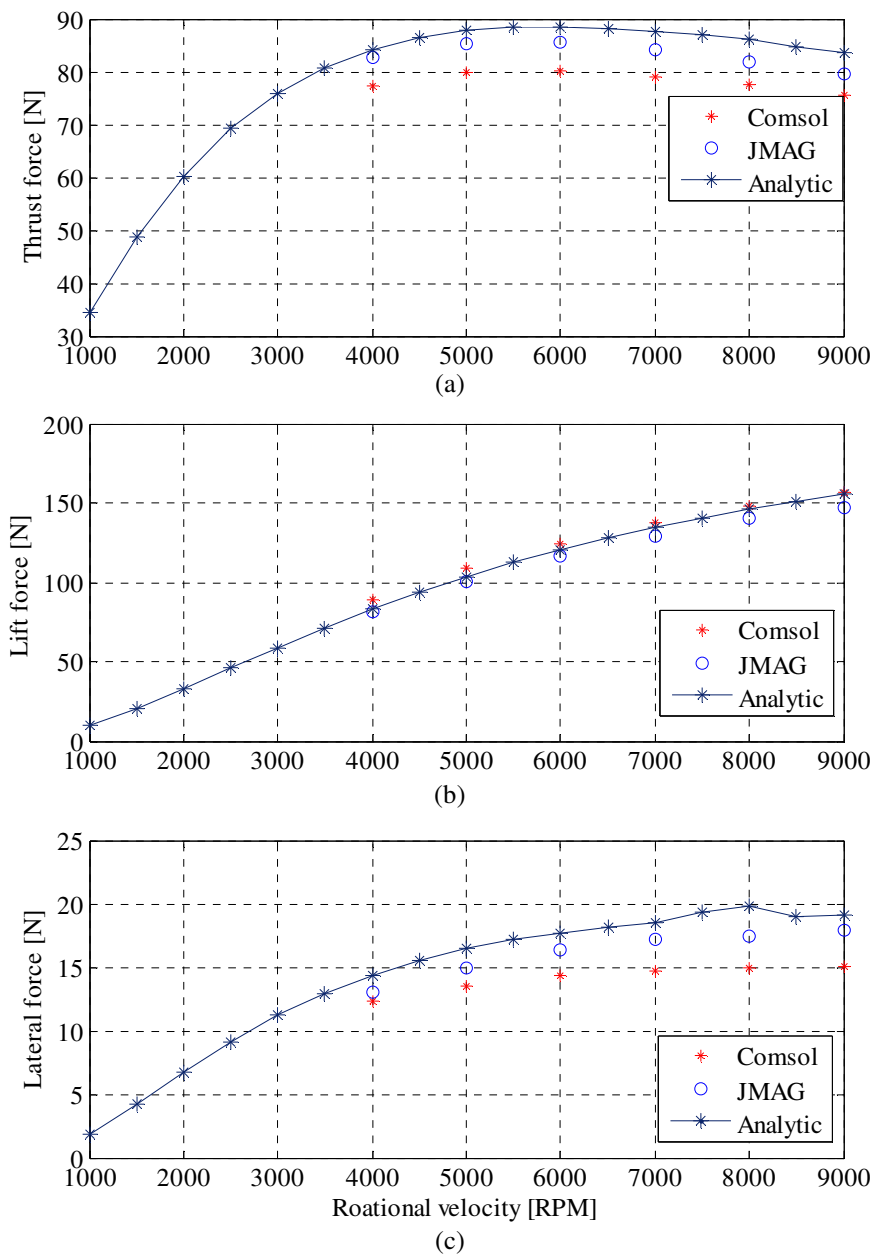


Figure 7.10. Comparisons of (a) F_x , (b) F_y and (c) F_z for 10mm lateral offset of the rotor at zero translational velocity.

The average computation time involved in calculating the force results for a single rotational speed value by the FEA and analytic model are listed in Table 7.3.

Table 7.3. : Computation time for analytic and finite element steady state models

Model type	Computation time
JMAG transient	5 hr 40 min
Current sheet based steady state model using Comsol v3.5a	8 min
Proposed analytic model using SOVP and TREE	32 s

The computation time of the proposed analytic model is larger than the models presented in previous chapters. This is mainly due to the need for the numerical computation of complex valued eigenvalues. Hence, if the eigenvalues can be calculated beforehand and stored in a look-up table, the analytic model can be made faster. The average accuracy of the developed analytic model with respect to the JMAG transient and current sheet based Comsol steady state models [13, 75] have been compared at 15mm lateral offset of the source as shown in Table 7.4.

Table 7.4 : Accuracy of the developed analytic steady state model using SOVP and TREE

Force	Error with JMAG transient [%]	Error with Comsol steady state [%]
Thrust	4.32	7.95
Lift	3.04	5.8
Lateral	3.3	6.23

7.6. Summary

Analytic 3-D steady state model of eddy current distribution has been developed using novel truncated region eigenfunction expansion approach to consider edge effect of a conductive medium when a magnetic source is located near the edge of the conductive medium. The analytical results agree really well with finite element results. The presented analytic model is more accurate than the models presented in previous chapter. But, the accuracy comes at the cost of computational burden due to the numerical calculation of eigenvalues. The key points of the developed model are summarized in Table 7.5.

Table 7.5 : Summary of the presented 3-D analytic steady state model using SOVP and TREE

Model assumptions	Model characteristics
<ul style="list-style-type: none"> • Conductive plate is linear, simply connected, homogenous and non-magnetic 	<ul style="list-style-type: none"> • Models the conductive and nonconductive domains using the SOVP. The conductive plate is modeled using both TE and TM potentials.
<ul style="list-style-type: none"> • Conductive plate is infinitely long, but has finite width and thickness 	<ul style="list-style-type: none"> • Can be applicable for any magnetic source
<ul style="list-style-type: none"> • Frequency is low 	<ul style="list-style-type: none"> • Computes the source field using magnetic charge sheet • Models only rotational motion of the source. • Computationally faster than FEA but inferior to other developed analytic models in this dissertation. • Most accurate of all the presented analytic models. Can accurately model the edge-effect of the plate. • Model is developed in Matlab.

CHAPTER 8 : EXPERIMENTAL RESULTS AND VERIFICATION

8.1. Introduction

In this chapter the 3-D analytic models using the second order vector potential and magnetic vector potential developed in Chapter 5 and Chapter 6 will be qualitatively verified against two experimental setups. The analytical force, electromagnetic torque and power transfer equations derived in Chapter 6 will be compared with the experimental results from 1 DOF pendulum setup and sub-scale maglev setup with four EDWs.

8.2. Comparison with a Pendulum Setup

8.2.1. Description of the Experimental Setup

In this experimental setup an EDW is vertically hung on one side of the circular aluminum guideway as a pendulum as shown in Figure 8.1. The EDW and guideway are free to rotate on their respective axes, thus enabling both the rotational and translational motion effects to be simulated experimentally.

A 16 segment 4 pole-pair Halbach rotor, as shown in Figure 8.2(a), assembled by Bird [13] has been used as the EDW in the experimental setup. The experimental setup, as shown in Figure 8.1 and Figure 8.2(b), was constructed by Paudel and Bomela. The parameters of the EDW and guideway are listed in Table 8.1.

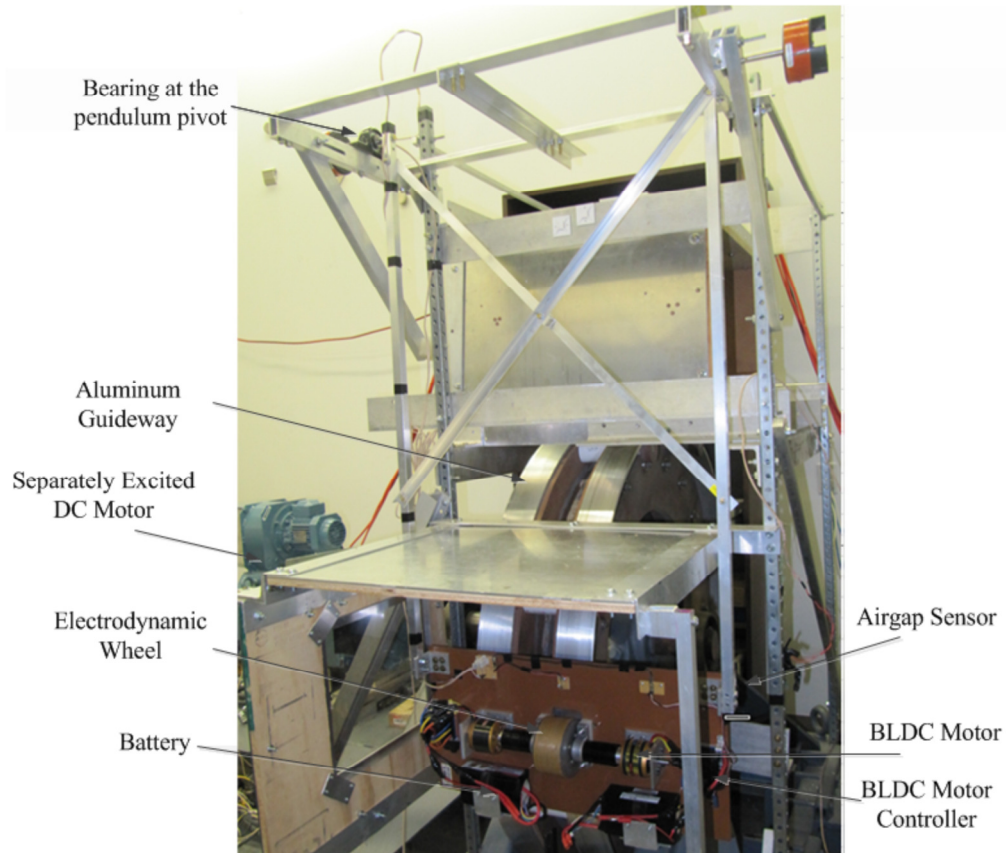


Figure 8.1. The experimental setup of a single EDW pendulum setup.

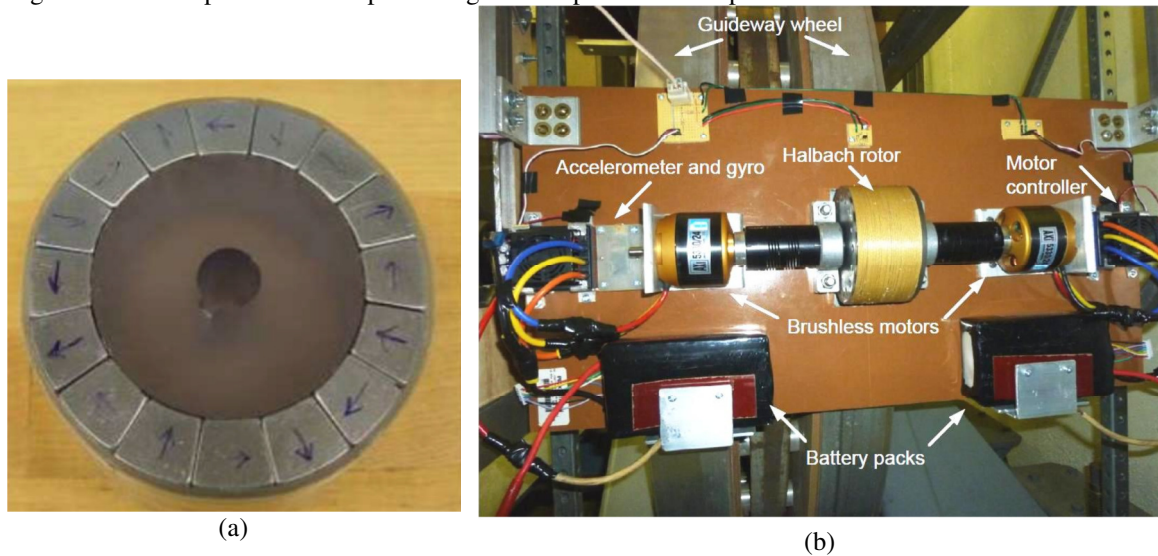


Figure 8.2. (a) Experimental four pole-pair EDW using 16 segmented NdFeB Magnets; (b) The experimental setup showing the guideway, EDW, BLDC motors and battery packs.

Table 8.1 : EDW and Guideway parameters for the Pendulum setup [14]

	Description	Value	Unit
EDW	Outer radius, r_o	50 ± 0.58	mm
	Inner radius, r_i	34.2	mm
	Width, w_o	50	mm
	Remnant magnetic flux density, B_{rem}	1.42	T
	Relative permeability, μ_r	1.055	-
	Pole pairs, P	4	-
	Sleeve thickness	2.6 ± 0.1	mm
Guideway	Conductivity (Al), σ	2.459×10^7	Sm^{-1}
	Width, w	77	mm
	Outer radius	600 ± 0.58	mm
	Thickness, h	6.3	mm
	Sheets separation	101	mm

In this setup the EDW is rotated by two Axi-5300/24 brushless DC (BLDC) motors with the parameters given in Table 8.2. A pair of battery packs (Turnigy 4.5Ah 6 cell 19.8 V) onboard the pendulum setup supplies the power to the motors, as shown in Figure 8.2(b). The speed of the BLDC motor is controlled by varying the pulse width to the Electronic Speed Controller (ESC). The guideway is rotated by a separately excited DC motor with the parameters given in

Table 8.3. The RPM of the separately excited DC motor and EDW or BLDC motor has been measured using a rotary encoder sensor and Hall Effect sensor respectively. The outputs from these sensors are fed to Matlab/ Simulink Real Time Window (RTW) through a National Instrument (NI) PCIe-2659 board. A laser displacement sensor was used to measure the oscillation of the pendulum. The sensor output was fed to Matlab RTW via the same NI board.

Table 8.2 : Axi-5330/24 Brushless DC motor parameters [14]

	Description	Value	Unit
Measured parameters using RLC meter	Per-phase inductance	30.17	μH
	Per-phase resistance	0.0181	Ohm
Parameters supplied by manufacturer	RPM/V	197	-
	Max. efficiency	97%	-
	Max. efficiency current	15-38	A
	Current capacity	65/30	A/s
	No-load current	1.5	A

Table 8.3 : ABB separately excited DC motor parameters [14]

	Description	Value	Unit
Armature winding	V_a	440	V
	I_a	69	A
	R_a (manufacturer supplied)	0.71	Ohm
	L_a (manufacturer supplied)	10.5	mH
	R_a (measured)	1.0	Ohm
	L_a (measured)	5.884	mH
Field winding	V_f	340	V
	I_f	2.44	A
	R_f (manufacturer supplied)	139.34	Ohm
	R_f (measured)	111.5	Ohm
	L_f (measured)	10.8	H
	Torque rating	132	Nm
	Power rating	26.1	kW
	RPM rating	1895	RPM

8.2.2. Dynamics of the Forced Oscillation

When the EDW rotates near the rotating guideway, the induced eddy currents in the guideway create the lift and thrust force on the EDW. The lift force acts along the horizontal direction and tries to repel the magnetic rotor away from the guideway surface whereas the thrust force attempts to vertically push the rotor along the surface of the guideway. Due to the action of the lift and gravity, the EDW eventually comes to rest after oscillation whereas the thrust force increases the effective weight of the vehicle. The equation of motion of the EDW pendulum is given by [14]

$$m' \frac{d^2 y(t)}{dt^2} + c \frac{dy(t)}{dt} + \left[\frac{dy(t)}{dt} \right] \zeta m' G + Ky(t) = F_y^{EDW}(v_x, v_y, w_m, g) \quad (8.1)$$

where

$$m' = m + \frac{F_x^{EDW}(v_x, v_y, w_m, g)}{G} \quad (8.2)$$

and

m = mass of the vehicle [kg]

c = viscous damping coefficient [Ns^2m^{-1}]

K = stiffness coefficient [Nm^{-1}]

ζ = sliding friction coefficient [Ns^2m^{-1}]

G = acceleration due to gravity [ms^{-2}]

g = air gap between the guideway and EDW pendulum [mm]

F_x^{EDW} = thrust force acting on rotating EDW [N]

F_y^{EDW} = lift force acting on the rotating EDW [N]

The second term in (8.2) takes into account the effect of the thrust force acting on the EDW by adding an extra mass term generated due to the thrust force. The measured damping and stiffness coefficients are given in Table 8.4.

Table 8.4 : Damping and stiffness coefficients from free oscillations [14]

Description	Value	Unit
Viscous damping, c	0.361	Ns^2m^{-1}
Sliding friction, ζ	1.9599×10^{-4}	Ns^2m^{-1}
Stiffness coefficient, K	76.8008	Nm^{-1}

Table 8.5 : Pendulum setup parameters [14]

Description	Value	Unit
Mass of setup without batteries	7.04	Kg
Mass of two Turnigy batteries	1.810	Kg
Length of the pendulum	1.307	m

The lift and thrust force are a function of the translational, v_x , heave, v_y , and rotational, ω_m , velocity as well as airgap, g . As mentioned in section 8.2.1, the airgap, translational and rotational velocity of the EDW have been continuously measured using the laser displacement, rotary encoder and Hall Effect sensors respectively. The heave velocity has been obtained by differentiating the measured airgap with respect to time. Using the steady state thrust and lift force equations (6.151) and (6.152) derived in chapter 6 and the parameters given in Table 8.4 and Table 8.5, the dynamic equation given by (8.1) has been solved in Matlab using Ode45 function [14]. The ode45 solver is

continuously supplied with the measured translational and rotational velocity of the EDW, however, only the initial values (at $t=0$) of the measured airgap and heave velocity are supplied to ode45. The solver then solves (8.1) using the 3-D analytical force equations and computes the airgap and heave velocity for the next time step. In this way, the airgap and heave velocity profile is obtained from ode45. The process is illustrated in Figure 8.3. The initial conditions used for the test are listed in Table 8.6. The computed air gap profile is compared with the measured data and is shown in Figure 8.5. A very close match is obtained.

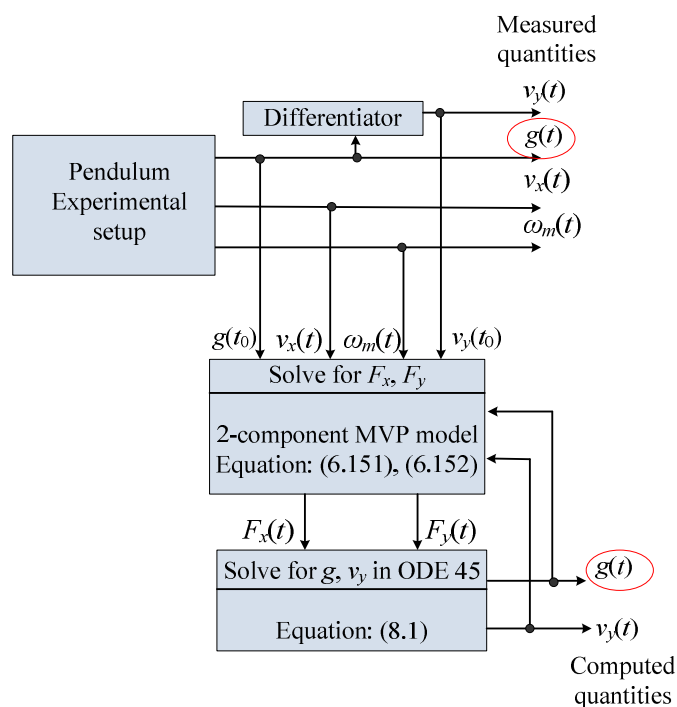


Figure 8.3. Flowchart of solving (8.1) using ode45 and 3-D analytic model. The measured and computed airgap are highlighted with red circle.

Table 8.6 : Initial conditions for test [14]

Parameters	Value	Unit
Pendulum equilibrium position, g	21.5	mm
Initial airgap, g	22.10	mm
Initial translational velocity, v_x	1.55	ms^{-1}
Initial angular velocity, ω_m	10.62	rads^{-1}
Initial heave velocity, v_y	0	ms^{-1}
Initial slip speed, s_l	-1.019	ms^{-1}

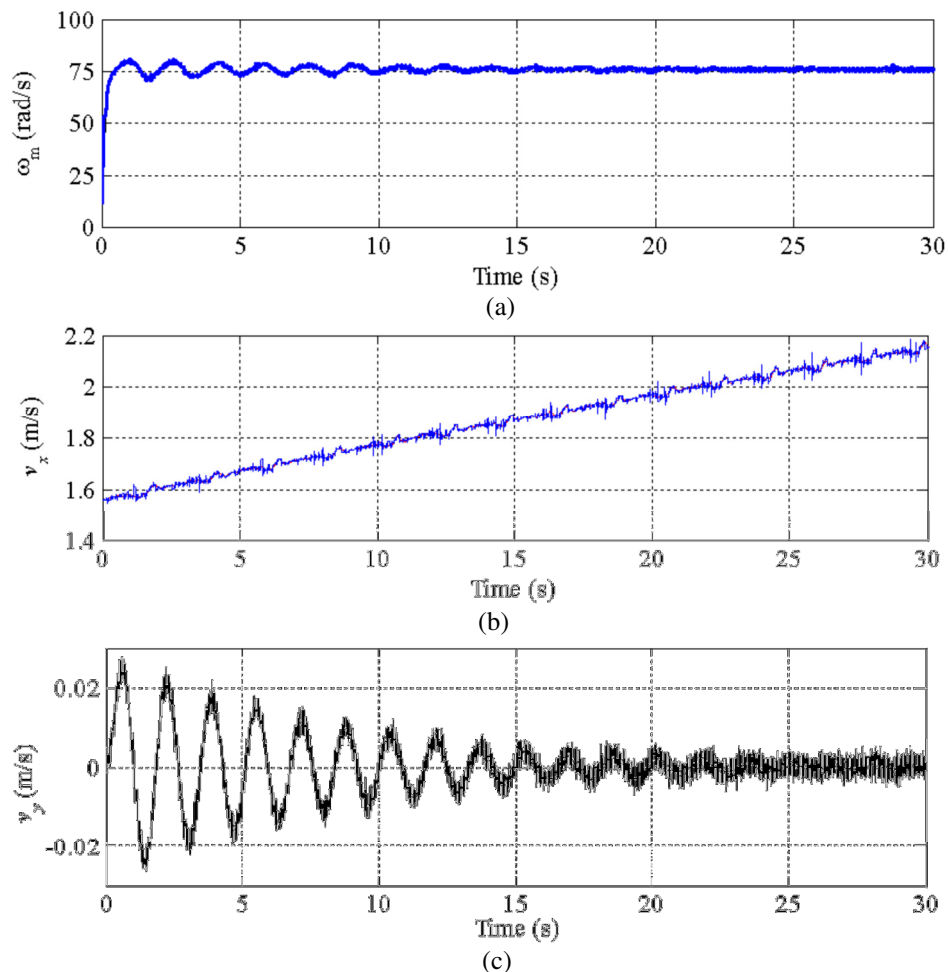


Figure 8.4. The measured (a) ω_m of the EDW, (b) v_x of the guideway and (c) v_y of the EDW [14].

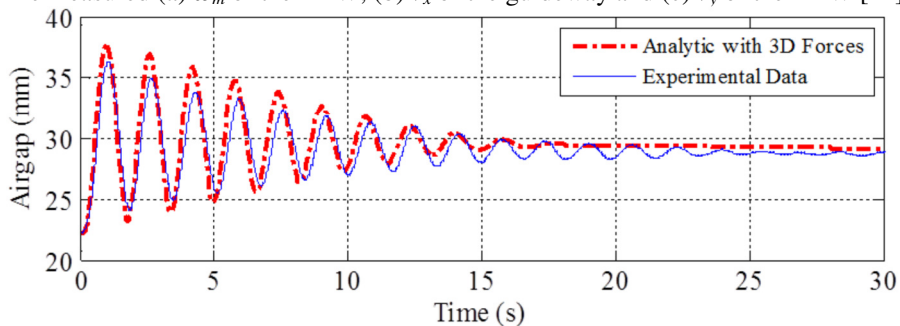


Figure 8.5. A comparison of the airgap profile between the analytic 3-D model and experimental setup.

8.3. Comparison with Multi-DOF EDW Maglev

An experimental setup as shown in Figure 8.6, Figure 8.7 and Figure 8.8 has been constructed by Paudel and Bomela in order to study the dynamics when a maglev vehicle utilizing four EDWs is operated above the circular guideway. The EDW vehicle has been kept translationally stationary while the circular guideway rotates producing the

translational velocity effect on the EDWs. In order to investigate the vertical damping characteristic of the EDW maglev the experimental setup has been designed to prevent motion along the x and z directions as well as angular yaw. Four laser sensors are located at each corner of the vehicle, as shown in Figure 8.6, and provide high fidelity airgap changes. The vehicle is able to move in the y direction (heave) as well as rotate around the x and z axis (pitch, roll) as illustrated in Figure 8.9.

8.3.1. Torque and Power Transfer Comparison

By experimentally sensing the current, I_a , drawn by the brushless dc (BLDC) motor controllers, the torque, T , of the motor can be measured using

$$T = K_t(D)I_a \quad (8.3)$$

where the torque constant, K_t is a function of duty cycle, D [217]. By measuring the rotational speed of the EDW, the output power of the BLDC motor can be measured using

$$P_o = K_t(D)\omega_m \quad (8.4)$$

where ω_m is the measured rotational speed of the EDW [rads^{-1}].

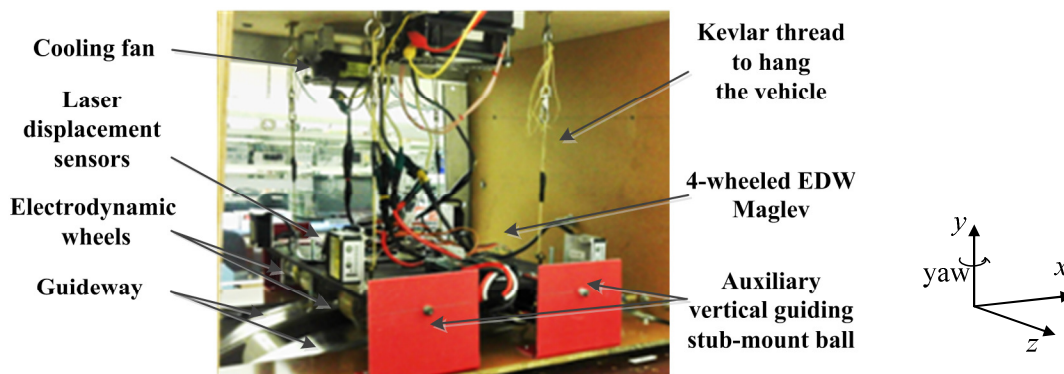


Figure 8.6. Electrodynamic vehicle setup with four laser displacement sensor.

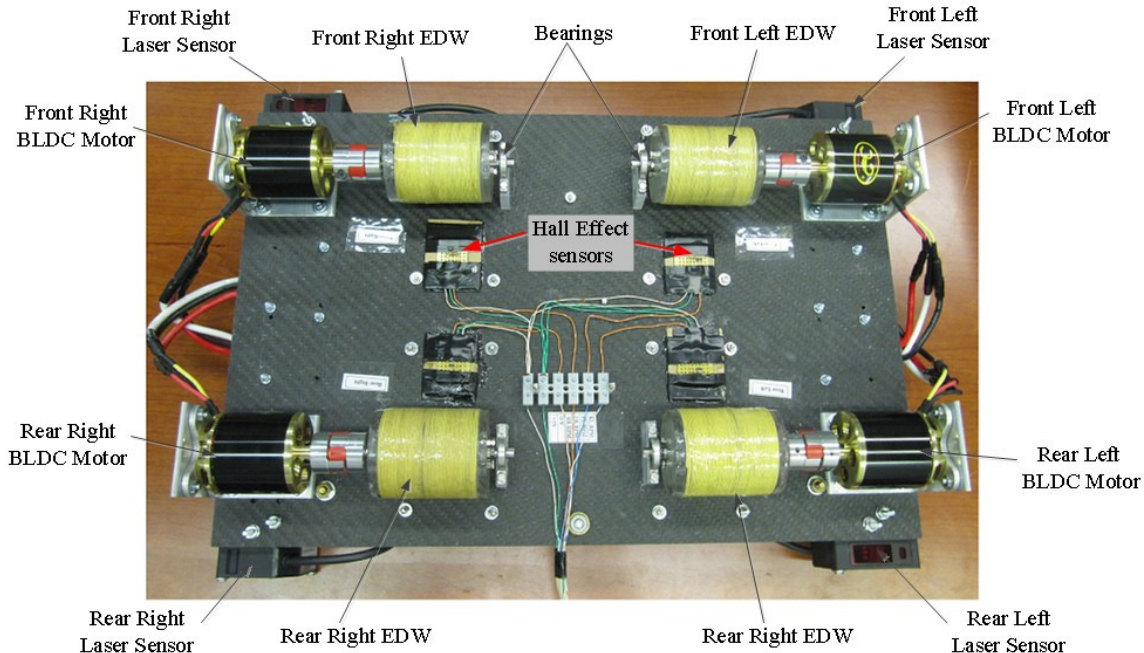


Figure 8.7. The underside of the sub-scale EDW vehicle.

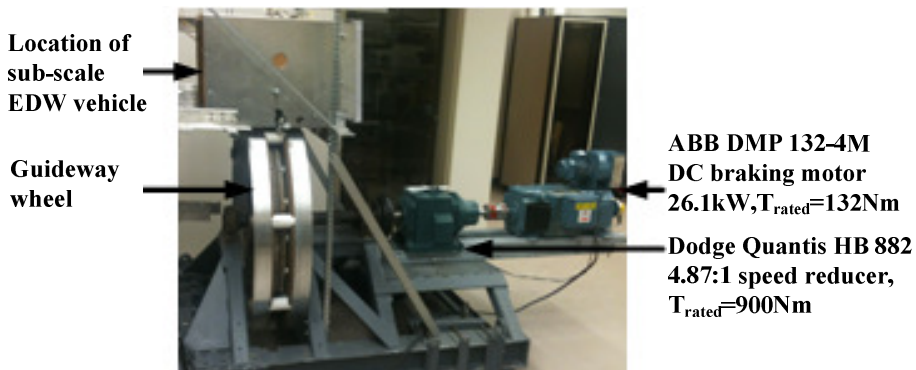


Figure 8.8. Electrodynamic vehicle setup with four laser displacement sensor.

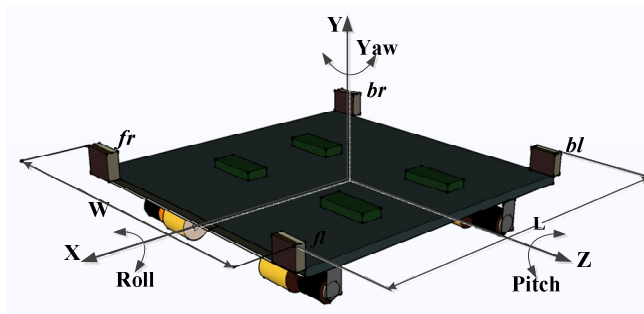


Figure 8.9. Maglev vehicle coordinate definition.

The parameters of the EDWs and guideway wheel used for this setup are listed in Table 8.7. Using the measured airgap, g , translational velocity, v_x , heave velocity, v_y , and

rotational speed of the EDWs, ω_m , the power output from the BLDC motors and electromagnetic torque acting on the EDWs are analytically computed using (5.163) and (5.165) respectively and compared with the experimental results. Figure 8.10 and Figure 8.11 show the measured rotational velocity and airgap of the EDWs whereas Figure 8.12 shows the translational motion of the guideway and heave motion of the front right EDW. The torque comparison for all the rotors is shown in Figure 8.13 while Figure 8.14 shows the total output power comparison. A close match has been obtained for all the rotors.

Table 8.7 : Multi-DOF maglev setup parameters

	Description	Value	Unit
EDW	Outer radius, r_o	26	mm
	Inner radius, r_i	10	mm
	Width, w_o	52	mm
	Remnant magnetic flux density, B_{rem}	1.42	T
	Relative permeability, μ_r	1.108	-
	Pole pairs, P	2	-
Guideway	Conductivity (Al), σ	2.459×10^7	Sm^{-1}
	Width, w	77	mm
	Outer radius	600 ± 0.58	mm
	Thickness, h	6.3	mm
	Sheets separation	101	mm

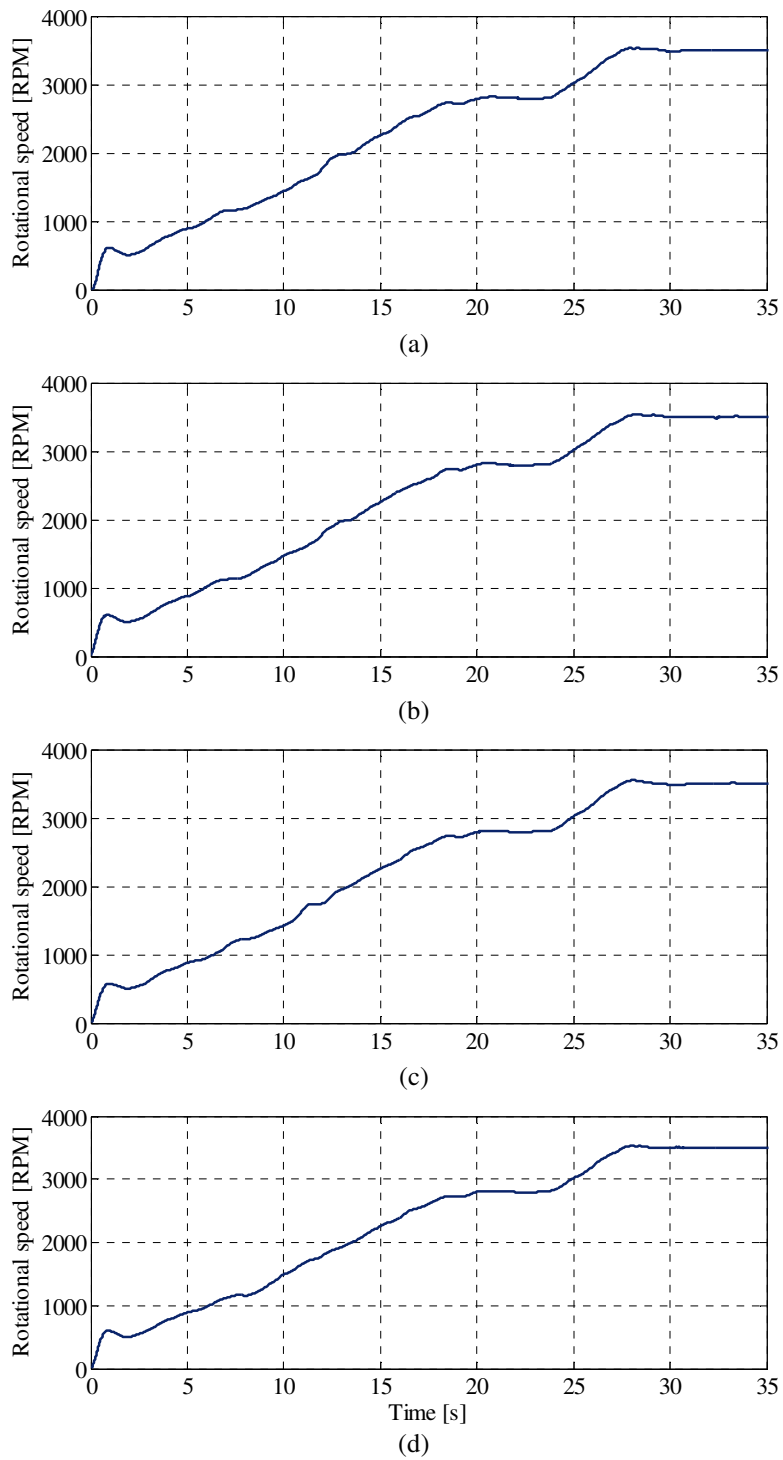
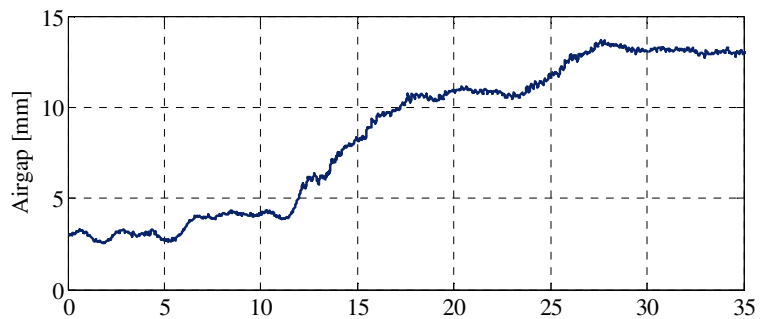
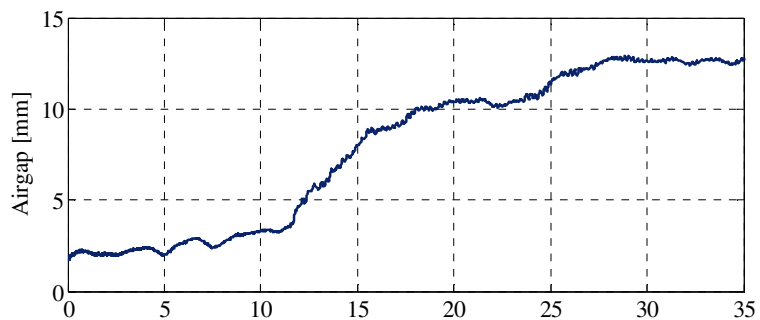


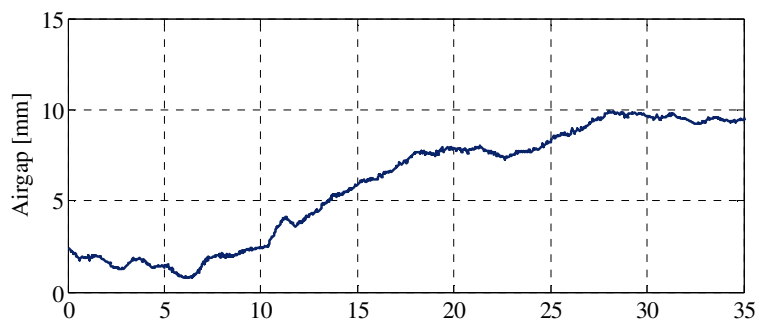
Figure 8.10. Measured RPM data for (a) front left, (b) front right, (c) rear left and (d) rear right EDW.



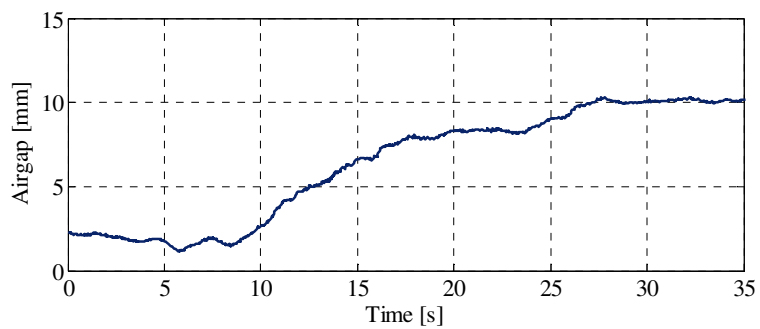
(a)



(b)



(c)



(d)

Figure 8.11. Measured airgap data for (a) front left, (b) front right, (c) rear left and (d) rear right EDW.

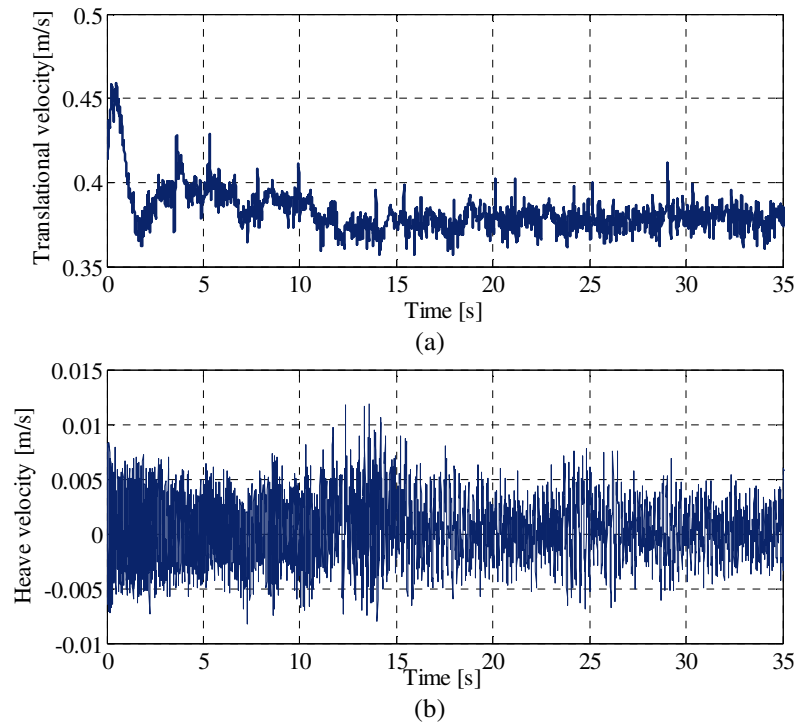
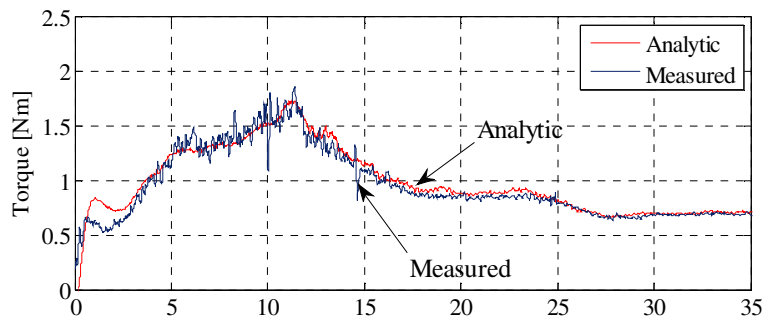
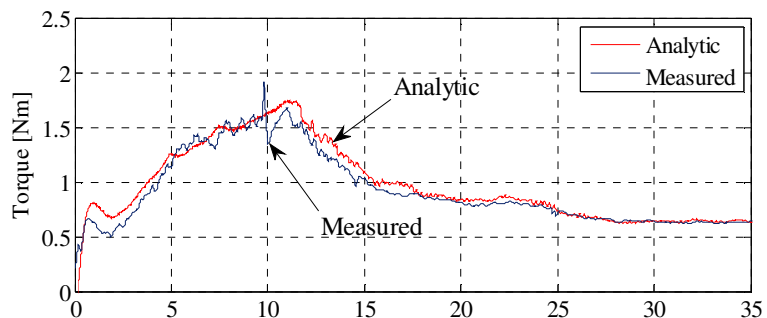


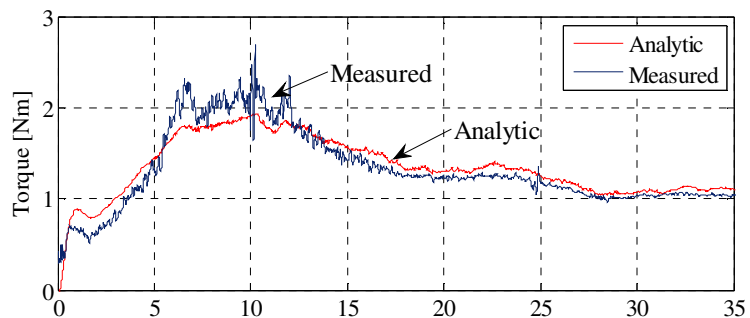
Figure 8.12. Experimentally measured (a) translational velocity and (b) heave velocity of the front right EDW.



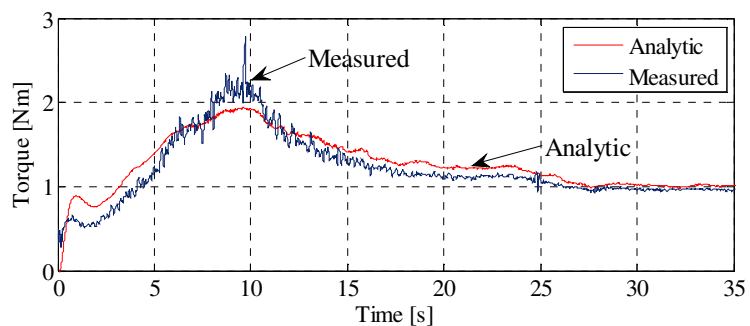
(a)



(b)



(c)



(d)

Figure 8.13. A comparison of the electromagnetic torque between the developed 3-D analytic model and experimentally measured results for (a) front left, (b) front right, (c) rear left and (d) rear right EDW.

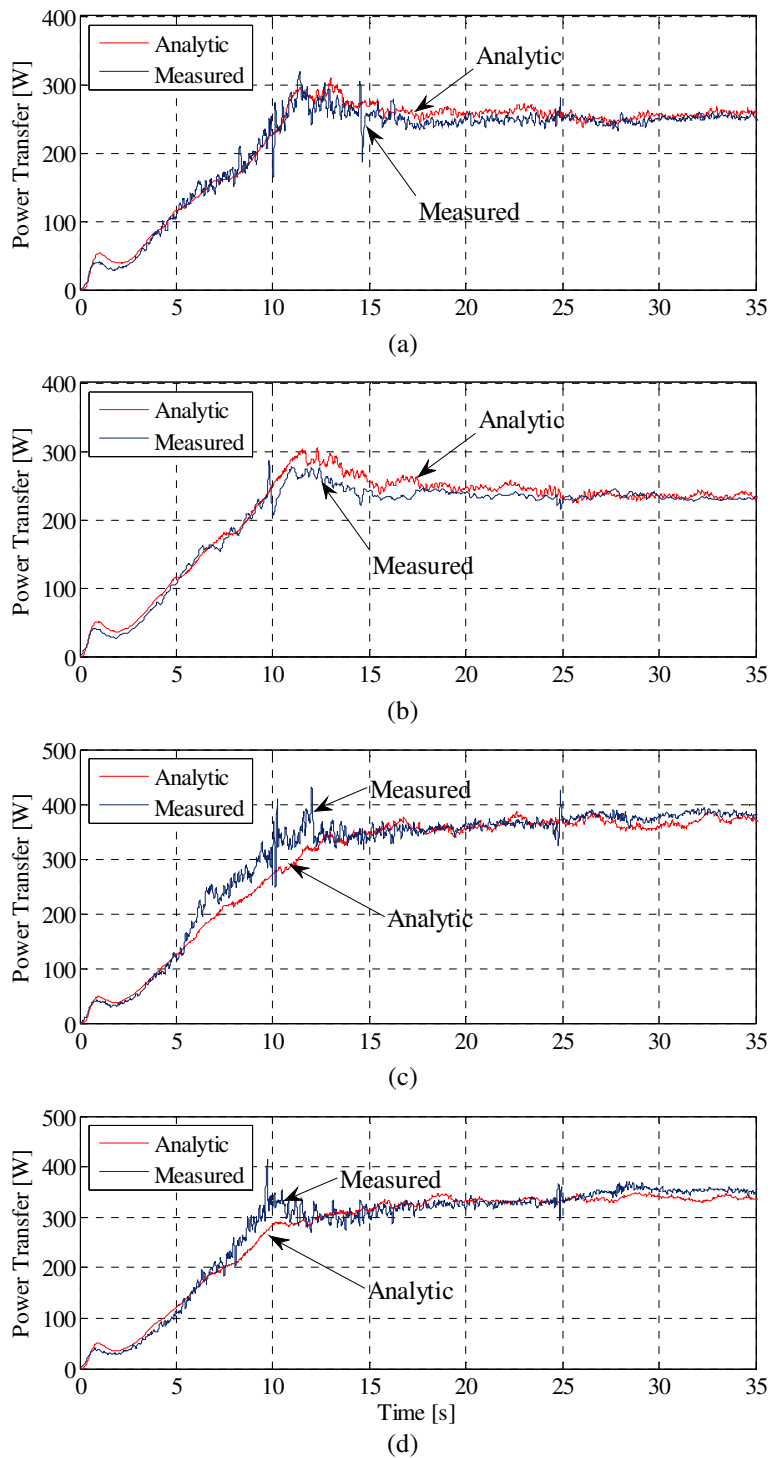


Figure 8.14. A comparison of the output power from BLDC motor between the developed 3-D analytic model and experimentally measured results for (a) front left, (b) front right, (c) rear left and (d) rear right EDW.

8.3.2. Lift Force Verification

The experimental setup with lift force sensors is shown in Figure 8.15. The force sensor produces an output voltage proportional to its deflection due to the applied weight. The output voltage is amplified using instrumentation amplifier for ease in measurement.

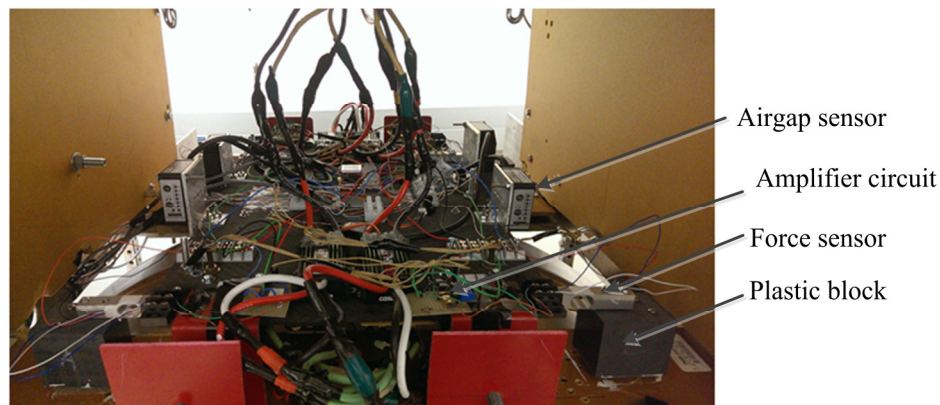
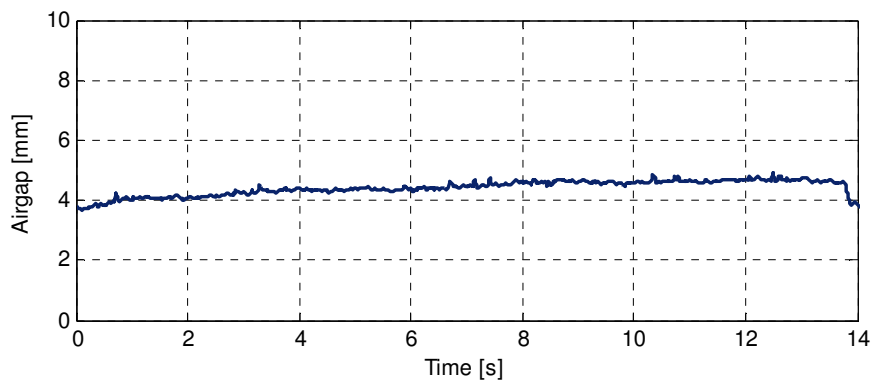


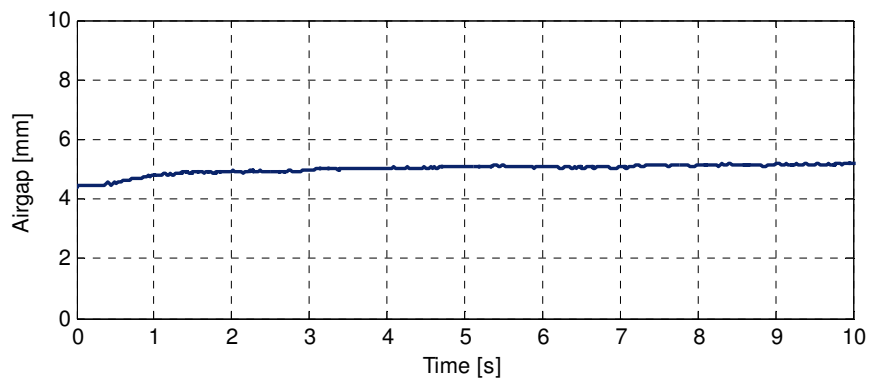
Figure 8.15. Electrodynamic vehicle setup with four laser displacement sensor.

In the setup one side of the sensor is attached to the vehicle and the other side is attached to a plastic block as shown in Figure 8.15. Thus the airgap between the vehicle and guideway remains constant over the duration of the simulation. Using the measured airgap, g , translational velocity, v_x , heave velocity, v_y , and rotational speed of the EDWs, ω_m , the lift force acting on the EDWs is analytically computed using (5.155) and compared against experimental results. The parameters of the EDWs and guideway wheel used for this setup are listed in Table 8.7. Figure 8.16, Figure 8.17 and Figure 8.18 show the measured airgap, rotational velocity of the EDWs and translational velocity of the guideway. The lift force comparison for the rotors is shown in Figure 8.19. There is one unwanted spike picked up by the Hall effect sensor at around 6s of the simulation of the rear left rotor as seen in Figure 8.17(a). This spike in the measured ω_m has directly resulted in a similar spike in the lift force result of the same rotor in Figure 8.19(a).

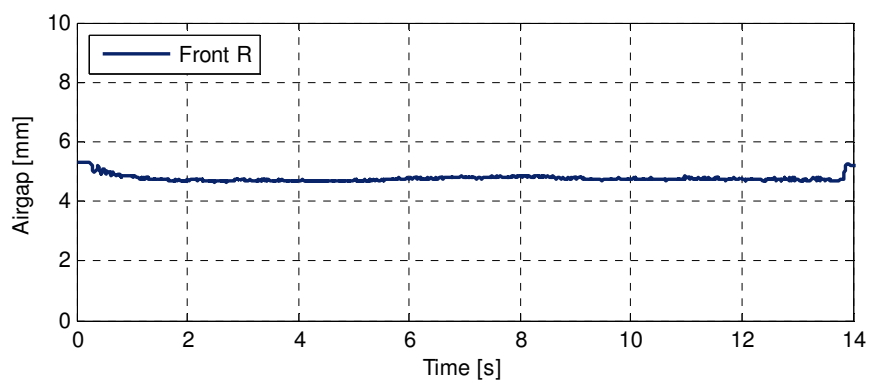
Overall good match has been obtained. The force comparison for the front left EDW could not be performed due to incorrect data from the corresponding airgap sensor.



(a)

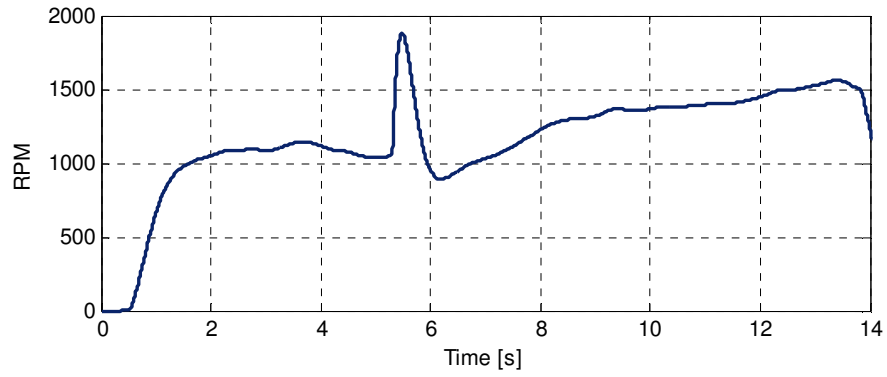


(b)

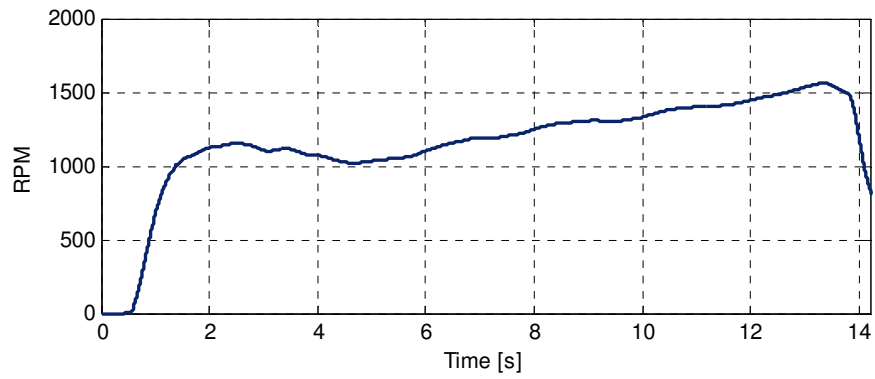


(c)

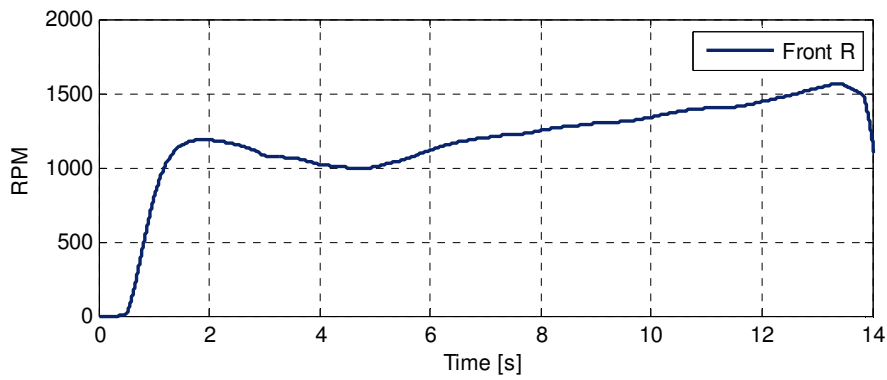
Figure 8.16. Measured airgap profile of (a) rear left, (b) rear right, (c) front right EDW.



(a)

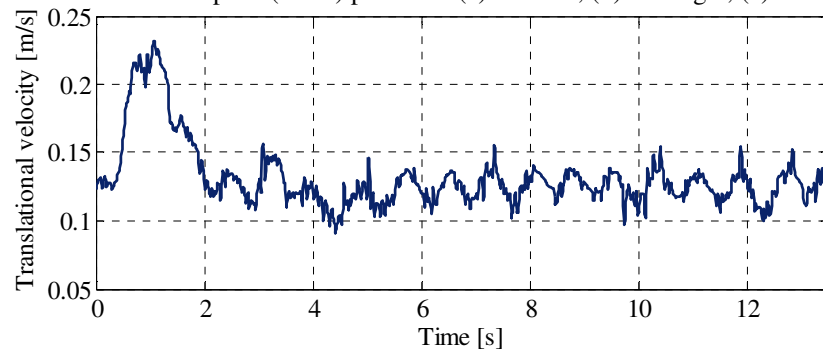


(b)



(c)

Figure 8.17. Measured rotational speed (RPM) profile of (a) rear left, (b) rear right, (c) front right EDW.

Figure 8.18. Translational speed, v_x , profile of the guideway

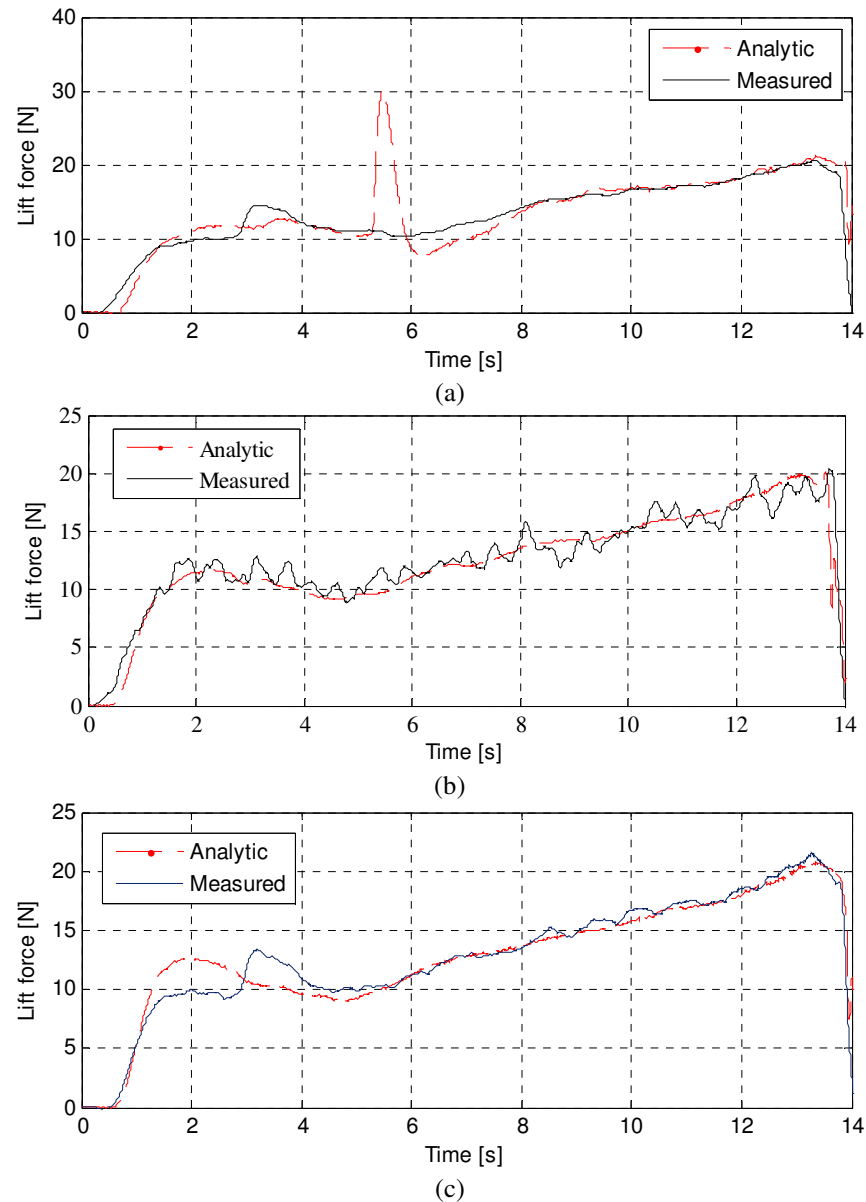


Figure 8.19. Lift force, F_y , comparison for (a) rear left, (b) rear right, (c) front right EDW between the second order vector potential based analytic model and experimental setup.

8.4. Summary

The developed 3-D analytic models have been compared with two experimental setups. Good performance of the analytic model has been achieved as the analytically predicted results closely followed the measured values in both setups.

CHAPTER 9 : CONCLUSION AND FUTURE WORKS

9.1. Introduction

The focus of this dissertation was to develop 3-D analytic and finite element models of the eddy current distribution in a conductive medium. The conclusion of the research work is presented in section 9.2. The contributions of this research are outlined in section 9.3. Section 9.4 describes the suggestions and recommendations for the future direction of this research.

9.2. Conclusion

A thorough analytic and finite element treatment of the eddy current distribution in a conductive medium has been presented in this dissertation which can be useful in a number of applications such as magnetic levitated vehicle, eddy current testing and eddy current brakes. The developed models are generic and thus can be applicable to any kind of magnetic source.

The static magnetic field of the magnetic source, which is a Halbach rotor in this research, has been modeled using fictitious magnetic charge sheet. The magnetic charge based source modeling technique helps reduce the field computation time and results in faster finite element and analytic based models. The finite element models developed in this dissertation are shown to be faster compared to the previously presented finite element models using current sheet based source modeling technique. A detailed analytic

treatment of the eddy current distribution, eddy current forces, torque and joule loss in a conductive medium has been presented in this dissertation. Different analytic formulations have been used to derive models of varying level of computational cost. The presented analytic models have been compared with two experimental setups and satisfactory performance has been achieved. The key points of the developed Comsol based steady state and transient FEA models have been summarized in Table 9.1. A comparison of the presented analytic steady state models is presented in Table 9.2.

Table 9.1: Summarization of the developed steady state and transient FEA models

Model assumptions	Major advantage	Computation time
<ul style="list-style-type: none"> • Conductive plate is linear, simply connected and homogenous • Conductive plate has constant conductivity and is non-magnetic • The source has uniform motion • Frequency is low 	<ul style="list-style-type: none"> • As the models do not physically model the magnetic source, the problem domain consists only of the conductive plate in air region. This leads to reduced simulation time. • The use of magnetic charge based source field computation also reduces the simulation time. 	<ul style="list-style-type: none"> • For the transient model: 54 min. • For the steady state model: 1 min 40s.

Table 9.2: Comparison of the proposed analytic steady state models

Model type	Model dimension	Calculation time [s]	Drawback(s)	Advantage(s)
SOVP (only TE potential)	Infinitely long and wide; finite thickness	0.038	Cannot produce correct lateral force. Not accurate in the presence of lateral offset.	Computationally fastest of all the proposed models
Two component MVP	Infinitely long; finite width; finite but small thickness	0.544	Error in lateral force in the presence of lateral offset; cannot model plate of arbitrary thickness	Computationally fast but inferior to the SOVP model with only TE potential.
Three component MVP	Infinitely long; finite width; finite arbitrary thickness	6	Error in lateral force in the presence of lateral offset	Can model plate of arbitrary thickness; computationally fast but inferior to 2-component and SOVP model with TE potential
SOVP with TE and TM potentials	Infinitely long; finite width; finite arbitrary thickness	32	Computation performance is inferior to the SOVP with only TE potential, 2 and 3-component MVP models.	Most accurate of the presented analytic models with and without lateral offset of the source; computationally faster than FEA models

9.3. Research Contributions

The major technical achievements and contributions of this research are:

1. A computationally efficient approach for the computation of the 3-D magnetic field due to arbitrary magnetic source has been presented using novel magnetic charge sheet concept and integral solution approach.
2. Computationally efficient boundary coupled A - ϕ finite element models have been developed to study the interaction between a moving magnetic source and conductive non-magnetic medium in transient and steady state conditions.
3. A fast 3-D analytic model based on only the TE potential of the second order vector potential has been developed to model the eddy current distribution in a conductive medium due to the motion of an arbitrary magnetic source. The conductive medium is assumed to have infinitely large length, width and small but finite thickness. The linear motion of the source in x , y and z -directions as well as its rotational motion has been considered for dynamic modeling. Also, the electromagnetic stiffness and damping coefficients have been derived analytically.
4. Two 3-D analytic models based on the magnetic vector potential have been proposed to model the field distributions in a conductive medium of infinite length, finite width and thickness. The only limitation of this model is its failure to model the lateral force when the source is laterally offset above the conductive plate, thus this is an approximate model. The model considers the linear motion of the source in the x and y -directions as well as its rotational motion.

5. An accurate treatment of the eddy current fields and forces including the edge effect of the conductive plate has been presented using the second order vector potential and truncated region eigenfunction expansion approach. Only rotational motion of the magnetic source has been considered in the model. However, its expansion to include the translational velocity is straightforward and has not been performed due to its computational burden.
6. The eddy current lift force, torque and power transfer calculated using the analytic models have been compared with two experimental setups. Satisfactory performance has been achieved.

The minor technical contributions of this research are

1. Segmented Halbach PM and surface mount PM rotors have been modeled using Comsol FEA software in 2-D and 3-D. These models are used to validate the magnetic charge based source modeling technique.
2. Finite element models have been developed in Magsoft flux software to model the eddy current field distribution in a conductive medium due to rotational motion of a segmented Halbach PM rotor.
3. Code has been written to convert the output of two-dimensional DFT into a double Fourier series which is used in source field modeling throughout the dissertation.

9.4. Future Research Works

The following directions of future research work have been identified:

1. The electromagnetic stiffness and damping coefficients have been derived analytically in this dissertation. However, the experimental verification of the

analysis has not been provided. Hence, experiments should be conducted to measure the damping and stiffness terms and verify the presented analytic results.

2. Work in underway for an EDW maglev vehicle on a flat aluminum guideway as shown in Figure 9.1. The mechanical dynamics of the vehicle needs to be considered in order to achieve the desired travel performance of the vehicle.

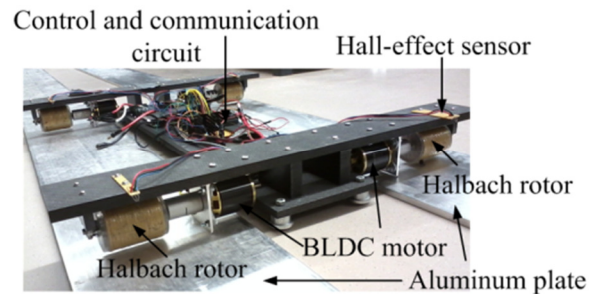


Figure 9.1. Experimental maglev vehicle with four Halbach rotors and flat aluminum guideway

BIBLIOGRAPHY

- [1] <http://www.census.gov/population/www/popclockus.html>.
- [2] <http://esa.un.org/unpd/wpp/unpp/p2k0data.asp>.
- [3] <http://www.forbes.com/sites/jeffmcmahon/2012/03/15/u-s-poised-for-passenger-rail-boom/>.
- [4] A. J. Severinsky and T. Louckes, "Hybrid Vehicles," US Patent, 2007.
- [5] <http://nissannews.com/en-US/nissan/usa/channels/us-united-states-nissan-models-leaf/releases/nissan-leaf-backs-into-the-future>.
- [6] http://www.greencarreports.com/news/1077444_june-plug-in-electric-car-sales-volt-stays-strong-leaf-low.
- [7] A. J. Severinsky, "Hybrid electric vehicle," US Patent, 1994.
- [8] <http://www.hybridcars.com/history-of-hybrid-vehicles/>.
- [9] P. J. Hills, "What is induced traffic?," *Transportation*, vol. 23, pp. 5-16, 1996.
- [10] M. Hansen and Y. Huang, "Road supply and traffic in California urban areas," *Transportation Research Part A Policy and Practice*, vol. 31, pp. 205-218, 1997.
- [11] "An Analysis of the Relationship Between Highway Expansion and Congestion in Metropolitan Areas," Surface Transportation Policy Project, Washington, DC 1998.
- [12] R. Cervero, *Road Expansion, Urban Growth and Induced Travel: a Path Analysis*.
- [13] J. Bird, "An Investigation into the use of Electrodynamical Wheels for High Speed Ground Transportation," Ph.D, Electrical Engineering, University of Wisconsin - Madison, Madison, 2007.
- [14] N. Paudel, "Dynamic suspension modeling of an eddy current device: an application to maglev," Ph.D, Electrical and Computer Engineering, University of North Carolina at Charlotte, Charlotte, 2012.
- [15] B. V. Jayawant, "Electromagnetic suspension and levitation," *IEE Proceedings A Physical Science, Measurement and Instrumentation, Management and Education - Reviews*, vol. 129, pp. 549-581, 1982.

- [16] B. V. Jayawant, "Review Lecture. Electromagnetic Suspension and Levitation Techniques " *Proceedings of the Royal Society A*, vol. 416, pp. 245-320, 1988.
- [17] D. L. Atherton and A. R. Eastham, "Limitations of levitation by iron-cored electromagnets," *IEEE Transactions on Magnetics*, vol. 10, pp. 410-412, 1974.
- [18] R. H. Borcherts, "Mathematical Analysis of 'Permanent' Magnet Suspension Systems," *Journal of Applied Physics*, vol. 42, pp. 1528-1529, 1971.
- [19] <http://www.maglev2000.com>.
- [20] D. L. Atherton, A. R. Eastham, O. Boon-Teck, and O. P. Jain, "Forces and moments for electrodynamic levitation systems--Large-scale test results and theory," *IEEE Transactions on Magnetics*, vol. 14, pp. 59-68, 1978.
- [21] D. L. Atherton, A. R. Eastham, C. Fombrun, and M. Chong, "Eddy current distribution and lift force for finite maglev strips," *Canadian Journal of Physics*, vol. 52, pp. 1203-1208, 1974.
- [22] <http://www.lanl.gov/orgs/mpa/stc/train.shtml>.
- [23] R. Goodall, "The theory of electromagnetic levitation," *Physics in Technology*, vol. 16, 1985.
- [24] G. R. Polgreen, "The ideal magnet-fully controllable permanent magnets for power and transport," *Electronics and Power*, vol. 17, pp. 31-34, 1971.
- [25] D. Atherton, "Maglev using permanent magnets," *Magnetics, IEEE Transactions on*, vol. 16, pp. 146-148, 1980.
- [26] W. J. Mayer and J. Meins, "THE USE OF ELECTROMAGNETS AND PERMANENT MAGNETS IN MAGNETIC LEVITATION TECHNOLOGY," *J. Phys. Colloques* vol. 45, pp. 739-745, 1984.
- [27] G. R. Polgreen, "Magnetic Suspension," in *Proceedings of the Institution of Mechanical Engineers*, 1966.
- [28] S. Earnshaw, "On the nature of the molecular forces which regulate the constitution of the luminiferous ether," *Transactions of the Cambridge Philosophical Society*, vol. 7, pp. 97-112, 1842.
- [29] J. R. Powell and G. R. Danby, "High-speed Transport by Magnetically Suspended Trains," presented at the ASME Winter Annual Meeting, New York, 1966.

- [30] J. R. Powell and G. T. Danby, "Magnetically Suspended Trains: The Application of Superconductors to High Speed Transport," *Cryogenics and Industrial Gases*, vol. 4, p. 19, 1969.
- [31] J. Powell and G. Danby, "Electromagnetic inductive suspension and stabilization system for a ground vehicle," US Patent, 1969.
- [32] G. T. Danby and J. R. Powell, "Levitation with null flux coils," US Patent, 1969.
- [33] J. R. Powell and G. T. Danby, "Magnetic suspension for levitated tracked vehicles," *Cryogenics*, vol. 11, pp. 192-204, 1971.
- [34] K. R. Davey, "Designing with null flux coils," *IEEE Transactions on Magnetics*, vol. 33, pp. 4327-4334, 1997.
- [35] J. Powell and G. Danby. (2003) Maglev: The New Mode of Transport for the 21st Century. *21st Century Science & Technology Magazine*.
- [36] B. Graeminger, "Electromagnetic Suspension Devices," U.K Patent, 1912.
- [37] Magnetic Levitation (Maglev) Technologies. *Japan Railway & Transport Review* 61-67.
- [38] S. Suzuki, M. Kawashima, Y. Hosoda, and T. Tanida, "HSST-03 system," *IEEE Transactions on Magnetics*, vol. 20, pp. 1675-1677, 1984.
- [39] J. E. Paddison, H. Ohsaki, and E. Masada, "Control strategies for Maglev electromagnetic suspension bogies," in *Proceedings of the 35th IEEE Conference on Decision and Control*, 1996., 1996, pp. 2796-2797 vol.3.
- [40] High-Tech for "Flying on the Ground". *Transrapid International*.
- [41] J. Meins, L. Miller, and W. J. Mayer, "The high speed Maglev transport system TRANSRAPID," *IEEE Transactions on Magnetics*, vol. 24, pp. 808-811, 1988.
- [42] <http://www.discovery.org/scripts/viewDB/filesDB-download.php?command=download&id=877>.
- [43] J. R. Powell and G. Danby, "A 300-mph Magnetically Suspended Train," *Mechanical Engineering*, vol. 89, pp. 30-35, Nov 1967.
- [44] J. Powell and G. Danby, "The Linear Synchronous Motor and High Speed Transport," in *6th Intersociety Energy Conversion Eng. Conference*, Boston, MA, 1971, pp. 118-131.

- [45] P. E. Burke, S. Kunts, and G. R. Slemon, "A dual linear synchronous motor for Maglev vehicles," *IEEE Transactions on Magnetics*, vol. 13, pp. 1415-1417, 1977.
- [46] R. D. Thornton, T. Clark, and B. Perreault, "Linear synchronous motor propulsion of small transit vehicles," in *Rail Conference, 2004. Proceedings of the 2004 ASME/IEEE Joint*, 2004, pp. 101-107.
- [47] M. S. Hosseini and S. Vaez-Zadeh, "Modeling and Analysis of Linear Synchronous Motors in High-Speed Maglev Vehicles," *IEEE Transactions on Magnetics*, vol. 46, pp. 2656-2664, 2010.
- [48] E. Levi, "Linear synchronous motors for high-speed ground transportation," *IEEE Transactions on Magnetics*, vol. 9, pp. 242-248, 1973.
- [49] D. L. Atherton, "Study Of Magnetic Levitation and Linear Synchronous Motor Propulsion," Canadian Institute of Guided Ground Transport, Queens University, Ontario, Canada, 1972.
- [50] J. F. Gieras, Z. J. Piech, and B. Tomczuk, *Linear Synchronous Motors: Transportation and Automation Systems*: CRC Press; 2 edition 2011.
- [51] A. A. Kuijpers, C. Nemlioglu, F. Sahin, A. Verdel, J. C. Compter, and E. A. Lomonova, "Force analysis of linear induction motor for magnetic levitation system," in *14th International Power Electronics and Motion Control Conference (EPE/PEMC), 2010* 2010, pp. S3-17-S3-20.
- [52] K. Davey, "Pulsed linear induction motors for Maglev propulsion," *IEEE Transactions on Magnetics*, vol. 36, pp. 3791-3797, 2000.
- [53] L. Shaoke, W. Dengwu, and C. Guirong, "Speed estimate for maglev train based on linear induction motor," in *International Conference on Electrical Machines and Systems, 2008. ICEMS 2008.*, 2008, pp. 855-857.
- [54] S. Yamamura, *Theory of Linear Induction Motor*: John Wiley & Sons Inc May 1973.
- [55] S. Davis and S. Dregel, "Transportation Energy Data Book," O. R. N. L. Center for Transportation Analysis, Ed., 25 ed, 2006.
- [56] J. Powell and G. Danby, "Energy Efficiency and Economics of Maglev Transport," in *Advanced Energy Conference*, Long Island, NY, 2008.
- [57] I. Boldea, A. Trica, G. Papusoiu, and S. A. Nasar, "Field tests on a MAGLEV with passive guideway linear inductor motor transportation system," *IEEE Transactions on Vehicular Technology*, vol. 37, pp. 213-219, 1988.

- [58] J. K. Kostko, "Self-Excited Synchronous Motors," *Transactions of the American Institute of Electrical Engineers*, vol. XLIV, pp. 447-460, 1925.
- [59] A. Cassat and M. Jufer, "MAGLEV projects technology aspects and choices," *IEEE Transactions on Applied Superconductivity*, vol. 12, pp. 915-925, 2002.
- [60] I. Boldea, "Magnibus, the Romanian linear inductor (synchronous) motor (passive guideway) maglev," *International Conference on Maglev Transport Now and for the Future.*, 1984.
- [61] J. A. Ross, "ROMAG transportation system," *Proceedings of the IEEE*, vol. 61, pp. 617-620, 1973.
- [62] J. F. Eastham and E. R. Laithwaite, "Linear induction motors as 'electromagnetic rivers'," *Electrical Engineers, Proceedings of the Institution of*, vol. 121, pp. 1099-1108, 1974.
- [63] E. R. Laithwaite, "Linear propulsion by electromagnetic 'river'," *Production Engineer*, vol. 53, pp. 219-223, 1974.
- [64] L. C. Davis and R. H. Borcherts, "Superconducting paddle wheels, screws, and other propulsion units for high-speed ground transportation," *Journal of Applied Physics*, vol. 44, pp. 3294-3299, 1973.
- [65] N. Fujii, G. Hayashi, and Y. Sakamoto, "Characteristics of magnetic lift, propulsion and guidance by using magnet wheels with rotating permanent magnets," in *IEEE Industry Applications Conference, 2000.* , 2000, pp. 257-262 vol.1.
- [66] N. Fujii, M. Chida, and K. Ogawa, "Three dimensional force of magnet wheel with revolving permanent magnets," *IEEE Transactions on Magnetics*, vol. 33, pp. 4221-4223, 1997.
- [67] N. Fuji, K. Ogawa, and T. Matsumoto, "Revolving Magnet Wheels with Permanent Magnets," *Electrical Engineering in Japan*, vol. 116, 1996.
- [68] N. Fujii, K. Naotsuka, K. Ogawa, and T. Matsumoto, "Basic characteristics of magnet wheels with rotating permanent magnets," in *Industry Applications Society Annual Meeting, 1994., Conference Record of the 1994 IEEE*, 1994, pp. 203-209 vol.1.
- [69] N. Fujii, S. Nonaka, and G. Hayashi, "Design of magnet wheel integrated own drive," *IEEE Transactions on Magnetics*, vol. 35, pp. 4013-4015, 1999.

- [70] J. Bird and T. A. Lipo, "An electrodynamic wheel: an integrated propulsion and levitation machine," in *IEEE International Electric Machines and Drives Conference, 2003. IEMDC'03.*, 2003, pp. 1410-1416 vol.3.
- [71] D. Bobba, "3-D Analytic based modeling of an electrodynamic wheel and the performance of electrodynamic wheels in series for urban transportation," Master of Science, Electrical Engineering, University of North Carolina at Charlotte, Charlotte, 2011.
- [72] B. T. Ooi and A. R. Eastham, "Transverse edge effects of sheet guideways in magnetic levitation," *IEEE Transactions on Power Apparatus and Systems*, vol. 94, pp. 72-80, 1975.
- [73] J. Bird and T. A. Lipo, "Modeling the 3D Rotational and Translational Motion of Magnets over a Conducting Guideway using a Combined Field and Lumped-Parameter Model," in *IEEE International Magnetics Conference, 2006. INTERMAG 2006.*, 2006, pp. 502-502.
- [74] J. Bird and T. A. Lipo, "A 3-D Magnetic Charge Finite-Element Model of an Electrodynamic Wheel," *IEEE Transactions on Magnetics*, vol. 44, pp. 253-265, 2008.
- [75] J. Bird and T. A. Lipo, "Modeling the 3-D Rotational and Translational Motion of a Halbach Rotor Above a Split-Sheet Guideway," *IEEE Transactions on Magnetics*, vol. 45, pp. 3233-3242, 2009.
- [76] S. Paul, D. Bobba, N. Paudel, and J. Z. Bird, "Source Field Modeling in Air Using Magnetic Charge Sheets," *IEEE Transactions on Magnetics*, vol. 48, pp. 3879-3882, 2012.
- [77] J. Bird and T. A. Lipo, "Characteristics of an Electrodynamic Wheel Using a 2-D Steady-State Model," *IEEE Transactions on Magnetics*, vol. 43, pp. 3395-3405, 2007.
- [78] J. Bird and T. A. Lipo, "Calculating the Forces Created by an Electrodynamic Wheel Using a 2-D Steady-State Finite-Element Method," *IEEE Transactions on Magnetics*, vol. 44, pp. 365-372, 2008.
- [79] N. Paudel and J. Z. Bird, "General 2-D Steady-State Force and Power Equations for a Traveling Time-Varying Magnetic Source Above a Conductive Plate," *IEEE Transactions on Magnetics*, vol. 48, pp. 95-100, 2012.
- [80] N. Paudel, J. Bird, S. Paul, and D. Bobba, "A transient 2D model of an electrodynamic wheel moving above a conductive guideway," in *IEEE International Electric Machines & Drives Conference (IEMDC), 2011*, 2011, pp. 545-550.

- [81] N. Paudel and J. Z. Bird, "Modeling the dynamic electromechanical suspension behaviour of an electrodynamic eddy current maglev device," *Progress In Electromagnetics Research B*, vol. 49, pp. 1-30, 2013.
- [82] N. Paudel, J. Z. Bird, S. Paul, and D. Bobba, "Modeling the dynamic suspension behavior of an eddy current device," in *IEEE Energy Conversion Congress and Exposition (ECCE), 2011*, 2011, pp. 1692-1699.
- [83] D. Chen, K. R. Shao, J. Sheng, and W. Yan, "Eddy current interaction with a thin-opening crack in a plate conductor," *IEEE Transactions on Magnetics*, vol. 36, pp. 1745-1749, 2000.
- [84] J. R. Bowler, L. D. Sabbagh, and H. A. Sabbagh, "Eddy-current probe impedance due to a surface slot in a conductor," *IEEE Transactions on Magnetics*, vol. 26, pp. 889-892, 1990.
- [85] M. Zec, R. Uhlig, M. Ziolkowski, and H. Brauer, "Finite Element Analysis of Non-Destructive Testing Eddy Current Problems with Moving Parts," *accepted for publication in IEEE Transactions on Magnetics*, 2013.
- [86] M. R. Weinberger, "Drag Force of an Eddy Current Damper," *IEEE Transactions on Aerospace and Electronic Systems*, vol. AES-13, pp. 197-200, 1977.
- [87] Z. Jun, D. Zigang, Z. Ya, W. Wei, W. Suyu, and W. Jiasu, "Performance Improvement of High Temperature Superconducting Maglev System by Eddy Current Damper," *IEEE Transactions on Applied Superconductivity* vol. 19, pp. 2148-2151, 2009.
- [88] Y. Zhang, H. Zhou, and H.-z. Sun, "Research of the orthoscopic permanent magnet eddy current damper in magnetic stage," in *2010 International Conference on Computer Application and System Modeling (ICCASM)*, 2010, pp. V14-354-V14-356.
- [89] S. E. Gay and M. Ehsani, "Analysis and experimental testing of a permanent magnet eddy-current brake," in *2005 IEEE Conference Vehicle Power and Propulsion*, 2005, p. 10 pp.
- [90] C. Jang-Young and J. Seok-Myeong, "Analytical magnetic torque calculations and experimental testing of radial flux permanent magnet-type eddy current brakes," *Journal of Applied Physics*, vol. 111, pp. 07E712-07E712-3, 2012.
- [91] D. Schieber, "Optimal dimensions of rectangular electromagnet for braking purposes," *IEEE Transactions on Magnetics*, vol. 11, pp. 948-952, 1975.

- [92] O. Cugat, J. Delamare, and G. Reyne, "Magnetic micro-actuators and systems (MAGMAS)," *IEEE Transactions on Magnetics*, vol. 39, pp. 3607-3612, 2003.
- [93] H. Chetouani, C. Jeandey, V. Haguët, H. Rostaing, C. Dieppedale, and G. Reyne, "Diamagnetic Levitation With Permanent Magnets for Contactless Guiding and Trapping of Microdroplets and Particles in Air and Liquids," *IEEE Transactions on Magnetics*, vol. 42, pp. 3557-3559, 2006.
- [94] P. Elies and G. Lemarquand, "Analytical optimization of the torque of a permanent-magnet coaxial synchronous coupling," *IEEE Transactions on Magnetics*, vol. 34, pp. 2267-2273, 1998.
- [95] L. Wang Yu, K. Liu Pin, J. Wu, and H. Ding, "Near-Optimal Design and 3-D Finite Element Analysis of Multiple Sets of Radial Magnetic Couplings," *IEEE Transactions on Magnetics*, vol. 44, pp. 4747-4753, 2008.
- [96] Y. D. Yao, D. R. Huang, C. C. Hsieh, D. Y. Chiang, S. J. Wang, and T. F. Ying, "The radial magnetic coupling studies of perpendicular magnetic gears," *IEEE Transactions on Magnetics*, vol. 32, pp. 5061-5063, 1996.
- [97] Y. Yeong-Der, G. Chiou, x, Ji, D.-R. Huang, and W. Shyh-Jier, "Theoretical computations for the torque of magnetic coupling," *IEEE Transactions on Magnetics*, vol. 31, pp. 1881-1884, 1995.
- [98] H. Jiang, R. Shuttleworth, B. A. T. Al Zahawi, and A. Power, "Variable speed latching magnetic actuator for a vacuum switch," in *Eighth International Conference on (Conf. Publ. No. 444) Electrical Machines and Drives, 1997* 1997, pp. 105-108.
- [99] S. Fu, X. Tang, and Y. Wu, "Analysis of magnetic latching mechanism in the application of bi-stable MEMS switches," in *5th IEEE International Conference on Nano/Micro Engineered and Molecular Systems (NEMS), 2010*, 2010, pp. 1044-1047.
- [100] M. Boukallel, E. Piat, and J. Abadie, "Passive diamagnetic levitation: theoretical foundations and application to the design of a micro-nano force sensor," in *IEEE/RSJ International Conference on Intelligent Robots and Systems, 2003. (IROS 2003). Proceedings. 2003*, 2003, pp. 1062-1067 vol.2.
- [101] G. Lemarquand and V. Lemarquand, "Annular magnet position sensor," *IEEE Transactions on Magnetics*, vol. 26, pp. 2041-2043, 1990.
- [102] G. Lemarquand, "Variable magnetic circuit torque sensor," *Journal of Applied Physics*, vol. 70, pp. 6630-6632, 1991.

- [103] R. Ravaut, G. Lemarquand, V. Lemarquand, and C. Depollier, "Analytical Calculation of the Magnetic Field Created by Permanent-Magnet Rings," *IEEE Transactions on Magnetics*, vol. 44, pp. 1982-1989, 2008.
- [104] E. P. Furlani, S. Reznik, and A. Kroll, "A three-dimensional field solution for radially polarized cylinders," *IEEE Transactions on Magnetics*, vol. 31, pp. 844-851, 1995.
- [105] F. Bancel and G. Lemarquand, "Three-dimensional analytical optimization of permanent magnets alternated structure," *IEEE Transactions on Magnetics*, vol. 34, pp. 242-247, 1998.
- [106] H. L. Rakotoarison, J. P. Yonnet, and B. Delinchant, "Using Coulombian Approach for Modeling Scalar Potential and Magnetic Field of a Permanent Magnet With Radial Polarization," *IEEE Transactions on Magnetics*, vol. 43, pp. 1261-1264, 2007.
- [107] N. H. Malik, "A review of the charge simulation method and its applications," *Electrical Insulation, IEEE Transactions on*, vol. 24, pp. 3-20, 1989.
- [108] O. M. Kwon, C. Surussavadee, M. V. K. Chari, S. Salon, and K. Sivasubramaniam, "Analysis of the far field of permanent-magnet motors and effects of geometric asymmetries and unbalance in magnet design," *IEEE Transactions on Magnetics*, vol. 40, pp. 435-442, 2004.
- [109] J. P. Selvaggi, S. Salon, O. M. Kwon, and M. V. K. Chari, "Calculating the external magnetic field from permanent magnets in permanent-magnet motors-an alternative method," *IEEE Transactions on Magnetics*, vol. 40, pp. 3278-3285, 2004.
- [110] J. P. Selvaggi, S. J. Salon, and M. V. K. Chari, "Employing Toroidal Harmonics for Computing the Magnetic Field From Axially Magnetized Multipole Cylinders," *IEEE Transactions on Magnetics*, vol. 46, pp. 3715-3723, 2010.
- [111] J. Selvaggi, S. Salon, O. M. Kwon, and M. V. K. Chari, "Computation of the External Magnetic Field, Near-Field or Far-Field, from a Circular Cylindrical Magnetic Source using Toroidal Functions," in *12th Biennial IEEE Conference on Electromagnetic Field Computation*, 2006, pp. 184-184.
- [112] J. A. Stratton, *Electromagnetic Theory* McGraw-Hill Book Company, 1941.
- [113] C. A. Balanis, *Advanced Engineering Electromagnetics*: John Wiley & Sons, 1989.
- [114] J. D. Jackson, *Classical Electrodynamics*, 3 ed. New York: Wiley, 1999.

- [115] D. J. Griffiths, *Introduction to Electrodynamics*. New Jersey: Prentice Hall, 1999.
- [116] Z. P. Xia, Z. Q. Zhu, and D. Howe, "Analytical magnetic field analysis of Halbach magnetized permanent-magnet machines," *IEEE Transactions on Magnetics*, vol. 40, pp. 1864-1872, 2004.
- [117] T. P. Theodoulidis and J. R. Bowler, "Eddy current coil interaction with a right-angled conductive wedge," *Proceedings of the Royal Society A: Mathematical, Physical and Engineering Science*, vol. 461, pp. 3123-3139, October 8, 2005 2005.
- [118] J. R. Bowler and T. P. Theodoulidis, "Coil impedance variation due to induced current at the edge of a conductive plate," *Journal of Physics D: Applied Physics*, vol. 39, pp. 2862-2868, 2006.
- [119] S. J. Salon, R. Palma, and C. C. Hwang, "Dynamic modeling of an induction motor connected to an adjustable speed drive," *IEEE Transactions on Magnetics*, vol. 25, pp. 3061-3063, 1989.
- [120] B. Aldefeld, "A numerical solution of transient nonlinear eddy-current problems including moving iron parts," *IEEE Transactions on Magnetics*, vol. 14, pp. 371-373, 1978.
- [121] B. Ancelle, J. Coulomb, P. Masse, G. Meunier, and J. C. Sabonnadiere, "Computer methods for electrical and magnetic devices designed by field analysis," *IEEE Transactions on Magnetics*, vol. 15, pp. 1671-1673, 1979.
- [122] A. Foggia, J. C. Sabonnadiere, and P. Silvester, "Finite element solution of saturated travelling magnetic field problems," *IEEE Transactions on Power Apparatus and Systems*, vol. 94, pp. 866-871, 1975.
- [123] S. Ratnajeevan and H. Hoole, "Rotor motion in the dynamic finite element analysis of rotating electrical machinery," *IEEE Transactions on Magnetics*, vol. 21, pp. 2292-2295, 1985.
- [124] C. W. Trowbridge and J. K. Sykulski, "Some key developments in computational electromagnetics and their attribution," *IEEE Transactions on Magnetics*, vol. 42, pp. 503-508, 2006.
- [125] A. Abdel-Razek, J. L. Coulomb, M. Feliachi, and J. C. Sabonnadiere, "Conception of an air-gap element for the dynamic analysis of the electromagnetic field in electric machines," *IEEE Transactions on Magnetics*, vol. 18, pp. 655-659, 1982.

- [126] Z. J. Cendes, D. Shenton, and H. Shahnasser, "Magnetic field computation using Delaunay triangulation and complementary finite element methods," *IEEE Transactions on Magnetics*, vol. 19, pp. 2551-2554, 1983.
- [127] A. Demenko, "Movement simulation in finite element analysis of electric machine dynamics," *IEEE Transactions on Magnetics*, vol. 32, pp. 1553-1556, 1996.
- [128] D. Rodger, H. C. Lai, and P. J. Leonard, "Coupled elements for problems involving movement [switched reluctance motor]," *IEEE Transactions on Magnetics*, vol. 26, pp. 548-550, 1990.
- [129] I. A. Tsukerman, "Overlapping finite elements for problems with movement," *IEEE Transactions on Magnetics*, vol. 28, pp. 2247-2249, 1992.
- [130] H. C. Lai, D. Rodger, and P. J. Leonard, "A finite element method for problems with moving parts," in *International Conference on Computation in Electromagnetics, 1991.*, 1991, pp. 211-213.
- [131] C. Golovanov, J. L. Coulomb, Y. Marechal, and G. Meunier, "3D mesh connection techniques applied to movement simulation," *IEEE Transactions on Magnetics*, vol. 34, pp. 3359-3362, 1998.
- [132] E. Kreyszig, *Advanced Engineering Mathematics*, 9 ed.: John Wiley & Sons., 2006.
- [133] M. Sadiku, *Numerical Techniques in Electromagnetics*: CRC Press, 2010.
- [134] W. A. Strauss, *Partial Differential Equations: An Introduction*: Wiley, 2007.
- [135] "User's Guide," Comsol Multiphysics, v 3.5a, pp. 426-435.
- [136] D. Rodger and J. Eastham, "A formulation for low frequency eddy current solutions," *IEEE Transactions on Magnetics*, vol. 19, pp. 2443-2446, 1983.
- [137] S. Williamson and E. K. C. Chan, "Three-dimensional finite-element formulation for problems involving time-varying fields, relative motion, and magnetic saturation," *IEE Proceedings A Science, Measurement and Technology*, vol. 140, pp. 121-130, 1993.
- [138] O. Zienkiewicz, J. Lyness, and D. Owen, "Three-dimensional magnetic field determination using a scalar potential--A finite element solution," *IEEE Transactions on Magnetics*, vol. 13, pp. 1649-1656, 1977.

- [139] D. Rodger, T. Karaguler, and P. J. Leonard, "A formulation for 3D moving conductor eddy current problems," *IEEE Transactions on Magnetics*, vol. 25, pp. 4147-4149, 1989.
- [140] O. Biro and K. Preis, "On the use of the magnetic vector potential in the finite-element analysis of three-dimensional eddy currents," *IEEE Transactions on Magnetics*, vol. 25, pp. 3145-3159, 1989.
- [141] T. P. Theodoulidis and E. E. Kriezis, *Eddy Current Canonical Problems (with Applications to Nondestructive Evaluation)*, 1st ed.: Tech Science Press, 2006.
- [142] L. N. Trefethen and D. Bau III, *Numerical Linear Algebra*: SIAM: Society for Industrial and Applied Mathematics, 1997.
- [143] H. Knoepfel, *Magnetic Fields: A Comprehensive Theoretical Treatise for Practical Use*: John Wiley & Sons, 2000.
- [144] K. J. W. Pluk, B. L. J. Gysen, J. L. G. Janssen, E. A. Lomonova, and J. W. Jansen, "Modeling of a finite, rectangular, conducting plate in an eddy current damper," in *XXth International Conference on Electrical Machines (ICEM), 2012*, 2012, pp. 2846-2851.
- [145] S. E. Gay and M. Ehsani, "Parametric analysis of eddy-current brake performance by 3-D finite-element analysis," *IEEE Transactions on Magnetics*, vol. 42, pp. 319-328, 2006.
- [146] J. D. Edwards, B. V. Jayawant, W. R. C. Dawson, and D. T. Wright, "Permanent-magnet linear eddy-current brake with a nonmagnetic reaction plate," *IEE Proceedings - Electric Power Applications*, vol. 146, pp. 627-631, 1999.
- [147] Y. Um, S. Torii, D. Ebihara, I. Sanjo, and Y. Tani, "The study on the measuring method of the eddy current on the eddy current brake," in *Ninth International Conference on (Conf. Publ. No. 468) Electrical Machines and Drives, 1999*, 1999, pp. 228-231.
- [148] T. Theodoulidis and J. R. Bowler, "Eddy-current interaction of a long coil with a slot in a conductive plate," *IEEE Transactions on Magnetics*, vol. 41, pp. 1238-1247, 2005.
- [149] A. Skarlatos and T. Theodoulidis, "Solution to the eddy-current induction problem in a conducting half-space with a vertical cylindrical borehole," *Proceedings of the Royal Society A*, vol. 468, pp. 1758-1777, 2012.
- [150] T. Itaya, K. Ishida, A. Tanaka, N. Takehira, and T. Miki, "Eddy current distribution for a rectangular coil arranged parallel to a moving conductor slab," *IET Science, Measurement & Technology*, vol. 6, pp. 43-51, 2012.

- [151] J. R. Bowler, T. P. Theodoulidis, and N. Poulakis, "Eddy Current Probe Signals Due to a Crack at a Right-Angled Corner," *IEEE Transactions on Magnetics*, vol. 48, pp. 4735-4746, 2012.
- [152] J. R. Bowler and N. Harfield, "Evaluation of probe impedance due to thin-skin eddy-current interaction with surface cracks," *IEEE Transactions on Magnetics*, vol. 34, pp. 515-523, 1998.
- [153] M. Chari, A. Konrad, M. Palmo, and J. D'Angelo, "Three-dimensional vector potential analysis for machine field problems," *IEEE Transactions on Magnetics*, vol. 18, pp. 436-446, 1982.
- [154] C. Biddlecombe, E. Heighway, J. Simkin, and C. Trowbridge, "Methods for eddy current computation in three dimensions," *IEEE Transactions on Magnetics*, vol. 18, pp. 492-497, 1982.
- [155] T. Morisue, "Magnetic vector potential and electric scalar potential in three-dimensional eddy current problem," *IEEE Transactions on Magnetics*, vol. 18, pp. 531-535, 1982.
- [156] W. Renhart, H. Stogner, and K. Preis, "Calculation of 3D eddy current problems by finite element method using either an electric or a magnetic vector potential," *IEEE Transactions on Magnetics*, vol. 24, pp. 122-125, 1988.
- [157] C. Emson and J. Simkin, "An optimal method for 3-D eddy currents," *IEEE Transactions on Magnetics*, vol. 19, pp. 2450-2452, 1983.
- [158] R. Pillsbury, Jr., "A three dimensional eddy current formulation using two potentials: The magnetic vector potential and total magnetic scalar potential," *IEEE Transactions on Magnetics*, vol. 19, pp. 2284-2287, 1983.
- [159] O. Biro and K. Preis, "Finite element analysis of 3-D eddy currents," *IEEE Transactions on Magnetics*, vol. 26, pp. 418-423, 1990.
- [160] O. Biro, K. Preis, and W. Renhart, "Finite element analysis of 3D multiply connected eddy current problems," *IEEE Transactions on Magnetics*, vol. 25, pp. 4009-4011, 1989.
- [161] T. Morisue, "A few formulation of the magnetic vector potential method in 3-D multiply connected regions," *IEEE Transactions on Magnetics*, vol. 24, pp. 110-113, 1988.
- [162] P. J. Leonard and D. Rodger, "Finite element scheme for transient 3D eddy currents," *IEEE Transactions on Magnetics*, vol. 24, pp. 90-93, 1988.

- [163] A. Kameari, "Three-dimensional eddy current calculation using finite element method with A-V in conductor and Ω in vacuum," *IEEE Transactions on Magnetics*, vol. 24, pp. 118-121, 1988.
- [164] D. Rodger and J. F. Eastham, "Multiply connected regions in the A - ψ three-dimensional eddy-current formulation," *IEE Proceedings A Physical Science, Measurement and Instrumentation, Management and Education - Reviews*, vol. 134, pp. 58-66, 1987.
- [165] L. Hannakam, *Elektrotech. Z.*, 1965.
- [166] C. V. Dodd and W. E. Deeds, "Analytical Solutions to Eddy-Current Probe-Coil Problems," *Journal of Applied Physics*, vol. 39, pp. 2829-2838, 1968.
- [167] J. R. Reitz, "Forces on Moving Magnets due to Eddy Currents " *Journal of Applied Physics*, vol. 41, 1970.
- [168] R. E. Beissner and M. J. Sablik, "Theory of eddy currents induced by a nonsymmetric coil above a conducting half-space " *Journal of Applied Physics* vol. 56, 1984.
- [169] S. Panas and E. E. Kriezis, "Eddy current distribution due to a rectangular current frame moving above a conducting slab," *Archiv für Elektrotechnik*, vol. 69, pp. 185-191, 1986/05/01 1986.
- [170] V. Subba Rao, "Perturbation technique for fields and forces due to current filaments moving above a conducting plate of finite thickness," *Physical Science, Measurement and Instrumentation, Management and Education - Reviews, IEE Proceedings A*, vol. 133, pp. 129-136, 1986.
- [171] S. Panas and A. G. Papayiannakis, "Eddy currents in an infinite slab due to elliptic current excitation," *IEEE Transactions on Magnetics*, pp. 4328-4337, 1991.
- [172] R. J. Ditchburn and S. K. Burke, "Planar rectangular spiral coils in eddy-current non-destructive inspection," *NDT & E International*, vol. 38, pp. 690-700, 2005.
- [173] R. J. Ditchburn, S. K. Burke, and M. Posada, "Eddy-Current Nondestructive Inspection with Thin Spiral Coils: Long Cracks in Steel," *Journal of Nondestructive Evaluation*, vol. 22, pp. 63-77, 2003/06/01 2003.
- [174] C. M. Butler, X. Xiao-Bang, and A. W. Glisson, "Current induced on a conducting cylinder located near the planar interface between two semi-infinite half-spaces," *IEEE Transactions on Antennas and Propagation*, vol. 33, pp. 616-624, 1985.

- [175] X. Xiao-Bang and C. M. Butler, "Current induced by TE excitation on a conducting cylinder located near the planar interface between two semi-infinite half-spaces," *IEEE Transactions on Antennas and Propagation*, vol. 34, pp. 880-890, 1986.
- [176] C. M. Butler, "Current induced on a conducting strip which resides on the planar interface between two semi-infinite half-spaces," *IEEE Transactions on Antennas and Propagation*, vol. 32, pp. 226-231, 1984.
- [177] P. Hammond, "The calculation of the magnetic field of rotating machines. Part 3: Eddy currents induced in a solid slab by a circular current loop," *Proceedings of the IEE - Part C: Monographs*, vol. 109, pp. 508-515, 1962.
- [178] J. W. Luquire, W. E. Deeds, and C. V. Dodd, "Alternating Current Distribution Between Planar Conductors," *Journal of Applied Physics*, vol. 41, pp. 3983-3991, 1970.
- [179] C. S. Antonopoulos and E. E. Kriezis, "Force on a parallel circular loop moving above a conducting slab and the eddy-current distribution," *IEE Proceedings A Physical Science, Measurement and Instrumentation, Management and Education - Reviews*, vol. 133, pp. 601-605, 1986.
- [180] K. R. Davey, H. C. Han, and L. Turner, "3D transient eddy current fields using the u-v integral-eigenvalue formulation," *Journal of Applied Physics*, vol. 63, pp. 991-996, 1988.
- [181] T. P. Theodoulidis, N. V. Kantartzis, T. D. Tsiboukis, and E. E. Kriezis, "Analytical and numerical solution of the eddy-current problem in spherical coordinates based on the second-order vector potential formulation," *IEEE Transactions on Magnetics*, vol. 33, pp. 2461-2472, 1997.
- [182] T. P. Theodoulidis and E. E. Kriezis, "Impedance evaluation of rectangular coils for eddy current testing of planar media," *NDT & E International*, vol. 35, pp. 407-414, 2002.
- [183] W. R. Smythe, *Static and Dynamic Electricity*, Second ed.: McGraw-Hill Book Company Inc., 1950.
- [184] P. Hammond, "Use of potentials in calculation of electromagnetic fields," *IEE Proceedings A Physical Science, Measurement and Instrumentation, Management and Education - Reviews*, vol. 129, pp. 106-112, 1982.
- [185] S. H. H. Sadeghi and A. H. Salemi, "Electromagnetic field distributions around conducting slabs, produced by eddy-current probes with arbitrary shape current-carrying excitation loops," *IEE Proceedings - Science, Measurement and Technology*, vol. 148, pp. 187-192, 2001.

- [186] J. R. Reitz and L. C. Davis, "Force on a Rectangular Coil Moving above a Conducting Slab " *Journal of Applied Physics*, vol. 43, 1972.
- [187] J. L. T. Klauder, "A Magnetic Field Diffusion Problem " *American Journal of Physics*, vol. 37, 1969.
- [188] S. H. H. Sadeghi and A. H. Salemi, "Field distribution due to a current-carrying loop of arbitrary shape above a conducting half-space," *IEEE Transactions on Magnetics*, vol. 32, pp. 4344-4346, 1996.
- [189] "Survey of Technology for High Speed Ground Transport," U. S. D. o. Commerce, Ed., ed. Washington, D.C, June 1965.
- [190] L. Urankar, "Survey of basic magnetic levitation research in Erlangen," *IEEE Transactions on Magnetics*, vol. 10, pp. 421-424, 1974.
- [191] L. Urankar, "Electrodynamics of Finite Width Guideway Maglev Systems in an Integral Equation Formulation," *Siemens Forschung Entwicklungsberichte*, vol. 8, pp. 204-208, 1979.
- [192] T. Theodoulidis and J. R. Bowler, "Interaction of an Eddy-Current Coil With a Right-Angled Conductive Wedge," *IEEE Transactions on Magnetics*, vol. 46, pp. 1034-1042, 2010.
- [193] A. H. Sodano, J. Bae, J. D. Inman, and K. W. Belvin, "Improved Concept and Model of Eddy Current Damper," *Journal of Vibration and Acoustics* vol. 128, pp. 294-302 2005.
- [194] C. M. Hebbert, "Some Applications of the Method of Images—II," *Physical Review*, vol. 17, pp. 157-160, 1921.
- [195] D. Rodger and J. F. Eastham, "Dynamic behavior of linear induction machines in the heave mode," *IEEE Transactions on Vehicular Technology*, vol. 31, pp. 100-106, 1982.
- [196] A. Musolino, R. Rizzo, and E. Tripodi, "Analytical model of a travelling wave multipole field electromagnetic launcher," in *16th International Symposium on Electromagnetic Launch Technology (EML)*, 2012, 2012, pp. 1-6.
- [197] E. P. Furlani, *Permanent Magnet & Electromechanical Devices*. New York: Academic, 2001.
- [198] F. C. Moon, *Superconducting Levitation: Applications to Bearings and Magnetic Transportation*: WILEY-VCH Verlag GmbH & Co. KGaA, 2004.

- [199] L. T. a. J. Tichy, "Stiffness and Damping of an Eddy Current Magnetic Bearing," *Journal of Tribology*, vol. 114, pp. 600-605, 1992.
- [200] R. F. Post and D. D. Ryutov, "Ambient-Temperature Passive Magnetic Bearings: Theory and Design Equations," presented at the 6th International Symposium on Magnetic Bearings, Cambridge, Massachusetts, 1998.
- [201] K. Higashi, S. Ohashi, H. Ohsaki, and E. Masada, "Damping Mechanism of the Superconducting Electrodynamic Suspension System," in *Nonlinear Electromagnetic Systems: Proceedings of the International IOS Press.*, 1996.
- [202] K. Yoshida and M. Takakura, "Magnetic damping and stiffness coefficients in superconducting maglev system with sheet guideways," *Electr. Eng. Japan*, vol. 99, pp. 797-804, 1979.
- [203] L. Urankar, "Intrinsic damping in basic magnetic levitation systems with a continuous sheet track," *Siemens Forschungs -und Entwicklungsberichte*, vol. 5, pp. 110-119, 1996.
- [204] B. T. Ooi, "Electromechanical stiffness and damping coefficients in the repulsive magnetic levitation system," *IEEE Transactions on Power Apparatus and Systems*, vol. 95, pp. 936-943, May/June 1976.
- [205] J. R. Reitz and L. C. Davis, "Force on a rectangular coil moving above a conducting slab," *Journal of Applied Physics*, vol. 43, pp. 1547-1553, April 1972.
- [206] J. Langerholc, "Torques and forces on a moving coil due to eddy currents," *J. Appl. Phys.*, vol. 44, pp. 1587-1594, Apr. 1973.
- [207] J. Miericke and L. Urankar, "Theory of electrodynamic levitation with a continuous sheet track - part I," *Appl. Phys.*, vol. 2, pp. 201-211, 1973.
- [208] J. V. Bladel and D. D. Zotter, "Magnetic levitation: The track currents," *Appl. Phys. B*, vol. 34, pp. 193-201, 1984.
- [209] F. Fu and J. Bowler, "Transient eddy-current driver pickup probe response due to a conductive plate," *IEEE Trans. Mag.*, vol. 42, pp. 2029-2037, 2006.
- [210] M. Fan, P. Huang, B. Ye, D. Hou, G. Zhang, and Z. Zhou, "Analytical modeling for transient probe response in pulsed eddy current testing," *NDT&E International*, vol. 42, pp. 376-383, 2009.
- [211] T. Theodoulidis, "Developments in calculating the transient eddy-current response from a conductive plate," *IEEE Trans. on Mag.*, vol. 44, pp. 1894-1896, 2008.

- [212] E. P. Furlani, *Permanent magnet and electromechanical devices materials, analysis, and applications*. San Diego: Academic Press, 2001.
- [213] O. D. Jefimenko, *Electricity and Magnetism*. New York: Meredith Publishing Co., 1966.
- [214] S. Paul and J. Bird, "A 3-D Analytic Eddy Current Model for a Finite Width Conductive Plate," *accepted for publication in COMPEL: The International Journal for Computation and Mathematics in Electrical and Electronic Engineering*, 2013.
- [215] T. P. Theodoulidis and J. R. Bowler, "Impedance of an induction coil at the opening of a borehole in a conductor," *Journal of Applied Physics*, vol. 103, 2008.
- [216] K. E. Atkinson, *An Introduction to Numerical Analysis*: John Wiley & Sons, Inc. , 1989.
- [217] S. Paul, W. Bomela, and J. Bird, "Dynamic Modeling of an Electrodynamic Maglev Vehicle," in *19th Conference on the Computation of Electromagnetic Fields (accepted for presentation)*, Budapest, Hungary, 2013.

APPENDIX A : DERIVATION OF CONTINUOUS FOURIER SERIES FROM DISCRETE FOURIER TRANSFORM (DFT)

At first conversion of a single dimensional discrete Fourier sequence into continuous Fourier series will be discussed and then double sided Fourier series will be considered.

An arbitrary function $f(x)$ of x for $x \in [0, l]$ is shown in Figure A. 1. To recreate the function using continuous Fourier series, $f(x)$ is sampled at N sampling points as shown in Figure A. 1 with the sampling interval of

$$\Delta x = l / N \quad (\text{A.5})$$

Hence the sampling frequency is

$$f_s = \frac{1}{\Delta x} = \frac{N}{l} \quad (\text{A.6})$$

According to Nyquist's sampling theorem, the sampling frequency (f_s) must be at least twice the maximum frequency of the sampled waveform.

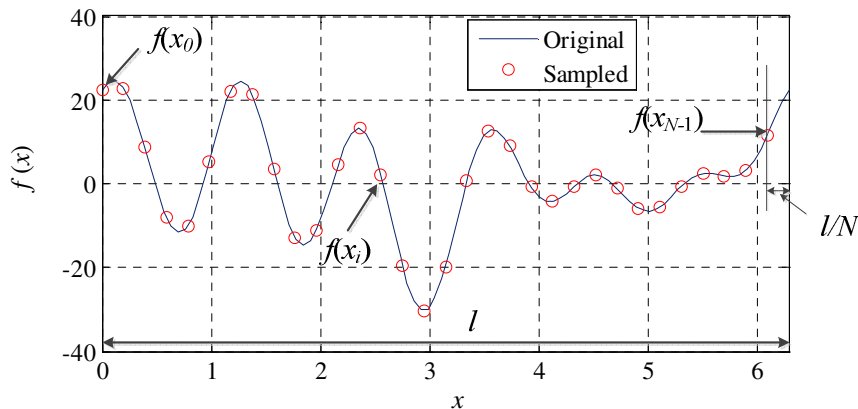


Figure A. 1. A continuous function $f(x)$ defined over l and its sampled form $f(x_i)$ is shown. Discrete Fourier transform is applied on the sampled function over l .

After taking discrete Fourier transform (DFT) of the sampled waveform $f(x_i)$, the resulting sequence comprises of the harmonics of $f(x)$ as given below

$$F_n = \sum_{i=0}^{N-1} f(x_i) e^{-j\xi_n x_i}, \quad 0 \leq n \leq N-1 \quad (\text{A.7})$$

are the Fourier frequency components of $f(x)$

where

$$\xi_n = \frac{2\pi n}{l} \quad (\text{A.8})$$

are the Fourier frequencies with respect to x

and

$$x_i = i\Delta x \quad (\text{A.9})$$

The magnitude and phase spectrum generated by DFT is shown below

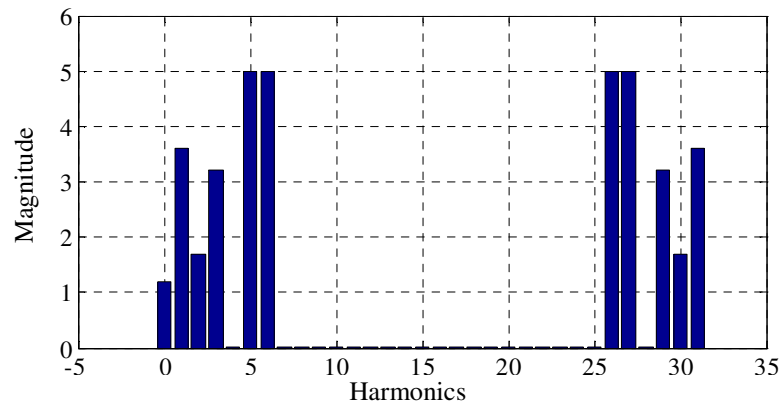


Figure A. 2. Magnitude spectrum of $f(x)$ after taking DFT using Matlab.

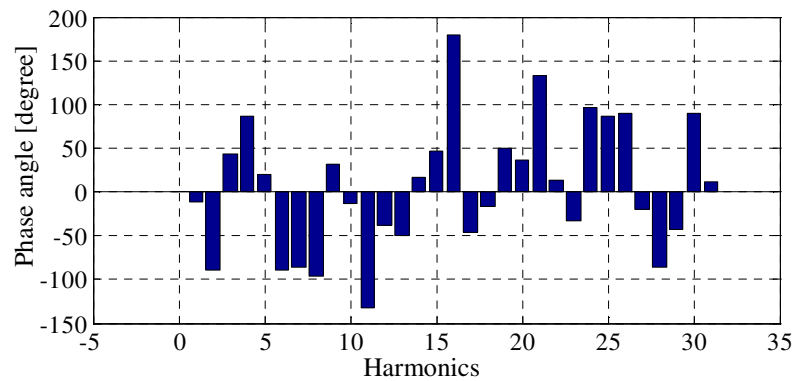


Figure A. 3. Phase spectrum of $f(x)$ after taking DFT using Matlab.

The magnitude and phase spectra given by Figure A. 2 and Figure A. 3 can be represented in terms of F_n in a more compact form as shown in Figure A. 4.

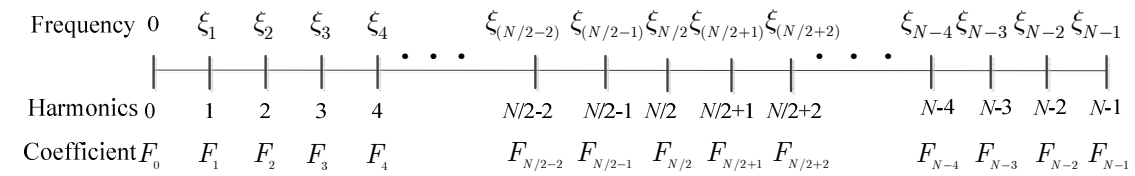


Figure A. 4. Discrete Fourier frequency components of $f(x)$ after DFT.

However, from the definition of DFT (A.7) and (A.8), it can be noticed that

$$\begin{aligned}
 \xi_{N/2+1} &= -\xi_{N/2-1} \\
 \xi_{N/2+2} &= -\xi_{N/2-2} \\
 &\vdots \\
 &\vdots \\
 \xi_{N-3} &= -\xi_3 \\
 \xi_{N-2} &= -\xi_2 \\
 \xi_{N-1} &= -\xi_1
 \end{aligned}
 \tag{A.10}$$

Using (A.10), the spectrum of Figure A. 4 can be modified to the one shown in Figure A. 5. It can be noticed that $F_{N/2}$ is a redundant component. However, it is noticed in Figure A. 5 that the harmonic components are not centered on the zero frequency component. Hence ‘*fftshift*’ command in Matlab is necessary to shift the frequency spectrum to its right as illustrated in Figure A. 6. Figure A. 7 and Figure A. 8 show the magnitude and phase spectrum of $f(x)$ after using ‘*fftshift*’. The spectrum is now symmetric with respect to the zero frequency or dc component. It must be noted here that if $f(x)$ is a complex valued function, either side of zero harmonic of Figure A. 6 may not be complex conjugate of the other side i.e. $F_{-(N/2-1)}$ may not be complex conjugate of $F_{(N/2-1)}$.

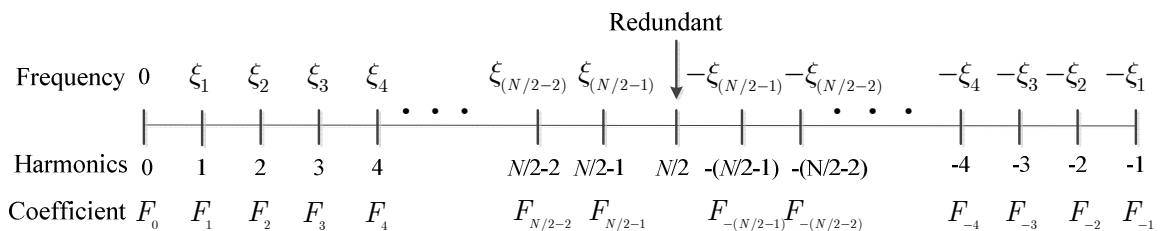


Figure A. 5. Frequency spectrum of $f(x)$ after taking DFT using Matlab.

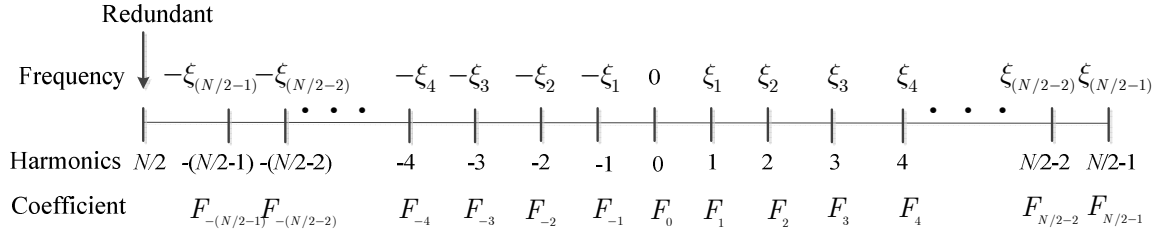


Figure A. 6. Frequency spectrum of $f(x)$ after taking DFT and using 'fftshift' command in Matlab. The spectrum is centered on the zero frequency component.

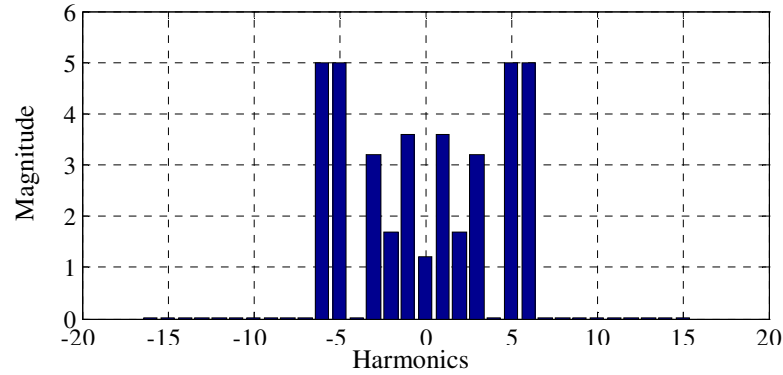


Figure A. 7. Magnitude spectrum of $f(x)$ after taking DFT and using 'fftshift' command in Matlab.

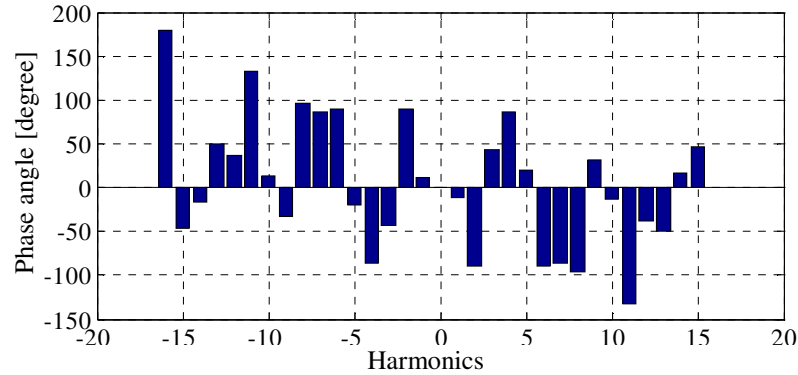


Figure A. 8. Phase spectrum of $f(x)$ after taking DFT and using 'fftshift' command in Matlab.

By observing the spectrum shown in Figure A. 6, the continuous function $f(x)$ can be written as

$$f(x) = F_0 + \sum_{n=1}^{(N/2-1)} \left(F_n e^{j\xi_n x} + F_{-n} e^{-j\xi_n x} \right) \quad (\text{A.11})$$

Or, in a more compact form using complex Fourier series notation,

$$f(x) = \sum_{n=-(N/2-1)}^{(N/2-1)} F_n e^{j\xi_n x} \quad (\text{A.12})$$

Equation (A.12) reconstructs $f(x)$ in continuous space over x -axis. Figure A. 9 shows the reconstructed function using (A.12) along with the original function $f(x)$. The Matlab code is provided in Table A. 1.

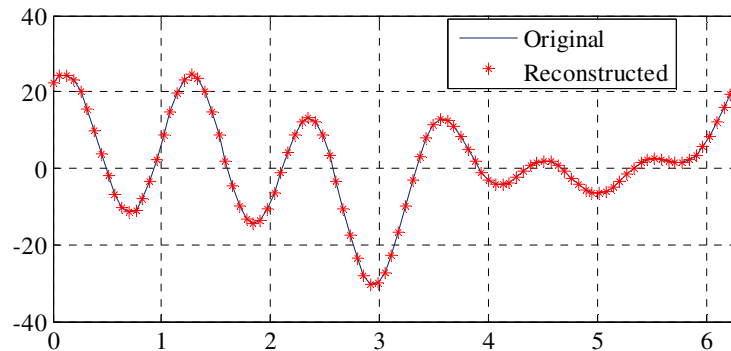


Figure A. 9. Original and reconstructed $f(x)$.

Table A. 1. Matlab code for reconstructing waveform using complex Fourier series and DFT

```

%% Calculate DFT sequence of any given function f(x)

L=2*pi;
period_X=L; % period of function f(x)
N=2^5; % Number of samples
x=linspace(0,period_X-period_X/N,N); % define sampling points

%% tabulate f(x) at x points
fx=1.2+3.4.*sin(2.*x)+6.4.*cos(3.*x+0.75)+7.2.*cos(x-0.2)+10.*cos(5.*x+0.35)+10.*sin(6.*x);

func_fft=fftshift(fft(fx)/N); % creates Fourier sequence

% Calculate coefficients of Complex Fourier Series
p=(1:N-1)';
wx=2*pi*(p-N/2)/L; % spatial frequency w.r.t. x

F0= func_fft(N/2+1); % coefficient of dc term
for count1=1:N/2-1
    F_pos(count1)= func_fft(N/2+1+count1); % coefficient of positive harmonics
    F_neg(count1)= func_fft(N/2+1-count1); % coefficient of negative harmonics
end

x2=linspace(0,L,70); % define new set of x

% computes f(x)
Orig_fx= 1.2+3.4.*sin (2.*x2)+6.4.*cos(3.*x2+0.75)+7.2.*cos(x2-0.2)+10.*cos(5.*x2+0.35)
+10.*sin(6.*x2);
figure; plot(x2, Orig_fx);grid on; % plots f(x) over x2

% Reconstruction of f(x)

Recon_fx=F0;
for p=1:N/2-1

```

```

Recon_fx=Recon_fx+ F_pos(p).*exp(1i*wx(N/2+p)*x2)+
                F_neg(p).*exp(1i*wx(N/2-p)*x2);
end
hold on; plot(x2,Recon_fx);grid on; % plots reconstructed f(x) over x2

```

The obtained complex Fourier series of (A.12) can be readily converted into a real series of the form

$$f(x) = \sum_{n=0}^{(N/2-1)} [a_n \cos(\xi_n x) + b_n \sin(\xi_n x)] \quad (\text{A.13})$$

By noting that

$$e^{j\xi_n x} = \cos(\xi_n x) + j \sin(\xi_n x) \quad (\text{A.14})$$

and

$$e^{-j\xi_n x} = \cos(\xi_n x) - j \sin(\xi_n x) \quad (\text{A.15})$$

it is easily found that

$$a_0 = F_0 \quad (\text{A.16})$$

$$a_n = F_n + F_{-n} \quad (\text{A.17})$$

$$b_n = j(F_n - F_{-n}) \quad (\text{A.18})$$

Reconstruction of a two-dimensional function using 2-D DFT follows the same procedure as single dimension. In 2-D, the frequency spectrum is not a line vector as was shown in Figure A. 6, but instead a matrix which, after using ‘*fftshift*’ looks like as shown in Figure A. 10. It is assumed that a 2-D function $f(x,z)$ is discrete Fourier transformed over the x and z directions with M and N samples respectively. The period of the function along x and z -axes are l and w respectively.

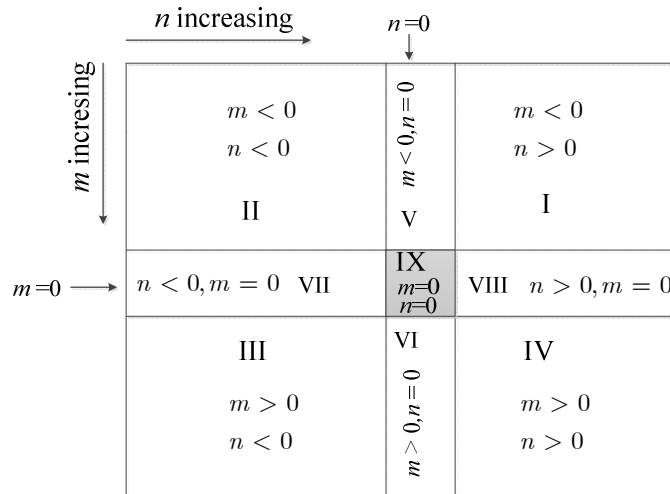


Figure A. 10. Discrete frequency spectrum of $f(x,z)$ after taking 2-D DFT and ‘fftshift’ using Matlab.

From Figure A. 10, $f(x,z)$ can be obtained from its frequency spectrum using the following double complex Fourier series

$$f(x, z) = \sum_{m=-\frac{M}{2}}^{\frac{M}{2}-1} \sum_{n=-\frac{N}{2}}^{\frac{N}{2}-1} F_{m,n} e^{j\xi_m x} e^{jk_n z} \tag{A.19}$$

where
$$k_n = \frac{2\pi n}{w} \tag{A.20}$$

and ξ_m is defined by (A.8).

Using (A.14) and (A.15), (A.19) can be written in terms of sine and cosine series as

$$f(x, z) = \sum_{m=0}^{\frac{M}{2}-1} \sum_{n=0}^{\frac{N}{2}-1} \left[a_m^x \cos(\xi_m x) + b_m^x \sin(\xi_m x) \right] \left[a_n^z \cos(k_n z) + b_n^z \sin(k_n z) \right] \tag{A.21}$$

Equation (A.21) can also be written as

$$\begin{aligned}
f(x, z) = c_{0,0} + \sum_{m=1}^{M/2-1} \left[c_m^x \cos(\xi_m x) + d_m^x \sin(\xi_m x) \right] + \\
\sum_{n=1}^{N/2-1} \left[c_n^z \cos(k_n z) + d_n^z \sin(k_n z) \right] \\
\sum_{m=0}^{M/2-1} \sum_{n=0}^{N/2-1} \left\{ A_{mn} \cos(\xi_m x) \cos(k_n z) + B_{mn} \sin(\xi_m x) \cos(k_n z) \right. \\
\left. + C_{mn} \cos(\xi_m x) \sin(k_n z) + D_{mn} \sin(\xi_m x) \sin(k_n z) \right\}
\end{aligned} \tag{A.22}$$

where the coefficients are given by

$$c_{0,0} = F_{0,0} \tag{A.23}$$

$$c_m^x = F_{m,0} + F_{-m,0} \tag{A.24}$$

$$d_m^x = j(F_{m,0} - F_{-m,0}) \tag{A.25}$$

$$c_n^z = F_{0,n} + F_{0,-n} \tag{A.26}$$

$$d_n^z = j(F_{0,n} - F_{0,-n}) \tag{A.27}$$

$$A_{mn} = F_{m,n} + F_{m,-n} + F_{-m,n} + F_{-m,-n} \tag{A.28}$$

$$B_{mn} = j(F_{m,n} + F_{m,-n} - F_{-m,n} - F_{-m,-n}) \tag{A.29}$$

$$C_{mn} = j(F_{m,n} - F_{m,-n} + F_{-m,n} - F_{-m,-n}) \tag{A.30}$$

$$D_{mn} = (-F_{m,n} + F_{m,-n} + F_{-m,n} - F_{-m,-n}) \tag{A.31}$$